Electron Correlation in the Two-Color Photoionization and Laser Dissociation of H_2^+

by

Averell Gatton

A dissertation submitted to the Graduate Faculty of
Auburn University
in partial fulfillment of the
requirements for the Degree of
Doctor of Philosophy

Auburn, Alabama
August 4, 2018

Keywords: COLTRIMS, Photoionization, Strong Field, Photo-Chemistry

Approved by

Allen Landers, Michael Fogle, Stuart Loch, Guillaume Laurent, Konrad Patkowski

Abstract

We have constructed, to our knowledge, a first of its kind two-color pulsed synchrotron (XUV) and strong field laser (IR) COld Target Recoil Ion Momentum Spectroscopy (COLTRIMS) experiment. We describe the design, operation, and commissioning experiments of the new machine. We also present the first scientific results from a two color experiment: the photoionization of H_2 with $18.49eV$ and $17.9eV$ XUV photons from the Advanced Light Source (ALS) at Lawrence Berkeley National Lab (LBNL) in the presence of a strong laser field ($1.2eV$, $\approx 1 \times 10^{12} W/cm^2$). We investigated the effects of the strong field on all aspects of the photoionization and subsequent dissociation processes proceeding directly from the single ionization or driven by the strong laser field. We employ statistical background subtraction as well as comparison between long and overlapped XUV-laser pulse configurations to sensitively observe changes to energy spectra and angular distributions of the photoelectron and the dissociated proton. We report observations of ponderomotive shifts in the photoelectron energy. However, we report no observation of interference fringes from light induced conical intersections that are expected to be present. Additionally, we report on possible hints of asymmetric proton emission in the laser driven dissociation from the retro-action of the photoelectron.

Acknowledgments

The road to graduation has been a long one, but the journey has been worthwhile. There are many tremendously talented and kind individuals who I have had the good fortune to meet over the past eight years. Little did I know I would study in a field so different from what I had originally intended to study, or that I would conduct most of my research not in Auburn, but in Berkeley California at Lawrence Berkeley National Lab. I could never have imagined the intentional community I found in Hillegass-Parker House, where I lived with 58 other graduate students. My experience in Auburn, in Berkeley, and at LBNL have been some of the most formative and joyful in my life, and I will cherish the memories of my journey.

For his good nature, compassion, and tremendous scientific insight and guidance, I thank my advisor Dr. Allen Landers. Throughout my graduate career, Allen was a source of lighthearted wisdom and encouragement when times were tough. It is not easy to stay committed to a program for 8 years, but it was Allen who's support was invaluable in helping me see it through to completion.

For his uncompromising standards, unimpeachable resolve, unparalleled expertise, honest integrity, and good heart, I thank my ex-officio advisor Thorsten Weber; who, for five years during my time at LBNL, molded me into the experimentalist I am today. I am a better scientist for the experience. It is hard to overstate the amount of patience required on Thorsten's part to oversee my development. Truly, Thorsten has given me the confidence to move forward in my feature endeavors.

For his joviality, wealth of scientific insight, and great spirit, I thank Dan Slaughter. Always a pleasure to work with, Dan's lightheartedness has kept me going when the going

got tough. His experimental expertise and scientific input were invaluable in running the two-color experiment.

For their unconditional love and support I thank my parents Jillian McNamara and Dave Gatton. Jillian, for her pragmatic attitude and example of a joyfully lived life. Dave, for his wisdom and for keeping my attention focused on the meaningful things in life. I have been blessed with two wonderful parents.

I thank the collaborators, the Germans Miriam Weller, Johnathan Neff, Florian Weigant, and Saijoscha Heck for their wonderful camaraderie during their stay at LBNL. I have learned more from them than I have trying to help them. I thank Travis Severt from Kansas State University for his invaluable help during beamtimes.

I thank my compatriots at LBNL: Kirk Larsen, Elio Champenois, Felix Sturm, Niranjan Shivaram, Brant Ablen, Dip Ray, and Travis Wright, without whom I would not have made it to the finish line.

I thank those Auburn gentlemen who made Auburn feel like home: Dylan Reedy, Peter Traverso, and Ivan Arnold. One could not ask for better friends. I thank Kamila Midor for her friendship and support while I was writing.

I thank all those people who have lifted me up at Hillegass Parker House. They have a special place in my heart.

With Love & Gratitude,

Averell Gatton

Table of Contents

List of Figures

List of Tables

Chapter 1

Introduction

It is best to begin this introduction in as broad a context as possible, by connecting the work of this thesis with the DOE grand challenge #3: "How do remarkable properties of matter emerge from complex correlations of the atomic or electronic constituents and how can we control these properties?" This goal connects to the AMO field via the "Direct manipulation of... the pathways of chemical reactions and the strength of chemical bonds..."[1]. Specifically this means controlling branching ratios, atomic motion, and even electronic motion in real time. To do so, we will need a detailed understanding of electron correlation, defined as the way electrons react to each other in atoms and molecules. Furthermore, we will need to go beyond the Born-Oppenheimer approximation, where the nuclei in a molecule are treated as fixed, and understand how electronic correlation drives and is driven by nuclear motion. These processes underlie the entire field of chemistry. We have advanced towards these goals by constructing a new 2-color laser-synchrotron experiment that is the first of its kind and is the subject of this thesis.

To achieve the grand challenge it is highly likely that strong laser fields must be used. However, our understanding of the photoionization processes in strong fields, particularly of excited states, is limited by current experimental methods. That is to say, that the very methods of studying ultrafast dynamics obscure the dynamics to be studied. Rather, most strong field laser experiments are instead probing processes that are inherently altered by the method of measurement. In a 2014 Nature Perspectives review article "What will it take to observe processes in 'real time' " [2] written by some of the most prominent scientists in the field, the authors state:

> "Formidable challenges have arisen that counterbalance the promise of these early successes. A strong probe light field can modify the potential surfaces and alter the dynamics one is trying to observe. As most measurements are performed in a complicated temporal regime in which two pulses overlap, simplified descriptions of the time-dependent wave function are insufficient. Most importantly, there is an urgent need to separate processes driven or altered by the various probing light fields from the natural time dynamics one is seeking to measure."

In comparison to "typical" spectroscopy, there has not been the same kind of simple, gas phase, high resolution, spectroscopic experiments exploiting synchrotron light sources applied to molecules in strong fields. It appears that some fundamental experimental steps were skipped as the field developed.

To study molecules in strong fields we have constructed a new apparatus to bridge the gap between synchrotron spectroscopy and ultrafast strong field physics. We have built a strong field two color synchrotron-laser Cold Target Recoil Ion Momentum Spectroscopy (COLTRIMS) experiment. Other groups, see [3] and [4] and reviews by [5] and [6], have constructed two color synchrotron experiments but none are capable of producing a strong laser field. This new machine represents the missing link between high resolution, high repetition rate synchrotron spectroscopy with relatively low repetition rate, wide bandwidth, ultrafast laser experiments.

With our new apparatus we are able to observe strong field dissociation of specific bound cation states selected by the tunable synchrotron light source. Conversely, a single, tunable, high resolution, high energy (XUV - XRay) photon from the synchrotron can be used to probe molecular behavior in a strong field. The synchrotron light is a weak field and is free from other confounding photon energies present in most high harmonic generation experiments. For example, synchrotron light is ideal for investigating deformation of polar molecules, changes in branching ratios, changes in the molecular potential around site specific atoms, all due to the presence of a strong field. Another possible direction of research is

alignment of large polar molecules where the axial-recoil approximation breaks down and the molecular frame cannot be reconstructed in post processing.

We will observe these effects with the power of COLTRIMS: the only experimental method capable of producing kinematically complete coincidence measurements of charged multi-particle fragmentation. COLTRIMS has its origins in atom-ion collision experiments and was part of a family of progressively more complicated coincidence spectroscopy that was driven by the widespread construction of tunable synchrotron light sources and the development of multi-channel plate detectors in the 70's, and 80's. Complete reviews of COLTRIMS can be found by Dörner et al. [7], Jahnke et al. [8], and Ullrich et al. [9]. COLTRIMS is an extremely powerful technique, and experiments are only limited by the imagination of the scientist, to list but a few: timing Inter Coulombic Decay (ICD) by mapping onto ion Kinetic Energy Release (KER) [10]: proton migration [11]: a molecular double slit [12]: symmetry breaking in H_2 [13]: probing electron localization [14]: producing the Fully Differential Cross Sections for H_2 [15] and D_2 [16] [17]: and many others too numerous to list here.

The experimental program with this machine is only in it's infancy, and there is no doubt a great number of interesting experiments in the future. The results from the first two beamtimes will be presented in chapter 6. Briefly, we have studied the strong field dissociation dynamics of hydrogen cation H_2^+ prepared by ionization with the synchrotron at just above the dissociation threshold. We investigated the light induced conical intersection caused by the strong field. Furthermore, it was recently discovered by Waitz et al. [18] that the photoelectron and bound electron remain correlated after photoionization and produce an asymmetry in the direct dissociation process (without the laser). We investigate whether any electron correlation remained between the photoelectron and the bound electrons during the laser dissociation.

1.1 Document Structure

This thesis is organized into six chapters. Chapter 1 is the introduction. Chapter 2 builds the scientific case for the two color photoionization (XUV) and concurrent laser dissociation (IR) of H_2. Chapter 3 describes all elements of the standard COLTRIMS experiment, followed by the elements for the two color extension. The third chapter ends with a feasibility rate estimation of the expected two color signal. Chapter 4 explains the general analysis procedure. Chapter 5 contains the experimental details specific to the results presented in chapter 6. In chapter 6, we present our analysis of the two color signal rate, ponderomotive shifts, potential photoelectron asymmetries, and angular distributions. We conclude in chapter 7. The appendix contains a wealth of other spectra including ponderomotive shifts and angular distributions for each of the four datasets from the experiment. An appendix on basic theory is also included. Of note, an extensive analysis and modeling of a COLTRIMS spectrometer can also be found in the appendix. Other minor appendices contain software code.

A note on writing style. Some portions of this document are colloquial or manual in nature and are not fit for publication in a peer reviewed journal. This is a deliberate choice on the part of the author to provide a more approachable and complete document for those who will use the two-color experiment in the future. However, the author would like to emphasize that the scientific results contained within this thesis are rigorous and meet the highest standards of scientific inquiry. A great effort has been made to present results at a level that exceeds the bar for peer review.

Chapter 2

Scientific Motivation

H_2, nature's simplest molecule, has been studied expansively. To inform this experiment, we can draw heavily from a great body of work, including laser dissociation [19], ultrafast studies of electron localization [20] [21] [22], symmetry breaking by lasers [23] [24] and synchrotron radiation [13] [25] [26], and others. We have constructed a two color experiment where we can measure photoionization of H_2 in a strong laser field near the dissociative threshold. There are a number of interesting processes that occur in this energy regime: chief among them is the light induced conical intersection in strong fields and the retro action of the photoelectron. In what follows, we outline these processes and discuss relevant literature before returning to the hypothetical processes in our specific experiment.

2.1 Retro-action

The retro-action of the photoelectron refers to the ability of the outgoing photoelectron to influence the dissociation of the parent cation after it has been ejected into the continuum. Specifically, the field of the outgoing electron couples the $1s\sigma_g$ and $2p\sigma_u$ states of the cation near the dissociation limit. This coupling breaks the symmetry of the dissociating cation such that the dissociating proton favors following the photoelectron. Equivalently, the remaining bound electron is localized on the proton furthest from the photoelectron, as imaged in figure 2.1. This was only recently predicted by Serov and Kheifets [27] and experimentally confirmed by Waitz et al. [18].

The literature contains ample evidence that there is a high degree of electron correlation in H_2. Essentially, the bound and continuum electron continue to influence each other after photoionization. While this electron correlation has been studied while both electrons are in

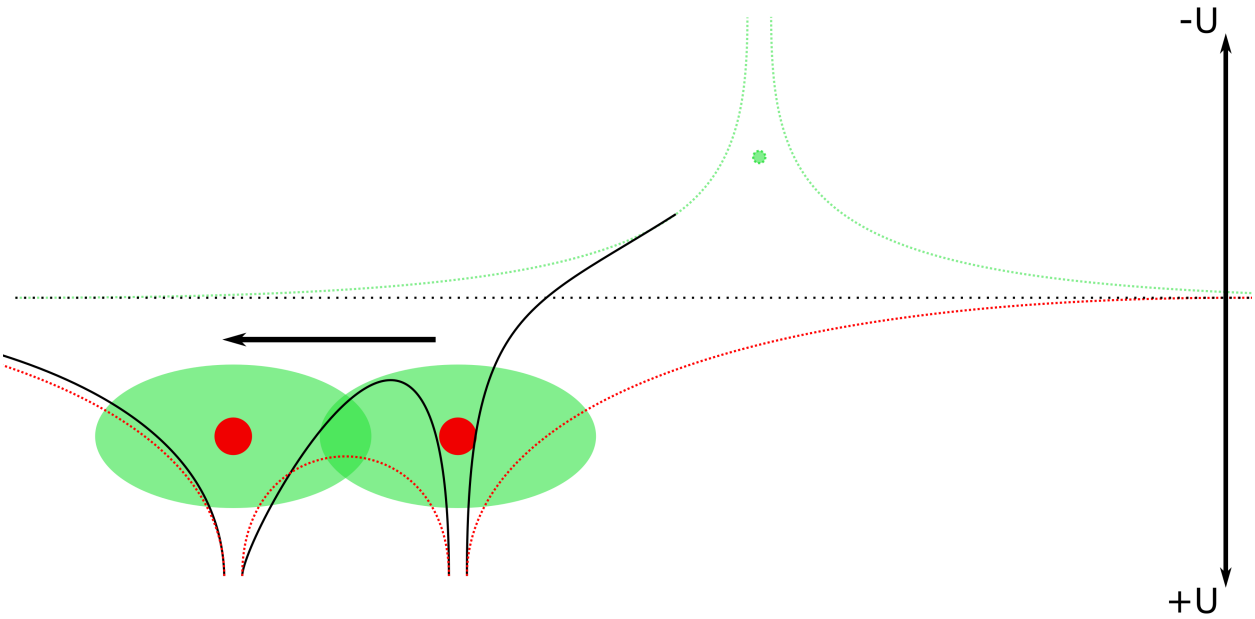

Figure 2.1: Schematic of the retro-action of the photoelectron (green circle) on the H_2+ cation represented by the two red circles with the remaining bound electron shown as a de-localized orbital over the two protons. Red and green dotted lines represent the potential of the protons and photoelectron. Black solid line represents the addition of green and red potentials. Arrow shows preferred location of bound electron

the continuum, and while one electron remains bound (Waitz et al. 's [18] work), there have been no studies of the correlation between bound and continuum electrons in a laser field.

We have independently confirmed the experimental results here in a series of COLTRIMS experiments at $18.3eV$, and $18.54eV$. Waitz et al. [18] noted that the asymmetry increases with lower electron kinetic energy. Intuitively, as the slower electron spends more time in the locality of the molecule the molecule will feel a strong retro-active field. We have investigated this effect for energies very close to the threshold and may have seen an oscillatory behavior in the asymmetry which we ascribe to a dependence of the retro-action on the wavelength and phase of the photoelectron wavefunction. For more details see the thesis of Saijoscha Heck, though this effect needs more investigation and at this time is just conjecture.

2.2 Light Induced Conical Intersections

In the case of laser driven strong field dissociation, the process is further complicated by the presence of a Light Induced Conical Intersection (LICI). Theoretically LICI arise from considering the dressed states in the Floquet picture. In the Floquet picture, the intensity of the laser is high enough that the Rabi flopping frequency in the rotating wave approximation approaches the vibrational period of the nuclear wave packet [28]. In this intensity regime, the absorption and re-emission of photons happens so often that different states are adiabatically mixed: curves are lowered and raised by one or more photon energies, as shown in figure 2.2. In H_2, the potential curves are well enough separated in energy that only the $1s\sigma_g$ and $2p\sigma_u$ curves play a role in the dissociation dynamics. The position of the curve crossing in H_2^+ is determined by the laser photon energy and the coupling is determined by the field strength [29].

In the mathematics of quantum mechanics, two new off diagonal matrix elements are added to the Hamiltonian potential matrix [30]:

$$U(R) = \begin{bmatrix} V_g(R) + \hbar\omega & V_{gu}(R) \\ V_{gu}(R) & V_u(R) \end{bmatrix}, \tag{2.1}$$

where R represents the internuclear distance, ω the laser frequency, and $V_{gu} = \hbar\omega_R/2$ is the coupling between terms with ω_R as the Rabbi flopping frequency. After diagonilzation of the matrix, the upper W_+ and lower W_- curves obey the equation

$$W_\pm(R) = \frac{V_g(R) + \hbar\omega + V_u(R)}{2} \pm \frac{1}{2}((V_g(R) + \hbar\omega - V_u(R))^2 + 4V_{gu}(R)^2)^{1/2}. \tag{2.2}$$

We can evaluate the spread in the energy levels by subtracting W_- from W_+ at the crossing point R_o where $(V_g(R_o) + \hbar\omega - V_u(R_o) = 0$, with the result

$$\Delta W_\pm(R) = 2V_{gu}(R)2\hbar\omega_R[cm^{-1}] = 2\gamma I[W/cm^2]^{1/2} d(R)[a.u.], \tag{2.3}$$

where $d(R)$ is the dipole moment in atomic units and $\gamma = 5.84 \times 10^{-4}[(1/W)^{1/2} * 1/a.u.]$ is a conversion factor [30]. The dipole moment is related to the polarizability $p(R)$ of the molecule and the electric field strength $d(R) = Ep(R)$. The polarizability of H_2^+ has been calculated by Bishop [31] and found to be $p = 237.462au$ close to the intersection of the $1030nm$ shifted Floquet state at $R = 5au$. With our experimental field intensities, we expect a state separation in the range of $(58, 218)meV$.

Three effects can occur in this picture: one, a new dissociation pathway is opened between the lower and upper curves of the adiabatic potential: two, the intensity of the field can depress the lower curve and this is termed bond softening: three, some states are trapped in the quasi bound upper potential, and this is termed bond hardening. Giusti et al. [29] provides a good review of bond softening.

Bucksbaum et al. [32] was the first to propose bond softening and study it experimentally. Aubanel et al. [30] was one of the first to theoretically investigate bond hardening of the molecular vibrations in the quasi-bound trapped adiabatic states. There has been a good deal of experimental work on studying the angular distribution of H_2^+ dissociated by strong fields. Early work focused on H_2^+ prepared by a laser pre-pulse or multi-photon ionized at the front of the strong field pulse. However, in 2000, Sandig et al. [19] was the first to strong field dissociate H_2^+ produced from an ion source. They found a dramatic difference in the angular emission patterns for vibrational states that are resonant with the crossing point of the diabatic (shifted) curves and the states that are close to the lower barrier (the adiabatic, or coupled, lower curve). For the states that dissociate close to the barrier, a strong alignment effect was observed to narrow the angular distribution of the dissociating proton. We will compare our data to that of Sandig in chapter 6. The alignment behavior was explained by Uhlmann et al. in [33] by application of full Hartree-Fock calculations - the calculated vibrational states are shown in figure 2.3 alongside our experimental distribution of photoelectron energies.

In general a conical intersection can exist only for potential curves in two or greater dimensions. The single dimension in a diatomic molecule demands avoided crossings between states of similar parity. In a strong field, the polarization of the light breaks the symmetry and introduces a second dimension along the field polarization axis and thereby the potential for a LICI. The LICI concept is a recognition that the two effects of bond hardening and softening are actually part of a two dimensional potential surface: one dimension being the bond length and the other the angle of the molecular axis with the polarization of the strong field [28]. The bound states in the upper adiabatic curve connect to the lower bond softened dissociative states by traversing a conical intersection when the molecule is perpendicular to the polarization ($\theta = \pi/2$). Halasz et al. in [28] theoretically studied LICI in D_2^+, predicting kinetic energy release and angular distributions. In a follow up work [34], the same authors predicted a direct signature of conical intersections in the interference of the two dissociation pathways for specific vibrational states of D_2^+. Natan [35] observed the effect in the dissociation of a molecular beam of H_2^+ with a $55fs$, $1.55eV$ $(795nm)$, $1 \times 10^{13} W/cm^2$ laser pulse. In more advanced experiments, Csehi [36] has demonstrated that CEP modifications of light induced conical intersections can be used to "follow" the vibrational wave packet of H_2^+ and increase the dissociation. They claim this is the first step to control the path of the molecule on the LICI surface.

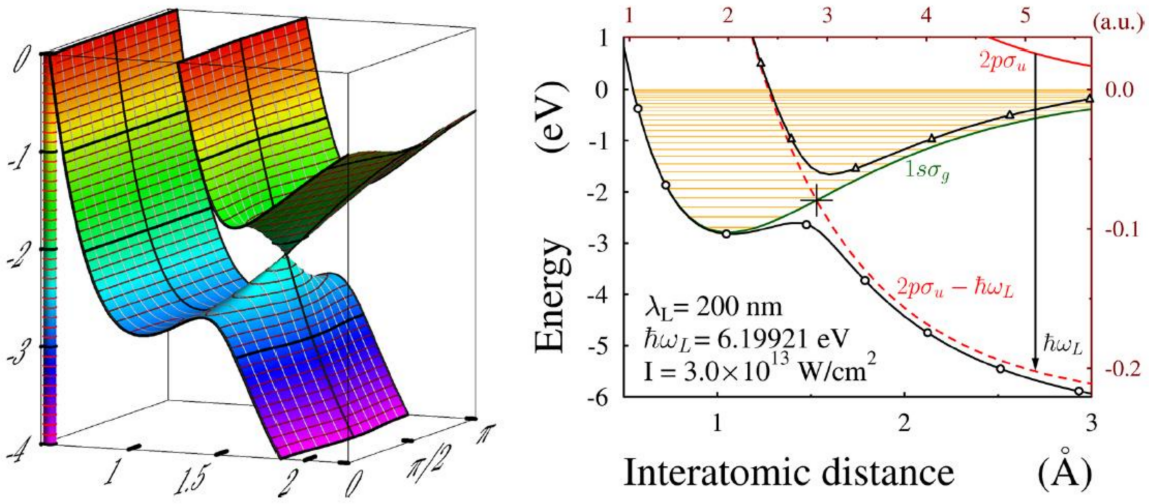

Figure 2.2: Image taken from [34]. Left: surface plot of the LICI. $\theta = \pi/2$ corresponds to the molecule perpendicular to the field, in which case the field has no effect. Right, a cut of the Floquet state avoided crossing at $\theta = 0$.

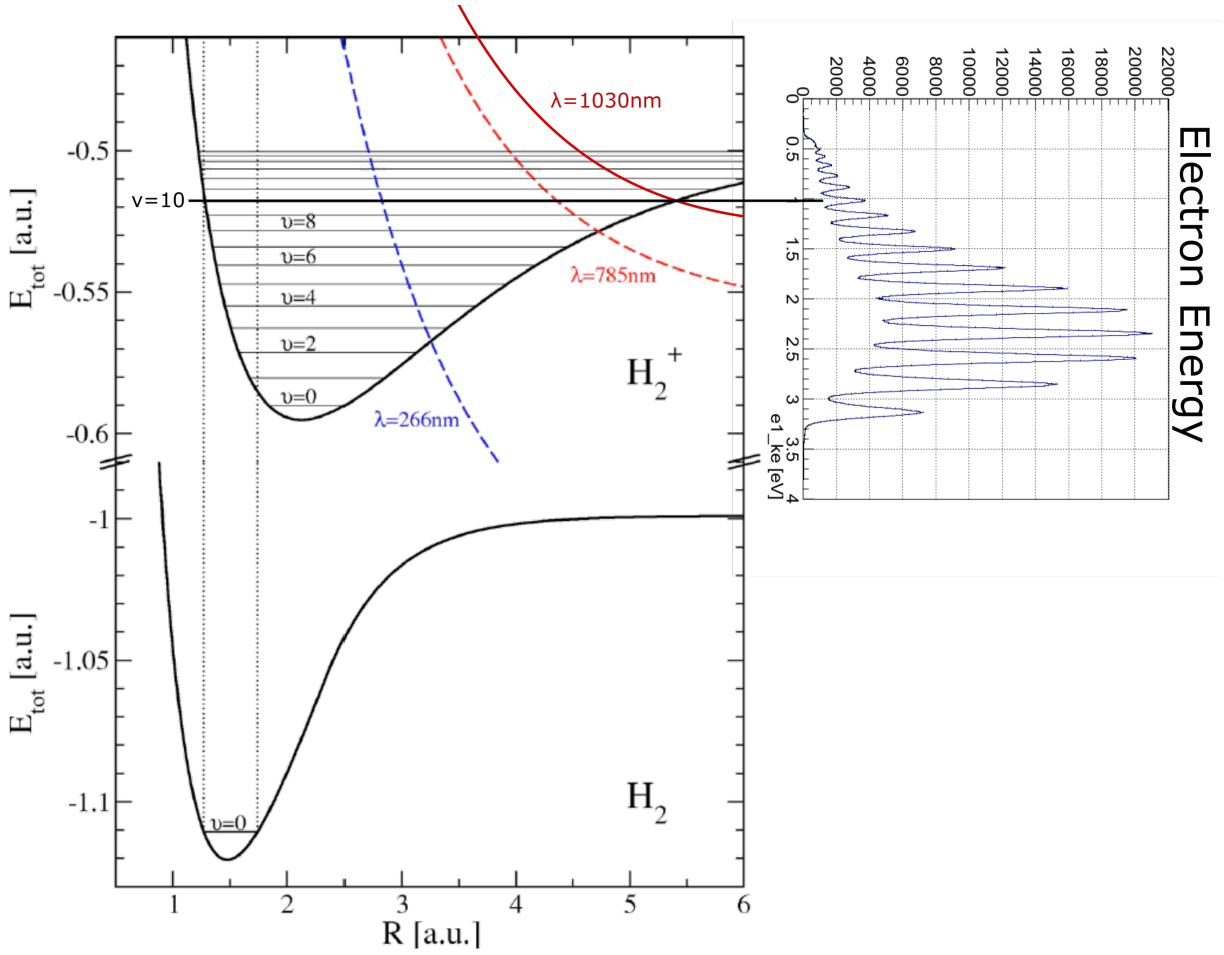

Figure 2.3: Left: Hartree-Fock calculations of the H_2 and H_2^+ potential curves taken from [33]. Colored curves show the $2p\sigma_u$ shifted one photon energy of the wavelength label. The Author has added a curve drawn to scale for $1030nm$ laser light and labeled the $\nu = 10$ resonant vibrational state. Right spectra: Electron energy distribution from the June 2017 2-color H_2 data.

2.3 Current Experiment

In our experiment, the laser can photo-dissociate the H_2^+ or ionize one of the fragments of the neutral dissociation channel discovered recently by Wei et al. [20]. The main scientific question was what effect, if any, would the outgoing photoelectron have on these laser driven dissociation processes? Can the photoelectron still break the symmetry? The germane experimental details are as follows: we ionized close to the photodissociation threshold of $18.08eV$ with the synchrotron radiation of $18.497eV \pm .015eV$ in the presence of a strong, $\approx 1 \times 10^{11} W/cm^2$, $1.2eV$, and long, $12ps$, laser pulse.

Many studies have shown that the two electrons in H_2 are inherently correlated. Waitz et al. in [25] found in synchrotron experiments on H_2 at $400eV$ that the quasi-particle dielectron displayed interference patterns where the single electrons did not. Similarly [26] showed that the relaxation of doubly excited states (at $37eV$) onto the dissociative gerade and ungerade states of H_2^+ can introduce chirality in the photoelectron distribution. Importantly the laser dissociation signal we observe may contain components of just such an excited state: as mentioned above, Wei [20] discovered a new neutral dissociation channel for doubly excited H_2 where the asymptotic products are a high lying Rydberg state and a ground state hydrogen. This channel intensity diminished as the pump photon energy was increased from $16.95eV$ to $17.45eV$ as a result of competition with the more typical bond softening route. In comparison, Wei's work represents a special case of neutral excitation, which was studied with an ultrafast pump-probe scheme by Sturm et al. [37]. They found the vibrational and dissociation dynamics of $^1\Sigma_u^+$ state to be complicated by Rydberg progressions. We may be able to observe a similar symmetry breaking from this channel if there are significant contributions at our higher energies. Since the above threshold dissociation is fast ($\approx 8fs$ [23]), we expect a purely dipole distribution that mirrors the dipole distribution of the photoelectron.

We are now finally in a position to talk of electron localization in the laser dissociation of a molecule and the potential for retro-action to influence this process. The laser can only

induce asymmetry by overlapping the gerade and ungerade states [23][38]. Wu et al. [23] studied the strong field ionization of H_2^+ by a circularly polarized femtosecond laser pulse and analyzed the angular streaking of the photoelectron. They found that even symmetric laser pulses can break the symmetry of dissociation by coupling the sigma and gerade states. This can occur in H_2^+ in the case of one photon absorption or in the case of three photon absorption and one photon emission. We expect that for our laser intensities the four photon process is vanishingly small and we observe no signature of it in our data. We conclude the laser driven dissociation alone must be completely symmetric in our experiment.

Fischer et al. [38] used Carrier Envelope Phase (CEP) stabilized lasers to study the dependence of electron localization on the vibrational motion of cation nuclei and discovered that the asymmetry is directly related to the position of the nuclear wave packet relative to the phase of the laser pulse and time delay of the probe pulse. To compare with our experiment, when we ionize into the laser dressed Floquet states, this is equivalent to zero time delay. The bandwidth of the synchrotron in our experiment is $\approx 10meV$ while the bandwidth of the laser pulse used in [38] is $\approx 700meV$. Consequently, the nuclear wave packet in our experiment is more de-localized spatially in the potential well of the cation. This corresponds to integrating the data in [38] over time delay. Again, no asymmetry would be observed when also integrating over the CEP. According to the experimental picture shown in 2.2, we can produce asymmetry by first absorbing a laser photon to the $2p\sigma_u$ and then coupling back down to the $1s\sigma_g$ state via the retro-action. The bound molecular states dissociated by the laser are too low in energy to be coupled to the repulsive curve by the retro-action alone. Therefore, the laser absorption serves as a universal time zero in this picture. The effect is more complicated in the Floquet picture where the retro-action might be considered as another perturbation to the potential curves. If the vibrational state energy is E_ν, the photoelectron energy E_e, the pump photon energy is E_{XUV}, the laser photon energy is E_{las}, the nuclear kinetic energy release E_{KER}, the dissociation limit is E_{diss},

and the retro-action coupling energy is Δ_r, the energy sharing must go according to:

$$E_e = E_{XUV} - E_\nu + \Delta_r$$

$$E_{KER} = E_{las} - (E_{diss} - E_\nu) - \Delta_r$$

The phase difference between the gerade and ungerade states determines the asymmetry direction. These phases are themselves determined by first, the time delay between ionization and dissociation, and second, by the location in the bound potential well at which the dissociating laser photon can be absorbed. In our experiment, the laser bandwidth is also extremely narrow and therefore the phase of purely laser dissociation must depend only on the time to dissociate. The photoelectron retro-action acts as a second probe pulse: taking the place of the 2ω and 3ω channels in figure 2.2. As with the laser, the phase of the coupling from the photoelectron is determined first by the time from photoionization and second by perturbation which is related to the distance of the photoelectron from the molecule. It is clear that the phase difference determining the asymmetry is commonly dependent on the time to dissociate, but varies as the photoelectron moves away from the molecule.

We would like information on the dissociation timescales in order to estimate the photoelectron distance. Xu et al. [39] recently measured the time for the bound electron to localize in the dissociating H_2^+ using $5fs$ carrier envelope stabilized (CEP) laser pulses. They found that the localization is complete within $8fs$ and within 8Å internuclear distance. Certainly, the photoelectron is still in proximity: a $.7eV$ photoelectron will travel 40Å Angstroms in 8 femtoseconds and have a wavelength of $\approx$ 14.5Å Angstroms. The potential field from the electron at that distance is $.35V$ and this is a significant fraction of the laser photon energy of $1.2eV$.

We can expect that the asymmetry will change for different vibrational states because the fixed phase offset from the laser and the phase from the energetically different electrons

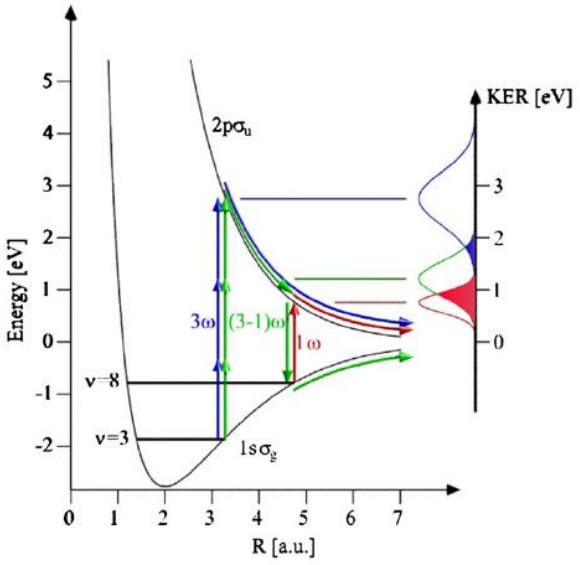

Figure 2.4: Image taken from [38]. Possible dissociation routes that interfere to produce asymmetry. In our experiment, the retro-action acts as the "second" photon.

both change. We can also expect a larger phase difference for higher vibrational states as the starting point for the nuclear wave packet moves to higher energies and shorter distances on the dissociating curve. We expect the retro-action coupling to be near the dissociation limit where the $1s\sigma_g$ and $2p\sigma_u$ approach within $.35eV$, as estimated from above as a conservative upper bound. We will fully discuss the experimental challenges and results of our measurement in chapters 5 and 6.

Chapter 3

Experimental Apparatus

This chapter covers all aspects of the COLTRIMS apparatus and two-color experiment. We begin in section 3.1 with a short historical introduction on the development of COLTRIMS as it relates to other coincidence techniques. In section 3.2, we describe the elements of a COLTRIMS end station. In section 3.3, we describe the elements of the two-color apparatus.

3.1 COLTRIMS Context

A brief overview of spectroscopic experiments to orient the reader and contextualize COLTRIMS is in order. A number of particle collection schemes preceded COLTRIMS. Originally, Kinetic Energy Release (KER) spectroscopy collected two ionic fragments on a single MCP, using high fields, long flight times, and without position information. Refinements on this technique included the Wiley-McLaren geometry [40] and position sensitivity, and led to what is effectively the ion side of a COLTRIMS spectrometer. Early versions used an electron energy analyzer, as in the Photoelectron Photo-Ion Photo-Ion Coincidence apparatus (PEPIPICO) [41]. Sacrificing position sensitivity in favor of energy resolution, the Doppler Free KER (DFKER) method uses collection of cations in two directly opposed spectrometer arms to completely remove thermal motion and produce extreme resolution of the KER release [42]. In the corresponding TOF-PEPECO experiment, a magnetic bottle with nearly 60% collection efficiency is used to direct electrons down a $\sim$ 10 meter long drift tube. Extreme energy resolution is obtained, yielding precise knowledge of the potential states and vibrational structures of the cation. Angular information is recovered in the $(\gamma, 2e)$ apparatus by using multiple electron analyzers in coincidence configuration. As

many as 10 hemispherical electron analyzers are today used in conjunction to measure triple differential cross sections (TDCS) [43][44]. All the methods mentioned above generally operate at a fixed energy of the projectiles (photons, electrons). One method that explicitly relies on tuneable energy sources is the Threshold Photoelectron Spectroscopy (TPeSCO), where electron analyzers are set to record only zero electron energy photoelectrons in coincidence as the projectile energy is scanned. This method maps the excited state cross sections as a function of the incident photon energy, yet the mechanism for the creation of zero energy electrons remains a mystery. By extension, one analyzer can be set to capture a fixed higher energy electron (TPEPECO) or an ion (TPEPICO) [45]. Most recently, an apparatus has been constructed to measure fluorescence photons in coincidence: the $(\gamma, 2\gamma)$ method [46]. This method is ideally suited for studying neutral dissociation of doubly excited states that would otherwise be obscured in ionization spectra. Finally, the close cousin of the COLTRIMS experiment is the Velocity Map Imager (VMI). VMI forsakes time of flight momentum information (though ion masses are still well seperated in time) by projecting a flattened momentum sphere onto an MCP and observing the distribution with fast cameras. VMI was widely adopted in ultrafast laser experiments where many particles are typically ionized by a single laser shot and coincidence is impossible.

COLTRIMS combines the position sensitivity of the PIPICO for ions with a confining axial magnetic field similar to the PEPECO measurement except with added position sensitivity. the interaction rate is kept low to reduce false coincidences to negligible rates: only single atoms or molecules interact with the light field of each shot. All particles, electrons and ions, are collected in coincidence for the full 4π solid angle. Therefore, COLTRIMS captures nearly the maximum information from the photoionization products, with the exception of measuring the spin of the electrons, the internal state of the cation(s), or detecting multiple neutrals. Analysis of the data allows for complete reconstruction of the momentum and energy of each collected particle. The experimentalist is able to post select the data, by application of gates, to examine state specific properties of the emission channels. If

the timescale of coulomb explosion of the parent molecule is short compared to it's rotational timescale, then the axial recoil approximation can be invoked, which asserts that the molecule can be oriented with momentum vectors at the instant of photo absorption. The molecule can then be fixed in space and all vectors transformed into the molecular coordinate frame.

3.2 COLTRIMS Apparatus

This section contains subsections describing each of the primary element of the COLTRIMS endstation. The subsection appear in the following order: vacuum chamber, jet, spectrometer, simulation software, MCP and delay line anodes, electronics, and beamline.

3.2.1 Vacuum Chamber

The Atomic Molecular and Optical Science (AMOS) group's chamber - the AMOS chamber - is a ten year old workhorse shaped like a giant potato chip kettle. The large central area makes for easy manipulation of the spectrometer at the expense of a larger pump volume and corresponding higher operating pressure. The large lid is sealed by a giant viton gasket o-ring covered by a small amount of ultra-high-vacuum silicone grease. the chamber is hardy and mobile, resting on 4 wheels attached to a supporting 4" 8-20 frame, and survives transport to the Advanced Light Source (ALS) over a rough brick patio twice a year for beamtime. The frame also supports a crane to winch the lid on and off. Many of these details can be seen in figure 3.1.

The assembled chamber is divided into five stages, named: source, second stage, chamber (spectrometer), differential stage, and jet dump. A diagram of the chamber setup is shown in figure 3.2. The source stage houses the nozzle of the supersonic jet and a conical skimmer, and typically reaches high 10^{-4} torr during jet operation. This stage is pump by a Pfieffer TC600 turbo with 920 L/s pump speed that is backed by a Varian TriScroll. The source stage is directly connected to the second stage by the first bypass. The second stage houses the

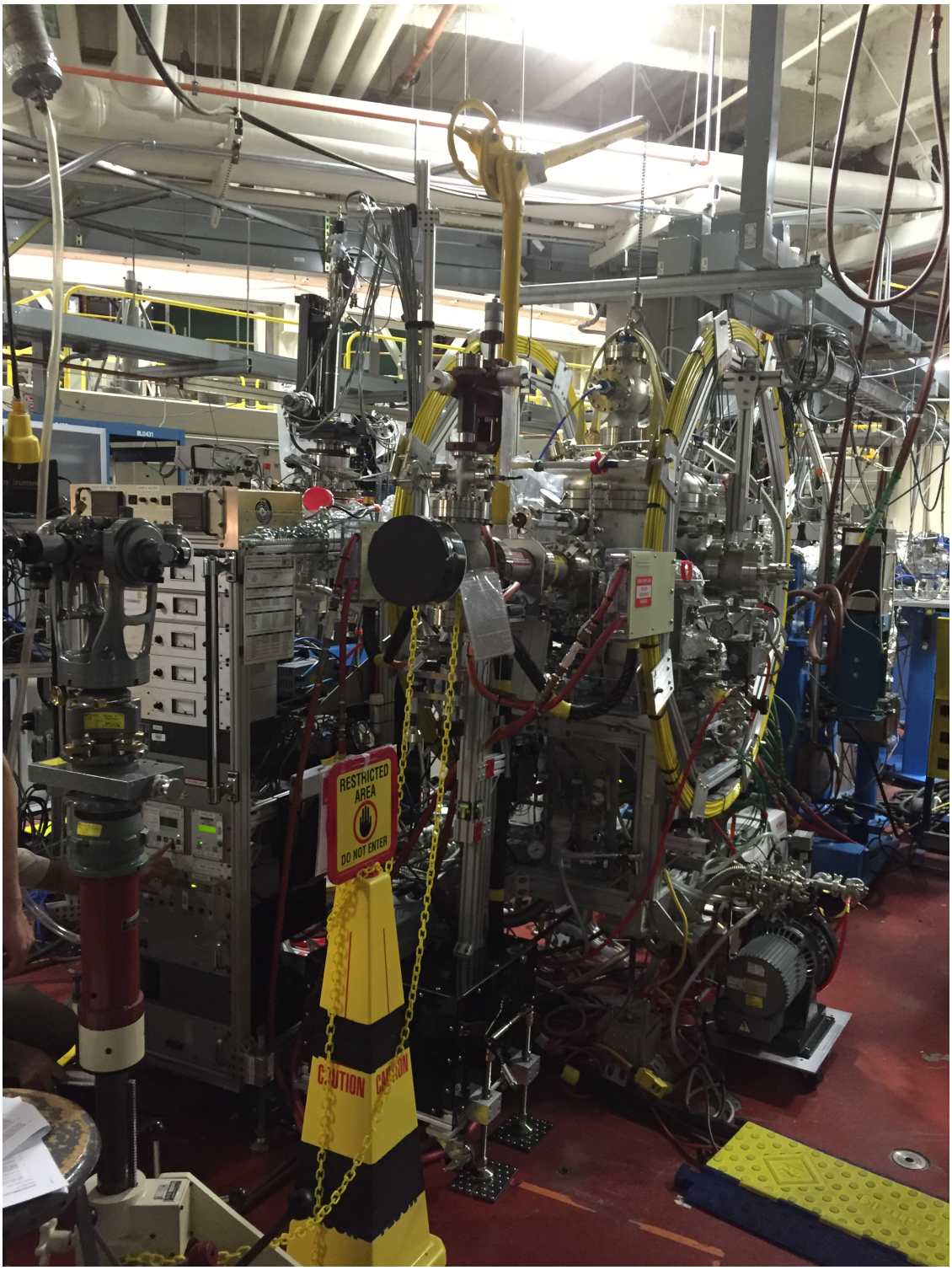

Figure 3.1: The AMOS chamber installed at Beamline 4.0 of the advanced light source. The yellow rings are the magnetic coils. The yellow crane is installed and connected to the lid. Various roughing pumps obscure the legs. The alignment telescope is on the far left edge of the image.

second skimmer of the jet and is pumped by a Balzers 240 Turbo (240 L/s) that connects to a dedicated second stage Anest Iwata scroll fore-pump. During operation the second stage has a typical pressure in the low 10^{-6} torr. The second stage is connected to the main chamber via the second bypass, which is located downstream of the main chamber turbo pumps. The third stage is the chamber proper, with the largest volume and the most leaks due to the viton gasket. The stage is pumped by a Balzers 240 and a Seiko Seiki STP 1000C (1000L/s) turbos backed by a Aidixen ACP 40G dry roots pump, and typically operates in the high 10^{-8} torr with the assistance of the liquid nitrogen cold trap. The trap has an endurance of 8 hours but is usually refilled every 4 hours to provide a 4 hour margin of error. The fourth stage is the differential stage connected to the chamber by a small tube. This stage is designed to provide a better vacuum for connecting to the beamline and is pumped Balzers 240 backed by a Pfieffer HiPace 80 pump. The fifth stage, the jet dump, consists of a drop down tube that catches the jet in a small volume and is pumped by a Balzers 240 connected to the second stage. A schematic of the vacuum plumbing and bypasses is shown in figure 3.3. An additional "secret" bypass exists as a fail safe way to re-route the roughing foreline should either pump backing the chamber and second stage fail; it is not generally used.

3.2.2 Jet

There is a great deal of literature on molecular beams, and most of the information presented in this section is summarized from [47] and [48]. The following section briefly elaborates on how a molecular beam is created from a supersonic expansion, initial skimmer, and second skimmer.

Target gases are piped to the jet through a gas manifold with three ports with lock-out tag-out hardware for toxic gas operation. The gas jet is created in the source chamber via expansion of pressurized gas into $1 \times 10^{-3} torr$ (typical gas operation pressure) through a variety of nozzles from $50 - 100 \mu m$ laser drilled into platinum disks. The free expansion from the nozzle is adiabatic meaning no heat is transferred to or from the environment. The

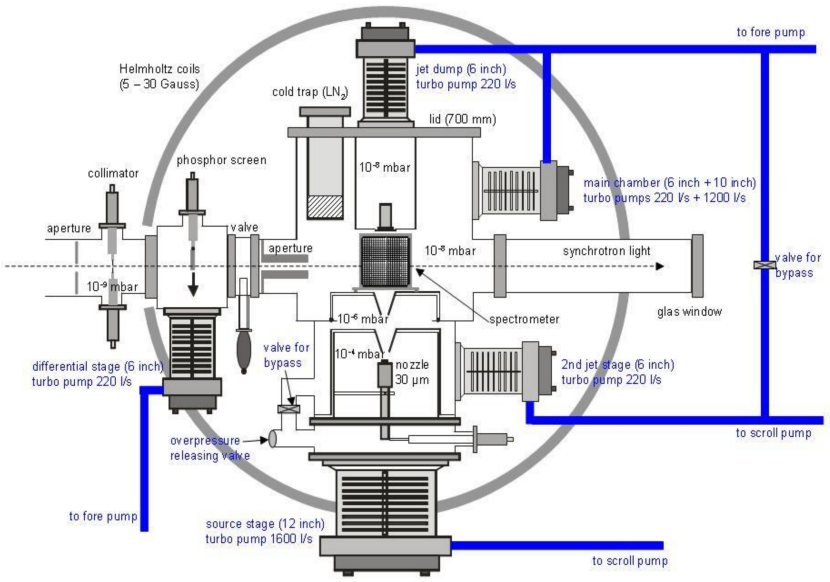

Figure 3.2: A diagram of the chamber layout.

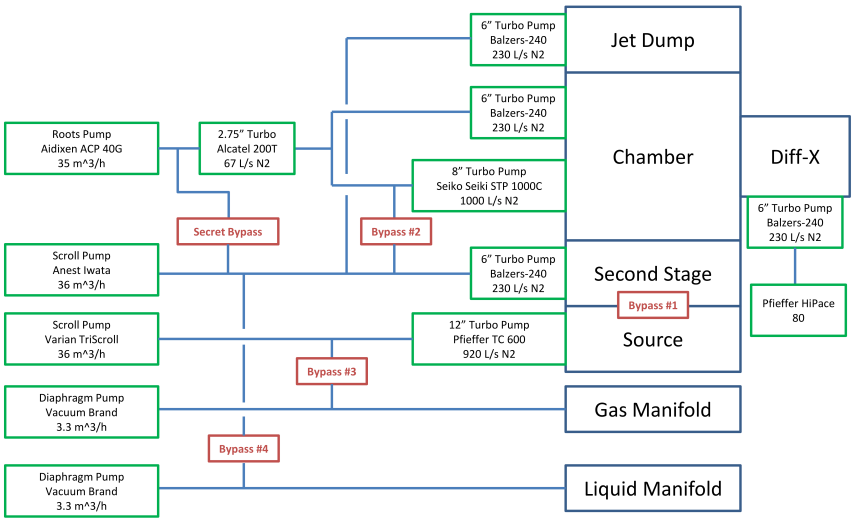

Figure 3.3: A schematic of the chamber vacuum system.

thermal energy of the gas is converted by the nozzle into axial velocity; the gas does work on its own mass by accelerating into the region of low pressure. The process of expansion is isentropic and reversible in that each differential volume of gas does not gain or lose heat energy. Just outside the nozzle the gas is dense enough to be treated as a homogeneous fluid and here the mach number describes the velocity distribution of the flow. An ideal gas will reach a speed

$$v_{max} = \sqrt{2\frac{\kappa}{\kappa - 1}\frac{R}{m}(T_o - T)}, \tag{3.1}$$

where $\kappa = C_p/C_v$ is the ratio of heat capacity at constant pressure to that at constant volume, R is the ideal gas constant, m is the molar mass, T_o is the initial temperature, and T the final temperature. The Mach number M is defined as the jet speed divided by the speed of sound and is given as

$$M = \sqrt{\frac{2}{\kappa - 1}\left(\frac{T_o}{T} - 1\right)}. \tag{3.2}$$

The rapid cooling by expansion reduces the speed of sound dramatically and mach numbers of 20 or greater are routinely achievable [48]. The speed of sound is

$$v_{sound} = \sqrt{\frac{\kappa k_b T}{m}}. \tag{3.3}$$

and it follows from the formula above that for a monatomic gas

$$v_{max} = \sqrt{\frac{\kappa k_b T}{m}}\sqrt{\frac{2}{\kappa - 1}\left(\frac{T_o}{T} - 1\right)} \tag{3.4}$$

$$= \sqrt{2k_b\frac{\kappa}{\kappa - 1}\frac{\Delta T}{m}} \tag{3.5}$$

For a monatomic ideal gas $c_p = 5/2R$ and $c_v = 3/2R$ hence $\kappa = 5/3$. Nitrogen, Oxygen, Hydrogen, and Helium gas have $\kappa = \{1.4, 1.395, 1.405, 1.667\}$ and $c_p = \{1.04, .919, 14.34, 5.19\}kJ*K/kg$, respectively. Some typical values of the maximum velocity as measured from our jet

are 1760 m/s for helium, 787 m/s for nitrogen, and 2944 m/s for molecular hydrogen. Assuming a conservative mach number of 20 quoted in the literature, and initial temperature of $300K$, we should approach $60K$ in the region just outside the nozzle where classical temperature still has meaning. However, using the equation for v_{max} and our experimentally determined jet velocities, we would expect temperatures on the order of $\sim 2K$ for O_2, N_2, H_2, and He. This suggests our jet mach number approaches 80, which is not unreasonable. If we assume that c_p remains constant with temperature then

$$v_{max} = \sqrt{\frac{2c_pT}{M}},$$

where M is the molar mass [49]. The temperature estimate by this equation using the empirical velocities and c_p above gives roughly the same estimate of $2K$. We can assume that the rotational and vibrational states reach this internal temperature, but the translational temperature parallel and perpendicular to this geometry do not, as described below. It should be noted that these values are incorrect for jets from cold reservoirs, particularly helium and hydrogen, which have strong intermolecular potentials at low temperatures [47].

For a sufficient pressure differential between the reservoir and expansion space, the nozzle generates a series of supersonic expansion waves. The shocks generated by the discontinuity are reflected and turned by the boundary with the ambient gas and the first skimmer. In such a way the shocks form a barrel, called a barrel shock. These shocks also reverberate to create a mach disk across the cylindrical symmetric flow. To create a more defined molecular beam separate from the ambient pressure of the expansion zone, a skimmer is used to separate a second differential pumping stage. The skimmer is conical shaped in order to reduce the shock it creates in the flow - a shock that could potentially destroy the flow through the aperture of the skimmer. The skimmer must also skim before the mach disk forms.

Inside the barrel shock the thermodynamic treatment of a freely expanding supersonic gas fails except for a region a few nozzle diameters outside the nozzle. The mean free path of the molecules becomes so large that the gas can no longer be treated as a homogeneous fluid. When these conditions are met, the velocity distribution of the gas perpendicular and parallel to the flow lines are large and a single temperature can no longer accurately describe either dimension. Instead of state variables, the gas dynamics must be built up from the microscopic Boltzmann equation modeling the specific nature of the gas collision, and for this a simple model of the scattering potential, such as the Lennard-Jones potential or hard spherical shell, of the gas atoms must be assumed. One common approach is to numerically solve the Boltzmann equation for the velocity distribution function and then fit a model distribution to estimate the temperature. A widely used model, the so called elliptical velocity distribution, is a composition of two separate Gaussian distributions modeling the parallel and perpendicular velocities:

$$f(\vec{v}) = n\left(\frac{m}{2\pi k_b T_\parallel}\right)^{1/2}\left(\frac{m}{2\pi k_b T_\perp}\right) \times exp\left(-\frac{m}{2k_b T_\parallel}(v_\parallel - u)^2 - \frac{m}{2k_b T_\perp}(v_\perp)^2\right), \tag{3.6}$$

where u is the average velocity. This distribution equals the maxwell distribution when the parallel and perpendicular velocities and temperatures are equal. More importantly, in the low density regime the concept of sound loses meaning and therefore so does the Mach number. A more physically relevant parameter is the speed ratio defined as the average jet velocity over the thermal velocity in the frame moving at the average jet velocity

$$S = \frac{u}{v_u}. \tag{3.7}$$

Of course the speed ratio only quantifies the jet velocity parallel to the flow direction. An experimentally determined formula for a variety of polyatomic gasses including N_2 is

$$S_\parallel = 5.4(P_o d)^{.32}, \tag{3.8}$$

where P_o is measured in Torr and d is the nozzle diameter in centimeters. Assuming the Gaussian distribution of the parallel velocity as before, the speed ratio is related to the relative velocity spread as

$$\frac{u}{v_u} = \frac{2\sqrt{ln(2)}}{S}. \tag{3.9}$$

From this equation it is possible to estimate the velocity spread in the jet direction.

Up to now we have neglected any mention of calculations or empirical formula for the perpendicular velocity. These calculations are much harder and must be determined on a case by case scenario. Suffice it to say that the literature gives a rough estimate that $r_\perp \approx 1/r$, but some reference value of r and temperature T_r must be determined. Typically these are chosen as the freeze point in the so called sudden approximation model, where the flow is considered to instantly transition from homogeneous fluid to straight streamline weakly interacting expanding cone. This transition occurs just a few nozzle diameters away from the nozzle. Given the small size of the nozzle, it is reasonable to treat the transverse velocity distribution as limited by the geometric configuration of the second skimmer. The jet has essentially reached its terminal velocity at the first skimmer. If we assume that a molecule starts anywhere in the nozzle, it will follow a straight streamline (with minimal perturbations due to perpendicular velocity) so that it passes the second skimmer. An estimate for the transverse momentum is then:

$$\Delta p_\perp = m \cdot u \left(\frac{d_{nozzle} + d_{2nd\ skimmer}}{l} \right), \tag{3.10}$$

where l is the distance from the nozzle to the second skimmer. Given the second skimmer diameter of $1mm$ and the distance of the to the second skimmer on the order of $10cm$, the perpendicular momentum spread is at least 100 times less than the parallel spread.

3.2.3 Spectrometer

What follows is a description of the spectrometer built specifically for two color experiments at the ALS. A birds eye view of the spectrometer as it sits in the chamber is shown in figure 3.6. A number of incremental improvements and modifications were made to the standard spectrometer design to accommodate laser operations. To remove lensing caused by the close proximity of the ion MCP to the mesh separating the final ion acceleration region from the interaction region, a booster region consisting of 3 round plates was added. This increased the distance from $\sim 5mm$ to $21.6mm$ and is thought to have substantially reduced fringe fields from the ion MCP. However, the large gaps in the spectrometer plates required to make way for the unfocused laser beam introduce other problematic fringe field effects. To compensate, the spectrometer plates were extended outwards horizontally from $150mm$ to $195.72mm$.

The spectrometer is constructed of 42 copper plates, 3 mesh holders, 3 booster copper plates, ceramic spacers, 8 ceramic rods, resistors between copper plates, and MCP holders. The components are stacked in a tower arrangement onto the ceramic insulating rods and structurally supported by a cage of sturdy steel bolts. Together these components define the fields in each region of the spectrometer. As shown in figure 3.4, each copper plate is $.4mm$ thick, $195mm$ wide and $150mm$ tall, with winglet cutouts on all four corners to make room for the structural support bolts, and a $130mm$ hole in the center. The ceramic spacers between elements in the stack are $5mm$ thick.

The spectrometer structure is diagrammed in figure 3.5, where the thick bars on either end represent the MCP (thickest) and MCP holder (outer and less thick), the blue elements indicate the mesh holders and the blue lines the side where the mesh is held. The black lines represent copper plates with the colors indicating the plate is cut in half (red) or into quarters (green), as described below. Typical operating voltages are graphed (not to scale), below the spectrometer diagram and the distances of each section are displayed above. The

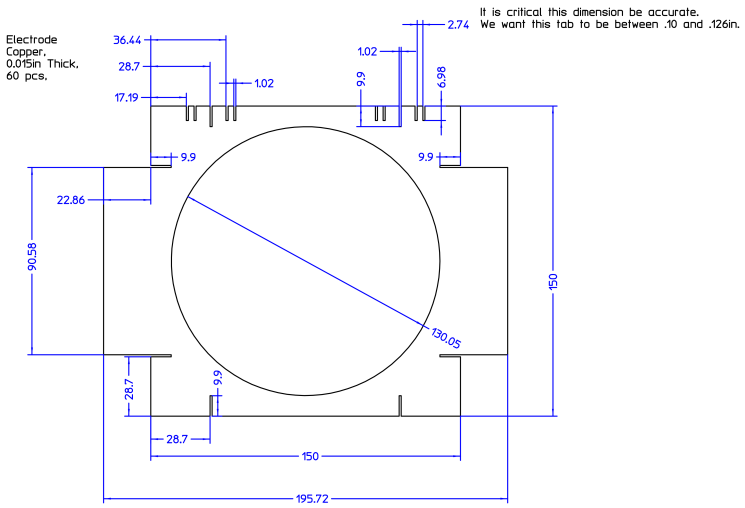

Figure 3.4: Spectrometer plate schematic, all values are in millimeters.

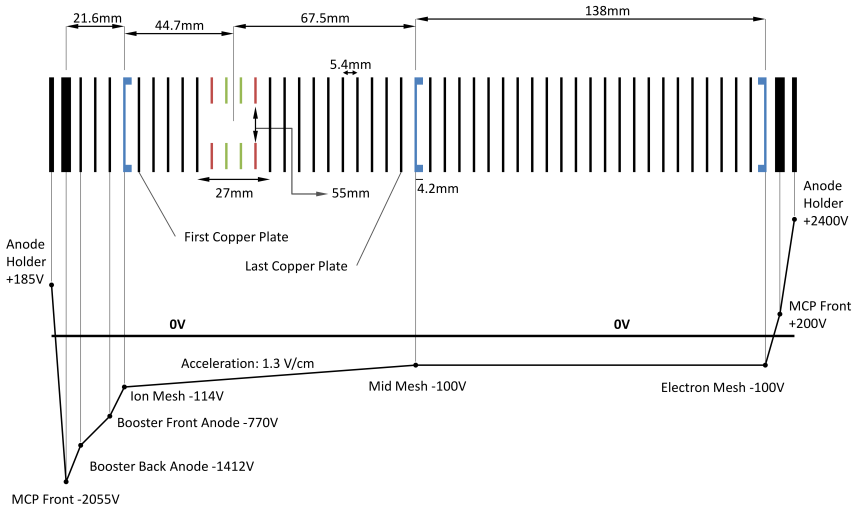

Figure 3.5: Diagram of the spectrometer regions and potentials configured to run with an acceleration field of $1.3 V/cm$. Potentials are not drawn to scale.

construction is described in the following paragraphs, beginning on the recoil ion side of the spectrometer and proceeding through each stage in the stack.

First in the stack is a booster region attached directly to the MCP holder. Three round booster copper plates spaced $5.5mm$ apart for a total of $22mm$ connected by 10.6Ω resistors are attached directly to the MCP front.

Next in the stack is the acceleration region starting with the $4.2mm$ ion mesh holder, with the mesh held on the ion MCP side, followed by 7 copper plates to the jet for a total distance of $44.7mm$ from the ion mesh to jet. Each copper plate in the acceleration region is connected by a $604k\Omega \pm 1\%$ resistor. Plates 6, 7, 8, and 9 are sliced through the middle along the direction of the laser light propagation to create a gap for the unfocused laser beam to travel through. The opening is $27mm$ wide and $55mm$ tall. These plates are connected top and bottom by special stiff capton insulated wire connectors that circumnavigate the opening to avoid obstructing the light. The 7th and 8th plates are further subdivided in the jet direction to make a small opening for the jet. The quadrants of the 7th and 8th plate are also connected by stiff wires that circumnavigate the jet. Between the 7th and 8th plate is the target zone. Continuing on from the 7th plate there are 12 more plates in the acceleration zone for a total of 19 plates before the middle mesh holder. The middle mesh is held on the acceleration side of the $4.2mm$ thick holder. The total length of the acceleration region is $112.2mm$, $44.7mm$ on the ion side and $67.5mm$ on the electron side.

Next in the stack is the drift region consisting of 23 copper plates. The first copper plate in the drift region is connected to the middle mesh by a $1.1M\Omega$ resistor. Each successive plate in the acceleration and drift region is connected by a $604k\Omega \pm 1\%$ resistor. The total length of the drift region is $138mm$. The last element in the drift region is the $4.2mm$ electron mesh holder, which is connected to the last plate of the drift region by one $604k\Omega \pm 1\%$ resistor and one $49.4k\Omega \pm 1\%$ resistor in series. The mesh is held on the side of the electron MCP. The last element is the MCP holder, separated from the mesh by $5mm$.

The mesh used in the spectrometer is made from a square pattern of $22\mu m$ wire, with approximate open area of 80%. the mesh is held tensioned and flat by a retaining gasket.

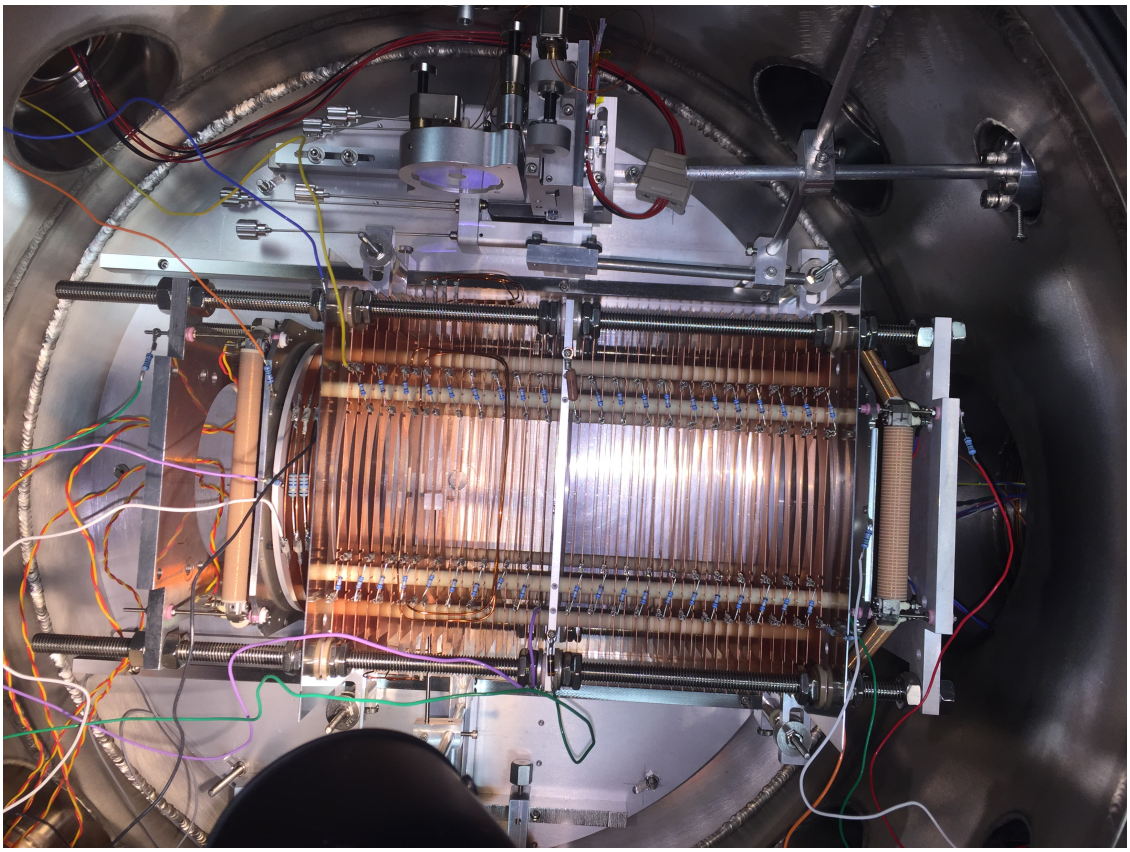

Figure 3.6: Chamber photo of the April 2017 beamtime. Backfocus mirror assembly center top with differential pump tube just visible above. Center: spectrometer with wiring to port flanges.

The spectrometer is connected to external ports of the vacuum chamber at five points, excluding the MCPs: the ion mesh, first plate in the acceleration region, last plate in the acceleration region, middle mesh, and electron mesh. Each connection to a mesh is made with a $30\Omega \pm 5\%$ resistor. The connections to the first and last copper plates have no resistors. The ion mesh and middle mesh determine the acceleration field strength via applied voltage to their connecting wires. In normal flat field operation the first plate is connected to the ion mesh and last plate connected to the middle mesh outside the chamber with $604k\Omega$ resistors.

The spectrometer can be configured into a line imaging mode by grounding all the plates in the acceleration region and applying voltages to both the recoil and ion mesh. The line

mode can in theory provide up to 30x zoom of the interaction region, though this functionality has not been tested. The potentials applied to the spectrometer are diagrammed at the bottom of figure 3.5.

The entire spectrometer assembly is held at a negative bias, with the exception of the anodes of the MCP and the electron MCP, to repel stray electrons. The anode elements do not have a large area on the side to accept stray electrons.

The spectrometer is constructed with Wiley McLaren space focusing geometry on the electron side of the spectrometer. This geometry ensures that the spatial distribution of the electrons in the time of flight direction does not factor into their time of flight. Said another way, the position dispersion in the spectrometer is zero to first order in the interaction region. The exact mechanism by which this can be achieved is intuitive: electrons that start higher on the potential surface enter the drift region at later time and with a greater velocity than electrons that entered the drift region at an earlier time. The particles will arrive at the same longitudinal position at some point in the drift region and a detector placed at this point will have zero time dispersion. Wiley & McLaren studied a three stage ion source and found the general formula for optimal time focusing (which they call space focusing), occurs when

$$D = 2s_o k_o^{3/2} \left(1 - \frac{1}{k_o + k_o^{1/2}} \frac{d}{/s_o}\right), \tag{3.11}$$

where D is the drift length, s_o is the length of the first acceleration region, d is the length of the second acceleration region, and $k_o = (s_o E_s + dE_d/s_o E_s)$, where E represents the electric field in the region denoted by the respective subscript. For a spectrometer with zero second acceleration region $D = 2s_o$, and this is the drift length ratio used in our spectrometer. It should be noted that the above equation results from considering only small deviations from the derivative of the flight time with respect to the first acceleration length: $dT/ds_o = 0$. About this point, the dispersion may be a quadratic minimum or maximum or an inflection

point. For the two stage spectrometer, the time function is

$$T[U_o = 0, s_o] = \left(\frac{m}{2qs_oE_s}\right)^{1/2}(2s_o + D), \tag{3.12}$$

where, U_o is the initial energy here taken to be zero. The first derivative is

$$\frac{dT[U_o = 0, s_o]}{ds} \times \delta s = \left(\frac{m}{2qE_s}\right)^{1/2}\left(s_o^{-1/2} - \frac{D}{2}s_o^{-3/2}\right) \times \delta s, \tag{3.13}$$

and is zero for all values of δs. The second derivative gives the a measure of the length scale where the approximation is valid:

$$\frac{d^2T[U_o = 0, s_o]}{ds^2} \times \delta s^2 = \left(\frac{m}{2qE_s}\right)^{1/2}\left(-\frac{1}{2}s_o^{-3/2} + \frac{3D}{4}s_o^{-5/2}\right) \times \delta s^2. \tag{3.14}$$

When $D = 2s_o$ this simplifies to

$$T[U_o = 0, s_o] \times \delta s^2 = \left(\frac{m}{2qE_s}\right)^{1/2} \times \left(\frac{\delta s}{s_o^{3/4}}\right)^2. \tag{3.15}$$

Clearly the perfect dispersion is a quadratic minimum that decays with characteristic length scale $s_o^{3/4}$ and at a rate equivalent to the square root of the inverse acceleration. The dispersion is then primarily controlled by the strength of the electric field, with high fields leading to broader dispersion curves that can handle larger interaction regions.

More generally, if we consider the arbitrary integral solution to the time of flight in the spectrometer, starting from the impulse equation

$$f[x]dt = dp, \tag{3.16}$$

where f is the force, we can integrate to write:

$$t = \int_{p_o}^{p_f} \frac{dp}{f[x]}. \tag{3.17}$$

We can exploit the knowledge that the field geometry is completely known with

$$\frac{dU[x]}{dx} = f[x], \tag{3.18}$$

(for electrons) and

$$p[x] = \sqrt{2mU[x]}, \tag{3.19}$$

leading to

$$dp = \frac{dp}{dx}dx = \frac{d}{dx}\sqrt{2mU[x]} \times dx \tag{3.20}$$

$$= \frac{1}{2}\left(\frac{2m}{U[x]}\right)^{1/2}\frac{dU[x]}{dx} \times dx. \tag{3.21}$$

Substituting these values into the integral equation gives:

$$t = \int_{x_o}^{x_f} \frac{1}{\frac{dU[x]}{dx}}\frac{1}{2}\left(\frac{2m}{U[x]}\right)^{1/2}\frac{dU[x]}{dx} \times dx \tag{3.22}$$

$$= \sqrt{\frac{m}{2}}\int_{x_o}^{x_f}\left(\frac{1}{U[x]}\right)^{1/2} dx. \tag{3.23}$$

Let us denote the integral above as a function G. G has only one argument, the starting position and of the particle $G = G[x_o]$. The function describes completely the properties of a spectrometer for particles with zero velocity. Let us consider a potential energy $U[x] = x^2$, then $G[x] = ln[x_f/x_o]$, and the derivative of time with respect to x_o is

$$\frac{dt}{dx_o} \approx \frac{x_o}{x_f}. \tag{3.24}$$

Therefore, dispersion is proportional to the ratio of the initial and final position. More generally, any function that maintains the same form from x_o to x_f will have a dispersion

equal to the integrand (the final position does not effect the dispersion):

$$\frac{dt}{dx_o} \approx \left(\frac{1}{U[x_o]}\right)^{1/2}. \tag{3.25}$$

For a linear field, $U[x] = A - Bx$, where A is some starting constant and B is the field strength in volts per centimeter. Choosing $A = 0$ at the interaction region shows that the time focusing dispersion goes as the inverse square root of the total energy imparted to the molecules. The spatial error in the spectrometer is calculated as

$$R_x \times x_o = \frac{\sigma_t}{\frac{dt}{dx_o}}, \tag{3.26}$$

where R_x is the error and σ_t is the timing uncertainty. Here we want a large error value to indicate that time of flight is very insensitive to changes in position.

3.2.4 SIMION

The SIMION field modeling program was used extensively to model the fields and flight paths of particles in the spectrometer. The program allows users to define electrode geometries and apply voltages to configurations of electrodes, solving Laplace's equation by finite difference methods on an equally spaced grid to produce the resultant potentials and electric fields in free space. Version 7 of the program can handle 1×10^7 geometric grid points on which to run a simulation. Though this appears to be a large number of points it is small for simulating 3 dimensional volumes. The number is entirely insufficient if we wish to model a mesh. Fortunately, our spectrometer is approximately cylindrically symmetric and SIMION has special provision for exploiting the symmetry of such geometry. The solution of the laplace equation can be completely determined by the specification of the axial cross section of cylindrically symmetric electrodes. Therefore, the geometric grid points can be distributed in a plane that is then revolved about the central axis to form the solid electrode geometry. To simulate the spectrometer in as high a detail as possible, we employed an

electrode grid with 3789 axial and 2400 radial grid points for a total of 9.7×10^6 gridpoints. The spacing between grid points is equivalent to $33\mu m$, which is fine enough to attempt a simulation of the grids in the spectrometer.

SIMION uses as input syntactical text files for definitions of electrode geometry. Select files used for the simulations shown here can be found in the appendix. A complete description of the geometry used for simulations would be verbose and therefore we focus on only a few elements. The interior free space of the spectrometer is constructed with exact dimensions in diameter and length. The spectrometer copper plates are 450 grid points tall and 15 grid points wide corresponding to $15mm$ and $.5mm$ respectively. The radial width of the plates is roughly half the true width while the axial width is close to the real value of $.4mm$. The square edges of the plates and the grounded support structure is not modeled.

The bounding box of the simulation is automatically assumed to be at zero potential. The real spectrometer boundary conditions are determined by the shape of the grounded chamber walls. The bottom side of the spectrometer is a few millimeters away from the chamber floor while the top and sides are tens of centimeters from the chamber wall and lid. The impact of this asymmetric boundary condition is no doubt small but may not be negligible. A SIMION simulation would require a very crude construction of the spectrometer because of the large asymmetric volume required to capture the chamber and therefore no simulation was attempted.

In regards to meshes, SIMION can implement unphysical perfect mesh that provides a perfect boundary between different potential regions and allows ions to fly through unobstructed. Perfect mesh are acceptable for simulating idealized operations.

The model geometry used here is accurate for the spectrometer designs used before 2016. The simulation does not include a longer acceleration region for the ions (7 plates instead of 5) or the "booster" region (to mitigate the fringe field by distancing the MCP from the mesh) found in the laser-COLTRIMS spectrometer. Nevertheless, the goal of the simulation

is only to determine the character of the fringe fields. More accurate simulations would be needed to empirically investigate actual field values suitable for use in a lookup table.

The fringe fields originate from poor shielding of the high potentials on the ion MCP which is held nearly 2000 volts lower than the mesh bordering the acceleration region. The high voltage on the MCP is imperfectly screened by the mesh. It is clear from experience with many datasets handled by numerous graduate and masters students that there exist strong fringe fields in the spectrometer acceleration region that can significantly distort the ion and electron distributions. This is particularly problematic for comparing low and high energy particles in highly differential measurements.

An accurate simulation of the mesh requires a grid on the same size scale and, as mentioned above, the wire used to create the square grid mesh are only $20\mu m$ wide. With the current geometry it is just possible to approach the correct size scale with a single grid point, roughly one and a half times too large. However, the SIMION manual claims that a single grid point used in a mesh will actually simulate a wire of $.4gu$, in our case $12\mu m$. We have not investigated this claim. Additionally, the mesh are square, whereas with the radial symmetry we can only form a "bullseye" circular grid. Despite the geometric difference, the amount of leaked field must be proportional to the open area. For this reason, the spacing of the radial mesh grid points was chosen to preserve the 80% open area of the square grid: four empty grid points were used between each mesh point. The open area ratio as a function of radius changes only as a function of $\delta r/r$, and will be essentially zero since $\delta r << r$.

The results of the mesh field simulation can be seen in figures 3.8 and 3.7. Figure 3.7 shows the unbiased field with the MCP at full voltage. Here the leaked field appears to be unphysical, The gradient of the field in the charge free region appears to have a non-zero divergence (within the equipotential line at 50V). Additionally, the leaked field is so large that it would destroy the experiment - clearly, the simulation can only handle lower fields. In contrast, figure 3.8 shows the fringe field when the spectrometer acceleration region has a $9V/cm$ field gradient and the voltage on the MCP has been reduced to $500V$. The field

appears physical with zero divergence in the source free region and is a better indicator of the nature of the fringe field.

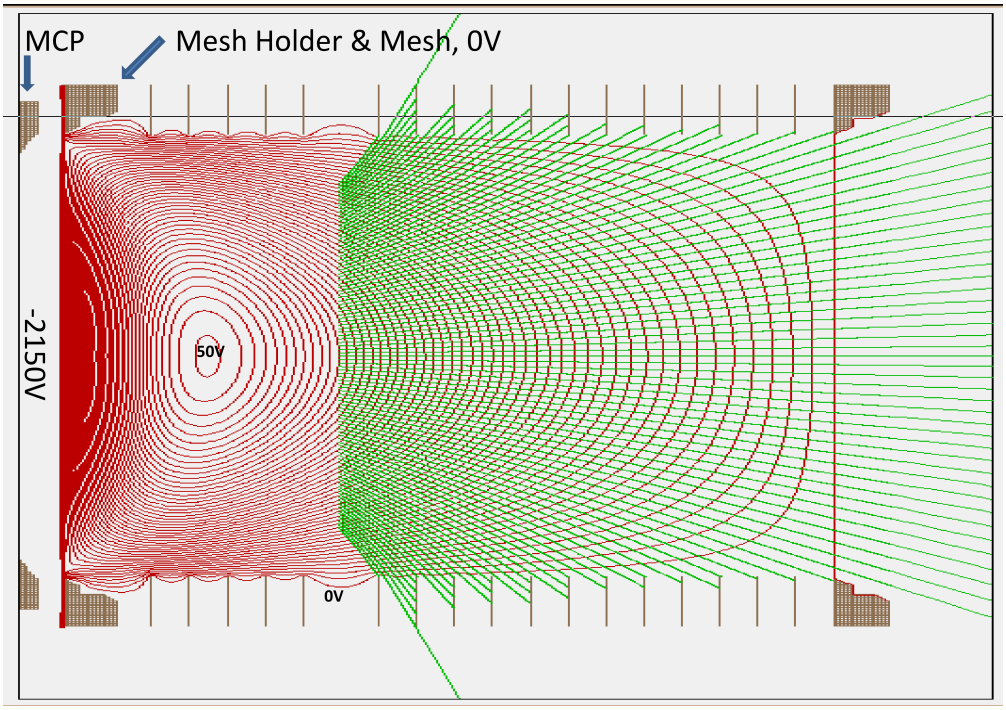

Figure 3.7: SIMION simulation of the leaked field. The lense was simulated with a radial mesh that maximized the capabilities of the software. A $-2150V$ potential is placed on the MCP. The simulated potential contours from 0V to 50V are shown in red. Also shown are the flight paths of electrons with zero velocity along a line that intersects the interaction point.

A direct imaging "line" mode was simulated with perfect mesh and a larger grid, 1818 points tall and 5396 points wide (1 grid unit is $.44um$), to accommodate the drift region. The results of the line mode simulation can be seen in figure 3.9, showing an isometric potential surface and the expanding flight paths of a line of ions. The saddle potential acts as a negative lens. The ions are arranged at the interaction point in a $.2mm$ line and expand to an $8mm$ line at the detector- a 40x magnification. Actual magnification will most probably be less for functional voltage values, as the voltages shown reduce the axial velocity of particles to nearly zero and this may prevent them from ever reaching the detector.

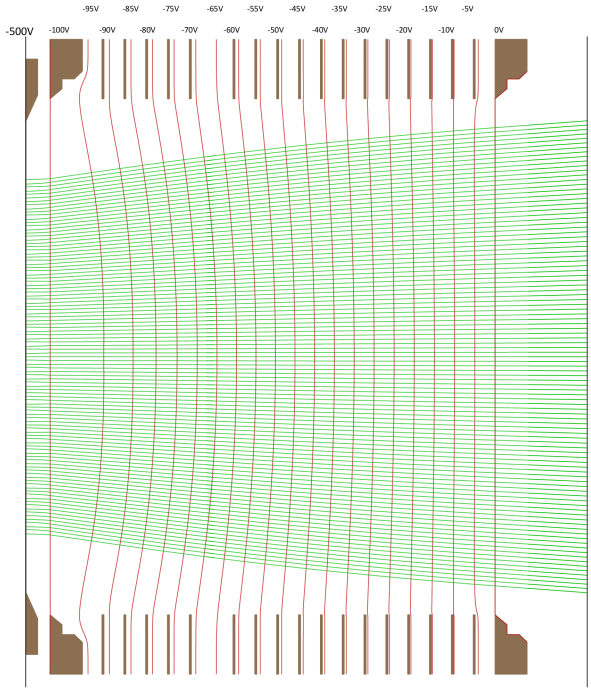

Figure 3.8: Simulated field leakage through a cylindrical mesh with an applied bias. Green lines are particle trajectories, red lines are equipotential curves. The applied field is $9V/cm$.

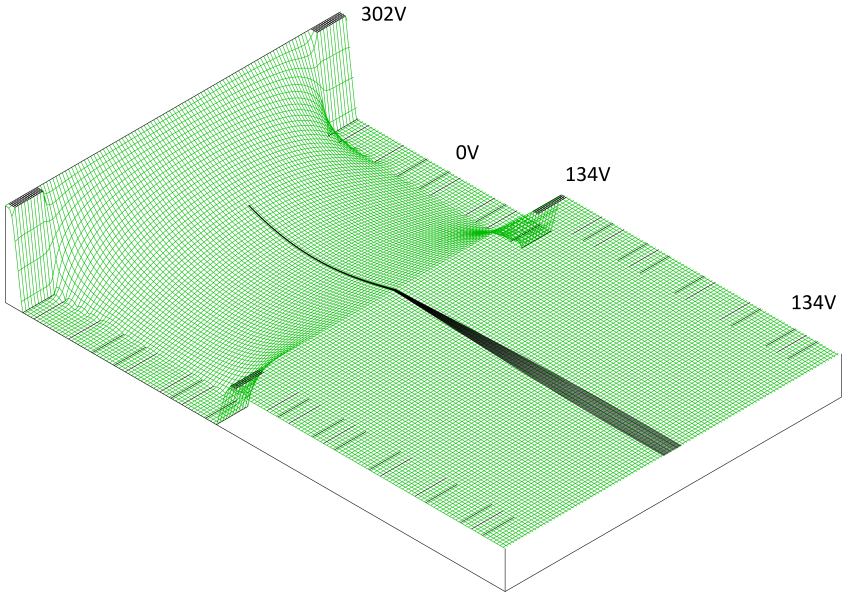

Figure 3.9: Isometric view of the potential surface in the line mode of the spectrometer. Ion trajectories are shown expanding from a $.2mm$ line to $8mm$ line at the MCP

3.2.5 MCP & Delay Line Anodes

Multi Channel Plate (MCP) detectors are composed of thousands of hollow glass fibers drawn together and cut into disks. The drawing process consists of forming progressively larger groups of fibers untill they can all be drawn together at the desired diameter. The hexagonal packing of the fiber groups leads to a noticeable hexagonal structure in particularly hot spots on the detector. The interior of the fibers, the channels, are coated with a thin layer of low work functionm high resistance semiconductor. Under high voltage gradients, the dielectric emits electrons when struck by a charged particle. These electrons casacade down the channel successively liberating more electrons and producing as much as 10^6 gain in charge for a two stage stacked chevron MCP.

The MCP has a finite open area of approximately 60%. Particles that strike the electrode surfaces and not the interior emitters will not produce an electron cascade. The upper limit on detection efficiency is then 60% but is further limited by the ability of the charged particles to trigger the electron cascade. For both electrons and helium ions, the maximum detection efficiency of 50% is achieved for particle energies of $500eV$. The detection efficiency also depends on the impact angle and for electrons maximum efficiency is reported to be 13 degrees from normal to the face of the MCP. Detection efficiency and signal strength is also a function of operating voltage with typical operating voltages are between $2kV - 2.4kV$.

The electron charge shower is collected at the back of the MCP by a delay line anode detector. The dealy line anode consists of wire pairs, signal and reference, that form a waveguide. Both wires are biased positive relative to the MCP back to attract the electron shower though the signal wire is held at an increased potential ($+50V$) relative to the reference wire to favor electron collection. Upon collection by the signal wire, a pulse is formed and propogated by the waveguide to the edges of the delay line where it is directed to ports on the chamber wall by insulated twisted wire pairs. Outside the chamber, the signals pass through decoupling boxes that seperate the high voltages of the anode assembly

from grounded LEMO cables that run to the signal processing electronics rack. The decoupling boxes are high pass capacitive filters with a tunable potentiometer. The time constant of the RC circuit to ground can be tuned to optimally transmit the signal pulse. Correct adjustment of these potentiometers reduces signal reflections which can produce false particle hits.

The accuracy of the delay line anode is related to the width of the time-sum of the signals used to encode the position on the line. The width of this time-sum is approximately $\delta t = 500ps$ and the conversion factor from nanoseconds to millimeters is approximately $.500mm/ns$. The total position encoded error is then on the order of $\delta r = .25mm$. Generally, the momentum error will be related to the spread of the incident electrons on the detector, with lower energy electrons more error prone. The electron shower has a time spread of $\sim 500ps$ which roughly corresponds to the pulse width used for hit timing on the MCP recharge signal. This pulse width does not represent the accuracy of the timing data though, because it represents the signal before being processed by the CFD (to be described in the next section). With a CFD, the timing resolution approaches $\sim 250ps$.

3.2.6 FAMP & CFD Analog Hardware, TDC, & COBOLD

Signals from the MCP layer anodes and capacitive voltage supply are processed with all analog NIM bin electronics. After transport over LEMO cable from the decoupling boxes, signals are fed into fast amplifiers (FAMP). These amplifier are specially designed to preserve the pulse shape while providing a gain of 10 to reach the preferred NIM operatin voltage range of $-.8$ to $-1.2V$. The amplified pulses are sent to a fan to provide diagnostic copies. One copy is sent to the constant fraction discriminator (CFD). The constant fraction discriminator is an analog to digital converter that removes the error in triggering off of pulses with varying height. The CFD provides a way to trigger at a specific fraction in the pulse time: the pulse will trigger relative to itself as opposed to an external threshold.

When a pulse enters the CFD, it is split by a fixed ratio into two arms. One arm is delayed by a user suplied LEMO cable on the front panel (typicaly $\sim 5cm \approx 150ps$) then attenuated to a fraction of its origina value and finally inverted. The other arm is left unaltered. The two arms are re-combined and fed to a trigger with a level determined by the walk value - set to just equal or slightly above the zero point crossing of the combined signal. Simultaneously, a regular threshold trigger determines if the pulse height is large enough to be considered a real signal. These two signal are fed in a zero crossing CMOS AND logic gate which triggers the output of a standard NIM signal. Operation and tuning of CFDs involves precision adjustment of the timing delay, attenuation fraction, walk threshold, and trigger threshold. More information is well documented in numerous theses and reviews, including [50] and [7].

Data was captured from the timing electronics by two Time to Data Cards (TDC, model TDC8HP) operated with the COBOLD online analysis and visualization program, both supplied by Roentdek. The TDC have a combined 16 channels and a timing resolution on each channel of $25ps$ [51]. The COmputer Based Online-offline Listmode Data analyser (COBOLD) program controls the TDC through the Data AQuisition dynamic link library (DAQ.dll) and visualizes the data in real time during the experiment using the DAta Analysis dll (DAN.dll). Both dlls in the program use syntactical cobold command files (.ccf) to provide custom control of the TDC and the online spectra. The use of this program is well documented in [52] and will not be present here.

3.2.7 ALS Beamline

Two color COLTRIMS experiments were conducted exclusively at beamline 10.0.1 at the Advanced Light Source (ALS). Beamline 10.0.1 is equipped with a extremely high energy resolution monochromator with a fixed angle between both arms and a rotating grating. The entrance slit is held at a fixed distance of 4m from the grating and the exit slit is on a 2m movable bellows. The three gratings provide an energy range form $17 - 80eV$, $80 - 200eV$,

and $200 - 480eV$ respectively. We used the first grating in our experiments. The beamline has a dramatic drop-off in intensity at the lower end of the first grating. To compensate for the drop in intensity, the entrance and exit slit must be opened, degrading resolution. However, even with sub optimal operating configurations the energy resolution is still on the order of tens of millielectronvolts. The beamline is controlled by a LabView program.

The beamsize was reported by the beameline scientist to be $200\mu m$ in the horizontal and $800\mu m$ in the vertical. The pulse length is nominally $\sim 80ps$. All experiments were conducted in the so called "2-Bunch" mode, with two electron bunches orbiting the synchrotron ring. The duty cycle of light pulses was $\sim 3MHz$ with a bunch (pulse) spacing period of $328.28ns$.

3.3 2-Color Apparatus

This section contains subsections describing each of the primary element of the 2-color apparatus. The subsection appear in the following order: laser, beam transport & geometry, position overlap, synchrolock, and rate estimation.

3.3.1 Laser

The laser used for the 2-color experiments was a custom built model from Q-Peak. The laser is a Yb:YAG crystal medium lasing at $1030nm$, with pulse width of $12ps$, up to $1MHz$ repetition rate, and a nominal $100W$ of average power. A brief description of the laser is in order, but more documentation can be found in the Q-Peak Manual [53] and final program report [54]. In the final oscillator design shown in figure 3.10, a $6 \times 6 \times 8mm$, 5% doped, Yb:YAG crystal was pumped by the focused beam of a 50W constant wave 940nm laser diode from Jenoptik GmBH. The crystal was held in vacuum and cooled on one side by a liquid nitrogen dewar. Mode lock was achieved via a SEmiconductor Saturable Absorber Mirror (SESAM) from BATOP GmBH placed at one end of the cavity as the turning mirror (specifications are found in [54]). During operation with a delivered pump current of 3.7A (8V, 29.6W) the oscillator would routinely output $6W$ of power and after a thorough cleaning,

near $8W$ of power. The output power fluctuated by approximately $\pm 5\%$, which proved to be a significant issue for the synchrolock timing system. The original timing system actuated mirror M2 (see figure 3.10), which was problematic because its motion walked the beam in the cavity, destroying mode lock. Not shown in figure 3.10 is an aperture that was added by Q-Peak to assist in mode lock: this aperture directly conflicts with walking M2. For this reason, the original synchrolock system was disabled and the output coupler was actuated to serve as the synchrolock mirror.

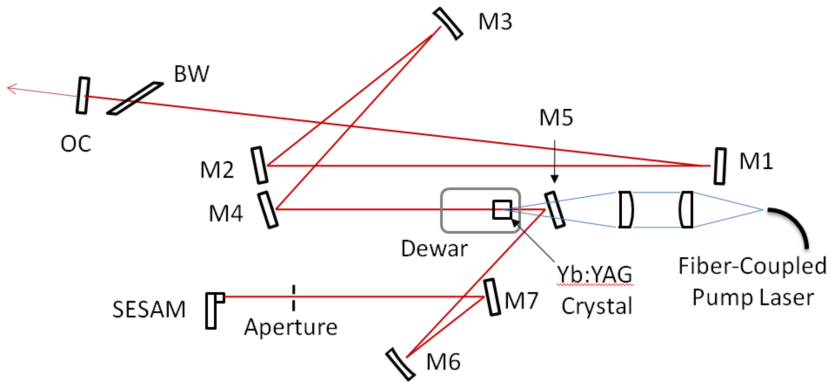

Figure 3.10: Illustration from [54] depicting the final layout of the laser oscillator. Mirrors are labeled M1 to M7. BW is a brewster angle window to force horizontal polarization. OC is the output coupler.

After the output coupler, the beam was originally sent by three folding mirrors to the pulse picker. However, we were concerned during the August 2016 beamtime that temperature changes in the oscillator were causing significant pointing changes. A point lock system using two cameras looking at leakthrough beams and two tip tilt staged driven by picomotors was implemented to correct for any pointing misalignment and ensure the beam passed safely through the pulse picker. This system was later found to have no effect and was disabled, though the cameras proved useful for alignment. The pulse picker supplied with the laser was not designed to handle the power output of the oscillator. The Conoptics model 350 pulse picker design was fluid filled and highly susceptible to thermal turbulence in the fluid and heat warping of the KDP crystal. The original pulse picker was replaced

with an air spaced design capable of handling the full output power. After the pulse picker, there is still a significant leakthrough of rejected pulses. The power in the rejected pulses was measured by photodiode to be around 4% of the picked main pulse. To absorb these small pulses, another saturable absorber mirror was placed between the output of the pulse picker and the input optical isolator of the amplification stage. The pulse picker is driven by an Conoptics RF power supply coupled to a Conoptics electronic countdown timing box. The timing box accepts a photodiode signal or a digital TTL signal as input to its internal countdown electronics, is able to count for as many as 9999 pulses before firing, and accepts an external TTL trigger pulse. The box has an internal $8ns$ delay to find pulse overlap between the RF drive and the laser pulse and a maximum rep rate of $62.5MHz$.

The amplifier is a four pass configuration as depicted in figure 3.12. Two 250W $940nm$ JOLD-250-CPXF-2P2 lasers from Jenoptik GmBH pumped the cryo cooled oscillator crystal. The laser was originally shipped with the pump lasers located inside the primary laser enclosure. The power cables were also inside the enclosure and when the amplifier was switched on at full power, these acted as giant heating elements that produced temperature swings as high as 20 degrees Celsius. To mitigate this problem, the pumps were relocated to a separate housing at the end of the laser table.

The amplifier had issues with white light generation when the pumps were close to maximum power. White light was visible at the entrance mirrors to the vacuum cavity housing the crystal. We believe that thermal focusing in the crystal was producing intensity high enough to generate white light in the housing windows. We could not fix this problem and instead limited the power of the laser to $\sim 40W$ total.

The beam profile was measured after attenuating the full power to appropriate levels with a waveplate polarizer combination and is shown in figure 3.11. Gaussian fits to the horizontal and vertical directions returned 95.69% and 95.86% confidence with 1σ beam diameters of $2199.02\mu m$ and $2093.85\mu m$ respectively.

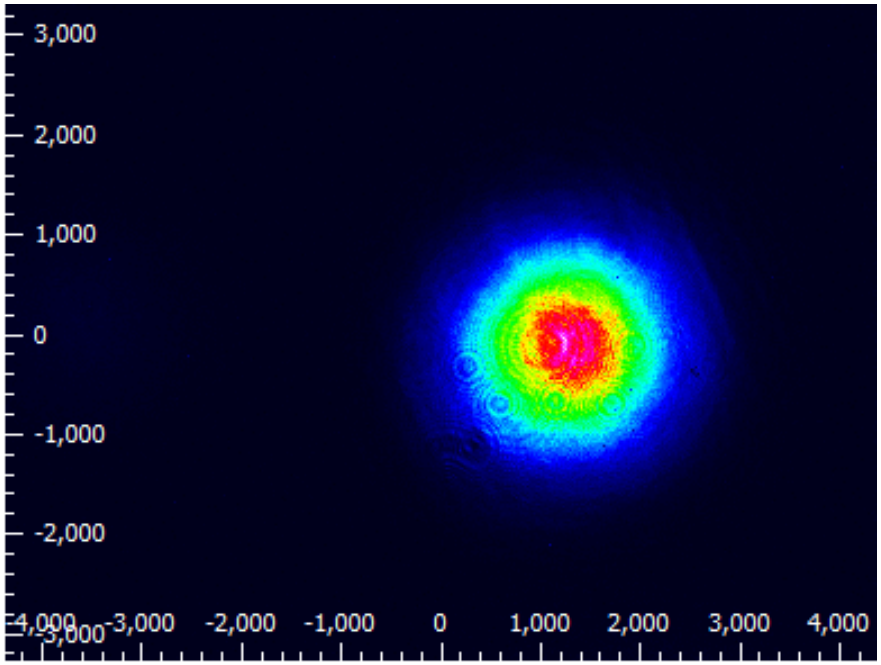

Figure 3.11: Beam profile measurement of the Q-Peak amplifier output. Units are in the micrometers. Beam diameter is approximately $2mm$.

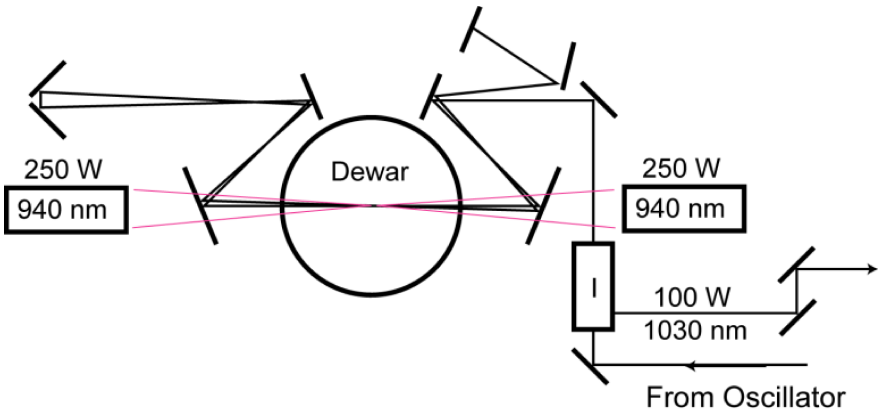

Figure 3.12: Illustration from [54] depicting the final layout of the 4 pass amplifier.

3.3.2 Beam Transport & Geometry

Guiding the laser beam from the laser table to backfocus was nontrivial. After exiting the Q-Peak enclosure the beam was put through a "shaper" that contained a wave plate polarizer combination for attenuating the beam, a half waveplate for rotating the polarization, and a spherical convex expanding mirror ($10cm$ focal length) in combination with a spherical concave collimating mirror ($1m$ focal length) separated by approximately $90cm$ in a telescope configuration for expanding the beam to 10 times its original size, roughly $20mm$. The telescope geometry was slightly off axis and introduced horizontal ellipticity into the beam mode. The beam was expanded to achieve a tight focus at the target.

After shaping The beam was then sent through a long $\sim 3m$ transport tube to a self contained "feeder" stage that connected to the beamdump of the COLTRIMS end chamber in a light tight enclosure. The feeder stage contained all the optics for aligning the beam onto the backfocus mirror in vacuum, $2m$ away from the last turning mirror.

The expanded beam was aligned to two irises on the shaper and two on the feeder. The shaper table housed a HeNe laser aligned to these irises which was used for coarse preliminary alignment of the back focus stage while the chamber was open. However, the size of the expanded beam rendered consistent alignment impossible using these irises. To align the laser beam onto the backfocus mirror, an IR camera with a telephoto lense was used to observe the backscattered intensity off the front and frosted back of the mirror, and the spot was used to determine the location of the beam.

Auto cad renderings of the chamber, spectrometer, and backfocus mirror mount are shown in figure 3.13. The laser beam enters through the beamdump and is back-reflected through the beamdump at an angle defined by the central position on the mirror and the interaction point.

Small drifts in the beam pointing were not thought to impact the position overlap at the target because of the compensation from the spherical backfocus and the long arm from the last turning mirror to the backfocus mirror. Assuming that the offset at the focus is a

linear function of the beam pointing, a focal distance of 17.5, a lever arm of $2m$, and that the position of the laser does not drift by more than a millimeter on the backfocus mirror (corresponding to angular pointing of $500\mu rad$), we can expect $(17.5cm/200cm) \times 1mm = 87.5\mu m$. Given that the focus size of the ALS is nearly $200\mu m$ it was reasoned that overlap would be maintained given random pointing fluctuations.

Electro-Optics & Optics

The in-vacuum focusing mirror was spherical concave, was $50.5mm$ in diameter, with a $175mm$ focal length, a $10mm$ hole centered and straight through, a scratch and dig specification of 10/5, and was manufactured by ARW Optical Corporation. The focal lenght was determined by measuring the final assembly of spectrometer and optical mounting stage configured in the chamber. The high scratch and dig specification was thought necessary to reduce scattering, which is likely to be more of a problem for higher energy laser photons. The mirror was coated by Lattice Electro-Optics Corporation with a high reflectance multilayer coating centered at $1030nm$. During the August beamtime, the mirror coating was found to have de-laminated from the surface of the mirror, producing a bubble wrap like appearance. We believe that this was caused by either the laser beam clipping the edge of the central hole and heating the mirror, causing tension locally in the substrate or by runaway de-lamination from exposure of the laminate edge around the hole to high vacuum. To solve this problem the mirrors were re-coated for the June beamtime with a different formulation and an offset bevel from the inner and outer edge. The offset ensures that the coating would not de-laminate from thermal stress around the edges of the mirror. The newly coated mirrors survived the beamtime with no visible damage.

Given the expanded $20mm$ laser beam used for experiments, the backfocus mirror was calculated to produce a gaussian beam waist of $12\mu m$ and a Rayleigh range of $400\mu m$ at the focus.

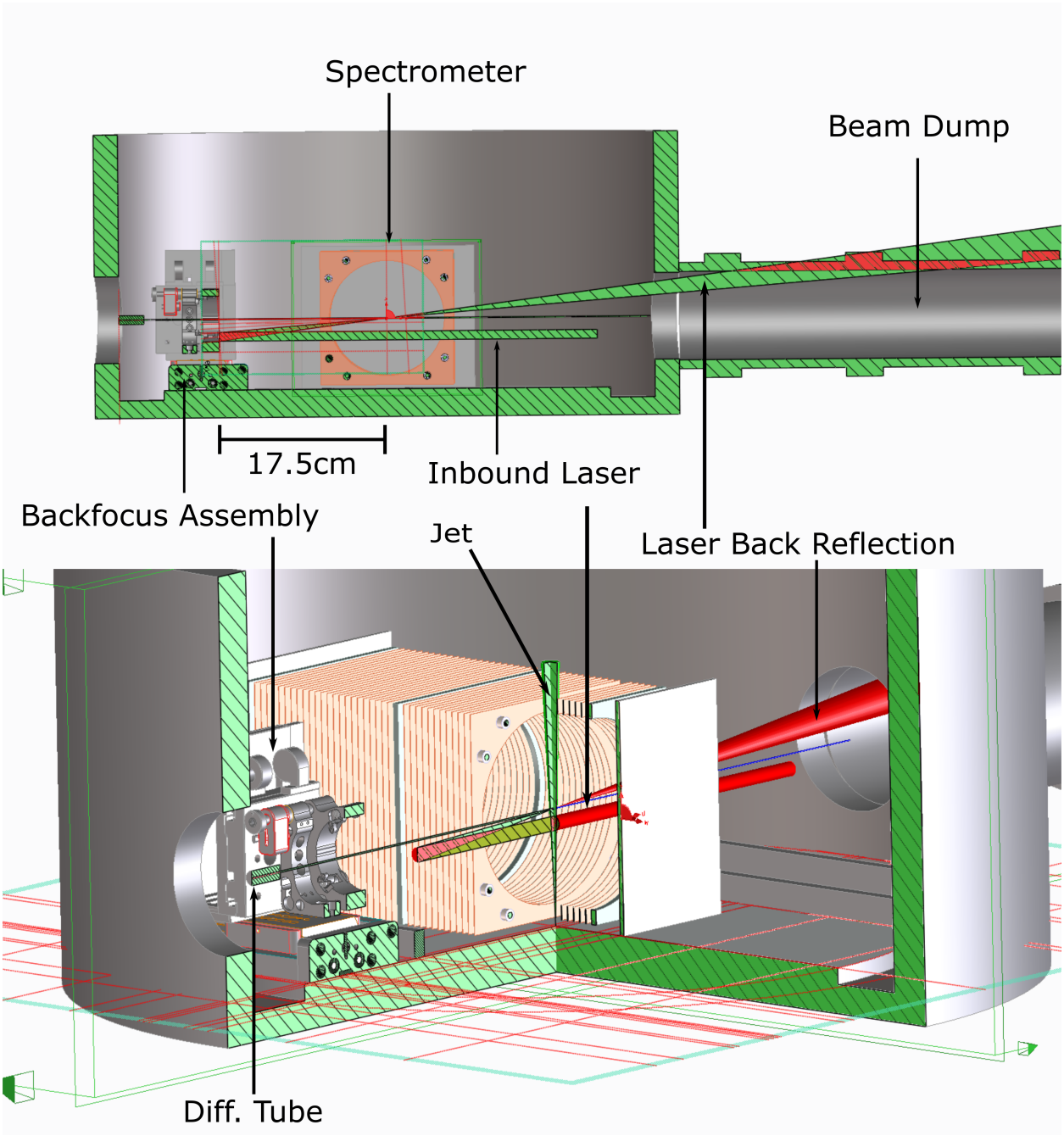

Figure 3.13: CAD renderings of the chamber, spectrometer, and backfocus mirror mount. The laser beam is modeled as a 10mm red tube incoming from the right. The beam is focused by the mirror and diverges into the common beamdump for the laser and ALS. The ALS beam is modeled as a thin smaller tube centered in the diff tube. The jet appears as a green vertical cone.

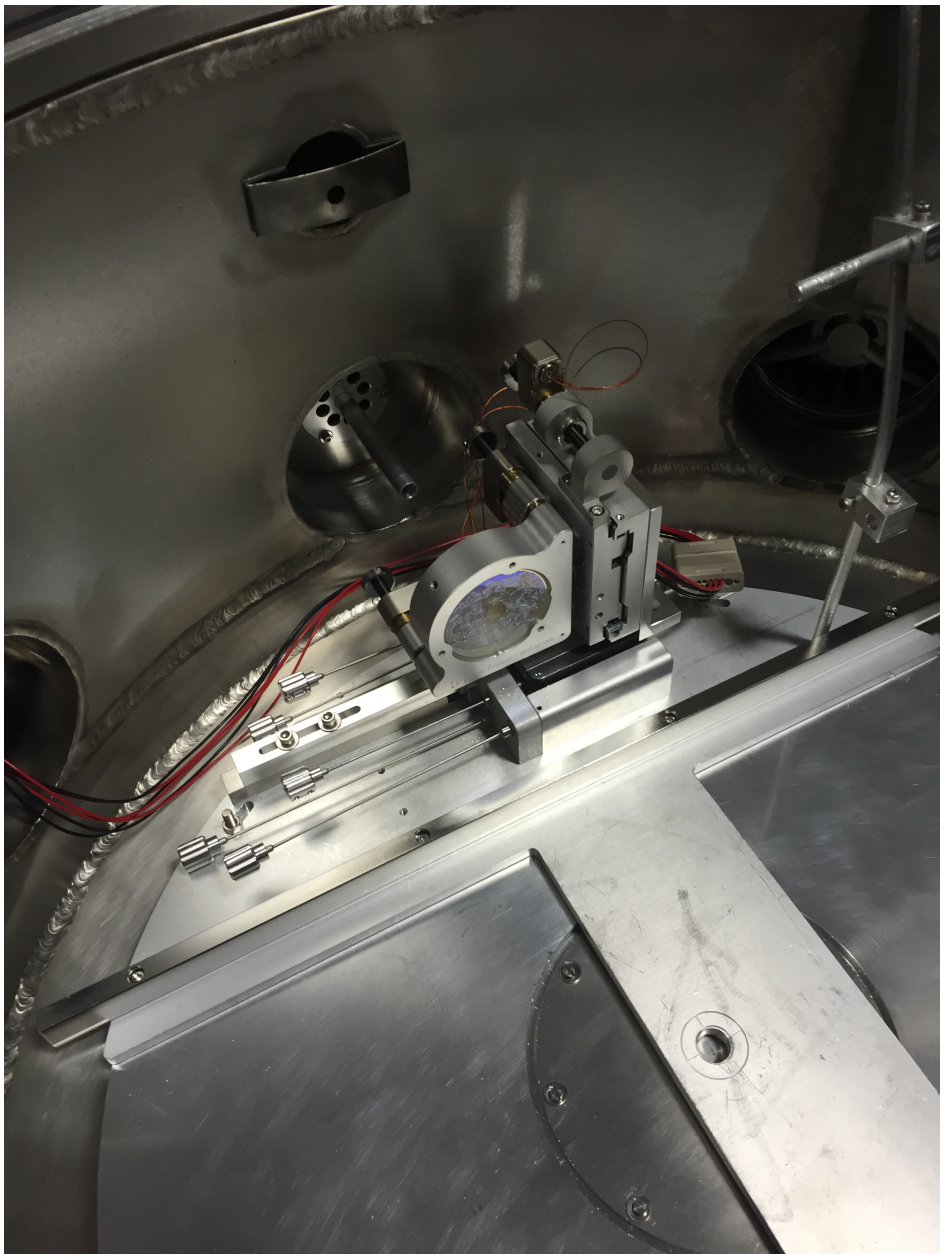

Figure 3.14: Picture of the backfocus mirror stage placed on the rail in the chamber. The mirror is 2 inches in diameter.

Turning mirrors for transporting the laser were supplied by Lattice Electro Optics. Mirrors were coated for $1030nm$, 45 degree incidence, and p polarization. The specification of p polarization meant that approximately 20% of the intensity was lost in the s polarization.

The in-vacuum actuated mirror stage was constructed from off the shelf components from ThorLabs and Newport corporations. The tip-tilt holding the backfocus mirror was a Newport model 8822-UHV, UHV compatible to $10^{-9}Torr$, and driven on each tip axis by picomotors for angular resolution of $0.7\mu rad$ and a total range of ± 3 degrees for tip and tilt. Given the focal length of the mirror this angular range corresponds to $\pm 10mm$ of motion at the focus - more than enough lateral movement to find the interaction region - and a position resolution of $122nm$ - more than accurate enough to overlap the micrometer sized laser focus with the ALS beam. The tip tilt was mounted to a Newport $1in$ linear translation stage retrofit for UHV environments and driven by a picomotor with $30nm$ position resolution - more then enough resolution to overlap the Rayleigh range of the laser focus and Jet-ALS target overlap, both on the order of a millimeter long.

The actuated assembly was held by a bracket on top of a Newport 5-axis manipulator for coarse alignment. The Five axis manipulator was fixed to the chamber floor by a stainless steel rail system that allowed for motion perpendicular to the beam. This motion coupled with the height adjustment afforded by the upright bracket provided another coarse alignment. All told, there were 11 degrees of freedom with which to adjust the stage. In practice, the five axis manipulator was found to be unnecessary as the coarse alignment could be accomplished almost entirely with the picomotor controlled elements.

3.3.3 Position Overlap

To ensure that the two beams were as close to overlap as possible prior to closing the chamber, the actuated picomotor assembly was used to steer the backfocus mirror such that a pilot He-Ne laser, aligned to the irises on the laser “shaper” and ”feeder” tables (significantly

upstream), was on target with a needle alignment tool positioned over the jet. This ensured that we were not "hunting in the dark" with the picomotors after we closed up the chamber.

Position overlap at the jet was achieved in vacuum using a phosphor paddle inserted into the spectrometer on a long arm actuated externally. The paddle was moved into the spectrometer until it clipped the jet as observed by a drop in pressure in the jet dump. Further movement to align the phosphor slide to the jet position was calculated using the measured paddle geometry. The ALS XUV spot on the phosphor was then photographed. The ALS was then blocked and the laser focus spot on the phosphor was photographed. Both images were loaded into a custom line-out program written by our collaborators at University of Nevada, Reno, to compare the central position of each spot in the vertical and horizontal directions. Gaussian fits to the line outs were used to determine the position. The tip-tilt picomoter stage was used to move the laser spot onto the x-ray spot by iterative pictures. An example picture of the laser spot on the phosphor is shown in figure 3.15. It is clear from examinations that the spot size of the laser appears larger than the XUV spot size. The spot size is a function of the available light intensity which is much greater for the laser.

The method of alignment was limited by the resolution of the photographs and the grain size of the phosphor. We made no attempt to characterize the grain size of the phosphor, but we observed variations smaller than the dot size when moving the laser beam during the overlap procedure. This indicates that the grain size was less than $50\mu m$ and was most probably compensated for by the Gaussian fitting procedure in the line out program. An 18 megapixel camera with $4.3\mu m^2$ square pixel size and $22.3mm \times 14.9mm$ sensor size in conjunction with a telephoto zoom lens and focal reducer functioned as a long working distance microscope. Telephoto lenses have a minimum working distance below which they cannot achieve a sharp focus on the camera sensor. A focal reducer decreases the f-number of the lens assembly and therefore the minimum working distance. We were able to achieve a $\sim 50mm$ field of view when focused on the phosphor which translates into a $\sim 4\mu m$ pixel

resolution. We estimate that 10 to 25 pixels span the narrow horizontal dimension of the ALS and laser spot sizes.

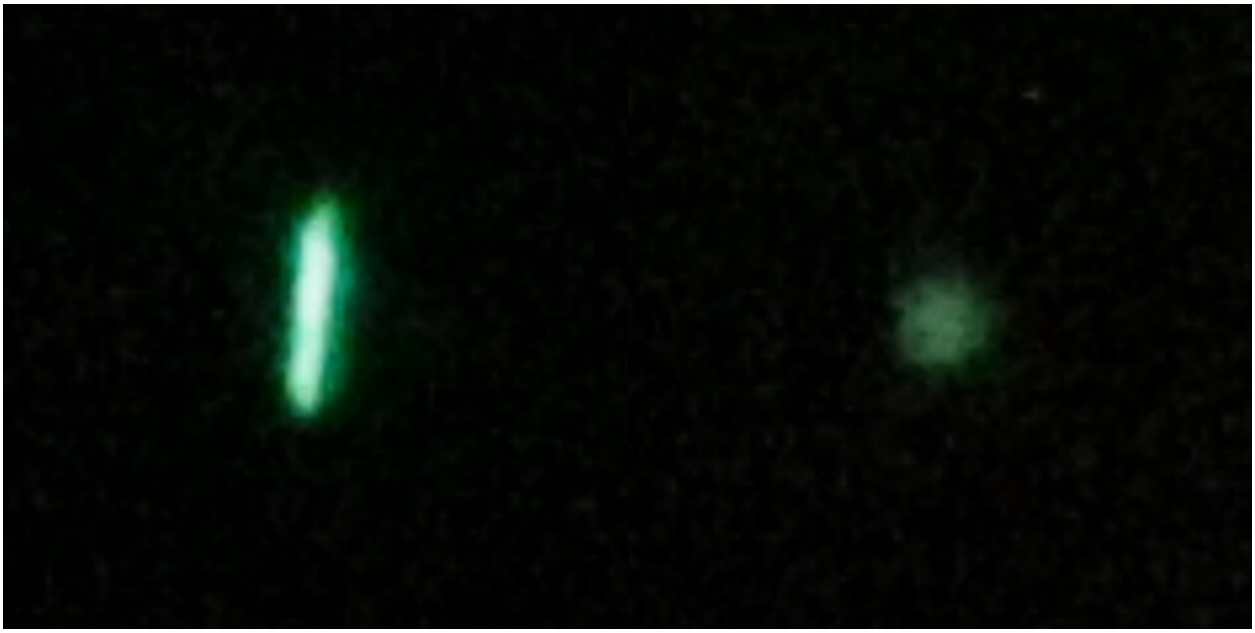

Figure 3.15: Typical high resolution photographs used for alignment. Left image: laser focus on phosphor. Right image: ALS spot at $18.44eV$ energy. To show more detail, the images have been clipped and expanded around the light spots.

3.3.4 Synchrolock

Synchrolock refers to the active stabilization of two pulse trains, here laser and synchrotron, such that their frequencies are locked to a single value and the pulses are synchronous with a fixed phase offset. An illustration of this concept for two digital pulse trains is shown in figure 3.16, taken from [55]. This section will describe the developement of each aspect of our custom synchrolock system. Before diving into specific discussion of each iteration, this section will begin with a general overview.

At its heart, the synchrolock system is a control loop that takes as input two pulse trains and outputs an error signal to adjust one of the pulse trains (the laser) to minimize the phase difference. In this sense, the error signal is a voltage and the laser acts as a voltage controlled oscillator in a phase lock loop (PLL) circuit. The system deployed at the

first successful 2-color beamtime (August 2016) used nim bin electronics to digitize a $1MHz$ photodiode amplifier signal and send it to an off the shelf digital AD9650 Phase Lock Loop (PLL) test board connected to the Q-Peak supplied synchronization box. By the next and most recent beamtime (June 2017), the system had evolved to use a $61.9MHz$ photodiode signal from the oscillator, an analog mixer, analog delay line, and a PID controller from Stanford Research Systems (SRS). Additionally, the custom electronics shipped with the laser had been bypassed to access directly the piezoceramic OEM driver in the Q-Peak timing box. Along the arc of this evolution, almost every combination of digital and analog system was implemented and tested.

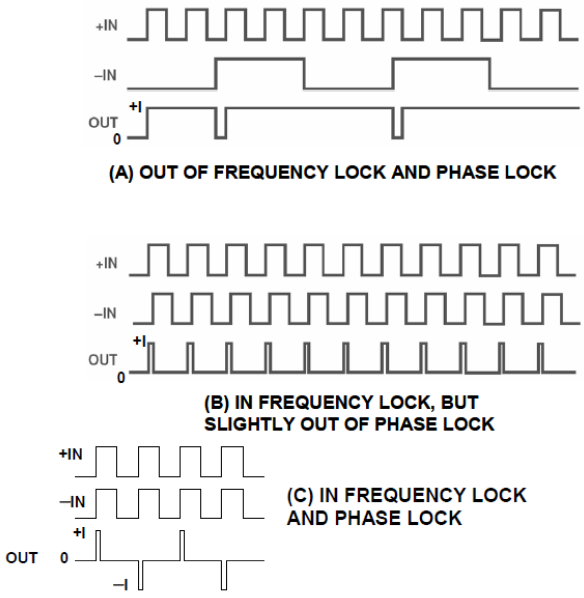

Figure 3.16: Illustration from [55] depicting two digital pulse trains out of frequency lock (A), synchronously out of phase (B), and in synchrolock (C). The two in signals correpsond to two pulse trians, and the out signal is that of a digital Phase Frequency Detect (PFD) circuit.

The scope of the timing problem is as follows: the bear minimum system requirements were to ensure that the laser pulse arrive at the interaction region before the XUV pumped molecule left the interaction volume due to jet velocity or field acceleration. Much of the interesting scientific work required that the laser pulse be overlapped with the XUV pulse such that the initial ionization of the molecule happens in the presence of the strong field.

This condition requires at least a timing jitter between the two pulses less than the width of the longest pulse: the synchrotron pulse width of approximately 80ps. Achieving low jitter over $\sim$ 100 hour timeframes is a technical challenge simply because measurement of long term drift is difficult and requires specialized and expensive phase noise analyzers. These tools are often optimized for communications applications with electronic infrastructure which is much different from a laser system. The timing system had to accommodate synchrolock between two pulse trains with frequencies that differed by the multiplication of a rational fraction. For example, during the August 2016 beamtime we operated with a laser pulse every third ALS pulse: a rational fraction of 1/3. Furthermore, arbitrary time offsets were required on both arms of the timing signals to ensure that overlap could be achieved at the target zone. These offsets introduce a phase offset to compensate for the arbitrary delay introduced onto one, the synchrotron arm (to zero out the electron time offset) and two, the propagation of the laser into the chamber. This was accomplished initially with SRS DG645 Gate and Delay Generator boxes in the first beamtime, and with cable delays and an RF trombone in the second.

The quality of the synchrolock is foremost impacted by how the timing signals are generated, second by how they are processed to create the error signal, and third by the adaptive mechanical response of the physical system to the error signal. Though noise can originate in the synchrotron or the laser, by far most of the noise comes from the laser: the synchrotron is well isolated and stabilized. Thermal expansion of the laser table and small changes in the pointing within the laser oscillator cavity produce slow drifts, while vibrations transmitted through the table to mirrors and the vibration in the feedback actuator assembly itself cause fast transients.

Any synchronization scheme begins with the electrical pulse trains generated from photon or projectile pulses. The ALS has a user timing system that provides very low jitter (4ps) signals to the user through a user timing chassis. A more accurate signal exists in the form of a specialized heliax cable transporting the RF driving signal of the synchrotron - but

this was unavailable and exceeded our requirements. The timing signals from the laser were generated by a leakthrough beam from a turning mirror striking a fast photo-diode. There are technical challenges in using a photodiode signal. First, the inherent power fluctuations in the laser pulses transfer directly to the photodiode pulse, causing the familiar problem that, for any fixed threshold digitization, the signal would trigger at different points for different laser shots. The exact same problem occurs with the signals from the COLTRIMS detectors, and the solution is to employ a FAMP and CFD combination. However, these elements themselves introduce a jitter of $70 - 250ps$. Second, the photodiode itself has inherent noise arising from thermal and voltage fluctuations known as Noise Equivalent Power (NEP), but this contribution is negligible for our strong saturation conditions, and is on the order of 10^{-9} smaller than the signal [56].

One relatively easy way to mitigate the laser power amplitude variations in the photodiode signal is to saturate the photodiode to extract its maximum response. Most of the variation in pulse height will occur at the top of the pulse and with a sufficiently strong pulse a low trigger value will narrow the distribution of trigger times. It is clear to see that the accuracy of a photodiode is limited by its response time to the light pulse and a faster rise and fall time will capture a more precise signal. The metric for describing the response time is the bandwidth of the photodiode: the bandwidth upper limit is the highest frequency in the Fourier transform of the fastest achievable output pulse. The photodiode cannot detect frequency changes beyond this limit. The bandwidth is limited by the quantum efficiency of the photodiode and the capacitance of the circuit [56] In the first beamtime we used a silicon diode with $350MHz$ bandwidth. In June 2017, we upgraded to a fiber coupled InGaAs diode with $5GHz$ bandwidth. The bandwidth of a photodiode can be converted into jitter by considering the phase error: the distribution of phase offset between consecutive pulses at a fixed frequency. For the two photodiodes above, if we assume as an upper bound the worst case scenario of a 10% error from the power fluctuations, the jitter would be $286ps$ and $20ps$ respectively. If, instead, we assume that only the NEP contributes to the error,

then the contribution to the jitter from the photodiodes is essentially zero. In modern systems, it is not uncommon for the total phase error to be on the order or 1 milliradian. The corresponding jitter would be $18ps$ and $1.26ps$ respectively.

The physical adjustment of the pulse train of the oscillator was achieved by piezo-actuation of the output coupler turning mirror. The output coupler was mounted on a spring loaded steel translation stage and the stage was driven by a piezo with $45\mu m$ of travel from PI ceramics. The piezo was a pre-loaded actuator stack with a ball tip - pre-loaded in the sense that a $50N/m$ spring in opposition to the piezo was contained in the housing and provided a pull resotring force. The piezo itself can supply $200N$ of push force but only $10N/m$ of pull force before fracturing from stress. The travel range was enough to alter the cavity frequency by $\sim 1kHz$: a frequency range more than enough to compensate for any temperature drifts encountered by the table in normal operation. However, downdraft from the dewar cryo system can cause significant warping of the table outside the normal compensation range.

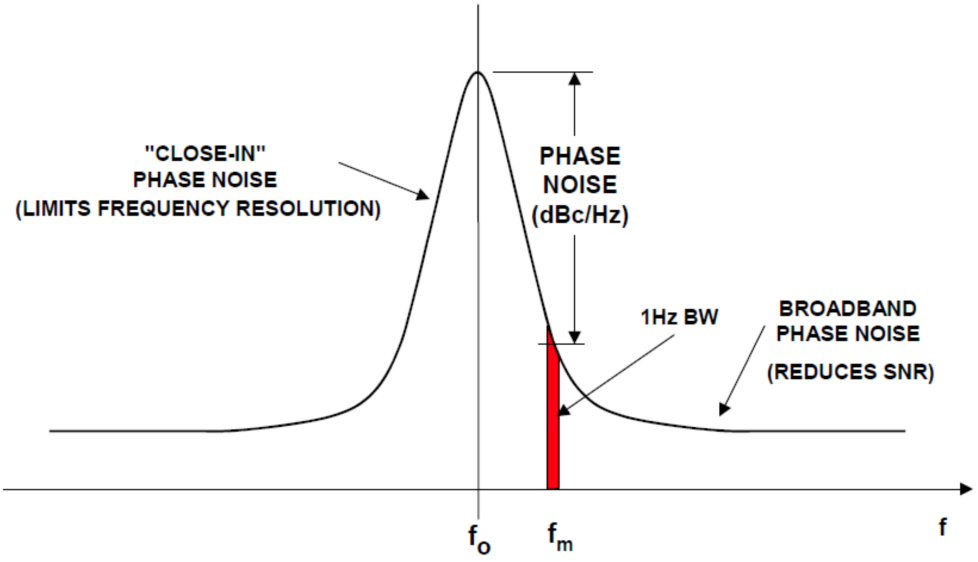

Figure 3.17: Illustration from [57] depicting phase noise in the sidebands of a frequency power spectrum.

Any real world pulse train has a spread in frequency. In the frequency power spectrum, a well stabilized pulse train will have most of its power concentrated about the central frequency f_o. Phase noise in frequency space is directly related to jitter noise in time space [57]. On each side of this frequency, some power will be distributed, rapidly falling to the background white noise level. This sideband power is noise: it represents the number of pulses that are out of phase with the ideal pulse train. For a pulse train with constant power, the sidebands directly translate to time space jitter via the equation:

$$J_{RMS} = \frac{\sqrt{2 * \int_{f_o}^{\infty} P[f] df}}{2\pi f_o}, \tag{3.27}$$

where J_{RMS} is the root mean square jitter in seconds, and the numerator is the square root of twice the integral of the power spectrum over a single sideband. Note that the power spectrum is given in units of dBc/Hz, where the reference value for the logarithm is the peak power at the fundamental frequency f_o, and in the equation above the explicit conversion from decibels to units of the fundamental power are omitted for clarity.

It is often the case that the power spectrum has sharp peaks away from the fundamental at resonant frequencies of the system. These peaks are called spurs, and can give clues to determine the source of noise. We observed a strong spur between $300Hz - 400Hz$ which we believe to be the vibration of the stage coupled to the $\sim 50N/\mu m$ spring in the piezo assembly. The coupling is accomplished by epoxy applied between the ball tip of the piezo housing and the side of the retro reflector translation stage. Assuming the stage has on the order of $100g$ of mass;

$$f_{stage} = \sqrt{\frac{k}{m}} \tag{3.28}$$

$$= \sqrt{\frac{C^2 50N/45\mu m}{100g}} = C \times 3.33kHz, \tag{3.29}$$

where f_{stage} is the resonant frequency and c is the coupling constant. If the coupling introduced by the epoxy is on the order of 10, not unreasonable given the plasticity of epoxy, that the resonant frequency of the stage can be excited by strong vibrations. The effect of these vibrations is to move the mirror of the cavity, which in turn affects the frequency. Given harmonic oscillator motion, the average displacement of the stage is half the total extension, and this corresponds to half the frequency range the piezo can affect: roughly $500Hz$. However this value would be reduced by active damping from the control loop or if the piezo was near to its maximum or minimum extension which was often the case. Additionally, the stage itself has an asymmetric driving force - $1000N$ push, $50N$ pull - that would affect the average position. On the whole we conclude that the heavy stage assembly has a resonant frequency that is too low to compensate for some of the vibrations on the laser table.

Synchrolock systems 1 & 2

The original synchrolock system, what we will refer to as version 1, is shown in figure 3.18. The primary timing signal was generated from the laser pulse in the amplifier, which has the advantage of guaranteeing that the correct "bucket" of light is always chosen. If pulses are chosen in the oscillator, then synchrolock can be achieved but is not enough to ensure that the correct oscillator pulse is picked by the pulse picker to align with the ALS pulse train. There would be a random time offset equal to $n \times T$, where T is the period of the oscillator and the integer n is determined by the pulse that begins the pulse picker counter and can range from 0 to 61 (for picking every 61st pulse).

The photodiode signal from the oscillator was attenuated and amplified close to the source in order to be sent through a long BNC cable to timing electronics cart. There it was further attenuated, inverted, and amplified by a FAMP and digitized by a CFD. The FAMP and CFD introduced jitter of at least $70ps$. The digital signal was used to trigger a gate and delay generator to provide an arbitrary delay with accuracy down to $\sim 50ps$. The gate and delay generator adds $\leq 30ps$ of time jitter for our delay range. The duty cycle of the DG645

output pulse was set to 50% and the pulse height to the standard TTL height appropriate for the AD9520 board. The AD9520 was used to divide the photodiode pulse train by 2 and the orbit clock by pulse train by 3 to phase frequency detect at the common denominator frequency of $500kHz$.

A custom loop filter, what is essentially a low pass integrator, was used to smooth the charge pump error signal from the board. The loop filter was designed with the ADISym PLL simulation software, and effectively controls the bandwidth (convergence window of the loop), integral, and gain. The error signal was fed directly into the Q-Peak control box and, somewhat incredibly, the system worked even with the deadbands built into the Q-Peak electronics.

System 1 produced a jitter on the order of 230ps and a drift on the order of 400ps, as demonstrated by the post processed bunchmarker data shown in figure 3.22. It is clear that the laser was moving back and forth across time zero. If the laser arrived before the ALS pulse, then it could not dissociate the H2, producing a sharp cutoff in data . What is unclear in the plots of figure 3.22 is how much of the apparent jitter is coming from the NIM bin electronics processing both bunchmarker signals and how much is actual time jitter. It appears given the two main spikes, that a significant amount of the observed jitter might be from the electronics. However, the large data sampling in the $H+$ no-laser channel definitely shows long term drift.

Clearly version 1 of the timing system was inadequate: data was lost whenever the laser moved before the ALS, and suboptimal data was collected during periods of long delays. After extensive conversations with Russel Wilcox of LBNL [58], a second loop operating in conjunction with the first loop was proposed. The second loop would function at $500MHz$ and would by rule of thumb provide a jitter of $.001mRad/2\pi \times 2ns \sim 400fs$. the idea was to combine the error signals in a custom loop filter such that the faster loop would smooth out the errors from the slower loop. This system, version 2, was never fully implemented because of issues designing an appropriate loop filter circuit. There was also the possibility

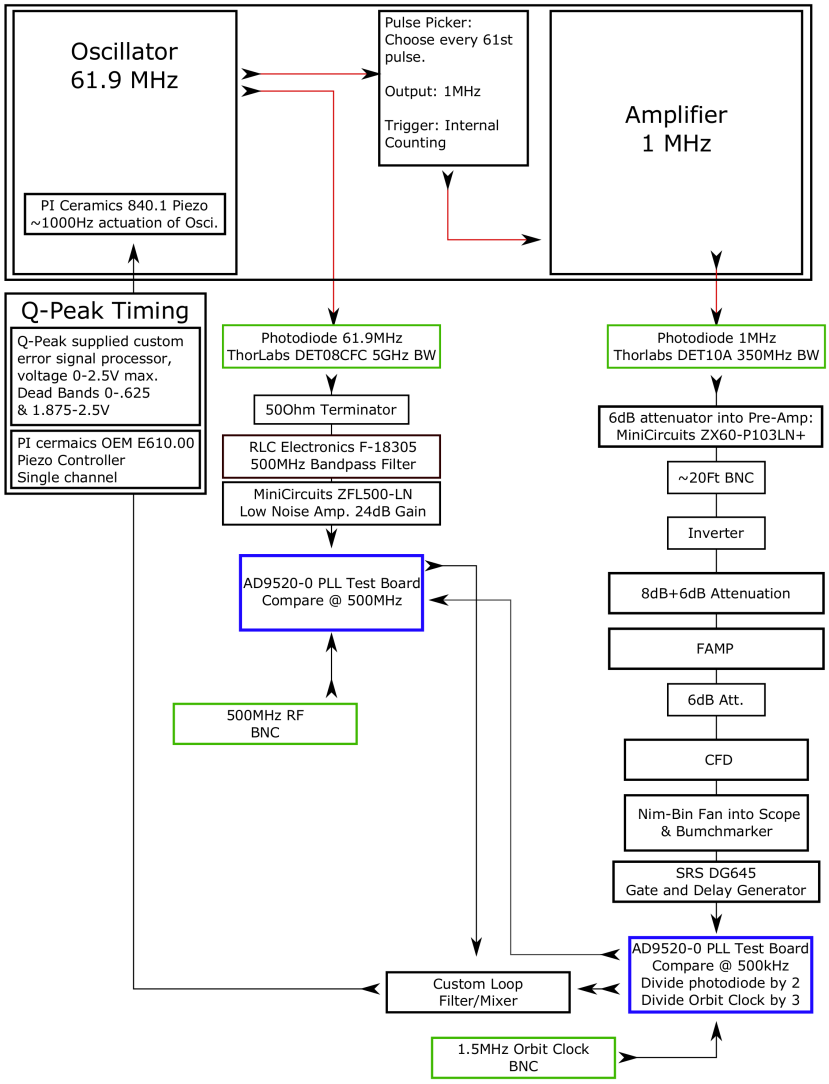

Figure 3.18: Block diagram of the original synchrolock timing system and the additional timing loop proposed after the first beamtime to improve performance. Red lines represent laser beams and black lines represent electrical cables. Green boxes are timing signal generators and blue boxes are comparators. See text for details.

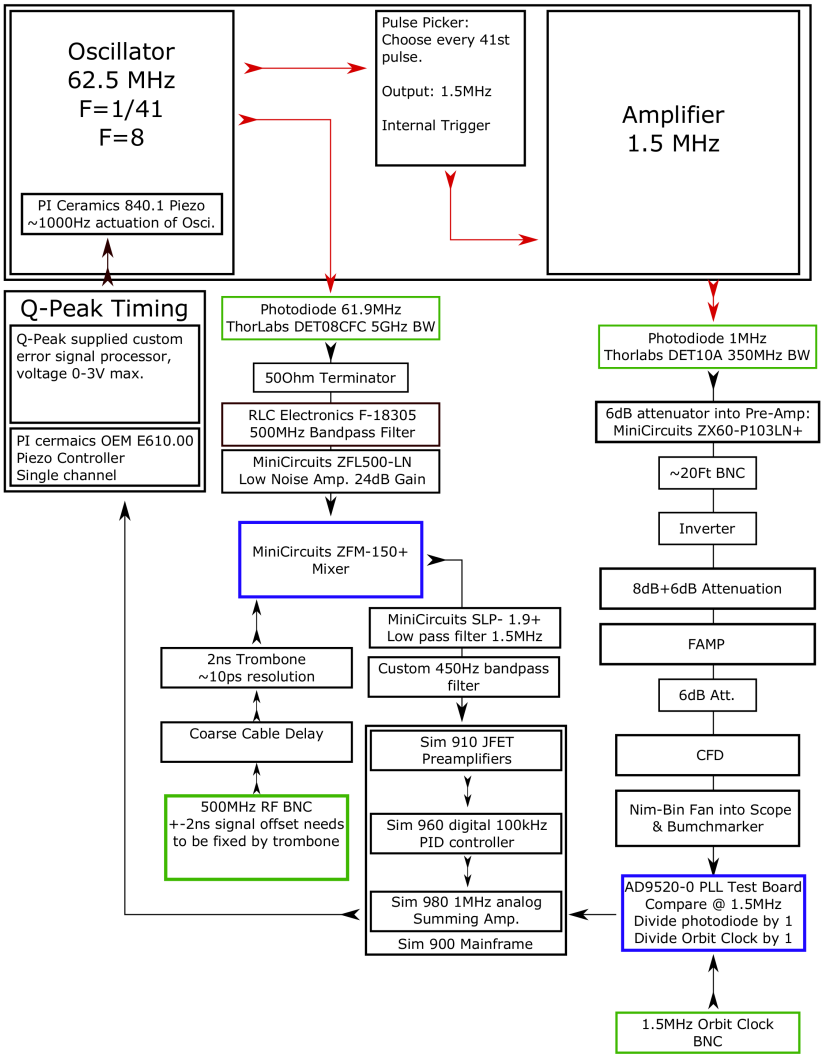

Figure 3.19: Block diagram of the synchrolock timing system with the attempted double loop. Red lines represent laser beams and black lines represent electrical cables. Green boxes are timing signal generators and blue boxes are comparators. See text for details.

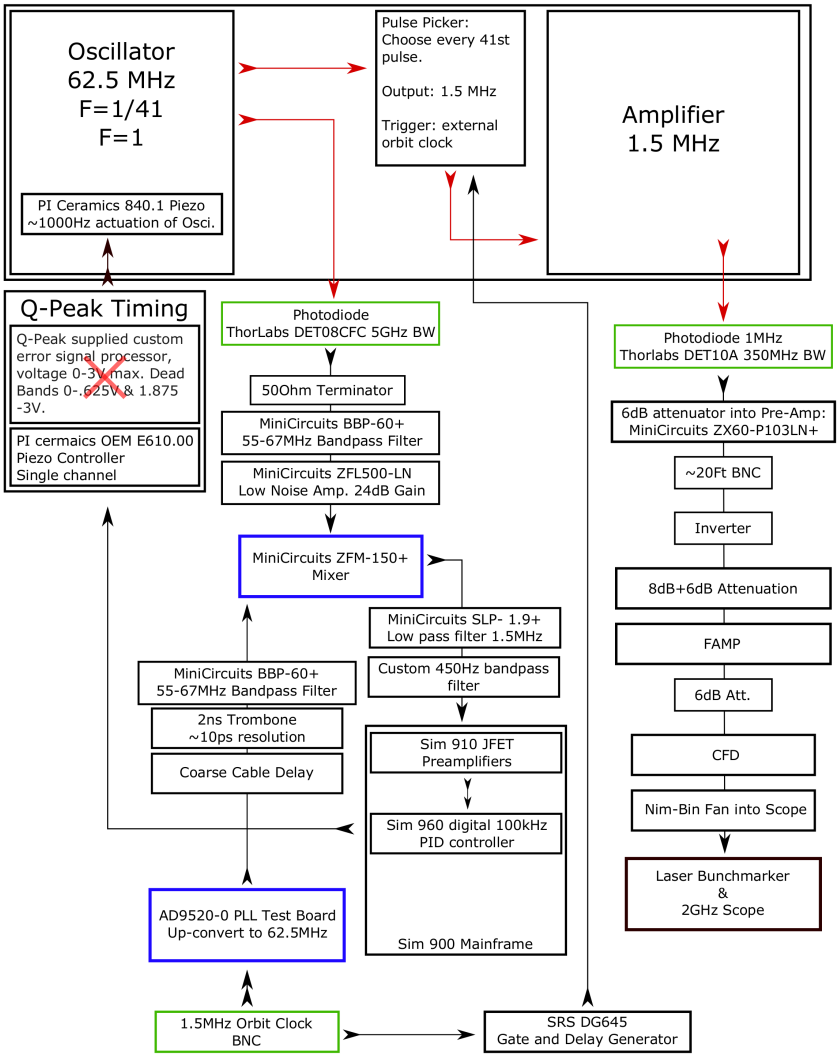

Figure 3.20: Block diagram of the final synchrolock timing system. Red lines represent laser beams and black lines represent electrical cables. Green boxes are timing signal generators and blue boxes are comparators. See text for details.

of having the slow loop disable the fast loop, as indicated by the gray arrow between the boards in figure 3.18.

Instead of the proposed design, an SRS summing amplifier was used to combine the version 1 signal with the output of an analog mixer as shown in figure 3.19. Briefly, the output of a fast 5GHz InGaAs photodiode was fed into a custom RLC electronics $\sim 500MHz$ bandpass filter specifically designed for the fundamental ALS driving frequency. The filter picks off the 8th harmonic from the photodiode and sends this to a fast amplifier and into an analog mixer. The second input to the mixer is a 500MHz sine wave from the user timing system.

The combination of both signals proved to be unstable. The mixer output could not be attenuated enough to be "invisible" to the AD9520 board. Ultimately the effect of the 500MHz loop was to introduce oscillations, falling short of realizing the two loop model. The poor version 1 loop was removed from the control loop entirely in favor of just the 500MHz loop. However, it was immediately discovered that the 500MHz loop was too sensitive to convergence onto a stable state. In other words, the lock bandwidth was too small or the table too noisy. The error signal initially fluctuated so fast as to vibrate the turning mirror out of position and destroy mode lock.

At this time it was realized that the deadbands in the Q-Peak electronics were unworkable. The deadbands prevented the loop from capturing the lock by effectively reducing sensitivity. The loop must instead lock the signal while it transits the active band. The box was modified to bypass the Q-Peak electronics and go directly into the PI Ceramics OEM driver, which accepted a 0-10V signal conveniently matched to the output of the SRS PID controller.

Both the analog and digital systems were tested again with the deadbands removed The 500MHz analog mixer loop failed as before. Interestingly, the AD9650 board was able to run at $61.5MHz$ by triggering directly off of the fast photodiode signal without a CFD conditioning. According to the method of measurement on the fast scope this iteration had

the least jitter, but it was impossible to control the parameters of the system. The lock window and response sensitivity of the digital PLL circuit are controlled by the loop filter component. The loop filter is a hard wired series of resistor-capacitor and capacitors that act as an integrator to the output of the board charge pump (current source). To start the lock, the board required that the timing signal rates be divided with the on board divisors by as much as 41 in order to increase the lock window. After the board had achieved lock, the dividers could be removed and the board would maintain the lock. Therefore, the system could not self recover without attention from a user.

The final iteration used in the June 2017 Beamtime is shown in figure 3.20. A second AD9520 was used to upconvert the orbit clock signal into a 61.5MHz signal to match the oscillator. The oscillator frequency was adjusted so that its pulse train was an exactly matched to the orbit clock (half the ALS frequency). The rational fraction between the laser and ALS pulse trains was 41/2. To ensure correct bucket selection, a channel on the DG645 triggered from the orbit clock was used to externally trigger the pulse picker. The delay on the channel was adjusted to pick the right bucket to be aligned (within one period of the oscillator) with the ALS light. The upconverted orbit clock signal was delayed with an adjustable cable delay (coarse delay) and a 2ns trombone with $\sim 10ps$ accuracy (fine delay). Both 61.5MHz signals were amplified and fed into an analog mixer, the output of which was passed through two low pass filters and into the SRS PID control. The SRS PID was tuned to cause convergence of the error signal to zero. Typical tuning values were $P = 10$, $I = 120$, and $D = 0$.

Synchrolock Jitter Measurement

We had five methods to measure the jitter during the experiment, in order of accuracy: the two color cross correlation measurement in Helium, a signal source analyzer, timing error signal from the analog RF mixer, a fast oscilloscope, and the post processed bunchmarker

time difference between the ALS and IR. Only the first method was inherently free of electronic noise: each other method in some way was compromised by the inadequacy of the electronics for this specific measurement.

The scope used to measure the jitter had a $1GHz$ bandwidth with 20 gigasamples a second. The scope was set to trigger, in persistence mode, on the rising edge of a user timing system digital signal clone while a second channel was used to observe a strong silicon photodiode signal from the laser. The time difference between the rising edges at 50% amplitude was recorded for $12k$ shots, the scope maximum. The scope automatically computes the RMS jitter from the $12k$ shots with a built in math function. Additionally, the cursors could be used to measure the spread of the leading edges, though this was good only for establishing an upper bound. This approaches the sample spacing of the scope and probably represents a lower bound of our measurement ability.

When available, a Signal Source Analyzer FSUP8 (FSUP) from Rhode & Schwarz was used to analyze the single sideband phase noise and integrate to measure the jitter. The FSUP was able to measure to within $20Hz$ of the central frequency of the oscillator. The integrated jitter measurement was below $20ps$, but large contributions to the jitter may have been hidden in the "close in" noise band. To measure this noise, the instrument must maintain a lock with the signal, maintain the stability of its own precise timing system, and integrate for a long period of time. Consequently, the FSUP may have been blind to the major sources of noise in the system.

The best available measurement of the timing jitter was the two color cross correlation measurement with the background free laser photoionization of XUV pumped Helium. We measured the rate of the two color signal as we swept the laser delay across time zero. We found the mid-point of the rate to be between $7.5 - 8.0cm$ extension of the trombone, and a the max rate was reached at $9.0cm$. The trombone was a two pass configuration so that the RF signal traveled $2 - 3cm$ of delay length to cover half the delay. This corresponds to $66.71ps$. Given the half width of the ALS pulse is $40ps$ and the width of the laser pulse

is $12ps$, we can estimate the the minimum cross correlation is approximately $52ps$. this suggests that the jitter is on the order of $10ps$ or less over short time durations. A more detailed measurement was undertaken and fit to an error function, as shown in figure 3.21. The measured cross correlation matches almost exactly with the zero jitter prediction. The somewhat unbelievable result implies that the jitter over any short measurement time is nearly zero.

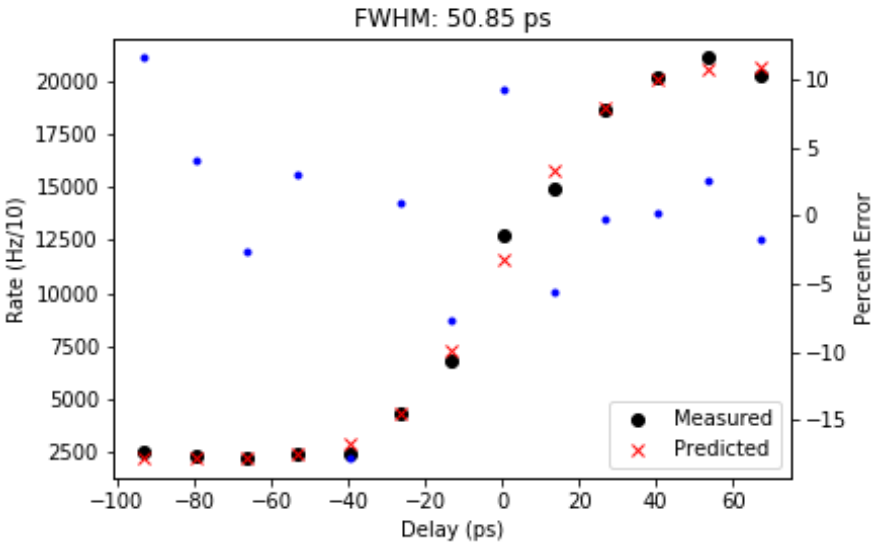

Figure 3.21: June 2017 cross correlation measurement on the background free two color signal from Helium - plot and fit courtesy Elio Champenois. Blue dots give the error from prediction for each measurement.

We also measured the jitter using the error signal produced by the RF mixer. The error signal is proportional to the sine of the phase angle between the two pulse trains. We measured the error signal before and after turning on the synchrotron system. The difference in the two amplitudes gives the phase noise which is directly related to the time amplitude of the jitter according to:

$$\delta t = \frac{arcsin(A_{lock}/A_{free})}{2\pi} * T_{mix}, \tag{3.30}$$

where the A are amplitudes of the error signal when the loop is locked or free and T_{mix} is the period of the sine waves input into the mixer. Here typical values are, $A_{lock} = 15mV - 30mV$, $A_{free} = 690mV$, $T_{mix} = 16ns$ $(61.9MHz)$, which yields a jitter measurement of $51.7ps$ with wings out to 110ps. This measurement is susceptible to noise given the near zero value of the error signal when the loop is locked.

There should exist a sharp edge at longer flight times where the laser precedes the ALS and no two color signal will be generated. On the short time difference side, the laser delay makes no difference. The direction of shorter laser delay for the August beamtime is clearly seen to be at later bunchmarker time differences as displayed by the sharp cutoff around $228.4ps$ in the two color signal histogram of figure 3.22. The delay for the June beamtime can be determined from examination of fits on H_2 two color datasets e and f as summarized in table 3.1. Clearly the longer delay in data set f shifts the time between bunchmarkers to smaller values. As expected given the similarities in the timing systems, the laser precedes the ALS when the bunchmarker difference is above some critical value.

For version 2 of the system, the oscilloscope measured its lower limit of jitter ($\sim 50ps$) and the FSUP measure a jitter of $\leq 20ps$. Post analysis of the data reveals that the bunchmarker timing collected by the TDC card may not be sensitive enough to measure the low jitter. A summary of the two color signals and Gaussian fits to representative cuts of the data can be found in table 3.1. Additionally, figures 3.22, 3.23, 3.24, 3.25, and 3.26 show histograms of events for the single color and two color dissociation of H_2 for the August dataset and the various data runs from June. As can be clearly seen in figure 3.22, the timing jitter and drift in version 1 was large enough to walk across time zero and produce a noticeable cutoff despite the inherent imprecision in the bunchmarker timing electronics. The same cannot be said for the June datasets b and d shown in figures 3.23, 3.24. Here the ALS and laser are overlapped according to the helium cross correlation measurements. Clearly the signal diminishes at certian times, most probably as a result of timing drift, but the drift is masked by the inherent jitter in the timing electronics. There is some chance that

Dataset	Collection Time	Delay	Time Offset	FWHM 1-Color	FWHM 2-Color
b	21h	$12ps$	$258.74ns$	$182ps$	$178ps$
d	12h	$0ps$	$258.93ns$	$179ps$	$176ps$
e	23h	$33ps$	$291.725ns$	$183ps$	$182ps$
f	17h	$\sim 900ps$	$290.79ns$	$182ps$	$184ps$

Table 3.1: Delays and Gaussian fit parameters for the June beamtime H_2 two color data runs.

the drop in intensity from the two color signal is caused by pointing changes in the laser, but we do not observe similar drops in intensity for data sets e and f, shown in figures 3.25 and 3.26, where the laser is delayed significantly.

It is clear that there is long term drift in the timing system on the order of hours over the collection time of data series b, d, e, and f. This drift would be invisible to the scope and FSUP. Gaussian fits of projections of the histograms onto the timing axis must represent an upper bound measurement of the jitter. We can get an estimate of the accuracy of the measurement by recognizing the line shape is a correlation between the jitter of the electronics, the jitter of the timing system, and the pulse width of the ALS ($80ps$) and laser ($12ps$). Fitting both sides using the long delayed ($\sim 900ps$) data series f reveals an asymmetric jitter profile; the short side has a FWHM of $204ps$, while the long side has a FWHM of $140ps$. This is most probably due to the asymmetric response of the output coupler stage to driving from the piezo. However, there is a noticeable drop in the right (higher time offset) width in dataset d, as seen in figure 3.24. The right side FWHM is only $117ps$, which is much shorter than the $\simeq 178ps$ recorded in dataset f. Here, the timing system may have swept time zero for long enough to statistically narrow the jitter of the electronics. Time zero appears to be somewhere very close to $259ns$.

3.3.5 Rate Estimation

We have so far not presented a feasibility study of the two-color experiment - will it work? This section contains calculations of the expected signal rate. We will begin with some

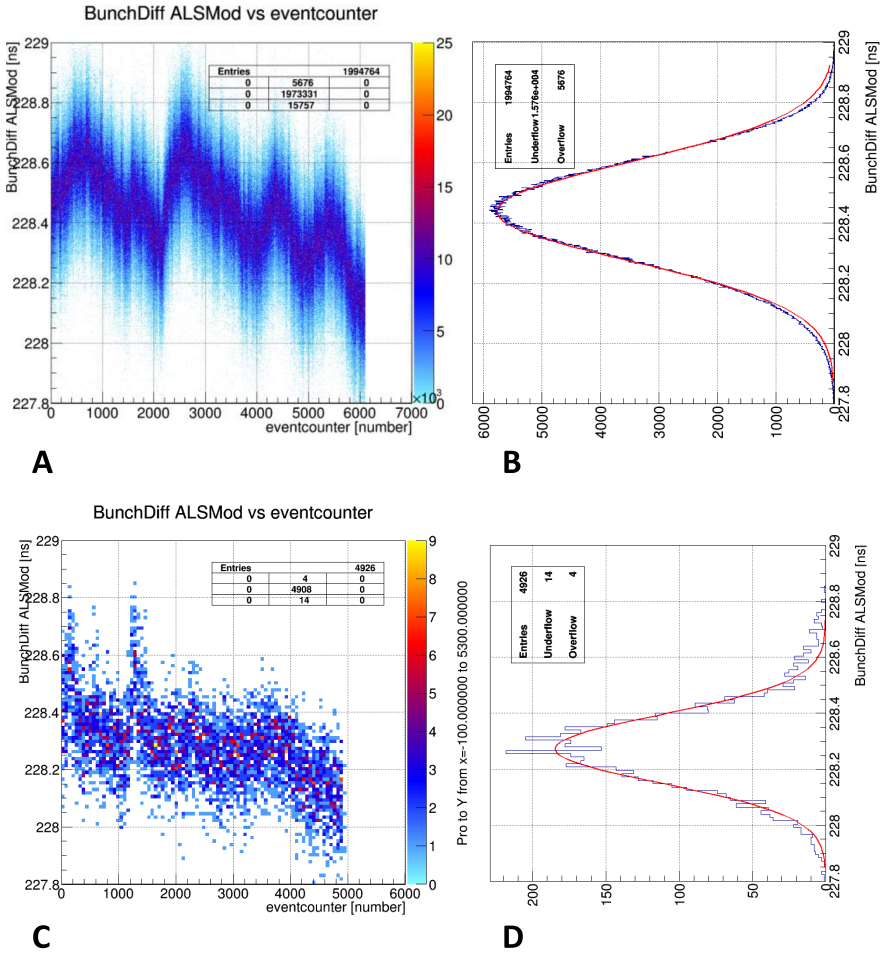

Figure 3.22: August 2016 jitter measurement from post processing data. A: time difference between laser and synchrotron bunchmarkers for the $H+$ channel. B: gaussian fit of A: center of fit 228.43ns, FWHM 386ps. C: same as in A but for H+ dissociated by the laser. Time zero appears around 228.4ps. D: same as in C: center of fit 228.43ns, FWHM 286ps.

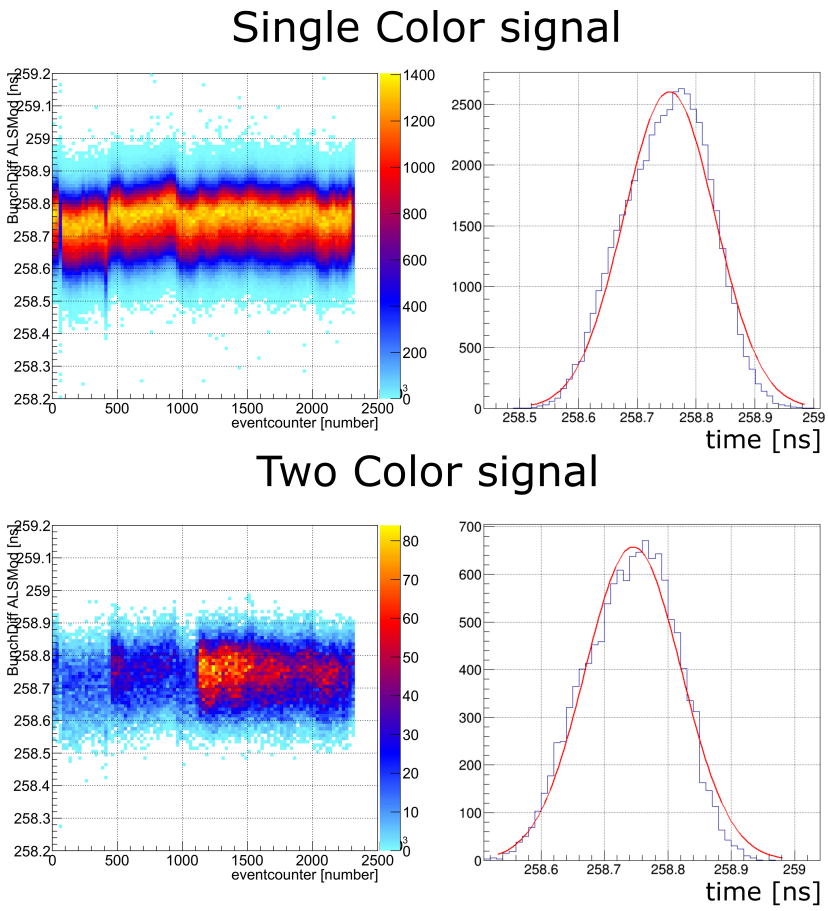

Figure 3.23: June 2017 jitter measurement from post processing the $H+$ channel from data series b. The event counter spans a $21h$ collection window. Top left, event counter vs bunchmarker time difference for the single color channel. Top right, Gaussian fit to the projection onto the time axis from 1.95e6 to 2e6. Center: 258.74. FWHM: $182ps$. Bottom left, event counter vs bunchmarker time difference for the single color channel. Bottom right, Gaussian fit to the projection onto the time axis from 1.1e6 to 1.35e6. Center: 258.74. FWHM: $178ps$.

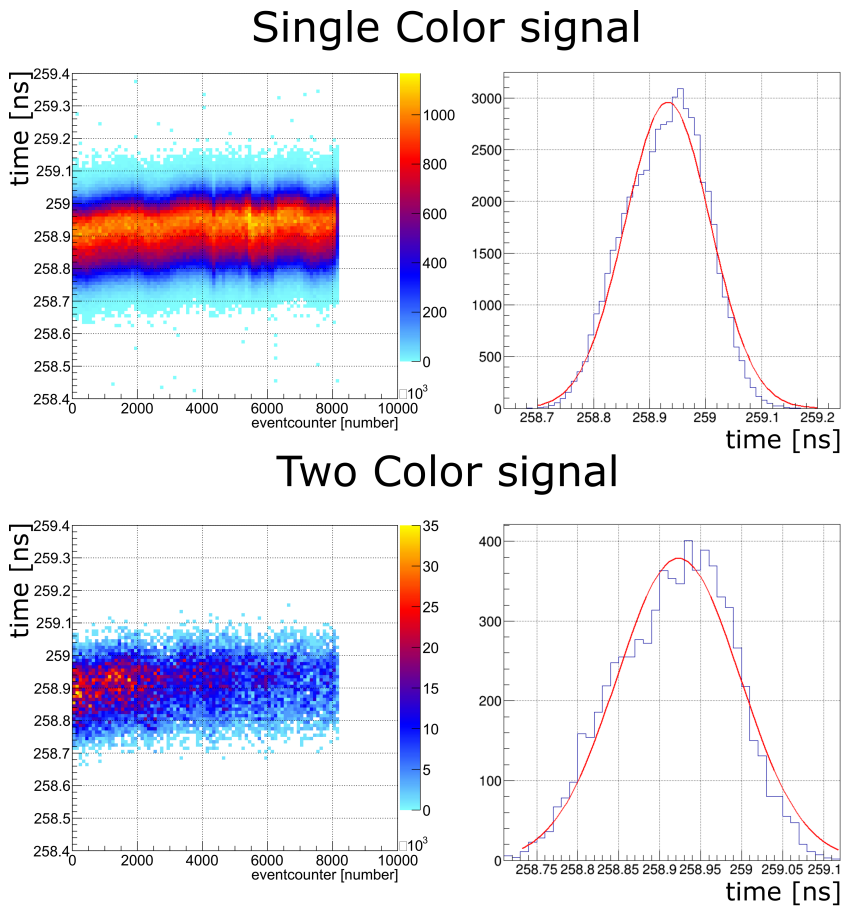

Figure 3.24: June 2017 jitter measurement from post processing the $H+$ channel from data series d. The event counter spans a $12h$ collection window. Top left, event counter vs bunchmarker time difference for the single color channel. Top right, Gaussian fit to the projection onto the time axis from 6.9e6 to 7.2e6. Center: 258.93. FWHM: $179ps$. Bottom left, event counter vs bunchmarker time difference for the single color channel. Bottom right, Gaussian fit to the projection onto the time axis from 4.3e6 to 8.5e6. Center: 258.93. FWHM: $176ps$.

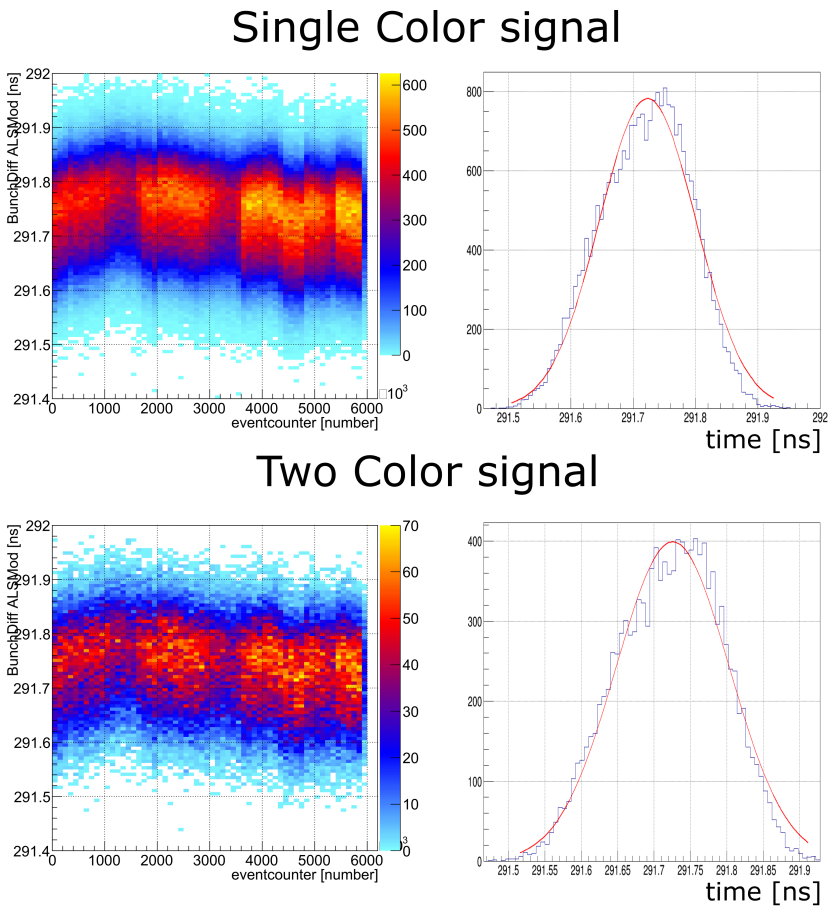

Figure 3.25: June 2017 jitter measurement from post processing the $H+$ channel from data series e. The event counter spans a $23h$ collection window. Top left, event counter vs bunchmarker time difference for the single color channel. Top right, Gaussian fit to the projection onto the time axis from 5.8e6 to 6.0e6. Center: 291.725. FWHM: $183ps$. Bottom left, event counter vs bunchmarker time difference for the single color channel. Bottom right, Gaussian fit to the projection onto the time axis from 5.2e6 to 6.1e6. Center: 291.725. FWHM: $182ps$.

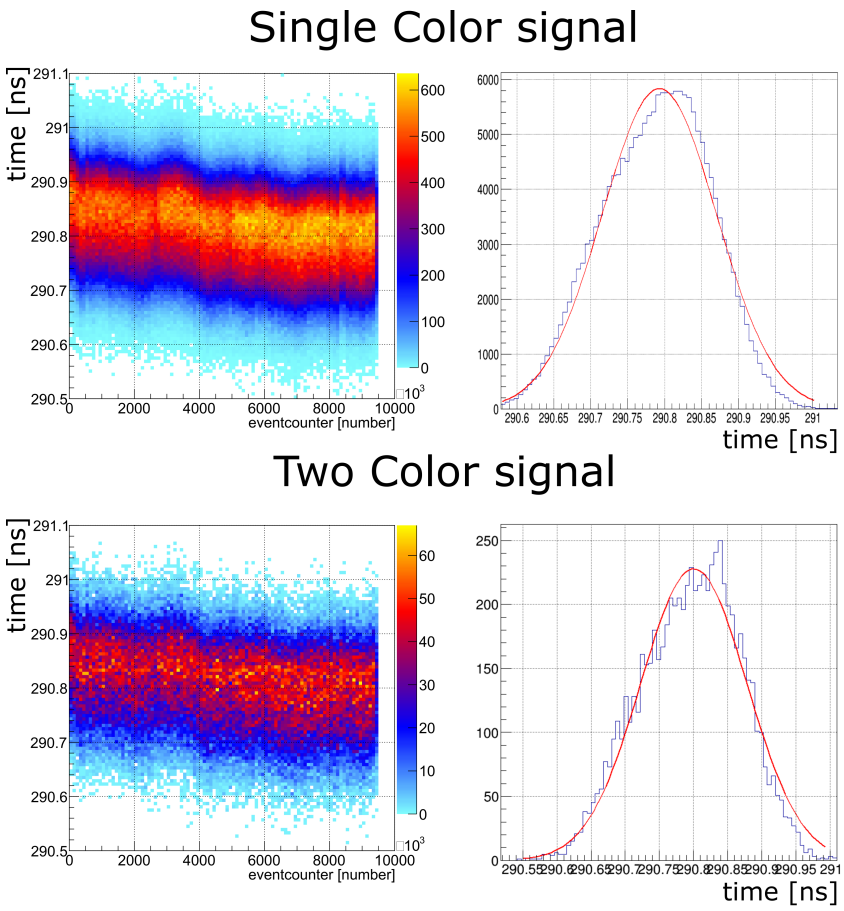

Figure 3.26: June 2017 jitter measurement from post processing the $H+$ channel from data series f. The event counter spans a $17h$ collection window. Top left, event counter vs bunchmarker time difference for the single color channel. Top right, Gaussian fit to the projection onto the time axis from 6.9e6 to 7.9e6. Center: 290.79. FWHM: 182.3ps. Bottom left, event counter vs bunchmarker time difference for the single color channel. Bottom right, Gaussian fit to the projection onto the time axis from 5.9e6 to 6.4e6. Center: 290.79. FWHM: 178.3ps.

basic assumptions that in the end will have a dramatic effect on the final rate. Unfortunately, these calculations can easily be off by an order of magnitude.

Beam quality M^2	Jet density	XUV photon number	Laser cross-section	Geometric overlap	Rate
2	$1 \times 10^{11} cm^3$	1×10^5	$1 \times 10^{-17} Mb$	.1	6×10^4 counts/day

Table 3.2: Indefinite parameters in the rate estimation model and typical values used during the design phase for the two color experiment.

First we consider the ALS and molecular beams. We calculate the volume of space pumped by the XUV, V_{XUV}, which is the intersection of the ALS beam with the jet. We assume the ALS outputs a fixed number of photons N_{XUV}. We assume a conservative jet density, ρ_{jet} well verified in the literature and other COLTRIMS experiments.

Next we consider the laser. We calculate the focal waist and Rayleigh range with parameters from the focusing optics. These values are dependent on the quality of the beam profile, which is clearly not perfectly Gaussian when it reaches the back-focus mirror. To compensate, we assume a beam quality factor of $M^2 = 2$. The beam waist is calculated as

$$w_o = \frac{M^2 \lambda}{\pi \Omega}, \tag{3.31}$$

where Ω is the beam divergence calculated from the optics and λ is the wavelength. The Rayleigh range is calculated as

$$R_o = \frac{\pi w_o^2}{\lambda}. \tag{3.32}$$

The geometry of the focus can be used to calculate the laser focal volume, V_l, by various models. The focal volume modeled as a tube or radius w_o and length $2 * R_o$ is most likely an underestimate. Conversely, a simple ray tracing model of two cones, axial and apex to apex, of length R_o and apex angle 2Ω, is likely an overestimate. A more intuitive model is to assume some arbitrary cross section and take only the volume where the probability to absorb one laser photon exceeds some value. Regardless, there is no reason to consider volumes larger than the pump volume of the ALS - described below. Finally, we calculate

the number of laser photons, N_l, from the pulse energy. These parameters are shown in table.

Now we estimate the number of molecules, M_{pump}, pumped in the XUV volume as

$$M_{pump} = N_{XUV} \times (\sigma_{pump} \times \rho_{jet} \times V_{XUV}). \tag{3.33}$$

We must assume some cross section, σ_{probe}, for the absorption of a laser photon. There are, however, so many laser photons that the probability greatly exceeds one. This indicates that the molecule will interact with the laser field by constant absorption and re-emission of photons - a process described by the Floquet model. Alternately, we can assume a fast process that only exists for a very short period of time, τ_{state}, before it can no longer absorb the laser photon. Regardless, only a fraction, η, of the pumped events will be able to absorb a photon. The equation for number of molecules that absorb a laser photon is then

$$M_{2-color} = \eta \times N_l \times (\sigma_{probe} \times M_{pump}) \times (\frac{\tau_{state}}{\tau_l}). \tag{3.34}$$

This equation assumes perfect geometric and time overlap which is far removed from the physical implementation.

To work towards an estimate we must begin to factor in geometric and time overlap. For the sake of argument we can assume a short lived state compared to the lifetime of the laser pulse but still long lived enough to guarantee a laser photon absorption. Under this assumption $M_{2-color} = M_{pump}$. Without jitter, the time overlap becomes the width of the laser pulse τ_l divided by the width of the XUV pulse, τ_{XUV}. When the drift/jitter width is considered, the time overlap becomes the ratio of time the laser pulse spends inside the XUV pulse, multiplied by the prior ratio:

$$g_{time} = \frac{\tau_{XUV}}{\tau_{jitter}} \times \frac{\tau_l}{\tau_{XUV}} = \frac{\tau_l}{\tau_{jitter}}, \tag{3.35}$$

where g_{time} is the time overlap factor and τ_{jitter} is the width of the jitter. Similarly, we can define the spatial overlap factor as:

$$g_{space} = \frac{V_l}{V_{XUV}}. \tag{3.36}$$

We must account for coincidence collection of one ion and one electron (the simplest case) with a fractional factor g_{coin}. Additionally, the relative duty cycle between the laser and ALS is accounted for by a the fraction $g_{duty} = f_{laser}/f_{ALS}$. Taken together, these fractions form the total fractional measurement, g, of the signal:

$$g = g_{time} \times g_{space} \times g_{coin} \times g_{duty}. \tag{3.37}$$

Finally, if we integrate for a certain period of time, T, we will only produce signal at the frequency of the laser (the lower repetition rate light source). The final observed counts are

$$signal = M_{2-color} \times g \times T \times f_{laser}. \tag{3.38}$$

With the reasonable parameter assumptions outlined in table 3.2, we calculated somewhere between 1×10^4 and 1×10^5 events could be collected in a 24 hour period. The rates we observed in the August 2017 H_2 experiment match these predictions. We will apply this model to estimate the cross section of the strong field dissociation of H_2 in chapter 6.

Chapter 4

Analysis

In this chapter we will give a procedural description of data analysis. At a certain point in analysis, each dataset requires unique plots to examine the physics. We cannot hope to describe how to generate these unique plots for every scenario. Instead this chapter will focus on how to refine the calibration upon which scientific conclusions can be made.

Calibration and analysis are run in a fully user customizable code solution written in C++ and distributed by Roentdek, called LMF2Root. LMF2Root's source code is open except for a few library subroutines that remain proprietary. The code is built in Microsoft Visual Studio as a collection of three "projects", LMF2Root, IPA, and ColAHeil, in one visual studio "solution". In principle other development environments can be used to compile the solution, though we have worked exclusively with Visual Studio. LMF2Root has over 10k lines of code, spread over 30 files. We have modified nearly every file in this program during our studies and created 1800 analysis spectra. Past iterations of the program also built upon a graphics processing platform called CUDA to provide rapid data calibration. we worked extensively with this, though ultimately it was abandoned in favor of a interactive command line program.

4.1 Reconstruction & Sum Correction & Position Correction

Data is written to disk by the time to digital converter (TDC) card as a list mode file (lmf). There are 16 channels available on the card, and each channel may have stored multiple signals on the collection buffer memory at the time the card was triggered to write. After a pre-defined number of events have been collected or a specified period of time has passed, the TDC card stops writing data to the buffer and instead streams the buffer to the

hard drive. The signals collected for this and many other experiments in the AMOS program are detailed in table 4.1 below.

TDC Channel	Signal	Description
0	ion MCP	MCP capacitive discharge
1	Electron MCP	MCP capacitive discharge
2	hex u1	Electron u-layer signal
3	quad u1	Ion u-layer signal
4	hex v1	Electron v-layer signal
5	quad v1	Ion v-layer signal
6	hex w1	Electron w-layer signal
7	Laser Bunchmarker	Laser photodiode timing signal
9	hex u2	Electron u-layer signal
10	quad u2	Ion u-layer signal
11	hex v2	Electron v-layer signal
12	quad v2	Ion v-layer signal
13	hex w2	Electron w-layer signal
16	Sync. Bunchmarker	Synchrotron timing signal

Table 4.1: A table of the TDC card inputs used for this and many other experiments. The input number corresponds to the position in the LMF file line.

The TDC is programmed to write data to the buffer after it receives a trigger signal, which can come from any of the channels. Generally, the TDC is set to trigger on the MCP signal from either the ion or electron detector. Each electron that hits the MCP will ideally generate signals on channels 1, 2, 4, 6, 9, 11, and 13. Similarly an ion hit should generate signals on channels 0, 3, 5, 10 and 12. Signals on channels 7 and 16 are usually collected after the card has been triggered. These signals are used to compute the position and time of a hit on an MCP detector. However, the collection of these signals is prone to failure. In the case of the ion and electron hits, the information is redundant. The position information is recorded by two timing signal in each dimension, and, taken with the capacitive MCP discharge signal, only one of these is strictly needed. Furthermore, the other layer signals can be used in place of the MCP signal. Complete failure of collection only occurs when the majority of the signals are missing. This is fairly uncommon when the detectors are run at the appropriate rates such that the MCP has time to recharge and generate strong

pulses on the delay lines. The more layers, the more redundancy, and for this reason typical experiments use a hex anode with 3 separate layers on the electron detector. The electron rate is typically 2 to 10 times greater than the ion rate due to background electrons and is concentrated in a time window on the order of tens of nanoseconds. Under these conditions, missed and confused signals are common. additional layers are not required on the ion detector as a quad (2 layer) detector is more than capable of handling the the maximum rate.

The redundancy in signals is also critical for collecting multi-hits on the MCP. Multi-hits occur when two particles land sufficiently close in time and space on the MCP such that the signals on the delay lines become confused and the MCP discharge signal is compromised for one or both of the hits. There is a deadzone in the time and position difference plots for multi-hits that arises when the charge on the MCP is depleted for a certain time within a certain radius from a hit. Additionally, if the hits land too close together in time and space, the MCP discharge pulse may be broadened and no longer reflect the correct hit time of either event. Multi-hits are particularly important in 2 electron coincidence experiments because the electrons are born at the same time and with similar energies: thereby generating many situations where signals are confused or lost. Again, the extra layer on the hex detector provides more information to disentangle these events.

Both lost signal inference and multi-hit disentanglement are handled by a proprietary program written by Roentdek and known as "Reconstruction". Before the data can be reconstructed, the layer anode time-sums and nonlinearities must be corrected as described below. These two tasks are also handled by proprietary Roentdek software included in LMF2Root called auto-calibration.

The position on a layer is calculated from the time difference between the two signals generated at each end of the layer anode by the electron shower produced by the MCP. The time difference is multiplied by a scale factor that converts from nanoseconds to millimeters. Typical values for 120mm layer anodes are $\sim 150ns$ and for 80mm layer anodes $\sim 80ns$.

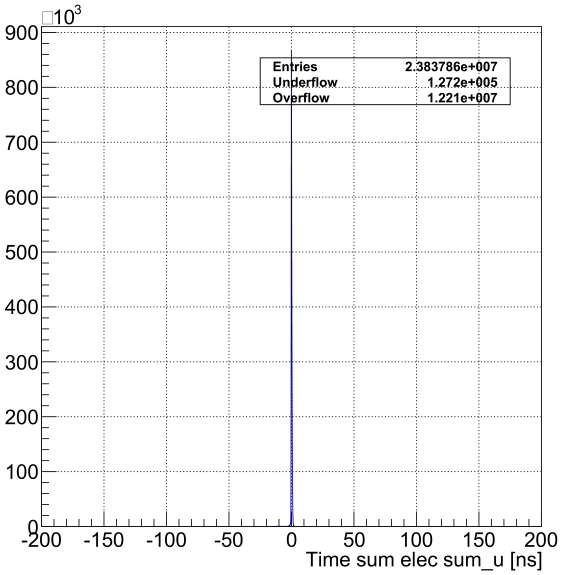

Figure 4.1: The time sum for the u-layer anode on the hex 80mm electron detector, centered by the timesum offset, parameter 313, in the lmf2root config file.

The first step in the analysis is to ensure the timesum of the anode layer signals are centered at zero, as shown in figure 4.1 for the ion quad detector u-layer. The timesum varies as a function of position on the anode as a result of wire spacing, thickness, and collection efficiency. The timesum is corrected by an automated and proprietary auto-calibration routine. A histogram of the corrected timesum automatically generated by LMF2Root is shown in figure 4.2. The next step is to ensure that the time to position calculations are correctly scaled between layers. The correct scale factors relative to the first layer are automatically calculated using the auto-calibration.

Once the layers have been auto-calibrated, the resort routine can be invoked. The inner workings of the resort routine are not available for inspection, but the routine does output the "method" used to reconstruct data events. There are unique methods for each case of missing signals as summarized in table 4.2. For single electron coincidence experiments, the vast majority of electrons and ions are passed with method 0. The situation is dramatically different for 2 electron coincidence experiments, where a majority of the second electrons may

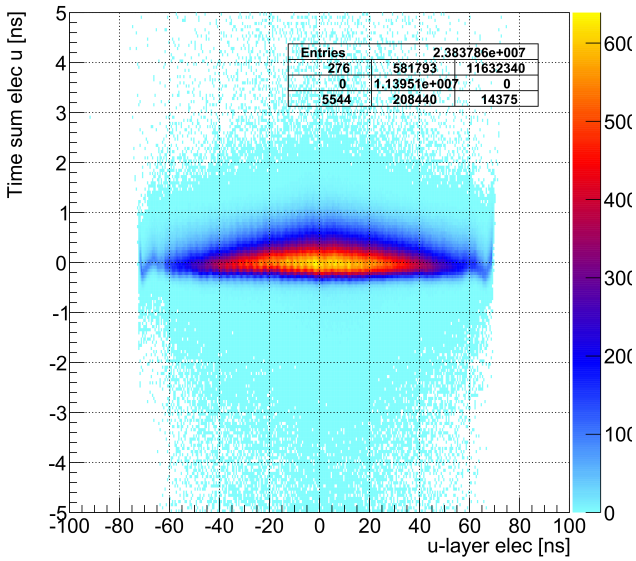

Figure 4.2: The time sum for the u-layer anode on the hex 80mm electron detector, centered by the timesum offset, parameter 313, in the lmf2root config file.

be reconstructed with the methods 15 and above. These methods are generally considered to have a higher risk of fabricating data events.

Recon. Method	MCP	u	v	w
0	1	2	2	2
1	1	0	2	2
2	1	2	0	2
3	1	2	2	0
4	1	1	2	2
5	1	2	1	2
6	1	2	2	1
7	0	2	2	2
8	0	0	2	2
9	0	2	0	2
10	0	2	2	0
11	0	1	2	2
12	0	2	1	2
13	0	2	2	1
14	1	2	1	1
	1	1	2	1
	1	1	1	2
15	1	2	1	0
	1	0	2	1
	1	1	0	2
	1	0	1	2
	1	2	0	1
	1	1	2	0
16	1	1	1	1
17	0	2	1	1
	0	1	2	1
	0	1	1	2
18	0	1	1	1
19	0	2	1	0
	0	0	2	1
	0	1	0	2
	0	0	1	2
	0	2	0	1
	0	1	2	0
20	1	1	1	-

Table 4.2: Reconstruction Methods and their input signals. Each u, v, and w layer has 0, 1, or 2 signals present. The signals have been grouped according to equivalent signal pattern. The higher the number of the reconstruction method, the more risk of fabrication. Methods 15 and greater are particularly risky. Note, method 20 can only be applied to quad detectors.

4.2 Pre-Sorting

Presorting is the process of taking the raw LMF file data and reducing it to a more manageable size with a coarse data selection. In the process the file is converted into a ROOT file for subsequent analysis. The majority of the data is background noise and should be eliminated at this step. Simple gates are placed on coincidence and around the position and times where the experimental signal is expected. At this point the calibration parameters are most probably too far off from their actual values to provide meaningful momenta and energy.

For single ionization experiments, the best way to eliminate background is to first demand that the ion of interest has a coincident electron with a time of flight within the range expected for electrons generated by photoinization in the spectrometer. Two simple gates on the ion flight time and the electron flight time serve this purpose. In addition, for double ionization experiments with a molecular fragmentation into two charged ions, a photo-ion photo-ion coincidence (PIPICO) line can be used. Conservation of momentum in the time of flight direction dictates that the points defined by the two flight times of the exploding fragments fall on a curved line. A time of flight gate centered on this line will faithfully select the photoionization events. An example of a pipico line and diatomic breakup are shown in figure 4.3. Gating in this tof-tof space is also a good way to capture three body breakups.

The current version of LMF2Root can call a presorter from the config file as detailed in the accompanying documentation "LMF2Root in a nutshell".

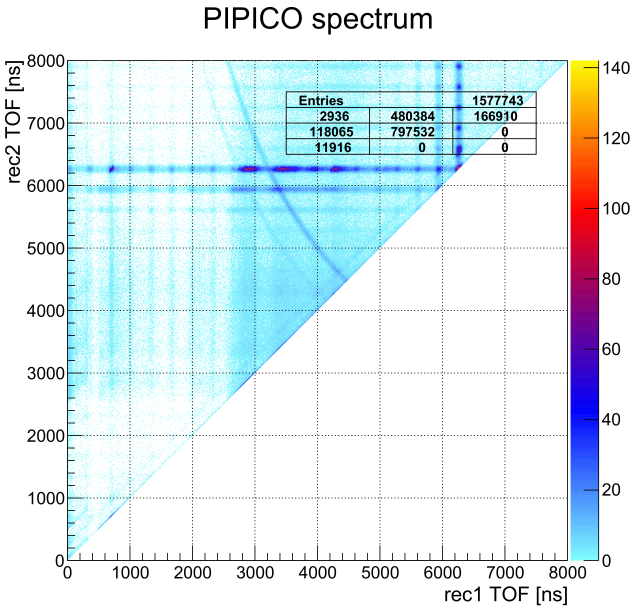

Figure 4.3: A raw data PIPICO plot showing a pipico line from the breakup of O_2 after photodoubleionization at 38eV. The pipico line is the faint curved feature beginning at $4500ns$.

4.3 Wiggle Runs and Electric Fields

Major unknowns in each experiment are the exact strength of the electric and magnetic fields and the true arrival time of the light: time zero. There exists an unknown time offset between when the ALS bunchmarker signal and the arrival time of the light at the interaction zone. To determine these quantities two special data runs are made.

The wiggle run, so called because the goal is to generate multiple cycles in the electron trajectory that look like wiggles with prominent nodes in the spectra, provides both the magnetic field strength and the time zero. To produce a wiggle run, the electric field is detuned to a very low value such that the electron flight time is longer than the electron cyclotron time period $t_e = 2\pi m/qB$. The photon energy is tuned such that the photoelectrons have enough energy to complete full cycles and return to the origin in the $\{x, y\}$ plane perpendicular to the time of flight direction. These orbits create nodes at the interaction region. When these conditions are met, multiple nodes are filled by the electron distribution. The spacing between nodes is directly proportional to the magnetic field. Additionally, the

first node must by definition exist at time zero. Therefore, if the node numbers n are known, the points defined by the node number n and the node time of flight position should fall on a line that intersects zero. If a few nodes are visible a line can be fit, and the offset in nanoseconds at $n = 0$ corresponds exactly to the bunchmarker time offset.

The wiggle run may also be taken without a reduced electric field and with a higher energy photoelectron. This setup typically only provides two nodes because the electric field is optimized to spread the electrons on the detector and the distribution is usually centered between nodes by design. However, for very low field strengths this may be the only option. In this case, the cyclotron frequency is large, so minor deviations are acceptable. The difference in cyclotron frequency may vary by a factor greater than three for low and high fields. The consequence of an incorrect time zero is to squash the transverse momenta of the electrons in one time of flight (tof) direction and to increase it in the other, creating an egg shape. This egg shape is similar to that induced by an incorrect electric field, though the electrons are much more sensitive to the time zero than to the electric field value. For the electrons, the field value and time zero are somewhat redundant parameters.

A second calibration run can be made with the experimental fields to calibrate the energy of both the electrons and ions. For the electrons, a simple helium run is sufficient and should be made with a photoelectron energy that matches the energy of the interesting experimental electrons. For the ions, a well defined kinetic energy release in a diatomic is preferred. A good choice is one of the many peaks in N_2 or the particularly strong peak in O_2. The idea is to adjust the fields to match the well defined energy and so achieve an absolute calibration.

Despite the accuracy of these methods, nonlinearities in the fields preclude common calibration between all breakup channels and electron energies. Each new mass and energy will require slight tweaks to adjust for stray fields, meaning that the methods of determining good calibration in the following section are all the more important.

4.3.1 Bunchmarker Timing

Electron flight times are determined relative to the light pulses of the ALS by reference to the user timing system. The system delivers an electronic TTL pulse to mark the passing of each bunch as they orbit the synchrotron. This 'bunchmarker' signal carries some fixed time delay from the arrival time of the light at the interaction point in the chamber. The delay originates from electronics, cable lengths, and the actual flight time of the light. The offset can be deduced from the wiggle run discussed in section 4.3 by fitting a line to the nodes of the wiggle. The offset for the zeroth node is then the time offset of the system. Often this time offset is compensated during the experiment with a delay generator box.

To extract the electron flight time, the time recorded for the electron must be matched with the time recorded for the bunchmarker train. The user timing system is an order of magnitude more stable and accurate than the experimental timing electronics, and each bunchmarker is taken as a reliable position for the entire bunchmarker train, each separated by the bunchspacing Δt. The experimental timing electronics sets time zero when it is triggered, usually on an ion collection. Therefore time zero is concurrent with the first ion hit. The TDC card then looks back in time and records the electron flight times, which are recorded as negative times. The TDC then looks forward in time and records a fixed number of bunchmarkers, which are recorded as positive times.

We desire the difference in time between the raw electron flight time and the light arrival time. We can write this formally as the difference in the correct light arrival time t_{light} and the electron TDC time t_{elec}: $e_{tof} = t_{elec} - t_{light}$. However, the recorded bunchmarker is related to the light arrival by $t_{light} = t_{bunchmarker} - x\ \Delta t - bunchmarker_{\delta t}$, where $bunchmarker_{\delta t}$ is the positive delay between from the light arrival time and the bunchmarker train. Here, x is some arbitrary integer of bunchmarker offsets, and increasing x only adds integer numbers of the bunchspacing to the flight time. As long as x is greater than the actual integer number y, the electron flight time can be recovered by taking the modulus with a very large value

for x:

$$e_{tof} = Mod_{\Delta t}[t_{elec} - t_{bunchmarker} + 1000\ \Delta t + bunchmarker_{\delta t}]. \tag{4.1}$$

This same formula can be applied to the laser timing system which supplies a laser bunchmarker to the timing electronics. In the August 2016 beamtime, the laser was run with a 3:1 duty cycle and therefore the laser bunchspacing was $3 * \Delta t$. The equation becomes

$$e_{1\ mod(3\Delta t)} = Mod_{3\Delta t}[t_{elec} - t_{laserbunchmarker} + 1000\ \Delta t - laserbunch_{\delta t}]. \tag{4.2}$$

However, the laser bunchmarker offset can take one value for each of the synchrotron pulses in the duty cycle. The correct offset must be determined with a two color signal. By gating on a laser produced signal, such as the dissociation of H_2^+ or the photoionization of excited helium, we can extract the correct time lag between the synchrotron and laser pulses.

4.4 Interactive Parameter Adjustment

Once the data has been paired down by presorting and the rough field values established the true process of calibration can begin. For a standard experiment with ions and electrons, there are 14 parameters for the spectrometer settings, 20 parameters for position and time corrections, and 26 parameters for the momentum corrections. Some of these parameters have a dramatic effect on the data and require highly tuned values, some only need have approximate values, and some are largely redundant despite subtle differences. Regardless, most of the calibration is tuned with the Interactive Parameter Adjustment (IPA) project of the LMF2Root solution. The IPA is a console based program that loads a predefined number of events (limited only by computer memory) onto RAM and is capable of re-processing the data with adjusted parameters on the fly. This allows rapid iteration to quickly find the correct values.

A note: it is at this point in the analysis that the work flow becomes in some sense circular. A rough calibration is needed to orient the detectors, and correct orientation is

needed for final calibration. Therefore, work must proceed from calibration to orientation and back to calibration. Similarly, rough position calibration are needed to move to momentum calibration, but often there are distortions in the momentum that can only be corrected by changes in the position. Often this is the case with analysis, that the work flow demands a clean signal to adjust some more advanced parameters, only to return to clean up the original parameters. In an iterative way then, the analysis should converge onto the best possible set of calibration parameters.

4.4.1 Spectrometer Calibration

The electron arm and ion arm of the spectrometer each have 6 common parameters that specify three acceleration stages: three lengths and three associated field strengths. The ion spectrometer has two additional parameters to specify the jet velocity and direction, and the electron spectrometer has two additional parameters to specify the magnetic field and direction. The reader may wonder why each arm of the spectrometer needs to be completely independent if they both share the same first stage acceleration field, albeit with different lengths. The answer is that lenseing from fields leaking through the mesh cause distortions for particles with different mass and for different flight paths in the spectrometer. Briefly, I will describe the sensitivity of each parameter - in general, the less time a particle spends in a region of the spectrometer, the less sensitive the defining parameters are.

The ion arm is a single acceleration region followed by another high field acceleration region in front of the MCP. This field is extended by a booster region to move the ion MCP further away from the mesh and prevent the high field at the surface from leaking into the interaction region. Typical values for the electric field in the spectrometer acceleration region are a few volts per centimeter: the field in the booster region is 1000 volts per centimeter. Changing the primary acceleration field has large effect on the distribution, shifting it around in momentum space. Changing the acceleration length of the ion arm has a less sizable effect. Both parameters create egg shapes if sufficiently detuned. In contrast

the booster arm length and field have essentially no effect and approximate values are good enough. The ions are already at high velocity in the booster and spend very little time there. The jet velocity effects momentum calculations directly and will introduce a slope in the yz direction if de-tuned. The direction of the jet is usually very close to perpendicular to the light path, but this can only be determined after a good momentum calibration (absent rotational parameters that can "correct" - incorrectly - the induced jet slope).

The electron arm in our experiments is somewhat more complicated because of the Wiley-McLaren drift second stage, but follows the general principles as above. The accelerating field has a large effect, the length less so, and drift length even less, and the final acceleration region almost none. Regarding the magnetic field, it has a large effect because it moves the theoretical nodes around in time of flight. The nodes will squash or stretch distributions in momentum space. The time offset can compensate this movement and is described in detail in the next section. The other subtle effect of magnetic field strength is to induce a rotation in the electron momentum. A change in the magnetic field changes the cyclotron period, and therefore changes the distance that the electrons travel in a cycle. A grossly mis-calibrated field may not noticeably distort the momentum into an egg if the time offset parameter compensates: but the rotation will remain.

The open question is how to determine if the "coarse" parameters are correct and, further, given that there are more parameters than there are ways to asses their validity, how do we proceed? The answer is that there is little to be done except to use the actual measurements of the spectrometer - which are good enough for coarse values - and to rely on the special runs described in the preceding section. Eventually though, the correct calibration is the one that produces nice round momentum spheres, and there is nothing that distinguishes two calibrations with slightly different parameters that by eye both have high quality spheres. Both calibrations should be seen as correct, and the durability of any physical effect under slight changes in parameters should be evidence that it is real.

4.4.2 Position Calibration

The interaction point for the ions and electrons should be centered on zero as best as possible. The ions are easy to center. The zero point for the conventional y axis is located by the center of the hot gas stripe width: the line formed by the ionization of background gas by the synchrotron beam. The zero point of the conventional x axis is the jet dot, which is the bright dot produced by single ionization of the jet.

Centering the position of the electrons is doubly important because the motion of the electrons in the magnetic field couples the x and y dimensions in computing the p_x and p_y momenta. Therefore, an offset in the position will distort both dimensions in the momentum in a non-linear way. Unlike the ions, the electrons do not have well defined alignment points with the exception of nodes generated by high energy photoelectrons. Alternately, the wiggle run can be used to center the distribution.

A second and more involved calibration corrects for the drift introduced by crossed E and B fields in the spectrometer. Ideally, the magnetic field is perfectly aligned with the electric field, but in practice this is rarely the case. The $E \times B$ drift velocity is

$$v_d = \frac{\vec{E} \times \vec{B}}{B^2}. \tag{4.3}$$

Clearly only the component of the B field perpendicular to the E field will introduce a drift. The drift is linear and the cumulative effect is a slope in the position versus time plots of the electrons. These plots are commonly called fish plots because of the resemblance to a common fish symbol. Figure 4.4 is a typical fish spectrum from O_2 ionization at 46eV. The nodes created by the cyclotron motion of the electrons are clearly visible. A linear offset is used to correct for the slope and bring these nodes in line with the x-axis. Many datasets do not have nodes present with the fields used to collect data: in these cases the correct slope must be found by eye. If the electrons have a continuous distribution (they are a "blob"), then tuning by eye is impossible. A useful trick for creating an artificial fish feature is to

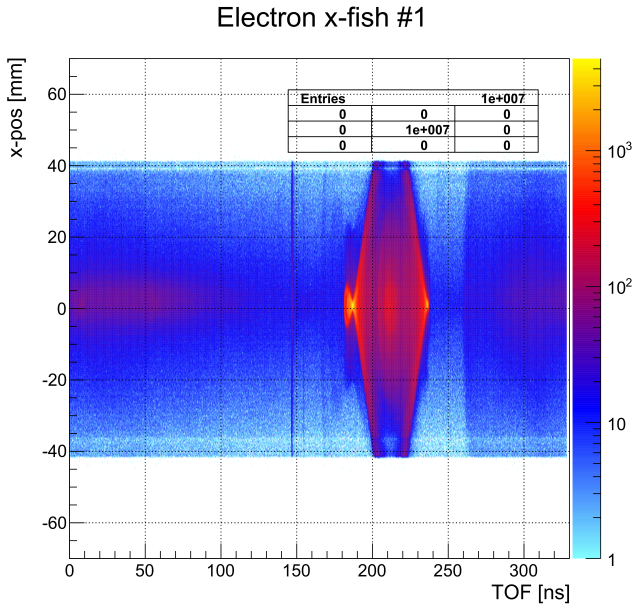

Figure 4.4: A raw data electron fish plot. No corrections have been applied. Photoionization electrons occupy the hot feature centered at 210ns. Note the left and right nodes, near zero x position, that frame the lower energy electrons.

establish rough energy calibration and then to gate on an energy slice of the ions. Energy conservation demands that this gate will produce a well defined energy in the electrons which will then transfer to a well defined fish plot.

4.4.3 Momentum & Energy Calibration

Once the positions are centered momentum calibration can begin. Calibration for the ions is also fairly straightforward for cases where the ion or ions receive a momentum kick and form what should be perfectly round momentum rings. In these plots the theta and phi angles plotted against energy should be flat. Energy is a function of momentum magnitude only and should be invariant. Theta angles define latitudinal lines on these momentum spheres:

$$\theta_x = arctan\left(\frac{x}{x^2+y^2+z^2}\right), \tag{4.4}$$

where the *arctan* ouput spans $(0, \pi)$. Phi angles define longitudinal lines:

$$\Phi_x = arctan2\left(\frac{y}{z}\right), \tag{4.5}$$

where $arctan2$ is the C++ math.h function that spans $(0, 2\pi]$ by computing what quadrant the arguments occupy. Theta angles integrate over the phi coordinate, and phi angles integrate over the theta coordinate, so neither angle is the perfect tool. Additionally, both angles have inherent advantages and weaknesses. For example, the theta angle is more sensitive to slight centering offsets, while the phi angle better records local deviations from the ideal momentum sphere. More information can be gained by plotting all six theta and phi angles over each cardinal direction: $\{\theta_x, \Phi_x\}$, $\{\theta_y, \Phi_y\}$, and $\{\theta_z, \Phi_z\}$. An example of the electron momentum spheres created by the vibrational bound states of H_2^+ in fig 4.5. Notice that this calibration is incomplete and there are definite distortions in what should be flat features created by the dipole momentum spheres.

The momentum of the electrons is calculated from two formula derived from solving the coupled second order differential equations of the electron cyclotron motion:

$$m\dot{\vec{v}} = -q(\vec{E} + \vec{v} \times \vec{B}) \tag{4.6}$$

which expands to;

$$m\dot{v}_x = -q\ v_y\ B_z, \tag{4.7}$$

$$m\dot{v}_y = q\ v_x\ B_z, \tag{4.8}$$

and

$$m\dot{v}_z = -qE_z. \tag{4.9}$$

Identifying $qB/m = \omega$ leads to the simplification by derivation and substitution:

$$\ddot{v}_x = -\omega^2\ v_x, \tag{4.10}$$

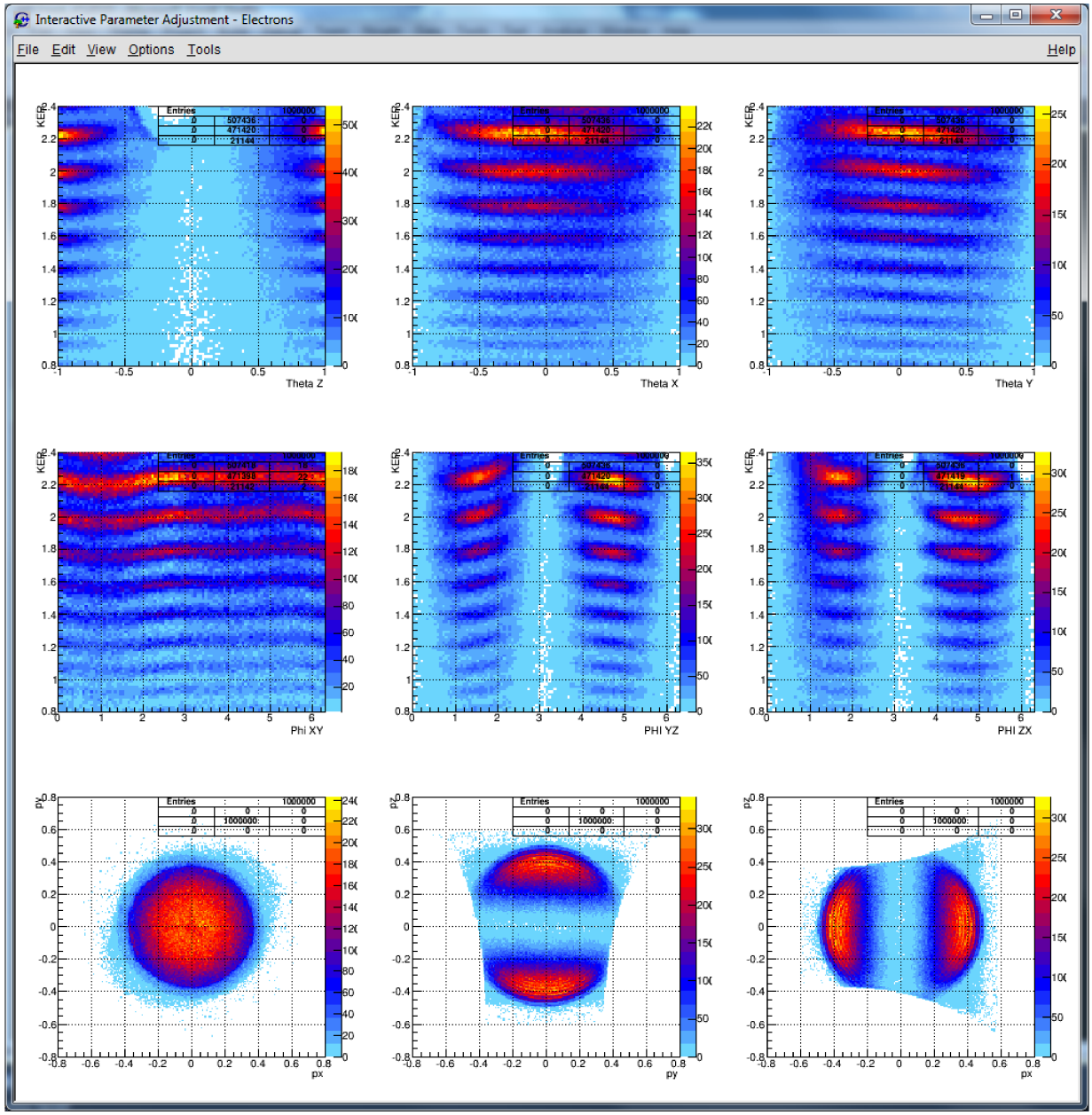

Figure 4.5: Typical electron momentum calibration spectra in the IPA. This dataset: August 2017 H_2 photoelectrons. Left column top to bottom: θ_z vs. energy, ϕ_z vs. energy, p_x vs. p_y. Center column top to bottom: θ_x vs. energy, ϕ_x vs. energy, p_x vs. p_z. Right column top to bottom: θ_y vs. energy, ϕ_y vs. energy, p_z vs. p_y.

$$\ddot{v}_y = -\omega^2 \; v_y. \tag{4.11}$$

These equations have solutions

$$v_x[t] = V_o \; cos[\omega t + \phi], \tag{4.12}$$

and

$$v_y[t] = V_o \; sin[\omega t + \phi]. \tag{4.13}$$

The constant V_o is determined by recognizing that the magnetic field does no work, so the initial velocity never changes and

$$|\vec{v}|^2 = v_x^2 + v_y^2 = V_o^2. \tag{4.14}$$

To solve these equations with two unknowns, we are give only the position in x and y and the time. Integrating form $t = 0$ to $t = t_o$ we find

$$x[t] = \frac{V_o}{\omega} \; sin[\omega t_o + \phi] - \frac{V_o}{\omega} \; sin[\phi]. \tag{4.15}$$

$$y[t] = -\frac{V_o}{\omega} \; cos[\omega t_o + \phi] + \frac{V_o}{\omega} \; cos[\phi]. \tag{4.16}$$

Now applying the half angle formulas to the above gives:

$$x[t] = \frac{V_o}{\omega} \; (sin[\omega t_o]cos[\phi] + cos[\omega t_o]sin[\phi]) - \frac{V_o}{\omega} \; sin[\phi]. \tag{4.17}$$

$$y[t] = -\frac{V_o}{\omega} \; (cos[\omega t_o]cos[\phi] - sin[\omega t_o]sin[\phi]) + \frac{V_o}{\omega} \; cos[\phi]. \tag{4.18}$$

Now simplifying to the quantities we wish to know, $v_x^o = V_o \; cos[\phi]$ and $v_y^o = V_o \; sin[\phi]$:

$$x[t] = \frac{-1 + cos[\omega t_o]}{\omega} \; v_y^o + \frac{sin[\omega t_o]}{\omega} \; v_x^o, \tag{4.19}$$

$$y[t] = \frac{1 - cos[\omega t_o]}{\omega}\ v_x^o + \frac{sin[\omega t_o]}{\omega}\ v_y^o. \tag{4.20}$$

To simplify calculations we introduce

$$\alpha = \frac{1 - cos[\omega t_o]}{\omega} \tag{4.21}$$

and

$$\beta = \frac{sin[\omega t_o]}{\omega} \tag{4.22}$$

to simplify the two equations above to:

$$x[t] = -\alpha\ v_y^o + \beta\ v_x^o, \tag{4.23}$$

$$y[t] = \alpha\ v_x^o + \beta\ v_y^o. \tag{4.24}$$

The solutions are finally:

$$v_x^o = \frac{\beta x + \alpha y}{\alpha^2 + \beta^2}, \tag{4.25}$$

$$v_y^o = \frac{\beta y - \alpha x}{\alpha^2 + \beta^2}. \tag{4.26}$$

Note that a positive magnetic field is taken as pointing in the same direction as the electric field. The directionality is contained in ω, and a sign change in magnetic field corresponds to a sign change in α only. If the magnetic field is taken as pointing in the negative direction as the electric field, the equations modify to:

$$v_x^o = \frac{\beta x - \alpha y}{\alpha^2 + \beta^2}, \tag{4.27}$$

$$v_y^o = \frac{\beta y + \alpha x}{\alpha^2 + \beta^2}. \tag{4.28}$$

Of critical note: it is impossible to correct for a mis-aligned electron detector by sign changes to the electron momentum. The momentum of the electrons is inherently coupled

to both spatial dimensions and if the detectors are not correctly oriented spatially, all bets are off as to the true momentum of the electrons relative to the ions.

Once both electron and ion momenta are calibrated, they must be scaled to preserve energy. That is, the energy lost by the electrons must be gained by the ions. Equivalently, in an energy map where the sum electron energy is plotted relative to the sum ion energy, the features should lie on a line with slope negative one. The correct procedure is to choose whichever has the better energy calibration between ions and electrons, and then to scale the other to bring the distribution of events onto the line.

4.5 Detector Orientation

Detector orientation is a critical and difficult step that usually requires at least a cursory calibration of both detectors. If the orientation needs to be changed, then the entire calibration needs to be re-optimized. The convention is to define the spectrometer cardinal directions in relation to the recoil detector. By convention, the photons should travel in the x-dimension, the jet in the positive y-direction, and the shorter time of flight should define the positive z-direction. There is no way to specify if the photons travel in the positive or negative x-direction and for this reason, the x-dimension is indeterminate. The recoil detector can be aligned by simple rotation of $\pm 90°$.

Now the electron detector must be aligned to the recoil detector and this is much more difficult. The electron detector is typically a hex detector with six valid rotations, $\{\pm 120, \pm 60, 0\}$, and two possible changes in sign $\{\pm x, \pm y\}$. There are 12 unique orientations of a hexagon by rotation and reflection, and if two transforms are required to align the detectors, then this amounts to $12^2 = 144$ different transformations, many of which are equivalent. The question is, what are the equivalent transformations for our x and y coordinates and what set of transformations should we consider?

The correct mathematics to describe these symmetry transformations is group theory. The detector is a hexagon with dihedral group D_6 symmetry, defined by the rotation axis

of $360°/6 = 60° = \phi$ and the reflection axes specified by lines through opposing midpoints of each side of the polygon (3 axes) and opposing vertices (3 axes). The mathematical generating definition for this group is written

$$D_6 = \langle r, s : r^6 = s^2 = 1, rs = sr^{-1} \rangle, \tag{4.29}$$

where r denots a clockwise 60° rotation, r^{-1} counter-clockwise rotation, and s a reflection. If each rotation of $n\phi$ and each reflection is numbered from 0 to n, then the operations follow the algebra

$$r_i r_j = r_{i+j} : r_i s_j = s_{i+j} : s_i r_j = s_{i-j} : s_i s_j = r_{i-j}, \tag{4.30}$$

with addition and subtraction of modulo 6. Note that r_0 is the identity operator. Of the reflection axes in this group, 2 are arbitrarily chosen as the cardinal directions. One of the axes going through the midpoints of the sides is defined as a cardinal direction (x or y) and the axis perpendicular to this is defined as the other cardinal direction (y or x) and must go through two vertices. If the first axis is numbered 0 and we proceed to count until we arrive at a perpendicular axis, that axis must be numbered 3 and we can denote these two reflection axes as s_0 and s_3. The available transformations in the code are then $\{s_0, s_3, r_0, r_1, r_2, r_3, r_4, r_5\}$.

There are exactly 12 unique orientations of the cardinal axes on the hexagon. This can be proven easily enough by noting that each pairwise combination of transformations is equivalent to a single transformation. Therefore, any number of transformation words in the group can be reduced to one of 12 unique transformations. Therefore, there are 12 orientations of the electron detector that must be explored. If we consider single transformations and pairwise words made of one reflection and one rotation then we have at our disposal 20 transformations. These must reduce to the 12 fundamental orientations. Equivalently, we are looking to add to the list above transformations that produce the missing $\{s_1, s_2, s_4, s_5\}$. The convention used in the code is to first rotate and then apply a reflection. According to

the algebra above, we require

$$r_1 s_0 = s_1 : r_2 s_0 = s_2 : r_1 s_3 = s_4 : r_5 s_0 = s_5. \tag{4.31}$$

Conveniently we can restrict the available transformations further by recognizing that rotations r_4 and r_5 are equivalent to r_2^{-1} and r_1^{-1} respectively. Finally, we can eliminate the confusing r_3 in favor of the dual reflection $s_0 s_3 = s_3 s_0$. Taken together, these tranformations span all possible orientations intuitively and are summarized in table 4.3. Upon examination, it is clear that we can further restrict the rotations to $\{0°, \pm 60°\}$ and still span all 12 unique transforms.

		x,y	-x,y	x,-y	-x,-y
		-	s_0	s_3	$s_0 s_3$
$0°$	r_0	r_0	s_0	s_3	r_3
$60°$	r_1	r_1	s_1	s_4	r_4
$120°$	r_2	r_2	s_2	s_5	r_5
$-60°$	r_5	r_5	s_5	s_2	r_2
$-120°$	r_4	r_4	s_4	s_1	r_1

Table 4.3: Cayley table of hexagonal detector operations that produce transformations for aligning cardinal directions $\{x, y\}$ to cardinal directions on a quadragonal detector. The row is applied first followed by the column, and the algebraic equivalent of the transform is written as the entry.

Now having sorted out a complete set of transforms, the problem of confirming the correct orientation arises. There are a few solutions to this problem. The first is to find some spectra in the ion molecular frame with a known distribution, and to test all possible orientations and choose the one that reproduces the known distribution. One such spectra that has been employed previously, and not by this author, is the photo-doubleionization MFPADs of N_2. I will not give a detailed account of this method, having no experience with it, except to say that both ion and electron momentum must be well calibrated to move to the molecular frame. The second is to use the recoil kick of the photoelectron to look for momentum conservation between the electron and ion. Generally this only works for very

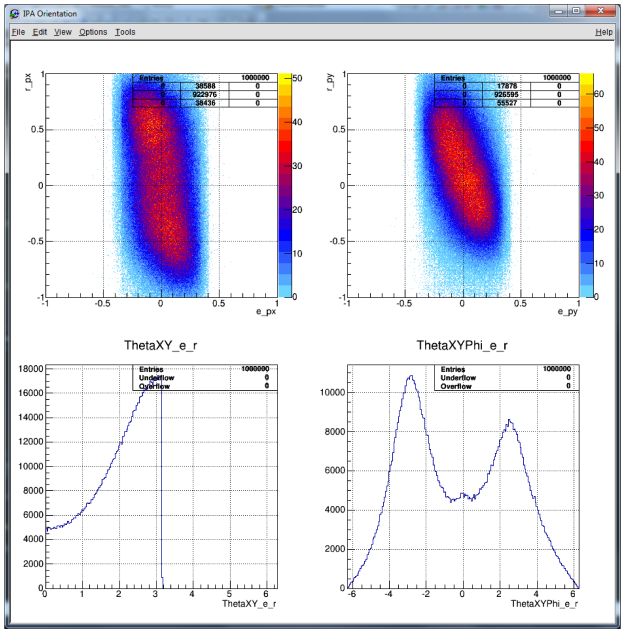

Figure 4.6: Orientation spectra in the IPA for June 2017 H2 data. From top left, clockwise, p_x momentum conservation, p_y, the θ angle between electron and ion, and the ϕ angle in the $\{x, y\}$ plane. Both angles are peaked at π.

light atoms like Hydrogen and Helium. The third is to use the detector ghost images (the crosstalk of the electron detector on the ion detector) to create correlated masks on both detectors that can be used for alignment.

A general trick that guarantees the correct angle is to look for the hot gas stripe on the electron detector. Though the electrons are diffused by the magnetic field, the asymmetry of the hot gas stripe is sometimes roughly translated to the electron detector. It is possible to ascertain on a log scale, that a certain direction on the detector contains an axis of greater intensity. This is the hot gas stripe and the correct angle can be found by rotating such that this axis is parallel to the x axis.

The momentum kick method is usually available if calibration wiggle runs were taken. The higher energy photoelectron required to illuminate the nodes in a wiggle spectrum produces a well resolve recoil in Helium. However, the angular distribution is a strong dipole, and given that the polarization is aligned to the tof axis the signal in the transverse x and y directions is weak. The momentum spectra themselves are shown in figure 4.6 and are

simply the electron momentum plotted vs the recoil momentum for the cardinal directions $\{x, y, z\}$ (z is omitted because it trivially determined by tof). The ion momentum is blurred by the width of the jet dot which is comparable to the translation imparted by the kick of the electron. The edges are clearly angled at 45° in the p_x dimension. In the p_y dimension the distribution appears angled at a slope of 60°, but this arises most probably from the velocity distribution within the jet, which we have no way to correct. We can only hope to offset the mean velocity and have no information to determine the individual velocities of each neutral. It is clearly visible in the angular plots, that the detector is oriented correctly in the $\{x, y\}$ plane. The spectra shown in the picture are the best defined of the four possible reflection combinations.

4.6 Consistency Checks

Any good analysis should have spectra the check for consistency over each aspect of data collection that might introduce misleading biases, features, or outright lies. The number of gates required to produce the spectra of interest make it entirely possible that some feature is manufactured by a coincidental interaction between two of these gates. For example, perhaps the interesting feature arises because one of the gates lets through some unwanted signal, and another gate trims this signal to look real. It is highly recommended that each gate in the analysis be verified with some spectra that is independent of the spectra to be gated on next. For example, it is good to verify that angular distributions are still smooth after creating gates on an energy map to isolate a particular reaction channel. It is always good to verify that small changes in the gates leading up to an effect do not substantially alter the effect under investigation.

Similarly, it is important to check that biases in the spectrometer or the MCPs, such as hotspots or field gradients, are not generating a signal. If there are enough statistics, the symmetry of the experiment can be exploited to compare different quadrants or halves of the detectors. It is rare for the physics inherent to the spectrometer to break the symmetry of the

molecular process caused by photoabsorption; this can only occur if the magnetic and electric fields, the jet velocity, or the propagation direction of the light, somehow affect the molecular process. The polarization and rotation of the light certainly can break the symmetry, but for example we consider linear polarized light along the tof direction. With this polarizaiton, all four quadrants are symmetric and identical and should produce the same experimental signal. Of course not all four quadrants of each detector are equal in background noise. On the ion detector, the hot gas stripe occludes the bottom half and the jet dot occludes the top half at well defined points in time. The electron noise is spread evenly in the transverse dimensions, but tends to accumulate in the z momentum direction that corresponds to the flight time with more area in the gated wiggle. That is to say that the background electrons are distributed roughly evenly in time and space and a momentum gate will naturally create a fish. This fish will grab background electrons preferrentially in short or long times of flight depending on which side of the wiggle the real electron distribution lives. If the distribution is exactly centered in a wiggle the background electrons will also be symmetric but this is rarely the case.

Finally, it is good to verify that no major changes have taken place over the data run by plotting quantities against the eventcounter. For example, if the ion energy would drift over the course of the run, then this might indicate a drifting field. If the angle of an electron dipole changes, then the magnetic field or polarization has drifted.

4.7 Nonlinear Fields and Lookup Tables

As mentioned previously, nonlinearities in the first stage acceleration field are a major problem in achieving good calibrations. The problem arises from the imperfect nature of metal mesh as a boundary between two different regions with a large jump in the electric field. The small gaps between wires in the mesh allow field to leak through. The ion MCP is very close to the mesh seperating it from the first stage, and the high field required to increase collection efficiency of the MCP leaks into the first stage. A mesh simulation was

attempted to quantify the field leak through and is described in section. The primary result of this effort is shown in figure 3.7. Examination of the red potential lines clearly show that there is a region of high potential created by the imperfect screen of the mesh. The quality of this simulation is suspect, because such a potential gradient would immediately destroy the functionality of the spectrometer. Nevertheless, it is clear that some form of leaked field is a major concern. The green lines are electron trajectories of electrons born with zero energy along the line bisecting the interaction point in the spectrometer. The distortion due to the field is apparent to the eye.

The leaked field problem is great enough to warrant significant design changes to the spectrometer. The new spectrometer designed for the two color experiments incorporates a booster stage to distance the ion MCP and lower the field strength required to increase efficiency. The effect is noticeable when comparing the O_2 2008 and N_2 2011 datasets taken with the old spectrometer with the datasets taken with the new booster spectrometer.

Despite the improvement in spectrometer design, the problem remains an open challenge for the analyst. In the presence of the leaked field, the acceleration field is no longer linear and cannot be solved by the typical Newton's method because there is no analytical way to compute the time of flight. Said another way, the reverse problem of solving for the initial momentum given the time of flight becomes mathematically and computationally very difficult. However, the forward problem, of starting with the momentum and computing the time to impact remains tractable by numerical integration. Therefore, I developed a numerical integrator capable of handling user coded nonlinear fields in the acceleration region of the spectrometer. The integrator was put to good use by masters student Jonathan Neff in his thesis, among others.

The fundamental principle of the integrator is to use a mathematical model for the nonlinear field and numercially compute a lookup table for a range of electron momentum values. Starting from a set of momentum values, the integrator is employed to map those values to times of flight. To increase accuracy, a large number of initial momentum values

are used. Real data time of flight is converted to momentum using linear interpolation. The large number of values demands an efficient integrator and a simple leapfrog integration method of the velocity was employed with a small step size to limit accumulated error and conserve energy.

Briefly, the equations of the integrator are

$$\dot{v}[t] = a = -\frac{q\ E}{m_e} + F[x] \tag{4.32}$$

$$\dot{x}[t] = v[t] + v_o \tag{4.33}$$

$$x[t] = x_o, \tag{4.34}$$

where $F[x]$ is the leaked field force function. The initial conditions to start the integration are

$$a_o = -\frac{q\ E}{m_e} + F[x_o] \tag{4.35}$$

$$v_{1/2} = \frac{\Delta t}{2} a + v_o \tag{4.36}$$

$$x_1 = x_o + v_{1/2}\Delta t, \tag{4.37}$$

where the subscripts denote the timestep or half step. With these initial conditions, the integration proceeds as follows:

$$a_i = -\frac{q\ E}{m_e} + F[x_i] \tag{4.38}$$

$$v_{i+1/2} = a\Delta t + v_{i-1/2} \tag{4.39}$$

$$x_{i+1} = x_i + v_{i+1/2}\Delta t. \tag{4.40}$$

Ten thousand integration steps at a constant $\Delta t = 30$ femtoseconds are used for each value of the momentum. Ten thousand individual momenta are calculated to generate the lookup table. The error of the leapfrog integrator is of the second order of the timestep, here roughly

six orders of magnitude less than the nanosecond. It is reasonable to assume that the error is smaller than that inherent in the position and time error in the data. The integrator is only applied in the nonlinear field region. Once the electron passes the mesh, the program switches over to analytical expressions to calculate the time spent in the second stage drift region and the third stage acceleration region. As previously explained, both these regions have a small effect on the flight time even when the calibration is detuned.

I experimented with a number of fringe field functions to try and correct distorted ion and electron momenta spheres. To begin with, I reasoned that the spectrometer could be treated as a superposition of the linear acceleration field and the field induced in a grounded cylinder with one end held at a constant potential. The potential in the grounded cylinder must obey the usual relation for a region with no source charges $\nabla^2\Phi = 0$ with the solution in the axial direction a combination of hyperbolic sine and cosine functions that match the boundary conditions. The only choice that matches the grounded mesh on the electron side with some potential induced or leaked on the ion side is the $Sinh[z]$ function. The derivative will give the field and convert this into $Cosh[z]$. Numerous iterations of these functions and other exponential functions did not produce satisfactory results, most probably because the spectrometer makes a poor grounded tube. The open plates that help to define the potential in the first stage are adequate when the field is flat between two large flat surfaces, but fail to contain a field with a radial component.

In the end, the most successful field geometry was a simple linear increase in the field at some predefined point close to the ion mesh:

$$a_i = -\frac{q\ E}{m_e} - \frac{q\ E_f}{m_e} l \tag{4.41}$$

$$l = 0, x < x_s \tag{4.42}$$

$$l = x, x > x_s, \tag{4.43}$$

where x_s is some start position and E_f is the corrective field strength, both determined by the user with the IPA. Johnathan Neff discovered this and deployed it to great effect in his Masters thesis. I have similarly adopted this technique in analyzing the O_2 2008 and N_2 2011 datasets.

Though powerful, the field correction above fails to account for the obvious fringe field in the radial direction. This could be done, but would require adding another dimension to the lookup table that accounts for the radial position of the particle. This in turn would require a two dimesional integration, which is another beast entirely. At some point, the excersize of generating nonlinear fields supercedes the requirement of a flat field to begin with. I can imagine a spectrometer where no mesh are employed. Instead, well known angular distributions are used in conjunction with complete trajectory simulations to produce lookup tables. A spectrometer without meshes would have a termendous advantage by enabling very low rate and very clean experiments.

In keeping with the previous line of reasoning, I have also attempted to use dipole electron distributions from Helium to generate a "perfect" electron calibration via lookup table. The core idea is to use a well known energy photoelectron distribution, preferrably at the energy of the interesting experimental electrons, and to "force" this distribution to be round by lookup table. I have created a routine that maps the energy ring from the clean helium signal onto a perfect momentum sphere by adjusting the electrons time of flight according to radial position. By using the radial position to bin the data and define the correction, we bypass directly working with fields or non-linear computations. Note that this is just one possible way to force the experimental distribution onto the sphere, other transforms may be more appropriate but are surely more complicated.

The proceedure is simple and begins with a user defined electron energy as a parameter: for helium this energy is known down to tens of millielectronvolts from the energy of the monocromater. A theoretical lookup table of 100 evenly distributed radial positions is generated by stepping the z momenta through the energy range. Given the energy and current p_z,

the radial momentum is derived and the radial position is analytically computed (the easy forward computational problem). The p_z momentum is stepped in a for loop with variable step size until the radial position steps over the center of the radial bin: then the theoretical flight time computed analytically from the initial p_z is recorded. Momentum in the z direction does not map one to one onto the radial dimension: for each positive z momentum there is an equivalent negative z momenta that produces the same radius. Therefore the calculations are repeated and stored for both positive and negative halves of the momentum distribution.

The large change in momentum required when moving from bins near the radial center out to the edge of the distribution nescessitates a varaible momentum step size. The step size is modififed as follows

$$dp_z = A\frac{r_o - r_{i+1}}{r_{i+1} - r_i}dp_{min}, \tag{4.44}$$

where r_o is the center of the bin, r_i is the ith computed radial position, $A = .01$ is a constant of proportionality that is tuned to provide convergence for all bins, and dp_{min} is the maximum momenta difference divided by 10^6. Additionally, the maximum step size is capped at $10^3 dp_{min}$ to prevent the step size from growing too large and overshooting the center of bin.

Next the average time of flight is accumulated from the data on a grid defined by the same 100 bins in the radial (xy plane) direction and 60 bins in the xy plane ϕ angle. In keeping with the theoretical calculations two grids are created, the experimental distribution is halved in two at the midpoint in order to seperate the electrons that first fly towards the ion detector (positive z momenta) from those that fly directly to the electron detector (negative z momenta).

Each of the 6000 radial-angular bins is given a unique correction by subrtracting the corresponding theoretical flight time from the experimental average of the bin. Even with

as many as a million events collected in the helium run, only a few hundred events would fill each bin and the error may be quite high. To compensate and introduce smoothing between bins, events were multiply counted. A single bin was filled with events from ± 2 bins in the radial and phi directions, including diagonal bins. In this way, the number of counts was multiplied by $4 * 4 = 16$. Average bin counts vary over the radial position with the hottest parts containing several thousands.

ϕ_{xy}	0	1.59742	3.19484	4.68576	6.28318	
Δt	-1.81796	-2.01438	-1.79826	-1.8388	-1.81147	
# entries	4687	5240	6386	5536	4620	

Table 4.4: Selected ϕ bin values for the 11.512mm radial bin. It is clear that time offsets are different for different theta angles.

When the lookup table is enabled, it adjusts the flight time of the electron by subtracting the correction table value for the bin the electrons landed in. Examination of the printed correction table gives a great deal of insight about the actual nature of the fringe field. As shown in table 4.4, the tof correction can vary by as much as $.2ns$ traveling around the ϕ angle. This a dramatic shift in the tof. Apparently, the fringe field is different in the top and bottom half of the spectrometer. A physical explanation for this might rest in the presence of grounded chamber floor. If the solution to the fringe field equation more resembles a verticle plate close to a flat grounded floor and opposite to another flat plate, then this would have a strong gradient in the vertical direction. The results of applying the lookup table are quite good: the electrons are forced to be perfectly round.

Alternately, using the same radial-angular bins, a radial momentum offset can be calculated using electrons of known energy from a Helium calibration run. The momenta can be scaled to fit a perfect momentum sphere corresponding to the exact known phototelectron energy. This is exactly the procedure used on the H_2 data presented in this thesis.

Chapter 5

H_2 Experimental Details

H_2 molecules were photoionized with $18.497eV \pm .015eV$ energy photons in a pulse of approximately 1×10^5 photons with a width of $\approx 80ps$ from beamline 10.0.0.1 at the Advanced Light source. Ionization took place in the presence of a strong IR laser field with photon energy of $1.2eV$, peak field intensity of $\approx 1.0 \times 10^{11} W/cm^2$, and $12ps$ pulse length. The H_2 molecular beam was prepared by supersonic expansion of room temperature H_2 gas of high purity from a $50um$ nozzle followed by two skimmer stages. The jet reached milli-electronvolt temperature sufficient to leave the H_2 in it's ground rotational and vibrational state.

Coincidence collection of photoelectron and ion was achieved by keeping the count rate low such that the probability of two XUV photoionization events in one shot of the ALS was two orders of magnitude lower than a single event. An H_2 molecule will take $74ns$ to transit the XUV pumped volume given the jet velocity of $2627m/s$. This is long enough that the pumped molecule will not leave the laser focus for the time delays used in the experiment yet short enough that a pumped molecule will exit the probe volume before the next laser pulse arrives. We can therefore guarantee that the laser dissociated molecules were mapped to the correct coincident electron.

The ALS cross-section spot size was approximately $1000\mu m$ wide by $200\mu m$ tall and the depth of the jet-ALS interaction volume was approximately $2mm$. The total ALS pumped volume is $2.0 \times 10^8 \mu m^3$. The spot size of the laser was considerably smaller. The exact value is not known because the laser mode was oblate before focusing. With our focusing geometry, a perfectly Gaussian beam mode would have achieved a $5.75\mu m$ beam waist and $100.82\mu m$ Rayleigh length. More realistic values are computed using a beam quality factor

of $M^2 = 2$, yielding a focal waist of $23\mu m$ and a Rayleigh length of $1.6mm$. The total focal volume of the beam waist multiplied by twice the Rayleigh range is $5.27 \times 10^6 \mu m^3$. The focal volume can also be estimated simply by assuming apex to apex double-cone geometry (from linear ray tracing) of the light over the Rayleigh range: the resulting focal volume is $3.44 \times 10^8 \mu m^3$. Via these two methods the ratio of the ALS focal volume to laser focal volume can vary from 0.26 to 1.72. If instead the overlap is limited to the laser focal region where the probability is 1 that a laser photon will be absorbed by a process with $100Mb$ cross section, again assuming simple apex to apex double-cone geometry, the laser volume is $1.33 \times 10^8 \mu m^3$ and the ratio of the two volumes is 0.67. This represents a best guess geometric overlap factor from geometric arguments for rate estimations.

The laser peak intensity at the focus can be estimated from the lowest energy vibrational states that were dissociated: here $\nu = 9$. If we assume that the crossing point is resonant with the 10th vibrational state and the depth of the barrier must be near to or lower than the 9th vibrational state, then given the peak to peak difference between the 10th and 9th states of $148mV$ (which is very close to the calculated value of $138.8eV$ [33]), this corresponds to $\sim 2.3 \times 10^{12} W/cm^2$. However, this neglects tunneling through the barrier of the adiabatic potentials. We can model this by approximating the cation molecular potential as a square well with a square barrier with width w equal to twice the distance between the classical turning point of the 9th and 10th vibrational state, $w = .28au$, and height h equal to the energy of the 9th vibrational state plus the separation between the two states, $.0053au$. We take as zero energy the bottom of the potential well and assume a plane wave of energy equal to the energy of the 9th vibrational state. Under these conditions, the amplitude of the tunneling wave will equal 8.4% of the wave trapped in the well. We further assume that the trapped well wave reflects from the barrier a number of times equal to the laser pulse period divided by the classical transit time of the square well, roughly 1591 reflections. Under these assumptions, practically all of the intensity of the wavefunction tunnels through the barrier and dissociates. Though this is most definitely an over estimate of the tunneling probability,

the simple calculation shows that a large fraction of of the 9th vibrational state can tunnel through the barrier of a relatively weak field. Additionally, we observe no dissociation of the 8th vibrational state, indicating that the barrier must remain quite high and wide at that energy level. These observations and calclation support our original estimate of the field strength of $\sim 1 \times 10^{11} W/cm^2$.

If we assume a that peak field strength is required to dissociate the 9th vibrational state via tunneling, then we can estimate the number of events in the other channels that are exposed to the strong field. From data set e, the ratio between the 9th and 10th vibrational state is 38.4% and we can conclude that at least this percentage of events in the 10th vibrational state experienced the strong field.

The ALS repetition rate was $3MHz$ ($328.28ns$ period) while that of the laser was $1.5MHz$ ($656.56ns$ period), for a duty cycle of 2. As described previously in section 3.3.4, we achieved a laser-synchrotron synchrolock with $\leq 100ps$ RMS drift over hour long timescales and possibly undetectable $\leq 1ps$ RMS jitter over minute long timescales. We took data with zero time delay for data runs b and d, and with longer delays of $\approx 33ps$ and $\approx 900ps$ in series e and f, respectively. There is evidence of significant long term drift in the fact that two color signals disappear and re-appear in series b and d, and a weak ponderomotive shift appears in series f where no shift should be observed.

During the beamtime there was an unusual event where vacuum was broken. The break occurred between data sets d and e, with background conditions continuing to improve as data set e was taken and reaching nominal values for data set f. As a result, the background conditions between datasets are different and care must be taken in making comparisons between datasets.

The polarization of the laser radiation was determined by examination of Helium two color data. An electron from the $1s^2$ shell was excited to the $1s4p\,^1P$ state ($23.742eV$ vertical energy) via a 23.7853 photon from the synchrotron, polarizing the atom in space by projecting the angular momentum of $l = 1, m = 0$ onto the axis of polarization: in the case

of figure 5.1 the z axis. Next both parallel and perpendicular laser polarization (relative to the synchrotron polarization) were used to ionize the helium atom into the continuum. The laser photon projects the bound orbital into the continuum as a partial wave with quantization axis along the laser photon polarization. The outgoing electron has wave vector k and angular momentum determined by selection rules. The electron must absorb a unit of angular momentum and a change in parity from the laser photon; the bound p-wave is transformed into a partial d-wave in the continuum. Histograms of the resulting momenta for parallel and perpendicular laser polarization are shown in figure 5.1. The spectra shown are integrated over the missing dimension in a so called "pancake" projection: for example, p_x vs. p_y is integrated over p_z.

The parallel laser polarization changes 1 ± 1 with $m_l = 0$ and projects both S and D waves: $1s4d \Rightarrow 1s(kd_0 + ks)$. The top left histogram of figure 5.1 shows the projection of the $d_0 + s$ orbital momentum distribution onto the yz plane: the quantization axis is along the z axis since both photon polarizations are aligned. The d_0 shape clearly dominates the distribution, and there is little character of an s wave. This result is expected because the laser photon breaks the symmetry of the already aligned atom. In the perpendicular case only the D wave with $m_l \pm 1$: $1s4d \Rightarrow 1skd_{\pm 1}$ is allowed. The center right spectra of figure 5.1 shows the $d_{\pm 1}$ orbital momentum distribution projected onto the xz plane.

From examination, it is clear that the distributions in the center left and top right histograms of figure 5.1 are oriented at an angle. This indicates the laser polarization is not purely horizontal or perpendicular. According to the optomechanic mechanism in the laser for switching polarizations, we can assume that the two orientations are very close to perpendicular to each other. By projecting the top and bottom halves of center left and top right histograms, the angle in the respective plane can be computed. We found the angle in the yz plane to be $\phi_{yz} = 3.62°$, as measured from the z-axis, and in the xy plane to be $\phi_{xy} = 5.143°$, as measured from the y-axis. The shift in the xz plane is negligible. These angles transform almost exactly into polar coordinates; with the z-axis as the poles and the y-axis

as the zero of the phi angle, the polarization coordinates become $(\theta_z = 3.62°, \phi_{xy} = 5.143°)$. The unit vector pointing in this direction is used as the laser polarization in the analysis.

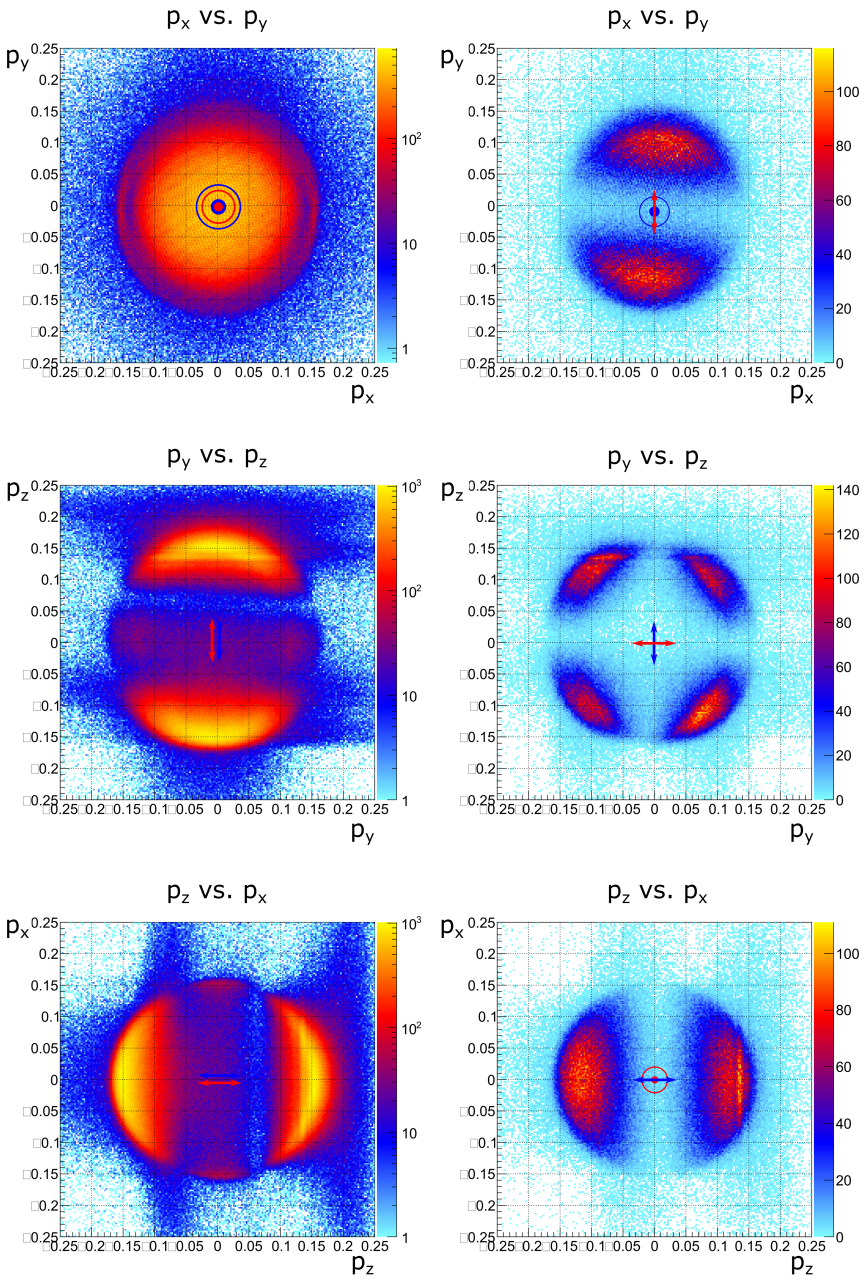

Figure 5.1: Helium 2-color data. Blue arrows and dots denote XUV polarization. XUV polarization is always aligned to the z axis. Red arrows and dots denote laser polarization. Left column, parallel polarizations. Right column, perpendicular polarization.

Analysis and calibration H2 was conducted according to the methods in chapter 4. Calibration of this data was complicated by the momentum sharing between ions and electrons. Generally speaking the momentum kick from the photoelectron on the cation is negligible. However for low mass and energy, the momentum of the photoelectron is a substantial fraction of the momentum imparted to the recoiling fragments from the breakup of the H_2^+ cation. To reproduce the Waitz [18] results, a transformation to the center of mass frame is required. The momentum of the photoelectron must be compensated according to:

$$\vec{p}_{cm} = \vec{p}_l + \frac{\vec{p_e}}{2},$$

where $\vec{p_{cm}}$ is the center of mass momentum vector of the H^+, $\vec{p_l}$ is the lab frame proton momentum vector, and $\vec{p_e}$ is the momentum of the photoelectron. The momentum correction to the photoelectron can be neglected and is below the resolution of the spectrometer.

For the kinds of delicate measurements of the angular distributions that we intend to make, this correction can make a difference. Critically, the calibration of the recoils and electrons are coupled. Poor calibration of the electrons will impact the ions and destroy the measurement. To compensate, a momentum lookup table was implemented with a helium dataset of definite energy. The lookup table is a sensitive way to correct for inhomogeneous fields in the spectrometer. In spherical polar coordinates, momentum space was divided up into 99 θ (latitude) and 59 ϕ (longitude) bins. An adaptive peak finding algorithm determined the average kinetic energy for each bin and the average momenta was scaled to match the correct momenta corresponding to the known energy. The radial momentum magnitude of each photoelectron from H_2 was then scaled equivalently. Results of the lookup table as applied to the helium data used to generate the table can be seen in figure 6.1: there is a marked improvement. Immediate application of the lookup table to the hydrogen data was not perfect. The slight differences in starting position and energy necessitate slight

modifications using momentum shift and stretch functions. Specific calibration spectra for each hydrogen dataset can be found in appendix C.

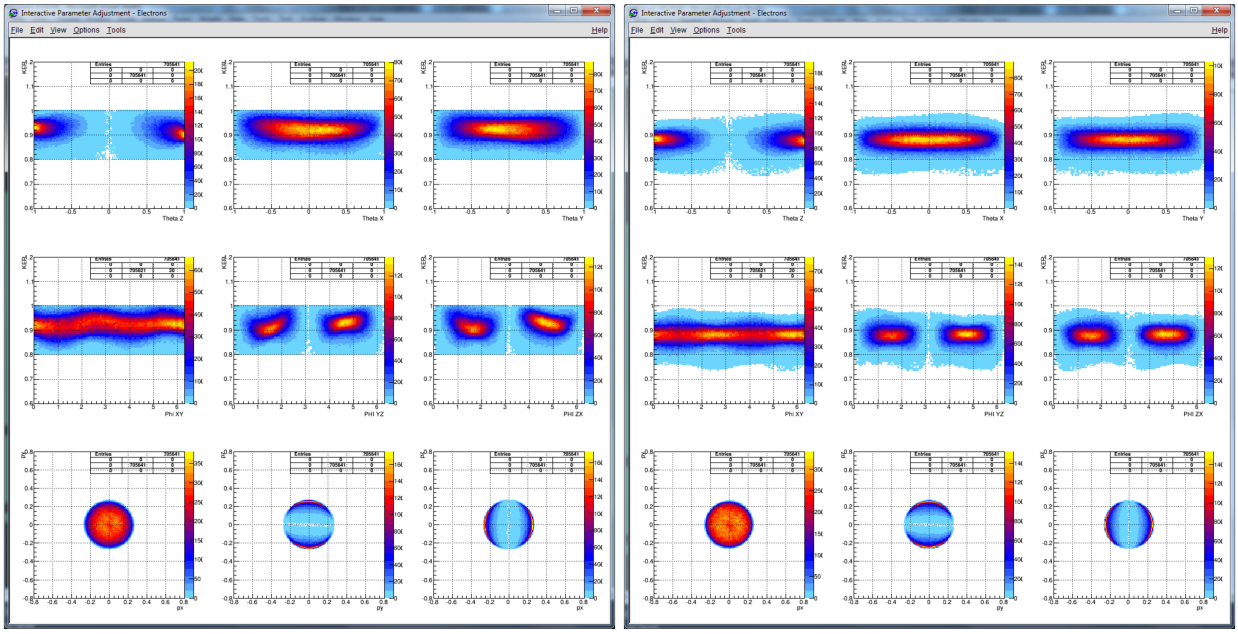

Figure 5.2: IPA spectra of the helium calibration electron distribution at .88eV. Left, best achievable calibration with regular parameters. Right, after the lookup table is applied.

Experimental interpretation was complicated because the synchrotron and laser light pulses could arrive simultaneously or with some temporal offset due to the synchrolock timing jitter and drift. As diagrammed in figure 5.3, when the time offset was set to zero there was a chance for the synchrotron to ionize the molecule directly into the laser dressed Floquet states produced by the strong field of the laser. When the two pulses were offset by long time delays, the laser would most probably not be present at all during the photoionization. In this case, we hoped to detect some form of long lived asymmetry retained by the cation that must be independent of the rotation of the nuclear axis, in analogy with the alignment induced in photon excited atoms.

The laser-on laser-off duty cycle affords us the opportunity to make difference measurements between the laser on data and the laser off data. This allows us to probe the effect of the laser on single ionization channels where no laser photon was absorbed but photons in the field were scattered. Specifically, we have tremendous statistics in both the single color

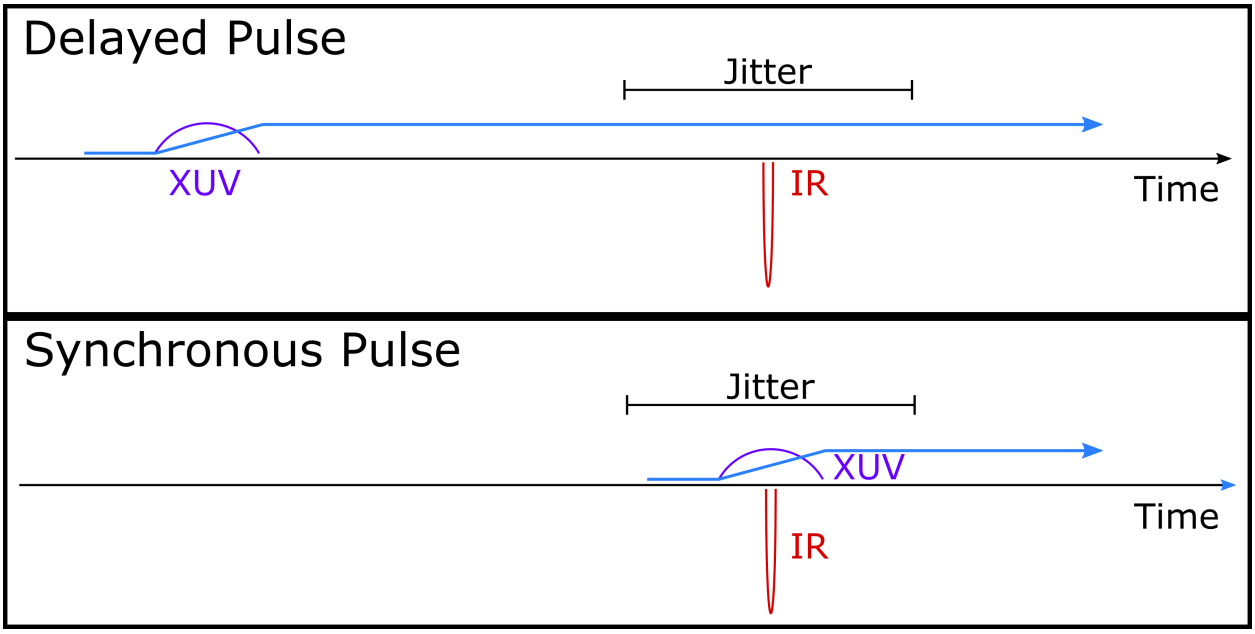

Figure 5.3: Schematic of time overlap. Magenta pulse: XUV. Red pulse: IR. Blue line: existence of photoionized stable H_2+. Top: laser pulse delayed. Bottom: laser pulse synchronous.

direct dissociation and in the photoionization that leaves a long lived bound dication. We can examine differences in energy and angle for these two cases. We are able to observe ponderomotive shifts in the latter which are cataloged for each data set in appendix D. Specific results for data runs e and f are analyzed in the next chapter.

For the laser dissociation channel where one photon has been absorbed, the laser-on laser-off duty cycle enables background subtraction within datasets that significantly improves the effective resolution of the measurement. In general, the background in each dataset is on the order of 10%, yielding at least an uncertainty of 10% in the measurement. With background subtraction the error becomes the square root of the sum of squares of each bin in a histogram. With our statistics on the order of $10k$ counts for two-color channels this is a dramatic reduction in error for most spectra.

Chapter 6

Experimental Results

We present the primary experimental results from the June beamtime in this chapter. Data from the August beamtime has been omitted because it is deemed to be of inferior quality. We begin by discussing the observed ponderomotive shift in photoelectron energy of the single photon absorption plus laser photon scattering channel. We proceed to discuss the two color absorption channel where the laser dissociates the bound H_2^+ dication. First we look for asymmetry in the MFPADSs to investigate retro-action of the photoelectron in the intense laser field. Next, we look for the appearance of - or lack thereof - interference fringes in the proton emission relative to the laser polarization.

There are only a few available angles and energies to analyze. The six variables are, in no particular order: the photoelectron energy, the photoelectron angle relative to XUV polarization, the photoelectron angle with the proton momentum vector (MFPAD), the energy release of the H_2+ dissociation, the proton angle with the XUV polarization, and the proton angle with the laser polarization. Additionally, the asymmetry of the MFPAD can be analyzed.

Laser light scattering can in principle shift the energy of the photoelectron, broaden the dissociation energy of the single color direct channel, and modify angular distributions. We have conducted a systematic analysis of possible effects, and have only found a strong signal in the ponderomotive shift.

An energy map of the H_2 data is shown in figure 6.1. The straight single color dissociation channel appears in the bottom left corner of the distribution. Above, the higher diagonal is the vibrational progression of the two color laser dissociation channel that begins

below $1.2eV$ photoelectron energy, which corresponds to the maximum depth a bound vibrational state can have below the dissociation limit before absorption of the $1.2eV$ laser photon can no longer dissociate the cation. The dissociated vibrational states progress downwards towards the dissociation limit of the hydrogen molecule. The reader can imagine shifting the upper diagonal to the left such that it lines up with the lower diagonal of the single color dissociation channel. The highest lying state in electron energy has been identified as the $\nu = 9$ vibrational state by comparison with the electron spectrum from H_2^+ in the same experiment. The next three states are $\nu = 10, 11, 12$ and have enough statistics for angular plots. The vertical columns arise from the jet dot pollution which can be removed by selective gating, but are left here to highlight the clean energy map phase space that the two color signal occupies.

We can estimate the probability for laser dissociation using the model described in subsection 3.3.5, and the assumed parameter values in table 3.2. With the experimental data we can measure directly the number of molecules left in the $\nu = 10, 11, 12$ bound vibrational states. We can use this information to eliminate the assumptions relating to the XUV absorption cross section. The geometric overlap is left to be determined and we will use a range of values computed in chapter 5: $g \in (.26, 1.)$. We will use dataset f, which has a long time delay, to ensure that all the H_2+ molecules interact with the laser pulse. The integrated probability to laser dissociate in all vibrational channels is between %16 and %58 percent. Specific counts can be found in table 6.1. By numerical coincidence, the conversion factor from probability to megabarns is $1.04 \times 10^{-18} cm^2$. The laser intensity appears to be high enough to dissociate resonant states with a very high probability, though the cross section for single photon resonant absorption is nearly an order of magnitude less than the initial photoionization.

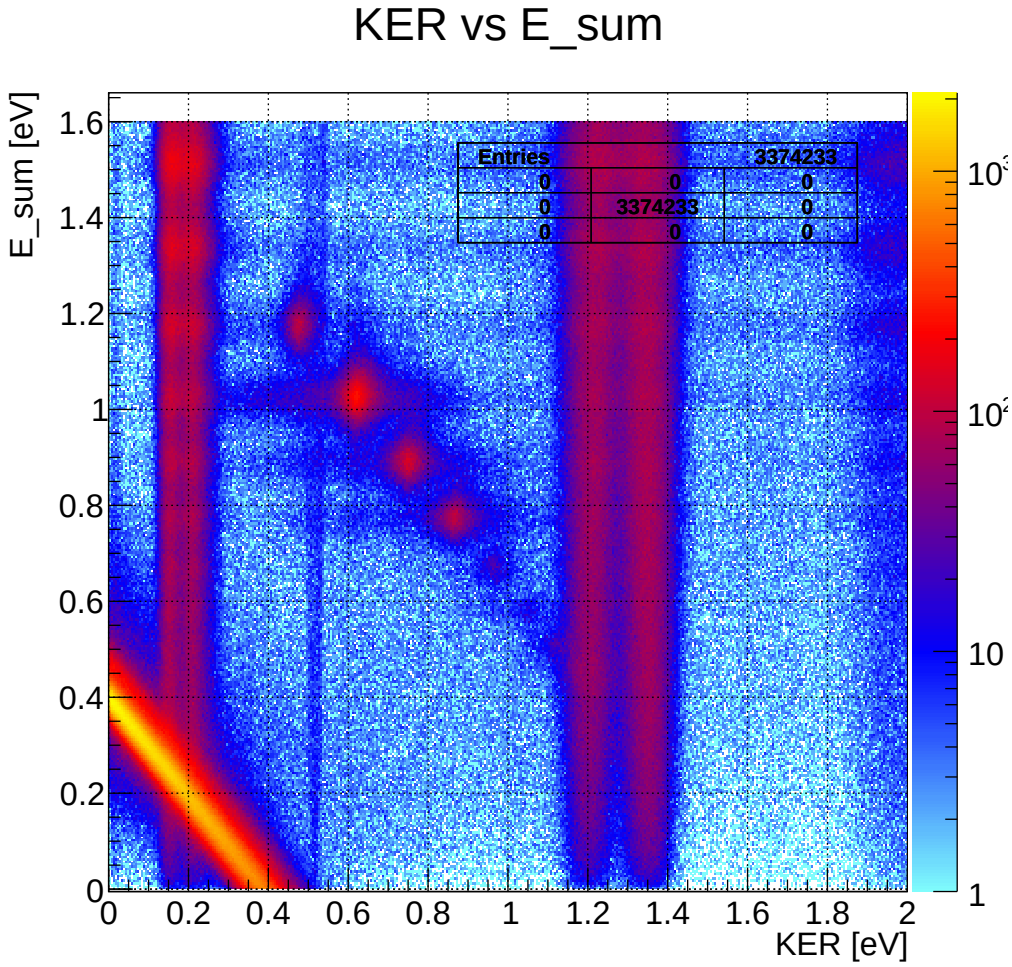

Figure 6.1: Energy map of the H^+ channel for data set f. Bottom left, direct dissociation. Middle dots, progression laser induced dissociation of vibrational states $\nu = 9, 10, 11, 12..$ approaching the dissociation limit. Vertical features, jet dot contamination.

		Total Counts	f	f Counts	2-Color Counts	Diss. Prob.
	$\nu = 10$		.017	538220	36834	(.0684, .2535)
f	$\nu = 11$	3.166×10^7	.013	411580	18718	(.0455, .1684)
	$\nu = 12$		.009	284940	12543	(.0440, .1630)

Table 6.1: Values for estimating the dissociation probability. Right column: ranges of dissociation probability for the low and high values of ALS-laser overlap. f is the fraction of the total counts in the laser dissociated vibrational channel. The conversion factor from probability to megabarns is coincidentally $1.04 \times 10^{-18} cm^2$.

6.1 Ponderomotive Shift

In addition to observation of the laser dissociation of H_2^+, we were able to observe ponderomotive shifts in the energy of the photoelectron as it escaped the laser focus. Ponderomotive spectra for each data set can be found in appendix D. The brightest peak in the photoelectron distribution originates from population of the 3rd vibrational state and is located at $2.37eV$. An electron with this energy will travel $\sim 11\mu m$ during the $12ps$ duration of the laser pulse, or roughly one micrometer per picosecond. Given the estimated beam waist of $\sim 25\mu m$, the electrons leaving the molecule in low lying bound vibrational states are not fast enough to make a complete transit of the laser focus within the laser pulse duration - the pulse can be considered on the edge of the "short" regime. With these conditions, a shift can be observed for photoelectrons born when the laser modifies the ionization potential or when the electrons receive a kick from the laser pulse after photoionization. For the expected intensities of $1 - 4 \times 10^{11} W/cm^2$ we calculate a ponderomotive shift of $10 - 40meV$. The FWHM of a Gaussian fit to the 3rd vibrational level photoelectron energy is $\sim 130meV$.

A schematic for the ponderomotive shift process is given in 6.2. From geometric considerations, it is obvious that dividing the electron momentum sphere along the time of flight axis (electron spectrometer side and ion spectrometer side) hemispheres will give an asymmetry which is some measure of the position of the jet dot in the ALS focus, as diagrammed in figure 6.2 part A. Electrons that fly into the intense portion of the laser pulse will shift

to lower energy, and those that fly out of the intense portion will shift to higher energy, as shown in figure 6.2 part B.

As diagrammed in figure 6.2 part C, a variety of scenarios can add or subtract energy based on the spatial position of the ionization point and the time lag relative to the laser. In the top scenario, if the electron transits the entire laser focus it will gain no energy. However, in the middle scenario, if the electron flies into the intense region of the focus as the laser pulse leaves it will lose energy. Conversely, in the bottom scenario, if the electron flies out of the high intensity region as the pulse arrives it will gain energy.

The statistically observed kick imparted to the electrons is a sum of the competing processes described above. If we restrict ourselves to considering only the electrons kicked by the laser after photoionization, then the momentum hemisphere corresponding to the spatial hemisphere containing the laser focus will receive a net negative energy kick. The opposite holds true for the other hemisphere. For the overlap configuration pictured in part A of figure 6.2, the majority of electrons will encounter an increasing ponderomotive barrier as they fly to the right. Conversely, the majority of electrons will receive a boost as they fly to the left. Critically, the electrons will have traveled far beyond the interaction region by $\sim 100ps$ and any observed shift gives some proof that the pulses were overlapped.

We can measure to high precision the shifts in energy that correspond to the ponderomotive shift because we have near infinite statistics for the bound vibrational cation channel. The results of both a direct subtraction and a chi squared fit are shown in figures 6.3 and 6.4 for electron and ion momentum half spheres respectively. A negative and positive shift is clearly present for the electron and ion hemispheres respectively. The net increase in energy for the electron side and net decrease in energy on the ion side indicates the laser focus was on the ion side of the ALS-Jet interaction volume. Given that our position overlap is at worst approximately %50 percent, we can conclude that the pulses were overlapped a significant amount of time.

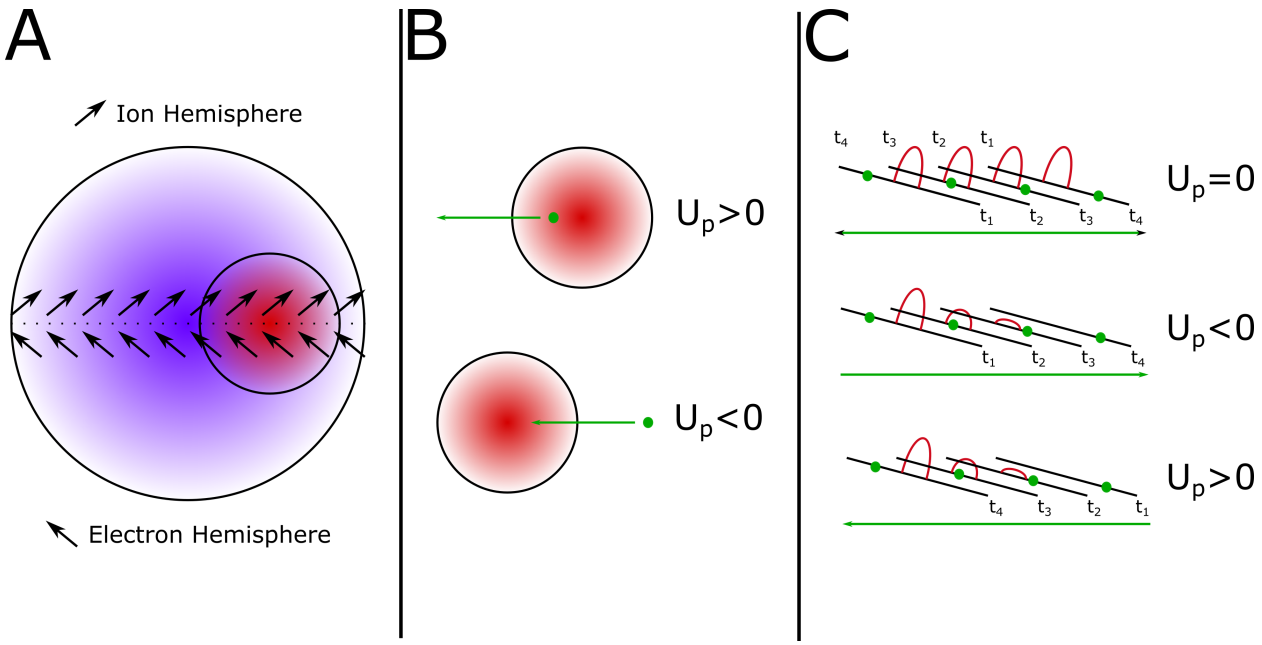

Figure 6.2: Diagram of the ponderomotive shift process. A: laser and ALS spatial overlap profile with photoelectrons represented by arrows pointing towards the ion detector (ion hemisphere) or electron detector (electron hemisphere). These groups will form the hemispheres of the momentum distribution. B: spatial transits giving rise to negative and positive energy shifts. C: spatial transits considering time evolution of the pulse.

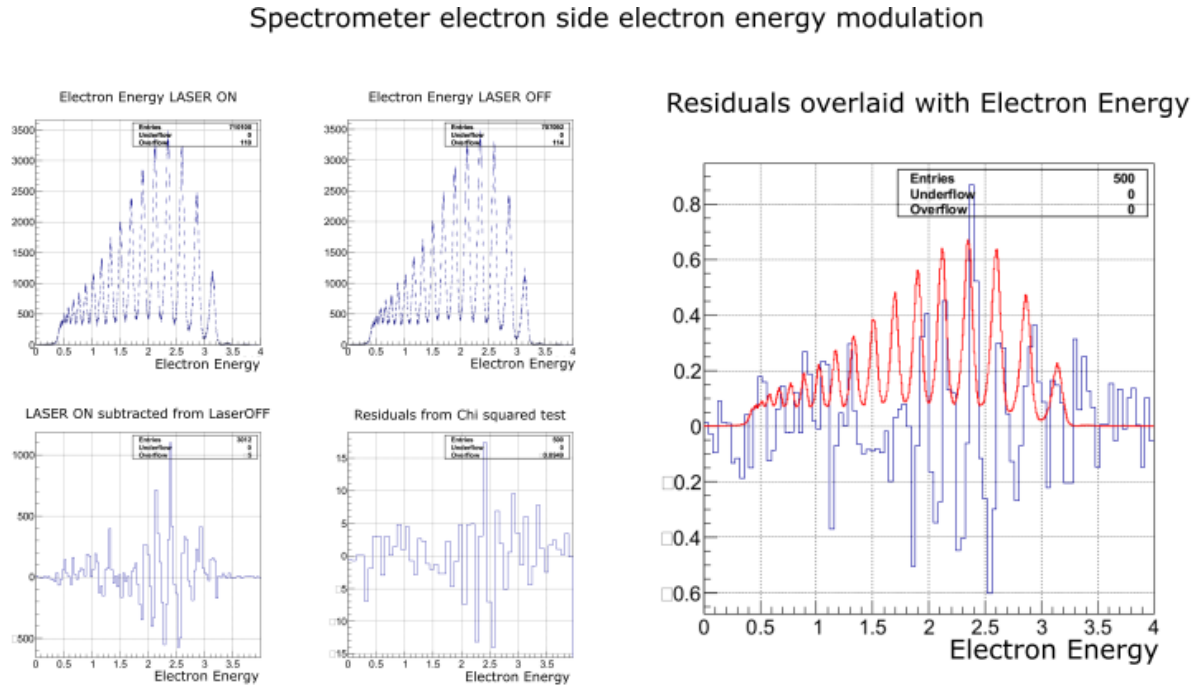

Figure 6.3: Energy spectra for the analysis of the ponderomotive shift for the electrons flying towards the electron detector. Data series e. Residuals are normalized. A positive shift is observed.

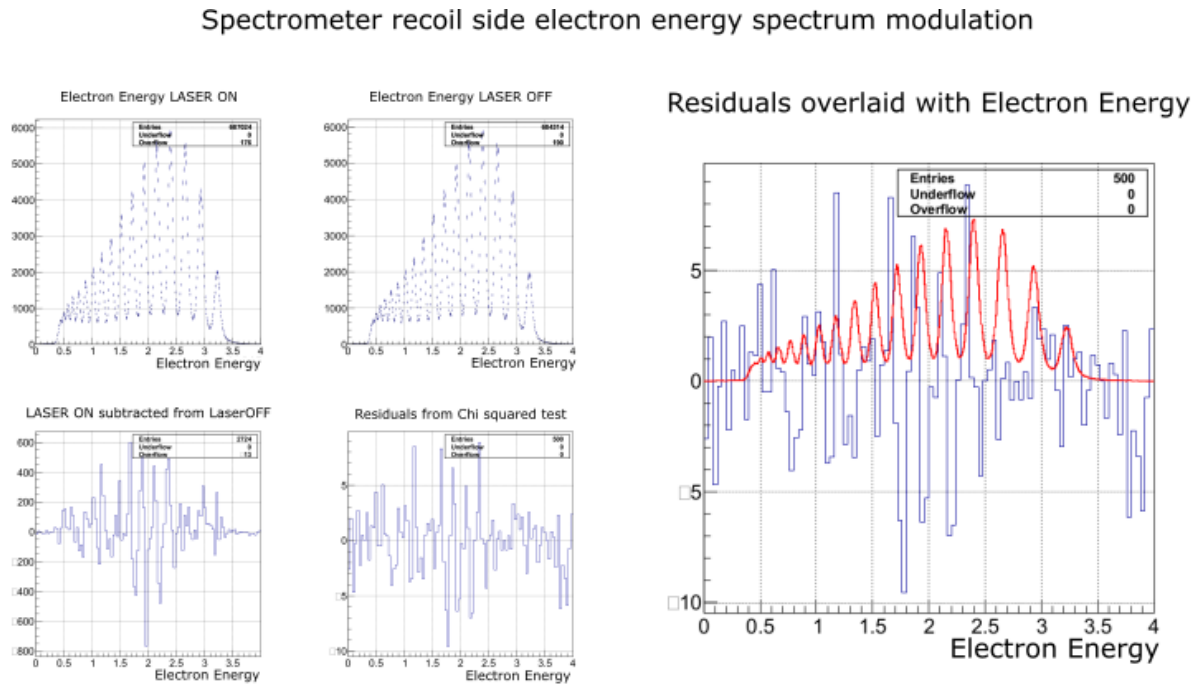

Figure 6.4: Energy spectra for the analysis of the ponderomotive shift for the electrons flying towards the ion detector. Data series e. Residuals are normalized. A negative shift is observed.

6.2 Asymmetry

Now we turn our attention to searching for asymmetries in the proton emission pattern as in the case of straight single photon ionization studied by Waitz et al. We apply the same analysis and quantify retro-action by an asymmetry parameter:

$$\delta = \frac{C_+ - C_-}{C_+ + C_-},$$

where we have divided the recoil frame polar angular distribution into two hemispherical bins: C_+ counts electrons ejected towards the proton and C_- counts electrons ejected opposite towards the neutral. For the direct dissociation channel, $\delta = .087$. In accordance with the two pulse widths and the jitter, we estimate that the laser was present at the moment of ionization anywhere from 5% to 10% of the laser dissociation events. If we expect a similar sized effect in the two color process, then we are looking for changes on the order of 1%.

Such resolution would seem unattainable given the $\sim 10\%$ background in the spectrometer. However, the background can be subtracted with a high degree of certainty. The Gaussian standard deviation error propagation for δ goes as:

$$\begin{aligned}
\sigma_\delta &= \sqrt{\left(\frac{C_+}{(C_+ + C_-)^2}\sigma_+\right)^2 + \left(\frac{C_-}{(C_+ + C_-)^2}\sigma_-\right)^2} \\
\sigma_\delta &\approx \sqrt{\left(\frac{1}{2C_+}\sigma_+\right)^2 + \left(\frac{1}{2C_-}\sigma_-\right)^2} \\
\sigma_\delta &\approx \sqrt{\left(\frac{1}{2C_+}\sqrt{\sigma_{L+}^2 + \sigma_{B+}^2}\right)^2 + \left(\frac{1}{2C_-}\sqrt{\sigma_{L-}^2 + \sigma_{B-}^2}\right)^2} \\
\sigma_\delta &\approx \sqrt{\left(\frac{1}{2C_+}\sqrt{C_+}\right)^2 + \left(\frac{1}{2C_-}\sqrt{C_-}\right)^2} \\
\sigma_\delta &\approx \frac{1}{2}\sigma_{+-}
\end{aligned}$$

where σ_B and σ_L represent the background and laser errors for the positive $(+)$ and negative $(-)$ hemisphere bins, we have neglected the standard error contribution from the background and we have recognized that either C_{+-} is very nearly always half of the total counts C. We define σ_{+-} as the error of resulting from the bins after subtraction of the background: $\sigma_{+-} = \sqrt{1/C_+ + 1/C_-}$. We desire $\sigma_{+-} < .002$ to ensure five sigma confidence. The background number of counts is much less than the laser signal, and is a good approximation for a minimum value. The standard deviation then goes as $1/\sqrt{N}$, with N the number of counts in each bin. To achieve the desired resolution we would need 1×10^6 counts in the background bin. A more realistic value is ≈ 500, yielding $\sigma_{+-} = .014$ and $\sigma_\delta = .07$. Clearly we are pushing the limits of our ability to resolve such an effect if it is as rare as we expect. However, if the effect is stronger than expected it should be visible. Examination of table 6.2 conclusively shows we do not see an asymmetry larger than the error in the measurement.

		Laser			Background			Subtracted			
		δ	C_+	C_-	δ	C_+	C_-	δ	C_+	C_-	σ_δ
	$\nu = 10$	.003	19767	19638	-.006	2502	2535	.004	17265	17103	.004
f	$\nu = 11$	-.007	9804	9941	-.0013	1095	1098	-.0076	8709	8843	.055
	$\nu = 12$	-.005	6502	6561	-.021	660	689	.003	5842	5872	.070
	$\nu = 10$	.004	13563	13450	.027	1326	1256	.001	12237	12194	.005
e	$\nu = 11$	.008	7016	6902	-.033	562	600	.01	6454	6302	.008
	$\nu = 12$	-.007	4348	4407	-.0369	378	407	-.004	3970	4000	.009
	$\nu = 10$	.003	3642	3617	.07	880	763	-.016	2762	2854	.014
d	$\nu = 11$	.006	1692	1714	.145	482	360	-.056	1210	1354	.020
	$\nu = 12$	.018	1115	1075	.010	339	278	-.0134	776	797	.025
	$\nu = 10$	-.007	9838	9977	.044	1008	923	-.013	8830	9054	.008
b	$\nu = 11$	.007	4891	5049	.130	678	522	-.025	4303	4527	.011
	$\nu = 12$	.035	3393	3159	.100	485	397	.025	2908	2762	.014

Table 6.2: Bin counts and delta values for the listed states from each data set. Error in the last column corresponds applies only to the subtracted measurement.

6.3 Angular Distributions

We present the various two color angular distributions in the following pages in a detailed comparison between data set e and f. Angular spectra for data sets b and d, as well as e and f with slightly different gates, can be found in appendix E. In the compiled figures that follow, two color signals without background subtraction are shown on the top row. Middle row spectra show the background signal. Bottom row images show the two color background subtracted spectra. The left column always contains the long delay data series f ($\sim 1ns$). The right column contains the short delay time overlap data set e ($\sim 33ps$). Gates were expanded from those used to produce table 6.2 to give a better sense of the background subtraction.

Briefly, the origin of the background is predominantly the hot gas stripe, which overlays the recoil momenta sphere for negative momentum in the time of flight direction (z-axis). This is clear from the plots of recoil axis relative to polarization shown in figures 6.6, 6.7, and 6.8; most of the counts in the background are localized from $90 - 270°$. When searching

the same spectra for signature interference fringes of the conical intersection, the left side of the distributions will be compromised.

We expect to see strong interference fringes in the emission patterns of proton angular distributions, and there is some structure, but the structure appears to arise from systematic errors. We do not observe any substantial fringes that could be considered well separated by their error bars or that appear reliably in all four data runs. We conclude that at our laser intensities there is limited bond hardening responsible for the interference fringes observed in [35] or that the effect does not exist.

It bears to examine closely the electron emission patterns to determine biases in the spectrometer. Electron emission patterns relative to polarization are shown in figures 6.9, 6.10, and 6.11. The background is evenly distributed in both forward and backwards time of flight though there are more counts in general for electrons that fly towards the electron detector: the left half of the distributions. Unfortunately, it appears there remain systematic errors in the electrons and ions which may obscure the sensitive dynamics we want to observe in the MFPADs.

Nevertheless, we can still compare the angular distributions of the dissociating cation to available distributions in the literature. Figure 6.5 contains a side by side comparison of the $\nu = 10, 11, 12$ vibrational states of H^+ polar angular distributions with the $\nu = 7, 9$ vibrational states from Natan [59]. Natan used a $30fs$, $795nm$, $\leq 2 \times 10^{13} W/cm^2$ laser to drive the photo dissociation. The seventh vibrational state is the closest state to the lower adiabatic curve in Natan's experiment while the tenth vibrational state is the next highest state in our experiment. Both these states are expected to have a strong narrowing of the distribution. Clearly there is a dramatic change in angular distribution between vibrational states in Natan's data. However, we observe no similar modulation in our data. The discrepancy must originate in the difference in wavelength, intensity, or pulse duration between the two experiments. However, it is remarkable that such a dramatic change could occur over one order of magnitude in intensity and $.37eV$ change in photon energy. This

leaves the timescale of the pulse as the parameter with a change of three orders of magnitude. It is possible that, given the slow rising edge of our pulse, we mainly drive resonant absorption before the intensity is high enough to cause any alignment. That is to say, the majority of H_2^+ dissociates at the front end of our pulse.

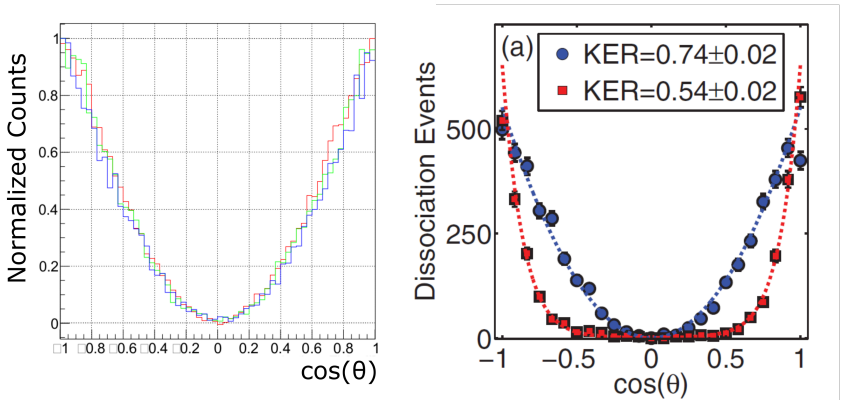

Figure 6.5: Left, spectra for $\nu = 10, 11, 12$, for red, green, and blue, respectively: recoil relative to polarization, data set f. Right, spectra from [59], for $\nu = 7, 9$, red and blue, respectively.

The electron emission pattern relative to the polarization for states $\nu = 10, 11, 12$ is shown in figures 6.9 6.10, and 6.11, respectively. The polarization is again fixed from 0° to 180°. These spectra are important because they reveal any biases in the spectrometer. Interestingly, some structural differences emerge between the f and e dataset. There are two possibilities to explain the structure. First, this could be just noise in the spectrometer and the resulting structure arises purely from statistical fluctuations. Second, the effects could be real if they result from ionization into the Floquet state, and potential elastic re-scattering of the photoelectron in the laser field. By eye, it appears that the $\nu = 10$ spectra are roughly the same, the $\nu = 11$ look substantially different, and the $\nu = 12$ may not have enough statistics to compare.

The electron emission relative to the proton emission for states $\nu = 10, 11, 12$ is shown in figures 6.12 6.13, and 6.14, respectively. In these plots, the proton emission is fixed at 0°. We hope to see some form of asymmetry in the emission of the electron that should be

present for the short delay data set e and absent from the long delay data set f. There are some striking differences between the data series e and f particularly in figure 6.14. Though we have already ascertained from table 6.2 that there is hardly a numerical difference in the δ value, there does appear to be a structural difference. Unfortunately, this is also the state with the least statistics. We would like to see a positive confirmation of an effect in the state with the most statistics: $\nu = 10$. No immediate difference is evident. On the whole, we must conclude that the effect is either non-existent or not strong enough to appear above the systematic errors in our measurement.

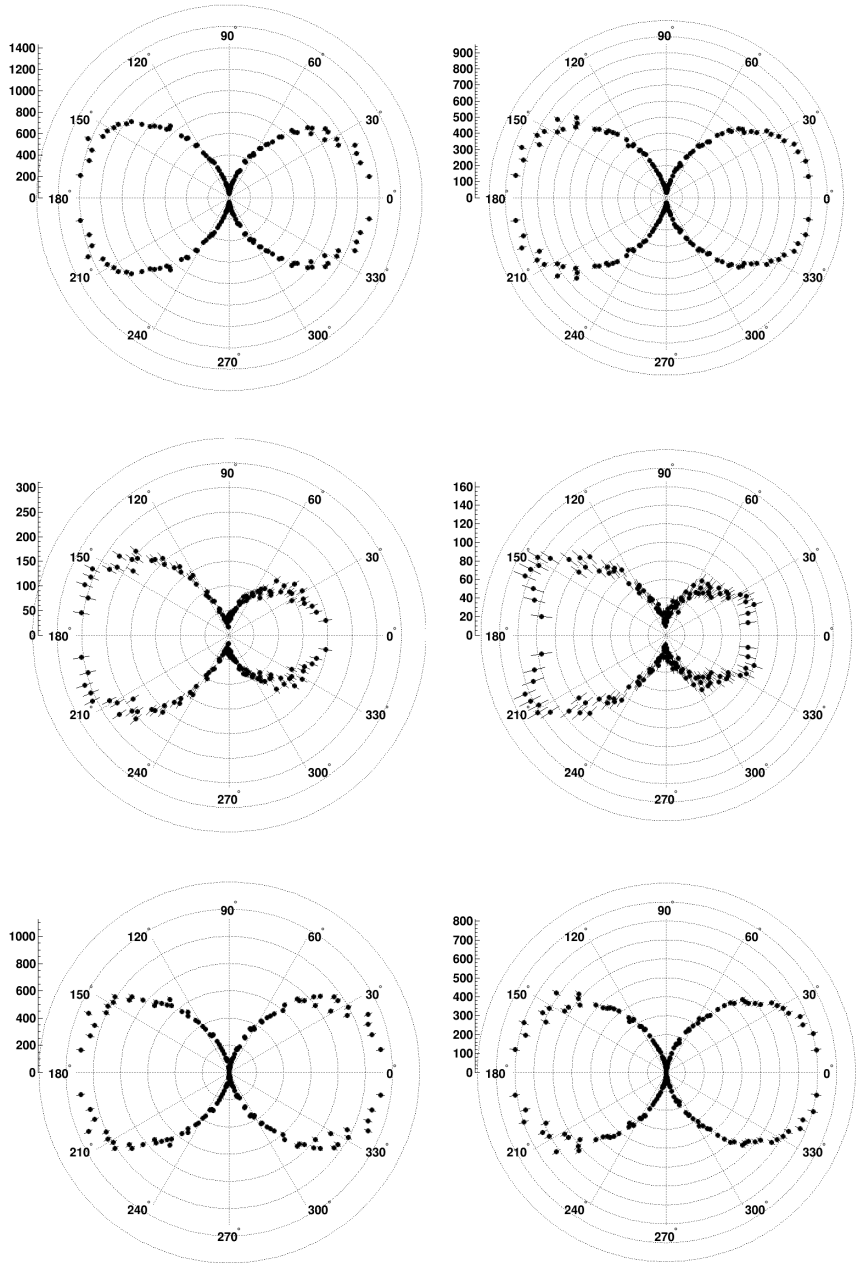

Figure 6.6: Spectra for $\nu = 10$, recoil relative to polarization. Top laser, middle background, bottom background subtracted. Left data set f: long delay. Right data set e: time overlapped.

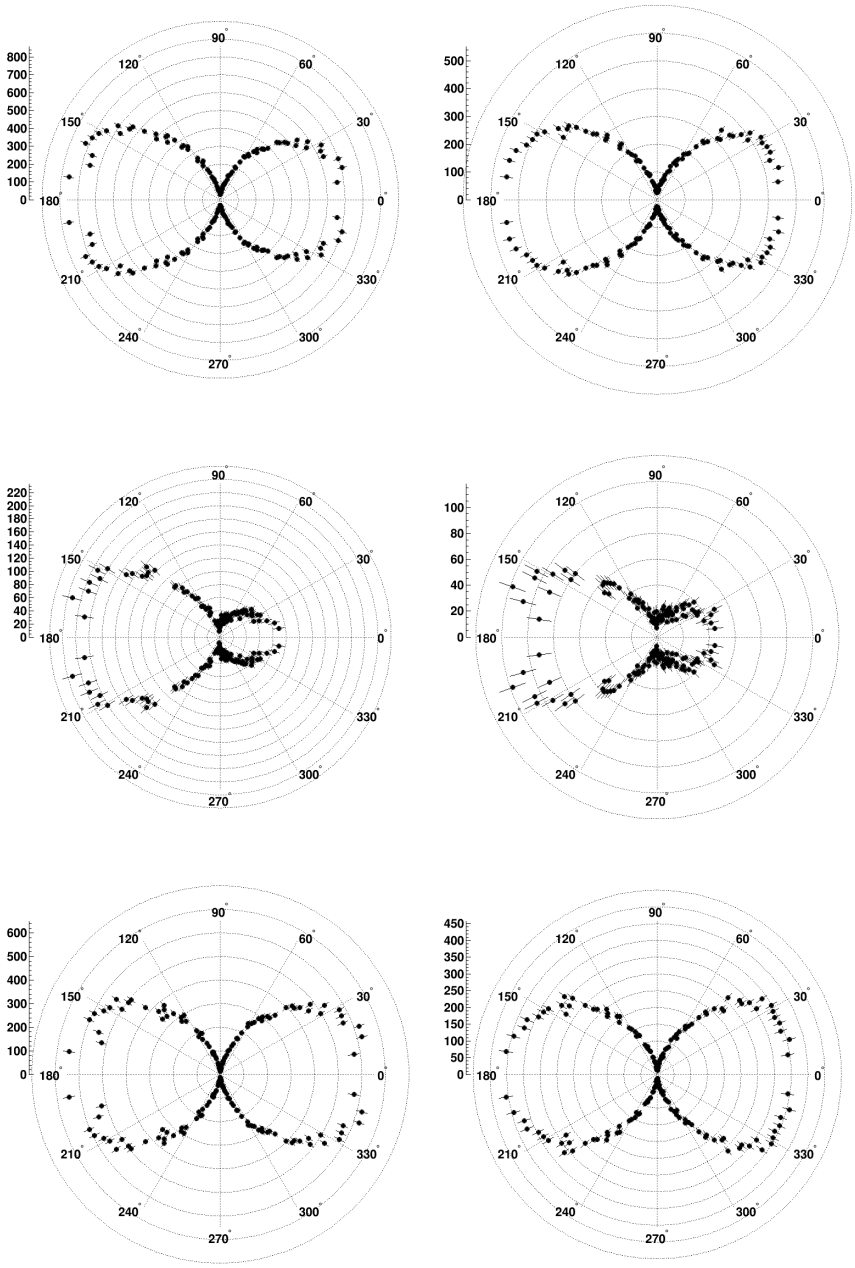

Figure 6.7: Spectra for $\nu = 11$, recoil relative to polarization. Top laser, middle background, bottom background subtracted. Left data set f: long delay. Right data set e: time overlapped.

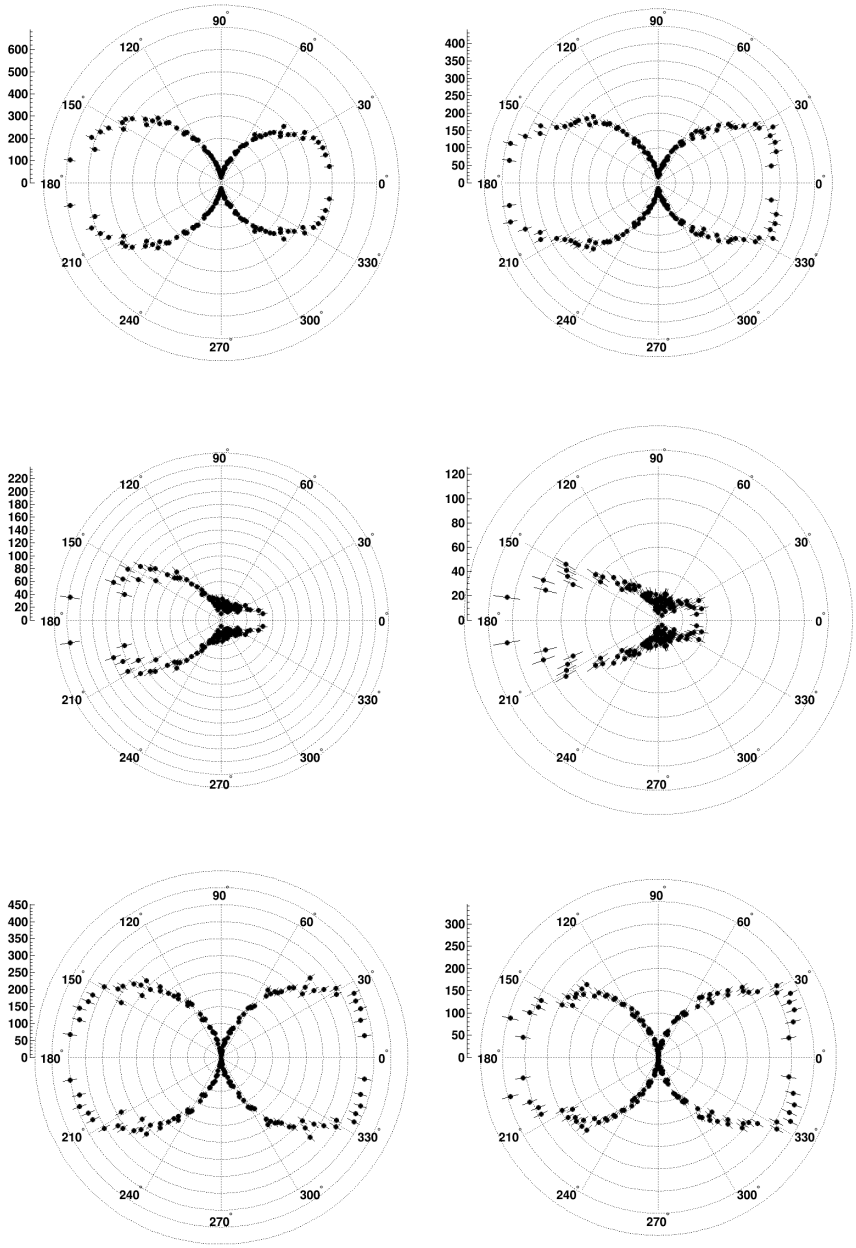

Figure 6.8: Spectra for $\nu = 12$, recoil relative to polarization. Top laser, middle background, bottom background subtracted. Left data set f: long delay. Right data set e: time overlapped.

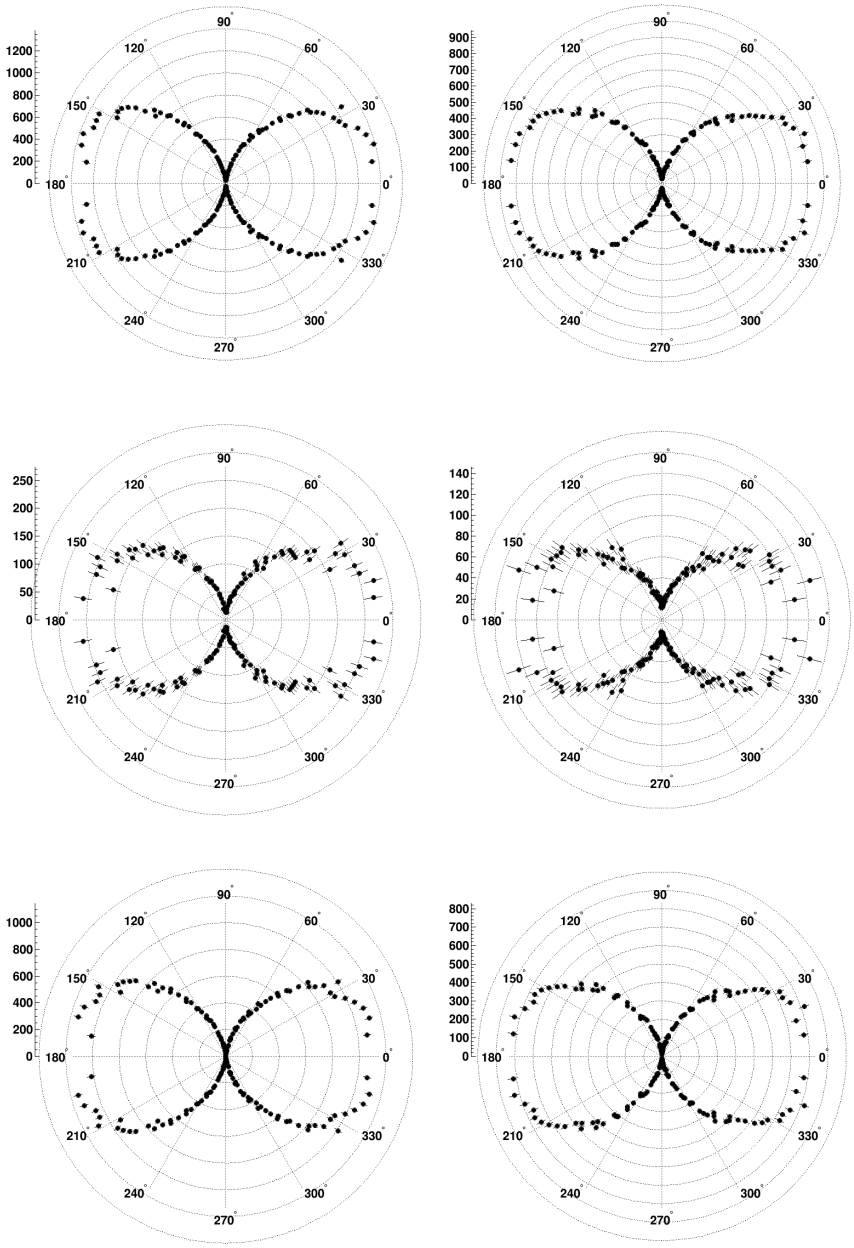

Figure 6.9: Spectra for $\nu = 10$, electron relative to polarization. Top laser, middle background, bottom background subtracted. Left data set f: long delay. Right data set e: time overlapped.

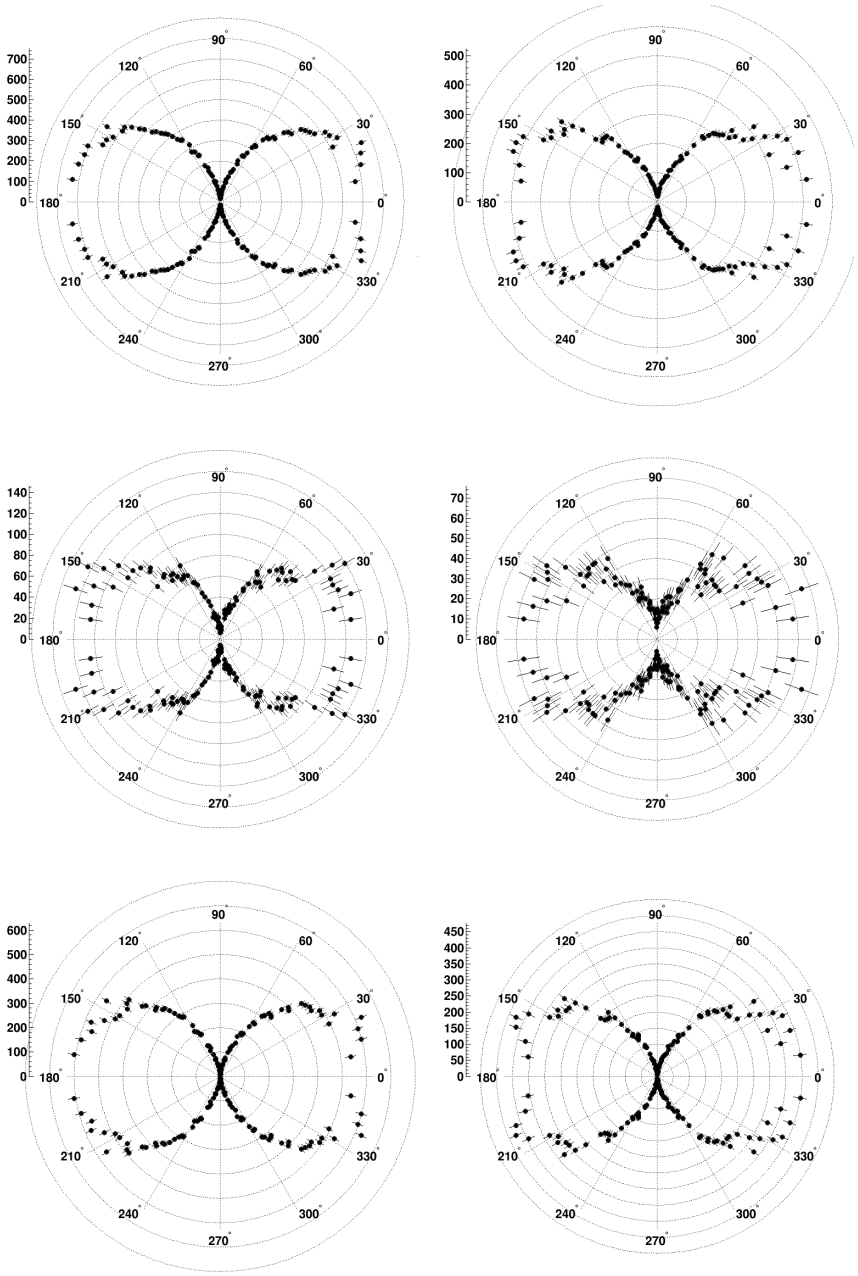

Figure 6.10: Spectra for $\nu = 11$, electron relative to polarization. Top laser, middle background, bottom background subtracted. Left data set f: long delay. Right data set e: time overlapped.

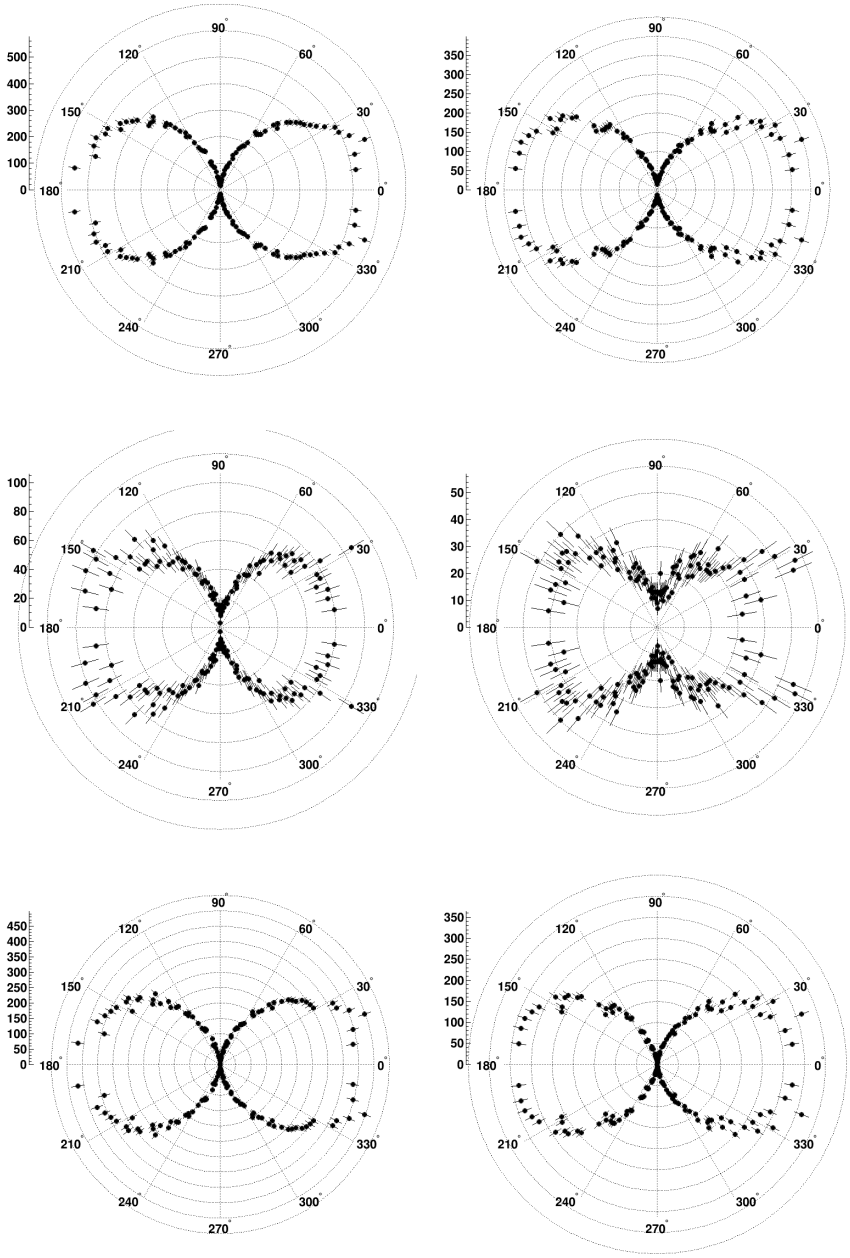

Figure 6.11: Spectra for $\nu = 12$, electron relative to polarization. Top laser, middle background, bottom background subtracted. Left data set f: long delay. Right data set e: time overlapped.

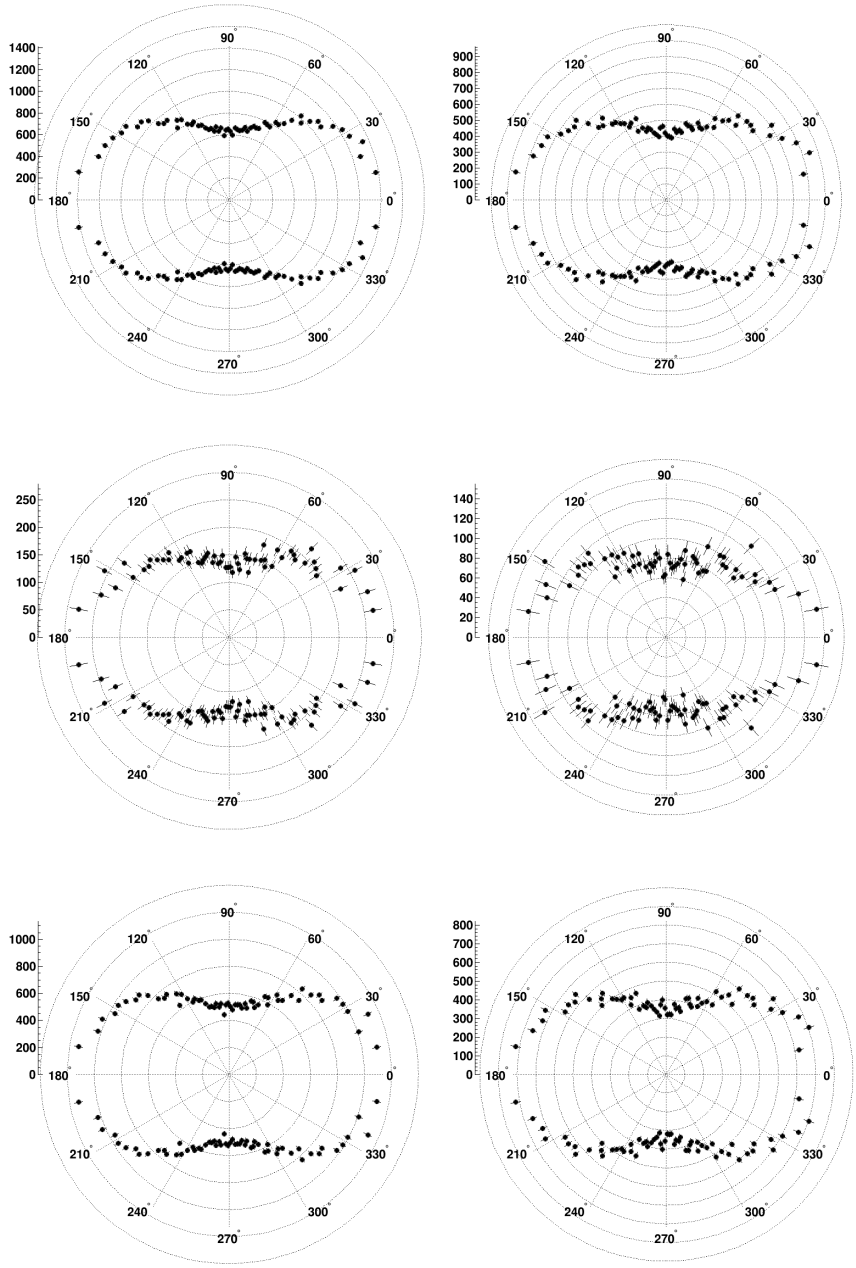

Figure 6.12: Spectra for $\nu = 10$, electron relative to recoil. Top laser, middle background, bottom background subtracted. Left data set f: long delay. Right data set e: time overlapped.

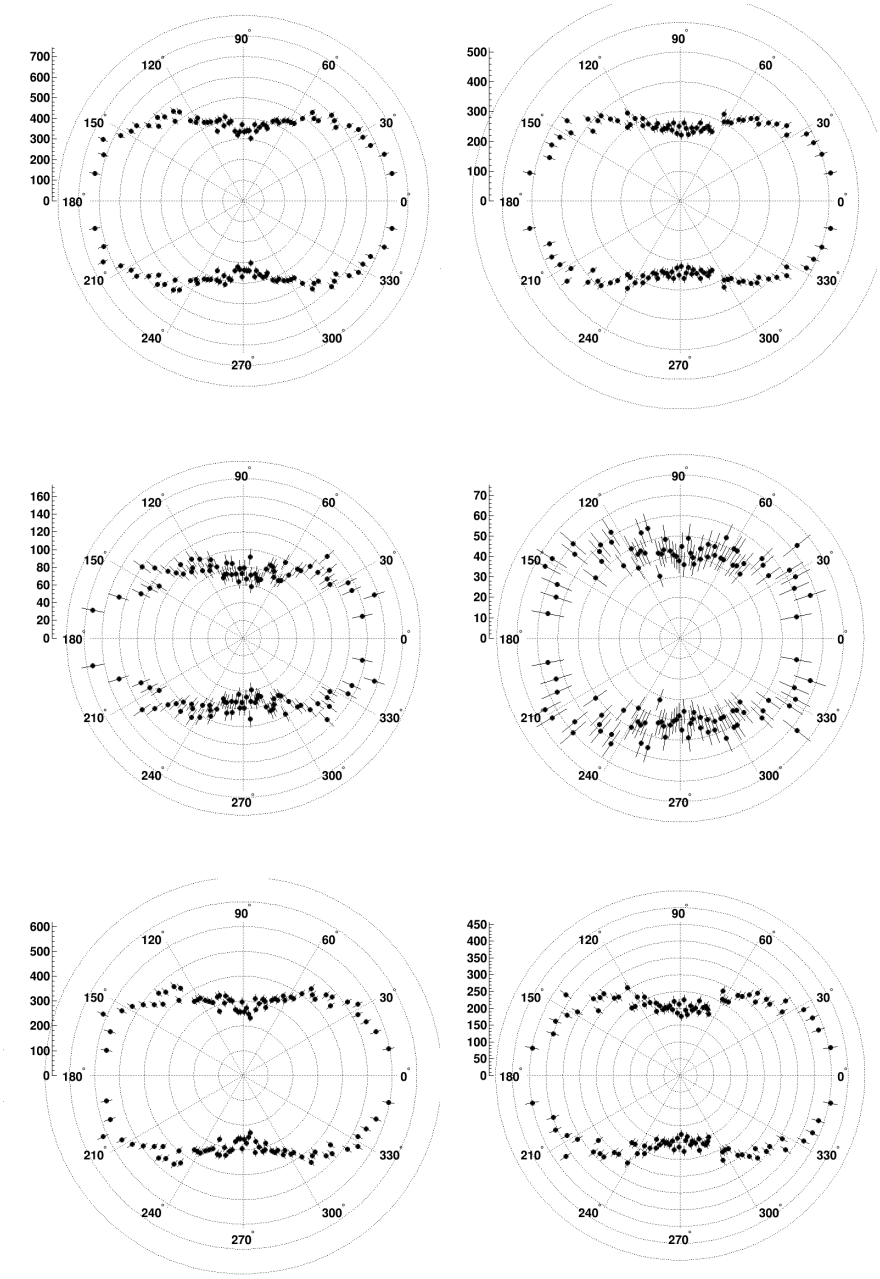

Figure 6.13: Spectra for $\nu = 11$, electron relative to recoil. Top laser, middle background, bottom background subtracted. Left data set f: long delay. Right data set e: time overlapped.

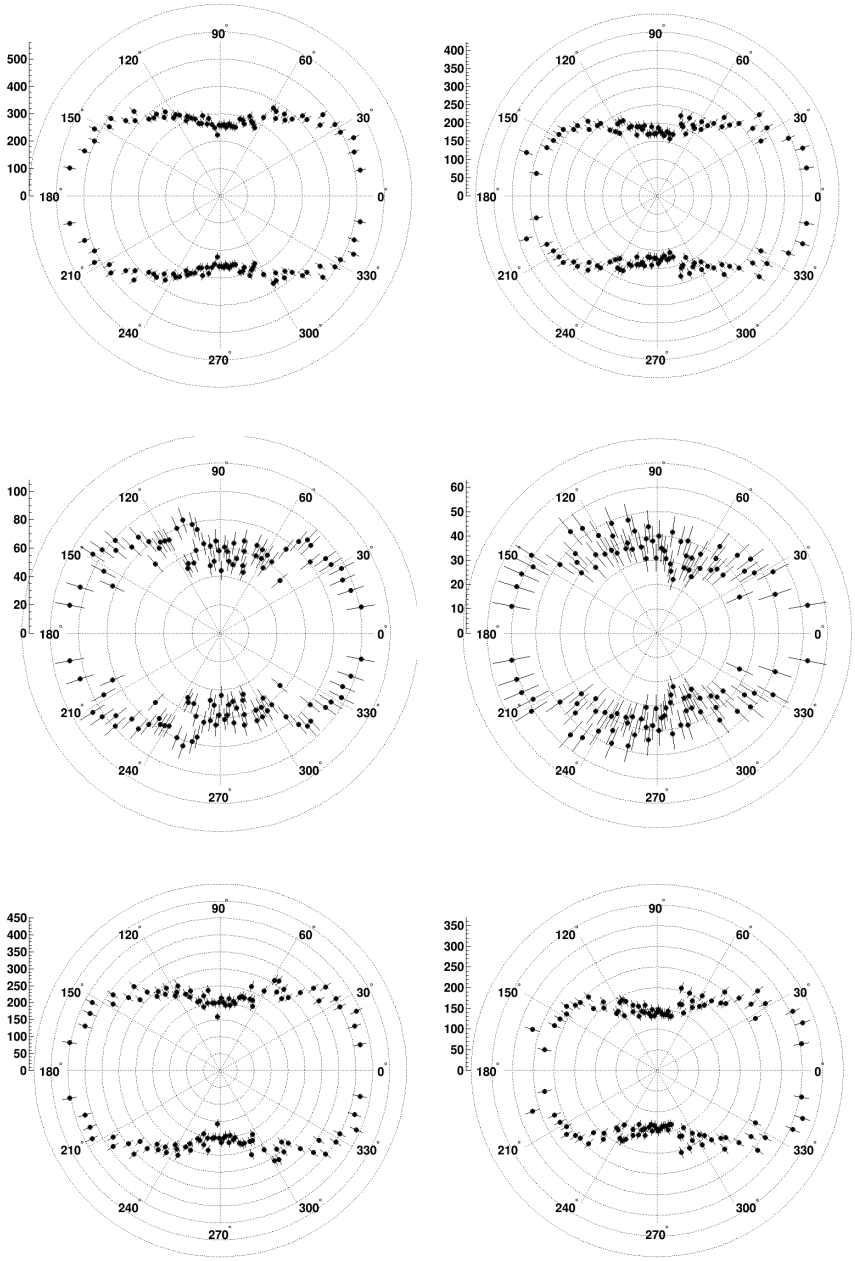

Figure 6.14: Spectra for $\nu = 12$, electron relative to recoil. Top laser, middle background, bottom background subtracted. Left data set f: long delay. Right data set e: time overlapped.

Chapter 7

Conclusion

In the preceding pages we have presented a two color synchrotron-laser COLTRIMS experiment including a detailed report on the construction and operation of the device. As a proof of principle experiment, we investigated photoionization of H_2 in the presence of a strong laser field. We elaborated on the two possible configurations of the light pulses: synchronous and delayed, and made estimates for the asymmetry effects we were able to resolve. We were able to observe a ponderomotive shift in the photoelectron energies. We observed no evidence of LICI interference fringes. Ultimately, we did not observe any asymmetry from the retro-action of the photoelectron onto the parent cation, or any long lived asymmetry in the H_2^+ cation. However, we did see hints of structural changes though these were obscured by systematic errors.

In closing we must report on our failed two color experiments. First, an attempt was made to lower the photon energy to just below the dissociation threshold of H_2 with the hopes that the slower photoelectrons would create a more readily observable retro-action effect. Unfortunately, the spectrometer fields were not set correctly and the jet dots and signal reflections obscure the brightest parts of the distribution as shown in figure 7.1. In a similar manner, we were unable to collect any D_2 data because it was overlain by background from residual H_2.

We also report failed attempts to observe any two color signal in the photoionization of O_2 at $18.24eV$ and CO_2 at both $19.2eV$ and $18.44eV$. The idea for these experiments was identical to that in H_2: use the ALS to ionize to a bound vibrational level of the cation and use the laser to drive dissociation. The fact that we did not observe a signal is interesting in that both molecules must have survived the full intensity of the field. Perhaps there was no

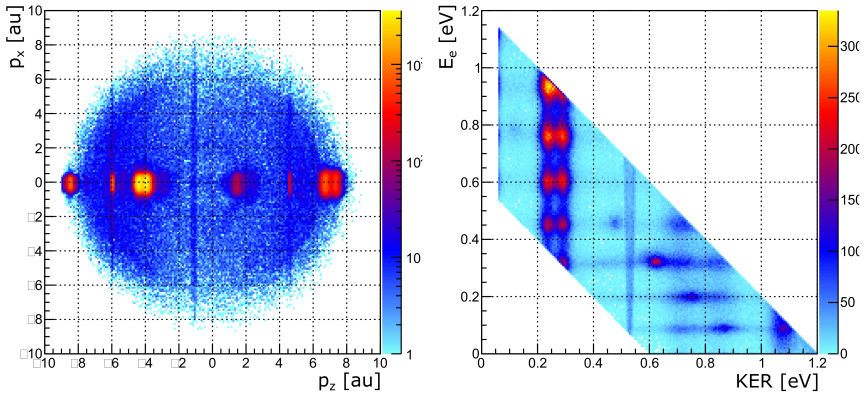

Figure 7.1: June 2017 H_2 data at $17.9eV$ XUV photon energy. Left: momentum projection showing bright jet dots obscuring the distribution. Right: energy map showing contamination.

dissociative state that could be coupled to the bound state by the laser photon energy. If this is true, given the probability of absorption it is likely spin flips were required for coupling. Or, the fact that there are multiple bonding orbitals for each molecule may indicate that multiple photons must be absorbed to drive a dissociation. We strongly suggest that a theorist be recruited to calculate transition probabilities between states of potential target cations.

While H_2 afforded a readily observable 2 color signal in a molecule it was a difficult first experiment. High statistics are required for background subtraction and observation of LICI interference fringes and retro-action. The statistics collected are, in fact, quite impressive. We have shown that it is possible to extract 2-color signals for channels that comprise only 1.7% of the total single ionization rate. This is comparable to some single photon doubleionization rates in various small molecules. Additionally, we are not exploiting the full power of COLTRIMS with only two particle coincidences. In retro-respect, a study of bound dications would perhaps have been more successful. The synchrotron tuneability and four particle coincidence determine exactly the initial and final states of the molecule, and it is possible to observe multiple fragmentation channels for more complicated molecules such as O_2^{2+}, N_2^{2+} and CO_2^{2+}. A bound dication is more inherently unstable than a cation, and

the separation between bound and dissociative curves is larger - perhaps more susceptible to coupling with a $1.2eV$ photon.

So far we have not exploited the strong field for any type of alignment. Our difference measurements have proven more than capable of yielding enough statistics to support alignment dependent photoelectron investigations of cation dissociation channels. We can more fully exploit the statistics by systematically rotating the polarization of the laser relative to the XUV, thereby exploring different photoionization alignments and dissociations. An ideal candidate for such an experiment is H_2O. It is both polar and contains two hydrogen bonds. On a most basic level, we have demonstrated that we can break hydrogen bonds with the laser. If nothing else, the author would like to stress that water affords the best scientific target for any future two-color beamtime.

Moving forward, a necessary upgrade is the installation of an OPA on the laser to provide tunable light. We have demonstrated more than adequate intensity to drive dissociation and therefore we can afford to trade some intensity for tuneability. The ability to tune wavelength would open the door to optimization of the strong field to resonantly transition between states of pumped (di)cations. In N_2 there exist long lived molecular auto-ionizations that may serve as good targets and a variety of small molecules have such states. Henceforth, we can open the door to state selective photoionization of cations above the double ionization limit.

In conclusion, there is a clear roadmap for future experiments and a great deal of physics to be studied. Taken together the future of the LASER-COLTRIMS machine looks bright.

Bibliography

[1] John Hemminger. *Directing Matter and Energy: Five Challenges for Science and the Imagination*. U.S. Department of Energy, 2007.

[2] Stephen R. Leone et al. "What will it take to observe processes in 'real time'?" In: *Nature Photonics* 8 (2014), pp. 162–166.

[3] P O'keeffe et al. "A photoelectron velocity map imaging spectrometer for experiments combining synchrotron and laser radiations". In: *Review of Scientific Instruments* 82.3 (2011), p. 033109.

[4] K Mitsuke, Y Hikosaka, and K Iwasaki. "Laser photoionization of polarized Ar atoms produced by excitation with synchrotron radiation". In: *Journal of Physics B: Atomic, Molecular and Optical Physics* 33.3 (2000), p. 391.

[5] DL Ederer et al. "Laser-synchrotron hybrid experiments A photon to tickle-A photon to poke". In: *Nuclear Instruments and Methods in Physics Research Section A: Accelerators, Spectrometers, Detectors and Associated Equipment* 319.1-3 (1992), pp. 250–256.

[6] FJ Wuilleumier and M Meyer. "Pump–probe experiments in atoms involving laser and synchrotron radiation: an overview". In: *Journal of Physics B: Atomic, Molecular and Optical Physics* 39.23 (2006), R425.

[7] R. Dörner et al. "Cold Target Recoil Ion Momentum Spectroscopy: a 'momentum microscope' to view atomic collision dynamics". In: *Physics Reports* 330.2 (2000), pp. 95–192. ISSN: 0370-1573. DOI: https://doi.org/10.1016/S0370-1573(99)00109-X. URL: http://www.sciencedirect.com/science/article/pii/S037015739900109X.

[8] T. Jahnke et al. "Multicoincidence studies of photo and Auger electrons from fixed-in-space molecules using the COLTRIMS technique". In: *Journal of Electron Spectroscopy and Related Phenomena* 141.2 (2004). Frontiers of Coincidence Experiments, pp. 229–238. ISSN: 0368-2048. DOI: https://doi.org/10.1016/j.elspec.2004.06.010. URL: http://www.sciencedirect.com/science/article/pii/S0368204804003408.

[9] Joachim Ullrich et al. "Recoil-ion and electron momentum spectroscopy: reaction-microscopes". In: *Reports on Progress in Physics* 66.9 (2003), p. 1463.

[10] F Trinter et al. "Evolution of interatomic Coulombic decay in the time domain". In: *Physical review letters* 111.9 (2013), p. 093401.

[11] B. Gaire et al. "Bond-rearrangement and ionization mechanisms in the photo-double-ionization of simple hydrocarbons (C_2H_4, C_2H_3F, and $1,1-C_2H_2F_2$) near and above threshold". In: *Phys. Rev. A* 94 (3 Sept. 2016), p. 033412. DOI: 10.1103/PhysRevA.94.033412. URL: https://link.aps.org/doi/10.1103/PhysRevA.94.033412.

[12] Dominique Akoury et al. "The simplest double slit: interference and entanglement in double photoionization of H2". In: *Science* 318.5852 (2007), pp. 949–952.

[13] F Martın et al. "Single photon-induced symmetry breaking of H2 dissociation". In: *Science* 315.5812 (2007), pp. 629–633.

[14] MS Schöffler et al. "Ultrafast probing of core hole localization in N2". In: *Science* 320.5878 (2008), pp. 920–923.

[15] M Gisselbrecht et al. "Photodouble ionization dynamics for fixed-in-space h 2". In: *Physical review letters* 96.15 (2006), p. 153002.

[16] Th Weber et al. "Fully Differential Cross Sections for Photo-Double-Ionization of D 2 _". In: *Physical review letters* 92.16 (2004), p. 163001.

[17] Thorsten Weber et al. "Complete photo-fragmentation of the deuterium molecule". In: *Nature* 431.7007 (2004), pp. 437–440.

[18] M Waitz et al. "Electron Localization in Dissociating H 2+ by Retroaction of a Photoelectron onto Its Source". In: *Physical review letters* 116.4 (2016), p. 043001.

[19] K. Sändig, H. Figger, and T. W. Hänsch. "Dissociation Dynamics of H_2^+ in Intense Laser Fields: Investigation of Photofragments from Single Vibrational Levels". In: *Phys. Rev. Lett.* 85 (23 Dec. 2000), pp. 4876–4879. DOI: 10.1103/PhysRevLett.85.4876. URL: https://link.aps.org/doi/10.1103/PhysRevLett.85.4876.

[20] Wei Cao et al. "Identification of a Previously Unobserved Dissociative Ionization Pathway in Time-Resolved Photospectroscopy of the Deuterium Molecule". In: *Phys. Rev. Lett.* 114 (11 Mar. 2015), p. 113001. DOI: 10.1103/PhysRevLett.114.113001. URL: https://link.aps.org/doi/10.1103/PhysRevLett.114.113001.

[21] K. P. Singh et al. "Control of Electron Localization in Deuterium Molecular Ions using an Attosecond Pulse Train and a Many-Cycle Infrared Pulse". In: *Phys. Rev. Lett.* 104 (2 Jan. 2010), p. 023001. DOI: 10.1103/PhysRevLett.104.023001. URL: https://link.aps.org/doi/10.1103/PhysRevLett.104.023001.

[22] M. F. Kling et al. "Control of Electron Localization in Molecular Dissociation". In: *Science* 312.5771 (2006), pp. 246–248. ISSN: 0036-8075. DOI: 10.1126/science.1126259. eprint: http://science.sciencemag.org/content/312/5771/246.full.pdf. URL: http://science.sciencemag.org/content/312/5771/246.

[23] J Wu et al. "Understanding the role of phase in chemical bond breaking with coincidence angular streaking". In: *Nature communications* 4 (2013), p. 2177.

[24] D Ray et al. "Ion-energy dependence of asymmetric dissociation of D 2 by a two-color laser field". In: *Physical review letters* 103.22 (2009), p. 223201.

[25] M Waitz et al. "Two-particle interference of electron pairs on a molecular level". In: *Physical review letters* 117.8 (2016), p. 083002.

[26] D. Dowek et al. "Circular Dichroism in Photoionization of H_2". In: *Phys. Rev. Lett.* 104 (23 June 2010), p. 233003. DOI: 10.1103/PhysRevLett.104.233003. URL: https://link.aps.org/doi/10.1103/PhysRevLett.104.233003.

[27] Vladislav V. Serov and A. S. Kheifets. "$p - H$ symmetry breaking in dissociative photoionization of H_2 due to the molecular ion interacting with the ejected electron". In: *Phys. Rev. A* 89 (3 Mar. 2014), p. 031402. DOI: 10.1103/PhysRevA.89.031402. URL: https://link.aps.org/doi/10.1103/PhysRevA.89.031402.

[28] Gábor J Halász et al. "Effect of light-induced conical intersection on the photodissociation dynamics of the D2+ Molecule". In: *The Journal of Physical Chemistry A* 117.36 (2013), pp. 8528–8535.

[29] Annick Giusti-Suzor et al. "Dynamics of H2+ in intense laser fields". In: *Journal of Physics B: Atomic, Molecular and Optical Physics* 28.3 (1995), p. 309.

[30] Eric E. Aubanel, Jean-Marc Gauthier, and André D. Bandrauk. "Molecular stabilization and angular distribution in photodissociation of H_2^+ in intense laser fields". In: *Phys. Rev. A* 48 (3 Sept. 1993), pp. 2145–2152. DOI: 10.1103/PhysRevA.48.2145. URL: https://link.aps.org/doi/10.1103/PhysRevA.48.2145.

[31] D M Bishop and L M Cheung. "Moment functions (including static dipole polarisabilities) and radiative corrections for H 2 +". In: *Journal of Physics B: Atomic and Molecular Physics* 11.18 (1978), p. 3133. URL: http://stacks.iop.org/0022-3700/11/i=18/a=010.

[32] P. H. Bucksbaum et al. "Softening of the H_2^+ molecular bond in intense laser fields". In: *Phys. Rev. Lett.* 64 (16 Apr. 1990), pp. 1883–1886. DOI: 10.1103/PhysRevLett.64.1883. URL: https://link.aps.org/doi/10.1103/PhysRevLett.64.1883.

[33] Mathias Uhlmann, Thomas Kunert, and Rüdiger Schmidt. "Molecular alignment of fragmenting $H_2{}^+$ and H_2 in strong laser fields". In: *Phys. Rev. A* 72 (4 Oct. 2005),

p. 045402. DOI: 10.1103/PhysRevA.72.045402. URL: https://link.aps.org/doi/10.1103/PhysRevA.72.045402.

[34] Gábor J Halász, Á Vibók, and Lorenz S Cederbaum. "Direct signature of light-induced conical intersections in diatomics". In: *The journal of physical chemistry letters* 6.3 (2015), pp. 348–354.

[35] Adi Natan et al. "Observation of Quantum Interferences via Light-Induced Conical Intersections in Diatomic Molecules". In: *Phys. Rev. Lett.* 116 (14 Apr. 2016), p. 143004. DOI: 10.1103/PhysRevLett.116.143004. URL: https://link.aps.org/doi/10.1103/PhysRevLett.116.143004.

[36] András Csehi et al. "Towards controlling the dissociation probability by light-induced conical intersections". In: *Faraday discussions* 194 (2016), pp. 479–493.

[37] FP Sturm et al. "Mapping and controlling ultrafast dynamics of highly excited H 2 molecules by VUV-IR pump-probe schemes". In: *Physical Review A* 95.1 (2017), p. 012501.

[38] Andreas Fischer et al. "Electron localization involving doubly excited states in broadband extreme ultraviolet ionization of H 2". In: *Physical review letters* 110.21 (2013), p. 213002.

[39] H Xu et al. "Observing electron localization in a dissociating H2+ molecule in real time". In: *Nature Communications* 8 (2017).

[40] WC Wiley and Ii H McLaren. "Time-of-flight mass spectrometer with improved resolution". In: *Review of Scientific Instruments* 26.12 (1955), pp. 1150–1157.

[41] S Hsieh and JHD Eland. "Charge separation reaction dynamics from pepipico using a position-sensitive detector". In: *Rapid communications in mass spectrometry* 9.13 (1995), pp. 1261–1265.

[42] M Lundqvist et al. "Novel time of flight instrument for Doppler free kinetic energy release spectroscopy". In: *Physical review letters* 75.6 (1995), p. 1058.

[43] P Bolognesi et al. “Photo-double-ionization of the nitrogen molecule”. In: *Physical Review A* 89.5 (2014), p. 053405.

[44] Volker Schmidt. “The power and beauty of (γ, 2e) experiments”. In: *Pramana* 50.6 (1998), pp. 501–514.

[45] George C King and Lorenzo Avaldi. “Double-excitation and double-escape processes studied by photoelectron spectroscopy near threshold”. In: *Journal of Physics B: Atomic, Molecular and Optical Physics* 33.16 (2000), R215.

[46] Takeshi Odagiri et al. “Inner-valence excited and multiply excited states of molecular oxygen around the double-ionization potential as probed by a pair of fluorescence photons”. In: *Journal of Physics B: Atomic, Molecular and Optical Physics* 42.5 (2009), p. 055101.

[47] H. Pauly. *Atom, Molecule, and Cluster Beams II: Cluster Beams, Fast and Slow Beams, Accessory Equipment and Applications*. Springer Series on Atomic, Optical, and Plasma Physics. Springer Berlin Heidelberg, 2013. ISBN: 9783662059029. URL: https://books.google.com/books?id=qrHxCAAAQBAJ.

[48] K. Schmid. “Supersonic Micro-Jets And Their Application to Few-Cycle Laser-Driven Electron Acceleration”. PhD thesis. 2009.

[49] Michael D. Morse. “2. Supersonic Beam Sources”. English. In: *Experimental Methods in the Physical Sciences* 29.PART B (1996), pp. 21–47. ISSN: 1079-4042. DOI: 10.1016/S0076-695X(08)60784-X.

[50] *The RoentDek Constant Fraction Discriminators DFD8c, DFD7x, CFD4c, CFD1c, CFD1x v.11.0.1701.1*. RoentDek Handels GmbH, Sept. 2017. URL: http://roentdek.com/manuals/CFD%5C%20Manual.pdf.

[51] *The RoentDek Constant Fraction Discriminators DFD8c, DFD7x, CFD4c, CFD1c, CFD1x v.11.0.1701.1*. RoentDek Handels GmbH, Sept. 2017. URL: http://roentdek.com/manuals/CFD%5C%20Manual.pdf.

[52] *CoboldPC 2002 User Manual v.6.2.90.2*. RoentDek Handels GmbH, Sept. 2017. URL: http://roentdek.com/manuals/CoboldPC%5C%20UserManual%5C%20(6.2.90.2).pdf.

[53] Kevin Wall. *Mode-Locked Cryo Yb:YAG Laser*. Q-Peak Inc., 2011.

[54] Kevin Wall. *Cryo-Cooled Lasers for Advanced Photoinjectors*. Q-Peak Inc., 2009.

[55] *Fundamentals of Phase Locked Loops MT-086 Tutorial Rev.0*. Analog Devices, Sept. 2017. URL: https://www.analog.com/media/en/training-seminars/tutorials/MT-086.pdf.

[56] Verena Mackowiak. *Noise Equivalent Power*. ThorLabs, Sept. 2017. URL: https://www.thorlabs.com/images/TabImages/Noise%5C_Equivalent%5C_Power%5C_White%5C_Paper.pdf.

[57] Walt Kester. *Converting Oscillator Phase Noise to Time Jitter*. Analog Devices, Sept. 2017. URL: https://www.analog.com/media/en/training-seminars/tutorials/MT-086.pdf.

[58] Russell Wilcox. Mar. 3, 2016.

[59] Adi Natan et al. "Quantum control of photodissociation by manipulation of bond softening". In: *Physical Review A* 86.4 (2012), p. 043418.

[60] W. C. Martin and W. L. Wiese. *Atomic Spectroscopy*. NIST, 1999.

[61] B.H. Bransden and C.J. Joachain. *Physics of Atoms and Molecules*. Pearson Education. Prentice Hall, 2003. ISBN: 9780582356924. URL: https://books.google.com/books?id=ST%5C_DwIGZeTQC.

[62] *Chemical Applications of Group Theory, 3rd Edition*. John Wiley & Sons, Incorporated, 2015. ISBN: 9781119115410. URL: https://books.google.com/books?id=pUj2rQEACAAJ.

Appendices

Appendix A

Basic Theory

A.1 Orbital Configurations

Most of the proceeding discussion is a summary of fundamental concepts from [60] and from [61]. Analytical solutions to the Schrodinger equation are known only for atomic and molecular Hydrogen; all other molecular solutions are approximations built from basis sets of functions that span the function space. The Schrodinger equation for the coulomb potential of a nucleus can be expanded in partial waves in spherical coordinates:

$$\Psi_{nlm} = \sum_{l=0}^{\inf} \sum_{n=-l}^{n=l} R_{nl}(r) Y_{lm}(\theta, \phi), \tag{A.1}$$

where R_{nl} is a Bessel function and Y_{lm} are spherical harmonics. This formulation is most accessible to experiment because the index integers n, l correspond directly to the total energy E_n and total angular momentum L. The Ψ_{nlm} are the familiar grade school "atomic orbitals" and photoionization in its simplest form can be understood as removing an electron from a specific orbital. Electron structure of atoms can be built up from orbitals in the central field approximation that neglects specific electron-electron interaction. When multiple electrons are present inner electrons screen the central potential from outer electrons, electrons repel each other, and the energy becomes dependent on both n and l. Electrons are fermions which must maintain an overall antisymmetric wave function and, therefore, each subshell of the atom can hold at most 2 electrons: one with spin up and one with spin down. Briefly, the notation for atomic shells is as follows; n is specified by a number, l by letters beginning with $s = 0$, and the superscript on s is the number of electrons in the shell. For example the electronic structure of neon is $1s^2 2s^2 2p^6$.

The state of an electron configuration is further specified by the coupling angular momenta with spin between electrons to produce the total orbital angular momenta L, total spin S, and total momenta J. The syntax for distinguishable electrons is $nln'l'^{\,2s+1}L_J$, where capital letters are used for composite momenta and the superscript denotes the number of spin degeneracies: for the single electron this is always 2, a doublet. For example, $2p^2P_{1/2}$. Spin and angular momentum add according to the algebra $(|l-l'|+1), (|l-l'|+2)...(l+l')$. The coupling between spin and orbital angular momentum between electrons produces different configurations of the electronic structure. The most common scheme for coupling equivalent electrons in a shell is to couple the total angular momentum L with the total spin S to get J and is known as Russell Saunders, or LS, coupling. Not all terms produced by the coupling are allowed by the Pauli exclusion principle. Since each filled shell must have zero angular and spin momenta, each unfilled shell can be computed using LS coupling starting from the lowest unfilled shell, progressively coupling shells to produce a final term. Each J and S from each subshell term can be added to produce the final electron configuration term. Alternately, the angular momentum l and spin s for individual electrons can be coupled to produce electron j, which can then be coupled to produce J. This is known as jj coupling - one of many other coupling schemes. Most importantly, the electron configuration carries with it the essential symmetry of the wave function, which is useful for understanding the physics of photoelectron emission even if the underlying orbitals are not exact.

Molecular orbitals are constructed from linear combinations of atomic orbitals. In the case of diatomic molecules, the molecular wave function is specified by the energy and the total angular momentum J projected onto the bond axis between atoms. The notation is analogous to that for atoms, with Greek letters replacing roman letters. For example, for individual electrons s, p, and d orbitals become σ, π, and δ. For diatomic molecules, a special superscript accompanies the term symbol to denote symmetry $(+)$ or antisymmetry $(-)$ with respect to reflection about the plane perpendicular to the nuclear axis. The subscript u and g indicates gerade or ungerade parity. Finally, just as in atoms, the total multiplicity calculated

from the total spin S is written as a prefix superscript. For example, a ${}^2P_{1/2}$ atomic term corresponds to a ${}^2Pi_{1/2}$ molecular term.

It should be noted that in complicated molecules with many atoms, the simple description of bonds between individual atoms within the molecule often fails. More advanced hybrid orbitals are required for an accurate description of electron distributions.

A.2 Molecular Symmetry

In the case of helium, the symmetry was broken by the polarization of the atom by the first photon. In molecules, symmetry is broken by the structure and position of atoms. The following discussion of group theory and its use in formulating molecular orbitals is informed by [62] and [61]. The symmetry of a molecule is described by the point group to which it belongs. A point group is the collection of all symmetry operations that transform the molecule into itself, leaving it unchanged by the operation. Two examples are the trivial identity transformation E that does nothing and the π radian rotation axes of a diatomic molecule that bisects the cord between the two atoms. Briefly, the notation for transformation is as follows. E is the identity. i is inversion of all coordinates through the origin. C_n is a proper rotation axis with rotation angle $2\pi/n$. σ denotes a reflection plane, where the subscripts h for *horizontal* and v for vertical may be applied to represent the plane perpendicular or containing a rotation axis. S_n is an improper rotation which consists of a rotation and reflection through a symmetry plane perpendicular to the rotation. These symmetry elements can be organized into classes. A class has the property that all other symmetry operators transform a class member into other members of the class. Alternately, the symmetry operations of a particular class all behave the same under transformation via other symmetry elements in the group. The symmetry elements are abstract in the sense that they can be implemented with an infinite number of mathematical representations using matrices to represent transformations. There are, however, only a limited number of

representations that cannot be simplified and these are called the irreducible representations. The irreducible representations are still collections of matrices, often with dimension 1.

$D_{\infty h}$	E	$2C_{\infty}^{\phi}$	...	$\infty\sigma_v$	i	$2S_{\infty}^{\phi}$	...	∞C_2		
Σ_g^+	1	1	...	1	1	1	...	1		x^2+y^2, z^2
Σ_g^-	1	1	...	-1	1	1	...	1	R_z	
Π_g	2	$2cos(\phi)$	...	0	2	$-2cos(\phi)$	...	0	(R_x, R_y)	xz, yz
Δ_g	2	$2cos(2\phi)$	...	0	2	$2cos(2\phi)$	...	0		(x^2-y^2, xy)
...	...	...	...	...	...	...	...	...		
Σ_u^+	1	1	...	1	-1	-1	...	-1	z	
Σ_u^-	1	1	...	-1	-1	-1	...	1		
Π_u	2	$2cos(\phi)$	...	0	-2	$2cos(\phi)$	...	0	x, y	
Δ_u	2	$2cos(2\phi)$	...	0	-2	$-2cos(2\phi)$	...	0		
...	...	...	...	...	...	...	...	...		

Table A.1: Character table for homonuclear diatomic point group $D_{\infty h}$. Left column, molecular orbital corresponding to the group representation listed in the row. Top row, symmetry elements by class. Third column: coordinates for basis sets. Fourth column: coordinates for products of fundamental coordinates.

A number of important properties can be derived from consideration of the trace, or character, of each matrix for each representation. This information is listed for each representation in a character table, a full explanation of which can be found in [62]. The character table of the symmetry point group of homonuclear diatomic molecules, $D_{\infty h}$, taken from [62] appears in table A.1. Importantly, it can be shown that combinations of atomic orbitals form a basis set for representations. This is why, in the left hand table A.1, the molecular orbitals for homonuclear diatomics are listed. The character of each matrix corresponding to the class of operators list at the top of the column comprises the body of the table. The single coordinates and rotations which form the bases sets for the representation in a row are shown in the third region. The fourth region contains similar coordinates and rotations but for products of the coordinates.

Symmetry dramatically simplifies the construction of molecular orbitals from linear combination of atomic orbitals through the scheme of symmetry adapted linear combination of atomic orbitals. The essential process is to find atomic orbitals that form basis sets for

a particular symmetry of the molecule, and then to use these to construct the basis sets for the molecular orbitals. This program guarantees that the basic molecular orbitals obey the symmetry of the molecule.

Appendix B

Detector Modeling & Rate Estimation

In this appendix, I will attempt to answer the question: "what processes can we resolve in a reaction microscope?". Each element of a spectrometer adds its own peculiar background signal and taken together, these background signals further limit the ideal resolution determined by the intrinsic properties of the MCP detectors and fields. In large part, a successful experiment rests on the ability to separate the desired experimental signal from the background noise in some phase space of the experimental parameters. For example, in photo-double ionization producing two ions, the coincidence can be exploited to both remove background and to select the desired breakup channel up to a point. Unfortunately, double ionization is by rule of thumb only one percent of the total ionization cross section: meaning there is a trade-off between accepting a lower overall rate in order to invoke a powerful data segregator. This kind of compromise must be considered in the search for experimental targets.

Given the limiting resource is beamtime, rate estimations determine the science we can hope to resolve and factor heavily into allocating beamtime during a data run. The number of untested parameters factoring into the rate estimates were a major concern for the LASER-COLTIRMS implementation. We use rules of thumb to give a best guess for what would be observable but admit that these estimates might be an order of magnitude off in either direction. Due to already borderline feasability, a break in the wrong direction could put targets beyond reach: the target would be too beamtime intensive to be practical or even possible. With the limited ability to conduct full analysis on the fly, we might waste significant beamtime on doomed experiments.

One can approach this problem multiple ways by choosing different mathematical models for the probability. In a simple rate experiment where the probability for an event to occur is proportional to the time interval of measurement (the rate is constant), for a large enough number of trials this becomes the poisson distribution. If I were to assume a poisson distribution in the spectrometer, I would treate the atoms illuminated by the light pulses (x-ray, laser) each as the seperate "trials" with some reaction probability that gives a stable rate. I would have to pretend that the x-ray and laser beams were completely continuous and that the detection of the events was "instantaneous". Most importantly, I would have to assume that the detection of signals from one event could not be confused with those of another. The current state of the art in COLTRIMS is to make these bold claims without support and assume the poisson distribution: the experimental error in any histogram bin is then given as the square root of the number of entries in the bin.

There are serious problems with the above assumptions. The light arrives in short pulses (shots) seperated by a period of time, so talk a rate per unit time is nonsensical and the appropriate metric is probability per shot. The spectrometer collects signals over a time window that spans multiple shots, so multiple events often occur in the same window of measurement and their signals can be confused. This is further exacerbated by the nescessity to pair ions and electrons in coincidence; there are many more electrons than there are ions. The measurement window is triggered on the positive collection of either ions or electrons (here I will work with data sets triggered by ions), implying that the spectrometer collects incomplete information on the probability per shot. We are left to deduce the probability per shot from the boxcar integrators run during the experiment and (see the next section) from the shape of the distributions of ions and electrons in the measurement window.

Together, the experimental reality indicates that the appropriate distribution to use in modeling the generation of events on a shot per shot basis is the normal distribution. It is helpful at this point to divide the measurement into four seperate levels of "event" production in the spectrometer. The first and most basic level are events that produce charged particles

(photo-ionization, -dissociation, ablation, backscatter etc.). Lets call these events reactions (photon-molecule reactions, ablation). These must follow the poisson distribution when integrated over the whole delivered photon and particle flux of the entire experiment: each is highly dependent on random processes. While these signals are interesting to pin down, they don't play directly into the computation of the errors because they are inferred and never absolutely measured. Rather, at the second level, each "event" is the detection of the individual particles at each detector. Lets call these "events" collections. Collections capture in a limited way all the processes in the spectrometer that produce ions and electrons. At the third level, the "event" is combination of all the collections during the triggered time window. Let's call these TDC events - the basic building block of COLTRIMS analysis delivered in list mode file from the time to data (TDC) data acquisition card. These events correspond to at most several tens of shots, meaning that the appropriate distribution for collections held in these events is the binomial distribution. Finally, at the fourth level, the TDC events are collected in aggregate, sorted, analysed, and binned into histograms for analysis. At the analysis level, the large number of events turns the binomial distribution into the normal distribution.

The errors at the fourth level determine what can be resolved by the experiment. Ultimately the type of error we are looking for is the erroneous coincidence of ions and electrons.

I will proceed with a more rigorous statistical analysis of the rate estimation using data from our first successful LASER-COLTIRMS experiment. The first goal is to compute the experimental signal strength needed to overcome the random fluctuations in the background. A second goal is to determine the level of statistics needed for background subtraction. The following two chapters, "Online Analysis" and "Signal Processing" cover the next two stages of data capture. In section B.1 a model of the spectrometer to determine self consistent rates and probabilities for observed distributions of ions and electrons. The primary background data signals and their effects will be considered. The model will then be used to determine signal capture from a second laser photon pulse.

B.1 A Model

In this section a self consistent model of a spectrometer will be constructed from the ground up. I begin by considering only single ionization events in a nearly background free spectrometer and then build upon this model by adding successive layers of noise.

B.1.1 Ion Detector

Each light shot from the ALS has some probability p of reacting with a molecule. Since each shot is independent, the distribution of interactions (n successes) over a number of shots (N trials) follows the binomial distribution:

$$P[X = n] = \begin{pmatrix} N \\ n \end{pmatrix} p^n (1-p)^{N-n}, \tag{B.1}$$

where X is the random variable describing the distribution of successes. In the ususal case the photon singly ionizes the molecule, though it should be mentioned that neutral photodissociation, radiative decay, and double ionization are possible. The interaction probability can be computed using the ratio of 1 hit to 2 hits on the ion detector taking care that the dominant signal is from single ionization. I will use the August 2016 H2 and He LASER-COLTRIMS data sets for figures and numbers but this analysis is equally valid for all data sets with this spectrometer construction. In these sets, the photon energy was $18.56eV$ and $23.795eV$ respectively, both energies too low to cause double ionization in the target jet or any background gases. The effects of higher harmonics and the MCP deadtime are neglected here but considered later. For the H2 data set, the ion rate meter registered approximately $5kHz$. Given the bunch spacing of $\Delta t = 328ns \Rightarrow 3.049MHz$ the expected probability is $5kHz/3.049MHz = 1/609.8$. This is a naive conclusion though, as the ions must first travel through a mesh with open area of 0.8 and then be collected by the MCP at an efficiency of 0.5, with a total collection efficiency of $c = 0.5 * 0.8 = 0.4$. Adjusting for the colleciton

efficiency $p = 1/(609.8 * 0.4) = 1/243.9$, or roughly 1 of every 244 ALS shots interacts with a molecule. This may come as a surprise to some, as the rule of thumb for coincidence experiments is an interaction probability at least greater than 1000. The general form for the probability given the preceding variables is

$$p = \frac{R\ \Delta t}{c}. \tag{B.2}$$

The probability of two interactions in a single shot is simply $P_2 = P_1^2$ and the ratio of the single interactions to the double interactions is P_1. This makes the double interaction comparable to about one third the higher harmonic signal which is approximately 1/100 of the fundamental harmonic in intensity. Double ionization processes are 1/100 the probability and therefore the probability of simultaneous double ionization is $(1/10,000)\ p$. However, if we consider a strong secondary laser pulse designed to saturate the absoprtion of a second photon then simultaneous excitation and single ionization may produce a confounding signal. The simultaneous signal will be analyzed in section B.2.

The probability, $P_{seperate}$, given the first success, of a second success after k attempts is given by the probability that a sequence of $k-1$ failures will occur before a success:

$$P_{seperate}[k] = p(1-p)^{k-1}. \tag{B.3}$$

This is just the geometric probability distribution and the integrated probability must be

$$P_{seperate}[\Delta n] = \sum_{k=1}^{\infty} p(1-p)^{k-1} = \frac{p}{1-(1-p)} = 1. \tag{B.4}$$

The average spacing between events is then expectation value for k

$$E_{seperate}[k] = \sum_{k=1}^{\infty} k\ p(1-p)^{k-1} = \frac{1}{p}. \tag{B.5}$$

The standard deviation of this spacing is

$$\sigma = \sqrt{\frac{1-p}{p^2}} = 243.5 \ . \tag{B.6}$$

Clearly, the standard deviation is large enough that events will occur within the same TDC time window frequently: one would expect the cumulative probability for a 30 trial window to be $p = .12$. However, this is an incorrect way to calculate the expected number of events with two single ionizations because it involves choosing the start of the geometric sequence at a particular point. The correct way is to assume the binomial distribution and count the number of states in the phase space. I will now proceed along these lines.

In the H2 data set, the ratio $A_{1,2}$ of single S_1 to double S_2 ionization events with an MCP signal is $A_{1,2} = S_1/S_2 = 48.42$. Requiring the MCP signal removes signal reflections which can contribute substantially to the apparent count rate; signal reflections are covered in the next chapter. The data was collected with an ion time window of $10\mu s$, corresponding to $N = 10\mu s/328ns = 30$. To compute the ratio of single to double hits, consider that the probability of a single hit in $N = 30$ trials is

$$P[X = 1] = \left(\begin{array}{c} N = 30 \\ \\ 1 \end{array} \right) p(1-p)^{N-1} = N \ p(1-p)^{N-1}. \tag{B.7}$$

However, because the TDC data acquisition is triggered on the ions for this data set the ion is constrained to the trial in the middle of the time window (as determined by the forward and reverse data capture windows of the TDC settings), reducing the probability by 30:

$$P[X \Rightarrow \text{time zero shot}] = p(1-p)^{N-1} = p(1-p)^{29}. \tag{B.8}$$

By similar logic, if there is a second hit in the window the probability is

$$P[X=2] = \frac{1}{N}\begin{pmatrix} N=30 \\ n=2 \end{pmatrix} p(1-p)^{29} = \frac{N!}{N*n!(N-n)!}\ p^2(1-p)^{N-2} \tag{B.9}$$

$$P[X=2] = \frac{30!}{30*2!(30-2)!}\ p^2(1-p)^{28} = \frac{29}{2}p^2(1-p)^{28} \tag{B.10}$$

and the ratio is

$$A_{1,2} = \frac{2\ p(1-p)^{29}}{c\ 29\ p^2(1-p)^{28}} = \frac{2\ (1-p)}{29\ p}, \tag{B.11}$$

where a factor of c appears in connection with the collection of the second ion. More generally

$$A_{1,2} = \frac{2\ (1-p)}{c\ (N-1)\ p}. \tag{B.12}$$

In the preceding argument, I have considered only the "first order" terms, in that I have neglected the possibility of, for example, the contribution of two photoionizations where the second ion is not captured. The complete term carries every possible combination of photoionizations and collections:

$$A_{1,2} = \frac{\sum_{k=0}^{\infty}(1-c)^k\ P[X=k+1]}{\sum_{k=0}^{\infty} c\ (1-c)^k\ P[X=k+2]}. \tag{B.13}$$

The values for higher order terms drop off very quickly given the low values for p and c and can be neglected.

Using the probability derived from the ion rate counter, the ratio $1/A_{1,2} = .06$, which is exactly half the value calculated by the geometric distribution. The above equation can be solved in tandem with the probability equation

$$p = \frac{R\ \Delta t}{c}, \tag{B.14}$$

and the experimental ratio $A_{1,2}$ for two of the following variables: the interaction probablity p, ion count rate R, or collection effieciency c. If we assume $c = .4$ then for the H2 data set the computed values are $p = 1/281.85$ and $R = 4327Hz$. These values are in line with the observed rates on the analog box car integrator of the MCP ion signal. The calculated rate R is dependent on the probability in a nonlinear way, but quickly approaches an asymptote. The calculated collection efficiency c is linearly dependent on R and quickly goes above unity as R is increased.

General features of the raw ion detector position data is displayed in fig B.1. The hot "jet" dot at the center of the image is generated by the intersection of the ALS beam with the gas jet and is seperated by the velocity of the jet from a residual "hot" gas line ionized by the travel of the beam through the spectrometer. Various hotspots appear on the detector as unstructured blobs. For the raw data with no gates applied, approximately 67% of the events in fig B.1 are found in the jet dot and 26% in the hot gas stripe, leaving 7% in the underlying carpet. The average carpet rate was estimated for the image using the four grey box areas and found to be 142 counts per square millimeter, which translates to 5% of the total and is in agreement the previous estimate.

In fig B.1 the thin line centered over the jet dot and in line with the hot gas stripe is generated by the tail of the jet distribution. The verticle extension of the jet dot can be explained by the generation of ions on the electron MCP and will be covered in the subsection B.5.

Position verse time plots in the x and y direction, commonly called fish plots, are shown in fig. B.2 and are instrumental in the current endeavor. The recoil x-fish plot shows the jet dot is discretely spaced in time by the bunchspacing of $328ns$. The dots at shorter time of flights are produced when the correct electron for the H2+ ion is not collected and instead is replaced by a second random electron or electron from another single ionization event occuring during the flight time of the ion. The dots that occur later in time are produced when a random electron is collected before the correct electron or when a prior

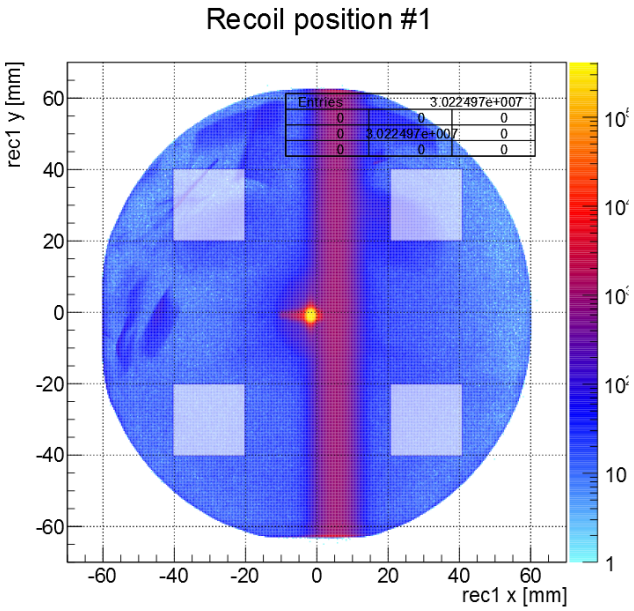

Figure B.1: The raw detector image from the August 2016 H2 data set. No gates are applied. Four quadrants were used to estimate the background ion carpet. The average value was 142 counts per square millimeter.

single ionization event's electron is collected but the ion is not. It is clear from the plots that the early jet dots are more probable than the later jet dots as is expected given the lower collection efficiency of the electrons.

Note that wherever the detector is hot, there exists a stronger background carpet in both position and time created by a higher chance of collecting a random electron. The sharply peaked and discrete nature of the jet dot in time and space facilitates gating it out of momenta spectra in the analysis. Conversely, the hot gas stripe appears to ride on a larger carpet because of it's thermal velocity distribution. The temperature can be estimated from the gaussian full width at half maximum of the hot gas stripe. To first approximation, the width of the stripe as projected onto the detector is the integral of the Maxwell-Boltzman velocity distribution over two spacial dimensions y and z, and is

$$F[x] = \frac{2\sqrt{2\pi}\ e^{\frac{-x^2}{2a^2}}(2a^2 + x^2)}{a}, \tag{B.15}$$

where $a = \sqrt{kT/m}$. I have neglected the velocity dependent broadening of the position distribution because the time distribution is small compared to the total flight time. The general form of the full width half maximum of a gaussian of variable y is $2\sqrt{2\ln 2}\ \sigma = 2.355\ \sigma$, however the equation above deviates from a gaussian for large x. The analytic form of the FWHM from the above equation can be used to find the temperature as follows:

$$FWHM = 2\sqrt{2}\ \sigma\sqrt{-1 - \text{ProductLog}\left(\frac{-1}{2e}\right)} = 3.664\ \sqrt{kT/m}, \tag{B.16}$$

where ProductLog(w) is the first solution to the transcendental equation $z = we^w$ and $\sigma = a$. For the H2 dataset, the width of the hot gas stripe is $7.43mm$ and the flight time is $2613ns$ yielding a FWHM velocity spread of $2843m/s$, which is roughly comparable to the velocity of the jet at $2672m/s$. Intuitively this makes sense because the hot gas is born from the clipped wings of the supersonic jet as it passes through the second stage skimmer: the FWHM as a measure of the velocity is then comparable to the original velocity of the jet. With these values, the temperature is calculated as $145.5K = 12.54meV$ for the August 2016 H2. As a cross check, $12.54meV$ equates to a hot gas stripe with average velocity in the plane of the detector of $5.73mm/tof$, approximating the measured full width half maximum value.

One might expect that this temperature would be equal to the chamber wall temperature. However, this gas has been cooled by rapid expansion in the nozzel and only interacts with the chamber walls a few number of times before being removed by a pump, meaning the gas would not have a chance to warm completely. It should be noted that the gas in the jet reaches a temperature of approximately $80K$ in frame of reference traveling at the jet velocity. The spread in time and space means the hot gas stripe cannot be removed in post analysis and is therefore a major source of error. Fortunately, the consistency of the hot gas stripe means it can be removed by background subtraction in a laser experiment as long as there are enough statistics to reduce the variance of the background.

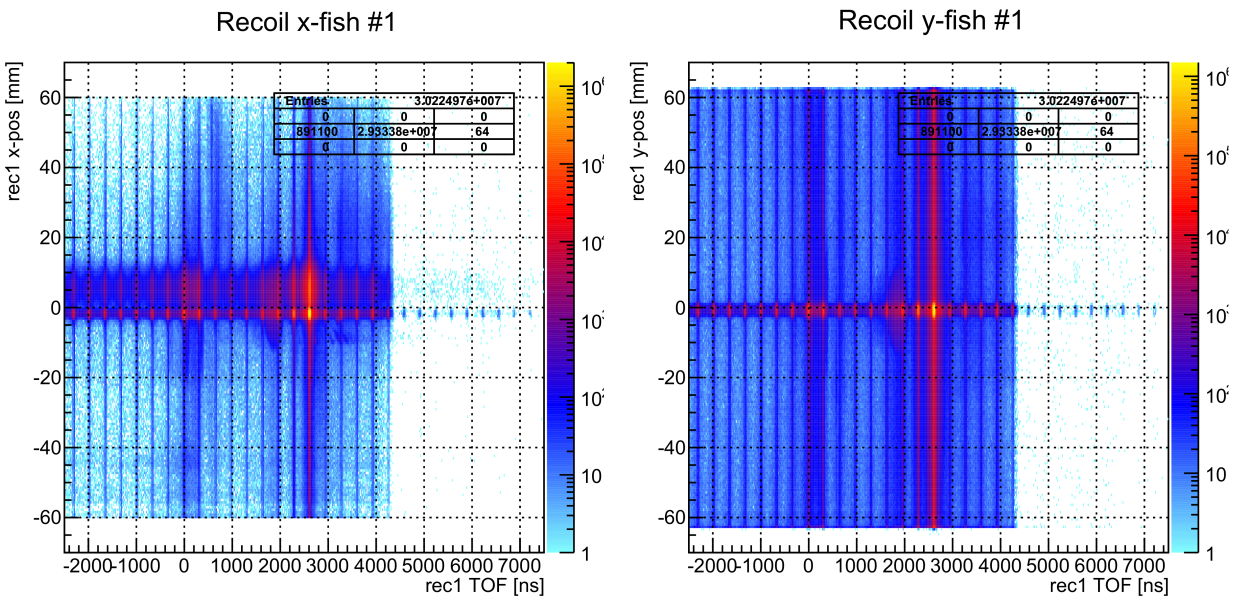

Figure B.2: Raw fish spectra from the August 2016 H2 data set. Note that the flight times displayed are calculated from electrons. A continuous (in time) background accompanies the hot gas stripe while the jet dot appears to be discretely spaced by the bunchmarker time. See text for further details.

Additionally, as shown in fig. B.2 and B.3 there is a mysterious stripe that spans the detector in the x and y direction and is correlated with either the ALS shot or with the the jet dot. A signal of this type is usually associated with a photon striking the detector and this may be a possibility: the primary beam of the ALS is imperfectly dumped into the chamber wall and as will be discussed in section B.1.3 is responsible for most of the background electrons. It may be that this reflected light also generates ions. Additionally, some flourescence may occur in highly excited molecules. Another possible source of the signal might also originate from crosstalk between the recoil detector layer anode wires on their way to the chamber wall. However, I will demonstrate in the next chapter that that these signals are a products of the reconstruction method and how it handles missed signals.

B.1.2 Ion Ghosts

Impact of charged particles on the spectrometer meshes and the MCPs generate additional charged particles. I call these "ghost" sources because the most prominent effect is

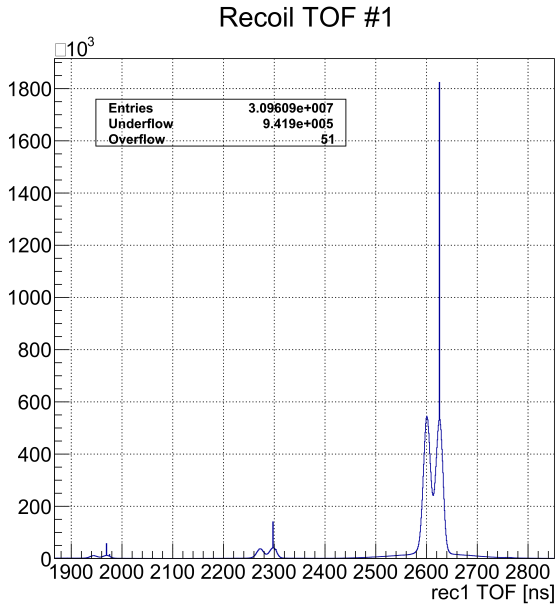

Figure B.3: The distribution of the raw recoil flight times shows a sharp artificial peak about $10ns$ from the center of the ion double peak.

a "ghost" image of the electron detector on the ion detector as shown in fig B.5. A useful tool in analyzing the correlations between electrons and ions is the time of flight modulo plot, figure B.4, where the ion flight time has been condensed by modulo into the interval $\{0, 3\Delta t = 984ns\}$ to facilitate a direct comparison of the electron and ion flight times. The ion modulus in figure B.4 is calculated:

$$r_{1\ mod(3\Delta t)} = Mod_{3\Delta t}[r_{1\ mcp} - e_{1\ mcp} + e_{1\ mod(3\Delta t)} + 1000\ \Delta t]. \tag{B.17}$$

where $r_{1\ mcp}$ and $e_{1\ mcp}$ are the raw mcp times of the recoil (ion) and electron, and Δt is the bunchspacing. The electron modulus is calculated

$$e_{1\ mod(3\Delta t)} = Mod_{3\Delta t}[e_{1\ mcp} - laser_{BM} - LaserBunch_{\delta t} + 1000\ \Delta t], \tag{B.18}$$

where $laser_{BM}$ is the laser bunchmarker time and $LaserBunch_{\delta t}$ is the laser bunchmarker offset. If we consider the dynamics of $r_{1\ mod(3\Delta t)}$ within a specific modular window of $3\Delta t$,

then the equation above simplifies to

$$r_{1\ mod(3\Delta t)} = e_{1\ mod(3\Delta t)} + C. \tag{B.19}$$

This is the equation of a line with a slope of one. Therefore, the correlated ions and electrons exist on 45 degree lines and the spread of the distribution about this line is goverend by the spread in the momenta of the electrons and ions.

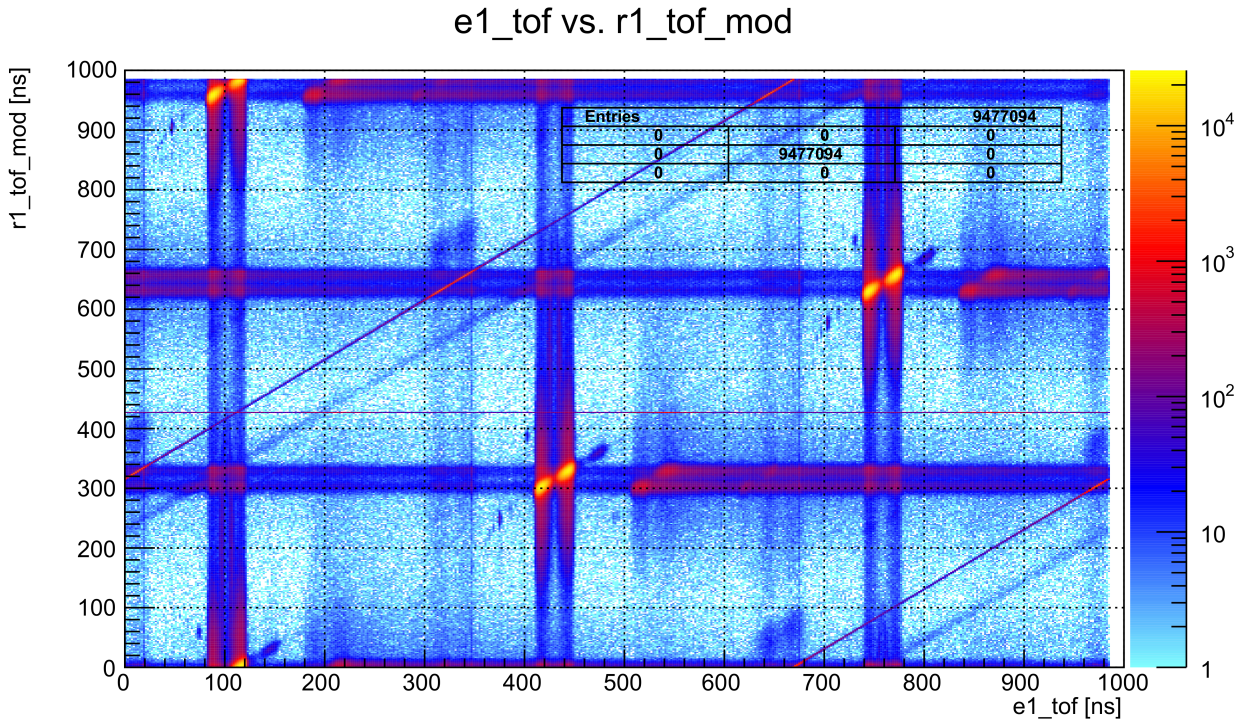

Figure B.4: The modulo 984ns of the ion flight time plotted with respect to the modulo 984ns of the electron flight time. The diagonal line is produced by the ion ghost. The brightest spots are the true electron-ion coincidences. Signal reflections on the electron detector produce the shadowing to the right of these spots. Capture of the incorrect electron produces vertical duplications at integer multiples of the bunchspacing. Signals produced by the laser would be distinct and not repeating in this plot.

The hottest spot is the jet dot, evenly distributed between the 3 bunchmarkers spanned by the laser bunchmarker. Other features are not products of photoionization but are created by impacts inside the spectrometer or by signal reflections. Time of flights of charged particles, with spectrometer field values from the August H2 dataset, generated on different

physical structures are listed in table B.1 and can be matched to the features in the modulo picture.

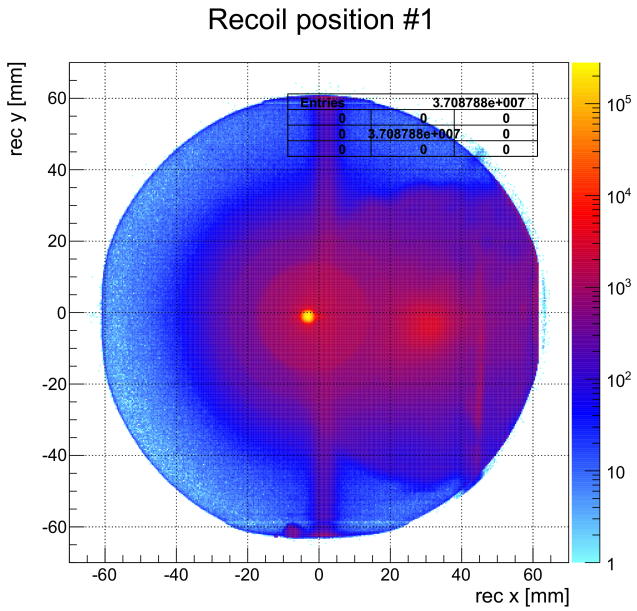

Figure B.5: The electron ghost image on the ion detector is visible to the right. This is a projection of the electron detector image from ions ablated of the detector surface and launched through the spectrometer to the ion detector.

	Spectrometer Flight times				
	Ion Detector	Ion Mesh	Middle Mesh	Electron Mesh	Electron Detector
Ion Detector	-	$m_e : 1.6ns$	$m_e : 5.6ns$	$m_e : 10.6ns$	$m_e : 10.6ns$
Ion Mesh	$m_{H_2} : 68ns$	-	$m_e : 66.3ns$	$m_e : 106ns$	$m_e : 107ns$
Middle Mesh	$m_{H_2} : 2.843\mu s$	$m_{H_2} : 2.843\mu s$	-	$m_e : \infty$	$m_e : \infty$
Electron Mesh	$m_{H_2} : \infty$	$m_{H_2} : \infty$	$m_{H_2} : \infty$	-	$m_e : 1.01ns$
Electron Detector	$m_{H_2} : 1.147\mu s$	$m_{H_2} : 1.147\mu s$	$m_{H_2} : 673.5ns$	$m_{H_2} : 45.2ns$	-

Table B.1: A table giving the flight times for charged fragments born with zero velocity at the location specified on the left most column, impacting at the location specified by the top row. A value of infinity indicates there is no field in the region and hence no or very long flight times. These flight times are approximate becaue fields values are not exact.

The ion detector has a strong accelerating field to increase collection efficiency whereas the interior of the MCP is strongly biased to accelerate electrons towards the back anode. Consequently, there is a sharp cusp of the electric field at the surface of the MCP and electrons can be pulled away from the MCP channels and accelerated towards the electron

detector. Given the field strengths and spectrometer geometry, in the August 2016 H2 data these electrons would arrive at the electron detector in roughly $10ns$; indeed there is an anomalous ion ghost image on the electron detector as shown in electron fish in fig B.6. Analysis of figure B.6 is complicated because the field setting places the jet dot at nearly an integer multiple of the bunchmarker spacing: the flight time for H2+ is $2615ns/328ns = 7.97$. With this offset, the center of the misplaced ion distribution will be $9ns$ behind the bunchmarker. The H2 data set is unusual in that the H2+ is light enough to absorb and appreciable kick from the electrons, splitting the jet dot into two halves with centers seperated by roughly $25ns$. Therefore, half of the jet dot distribution will hit the detector at $-12.5ns - 9ns = -21.5ns$ before and half will hit after ($+3.5ns$) the bunchmarker signal. Ghost electrons are born at these hit times and hit the electron detector 10ns later at times $\{-11.5ns, +13.5ns\}$ relative to the bunchmarker and are split by the modulo routine into the respective times: $\{13.5ns, 316.5ns\}$. The ion time of flights are calculated by adding these computed electron time of flights: hence the observed distributions. This is clearly visible in ion fish in fig B.6 where part of the ion distribution is sharply split into two halves. The ion ghost accounts for the anomalous uptick in count rate of these two jet dots near time zero, superimposed on the regular jet dot.

As proof that the process is creating electrons on the ion detector, examine the sharp 45 degree line in the modulo plot figure B.4. If the electron is generated by the ion, then no matter the time the ion lands, the electron will always be a fixed offset from that time. In other words, the electron time will exactly cancel the variance in the ion time of flight and the line relating the electrons to the ions will be very sharp. Indeed, if a gate is placed on this line, the electrons that appear are exactly those identified as the ghost image.

We can estimate the ghost electron rate relative to the jet dot rate by integrating the electron detector ghost counts. The counts are clearly seperated from the real electron distribution in the electron fish and can be summed by integrating a $30ns$ window over the electron ghost region tof histogram and subtracting the average background on the

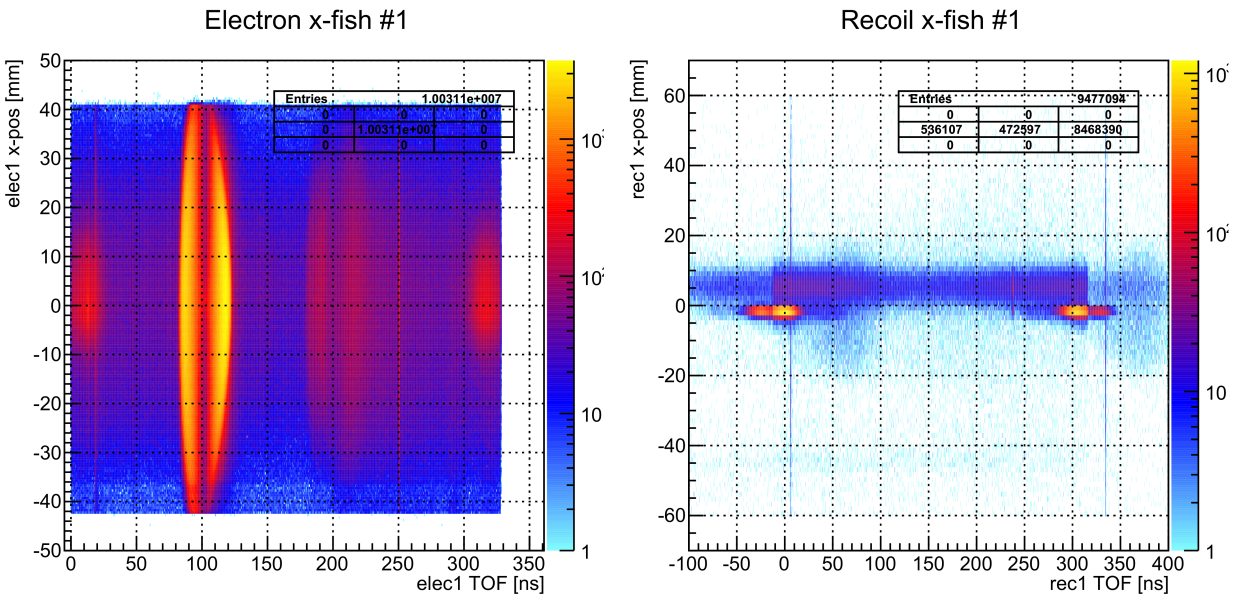

Figure B.6: The electron fish spectrum displays the ion ghost as the hot spot in the time ranges $\{0, 10ns\}$ and $\{300, 328ns\}$. The jet dot corresponding to these electrons is split between the two bunchmarkers and is thereby divided between the bunchmarker at 0 and the bunchmarker at $328ns$. The recoil fish has been gated to require good mcp signals, ions, and electrons.

electron detector. Total ghost electron hits relative to jet dot ion hits is approximately $3.53e5 : 6.75e6$, respectively. Consider now that the electrons must fly through all 3 meshes and be collected and the ions must fly through the ion mesh and be collected, a scaling factor of $(0.8 * 0.5)/(0.8^3 * 0.6) = 1.30$ must mulitply the ratio. The ratio between the jet dot and ion detector ghost rate is found to be 6.8%. In fact, the ion ghost electron distribution position can be shifted around merely by changing the spectrometer field, implying that a poor choice in field can center this distribution on top of the good electrons, polluting the data. Ghost ion electrons are a significant source of error and demonstrates that correlated charged particle generation originates from both the ions and the electrons.

B.1.3 Electrons

I will proceed to analyze the electrons in the same manner as the ions. Electron count rates are ususally anywhere form 2 to 5 times the ion count rate due primarily to reflected x-rays impacting on the spectrometer surfaces. The electron proabability distribution within an event can be modeled as a binomial distribution with an ALS shot taken as a single trial and the number of trials, N, governed by the data collection time window triggered by the ion MCP signal. To begin with, in the case of the ions the binomial distribution probabilities must be modified to reflect that data acquisition was triggered on the first ion. The electron distribution is sampled accurately if these windows are randomly distributed. In the preceding section I have shown that to a first approximation the ions are randomly distributed.

Any discussion of the electron rate must take into account the electron ghost image on the ion detector. The electron ghost is stronger than ion ghost because there is no cusp in the bias of the electron MCP and ions generated at the electron MCP do not have to overcome a cusp like in the case of the ion detector. Multiple electron impacts make it more probable that electron ghost ions will be generated and trigger an event and this is likely the reason for the increase in the tail of the electron count distribution beyond what would be expected with a binomial model. The probability of the creation of a ghost ion can be estimted from the august 2011 02 data where the ghost image is clearly visible and integrable. Roughly 6% of the image counts are in the electron ghost and, accounting for the transmission and collection coefficients this yeilds $.06/(.8^3 * .5) = 16\%$ probability of ghost ion generation relative to the total number of collected ions.

The electron count rate for the August 2016 H2 data set was roughly $20kHz$, yielding a probability of $p = 1/58.55$ with a collection efficiency $c = .8 * .8 * .6$ that accounts for the extra mesh and higher collection efficiency of the MCP for electrons. The ratio of hits $A_{\alpha,\beta}$, where the subscripts denote the number of electrons collected is then easily computed as

$$A_{\alpha,\beta} = \frac{P[X=\alpha]}{P[X=\beta]} = \frac{c^\alpha}{c^\beta}\frac{(N-\beta)!\ \beta!}{(N-\alpha)!\ \alpha!}\frac{p^\alpha(1-p)^{N-\alpha}}{p^\beta(1-p)^{N-\beta}} \tag{B.20}$$

and for the useful case of $\beta = \alpha + 1$:

$$A_{\alpha,\alpha+1} = \frac{1}{c}\frac{\alpha+1}{N-\alpha}\frac{1-p}{p}. \tag{B.21}$$

Table B.2 lists ratios computed with the probability given by the rate meter, and the measured ratios.

	Ratio				
	$A_{0,1}$	$A_{1,2}$	$A_{2,3}$	$A_{0,2}$	$A_{0,3}$
Computed	1.918	3.969	6.166	7.613	46.94
Adjusted Comp.	4.995	10.34	16.06	51.63	318.3
Experimental	1.261	6.844	4.230	8.628	36.50

Table B.2: A table of the count rate ratio's for the August 2016 H2 raw data. Computed values were calculated with the probability obtained from the rate meter: $p = 1/58.55$ without including collection efficiency terms. Adjusted values included collection efficiency. Experimental values are directly obtained from the raw data by integrating the electron hits for $n_{elec} = 0, 1, 2, 3...$

There is a clear discrepancy in table B.2. The experimental $A_{1,2}$ is larger and $A_{2,3}$ is smaller than the computed values, suggesting that there are fewer 2 hit counts than there should be. The experimental $A_{0,1}$ is smaller than the computed value, indicating that there are either fewer 0 hit events, or more 1 hit events. Taken together it is clear that the distrubution does not follow the binomial distribution. How can this be explained? A good agreement is obtianed if two seperate distributions are used: one to account for photoionization and the other to account for the electrons generated from backscattered x-rays. I have shown previously that the rate of ion generation for this dataset can be calculated from the ion hit ratios and is $R_{ion} = 10.82kHz$. This implies that of the $20kHz$ recorded on the electron mcp signal rate meter, roughly $R_{ion} * c_{elec} = 4152Hz$ is registered from photoionization generated electrons and the remaining $15kHz$ is generated by backscatter.

Critically, the photoionization garuantees at least one electron is generated for each window, tilting the distribution towards events with at least 1 electron.

If we take the backscatter rate as $20kHz - 4152Hz = 15848Hz$ the probabilitiy is $p_{backscatter} = 1/73.85$ when collection efficiency is accounted. I have already computed the probability of photoionizaiton to be $p_{photo} = 1/243.9$. It is important to note that the backscatter process cannot be measured unless the photoionization process occurs to generate an ion and therefore a collection window. Some of the possible cases for electron capture are summarized in table B.3 below.

	# of electron hits								
	0	1	1	2	2	2	3	3	3
Photoionization	1x	1	1x	1	2	1x	1	1x	2
Backscatter	0	0	1	1	0	2	2	3	1

Table B.3: Possible electron generation and capture scenarios to produce the observed number of electron hits. Some scenarios listed are used to model the spectrometer, but many more scenarios exist ad infinitum. Numbers with an x represent generated electrons that were not collected.

In table B.3, the higher probability scenarios are those where the a single photoionization electron was generated but not collected. These events have a $1 - c_{elec} = 66\%$ probability of occuring for any particular photoionization and therefore represent a significant portion of the signal. An exhaustive model of all possible combinations can be implemented using probability density function of the binomial distribution $F_B[N, n, p]$, where N is the number of trials, n the number of successes, and p the probability of success. The probability that a photoionization event has n successful electrons is then

$$P_{photo}[X = n] = \sum_{j=1}^{\infty} \sum_{i=0}^{\infty} F_B[30, i, p_{back}]\ F_B[30, j, p_{photo}]\ F_B[i + j, n, c_{elec}]\ F_B[j, 1, c_{ion}]. \quad \text{(B.22)}$$

The terms are, from left to right, the probability of generating i electrons from backscatter, the probability of generating j ion/electron pairs from photoionization, the probability of collecting n electrons from the $i + j$ generated electrons, and the probability of collecting

at least one ion to trigger the collection window. Additionally there is a possibility that photoionization is not inovlved at all, and that the electron ghost ions actually trigger the event window:

$$P_{e\ ghost}[X = n] = \sum_{k=0}^{\infty} F_B[30, k, p_{back}]\ F_B[k, n, c_{elec}]\ F_B[k, 1, p_{ghost}]. \tag{B.23}$$

Here the only new term is the last and it models that at least one electron hitting the electron detector generates a ghost ion that is collected: the whole process is modeled as a single probability $p_{ghost} = .06$ previously stated for generation and capture of a electron ghots ion.

The probability of an event having $X = n$ electrons is the addition of both P_{photo} and P_{ghost}. The ratio of the experimental rates is just the ratio of the $X = n$ probabilities. The modeled rates are shown to be in good agreements with the experimental values in table B.4. There is some discrepancy in the $A_{2,3}$ and $A_{0,3}$ which are 2.78 and 2.49 times too

	Ratio				
	$A_{0,1}$	$A_{1,2}$	$A_{2,3}$	$A_{0,2}$	$A_{0,3}$
Model elec ghost	1.250	6.367	11.92	7.958	94.82
Model elec + ion ghost	1.197	5.199	9.628	6.225	59.94
Experimental	1.262	6.890	4.247	8.695	36.93

Table B.4: Comparison of the modeled ratio versus the measured ratios. The modeled values use the probability derived from the electron rate meter and the probability computed for the ions.

large respectively. This indicates that there are other contributions for higher electron count events; the ion ghosts is a good candidate for the production of these extra electrons. By integrating the electron fish over the ion ghost image a percentage of the total count rate can be determined for 1, 2, and 3 electron events and are found to be 4%, 16%, and 22% respectively and 7.5% overall for events containing up to 3 electrons. However, simply adding these values into the model does not yield much insight. An attempt was made to directly incorporate the generation of the ion ghost electrons by assuming a given experimental probability for the generation and capture ion ghost electrons, $p_{ion\ ghost}$, and adding the

following term to the total probability:

$$P_{ion\ ghost}[X = n] = \sum_{j=1}^{\infty}\sum_{i=0}^{\infty} F_B[30, i, p_{back}] \\ F_B[30, j, p_{photo}]\ F_B[i + j, n - 1, c_{elec}]\ F_B[j, 1, c_{ion}]\ F_B[j, 1, p_{ion\ ghost}]. \quad \text{(B.24)}$$

As listed in the second row of table B.4, the results is mixed and does not solve the problem of the weaker than expected $A_{0,3}$ term.

The addition of the $P_{ion\ ghost}$ term without subsequently adjusting the input probability for the backscatter electron generation distorts the model. In actuality, the existence of the additional source means that the probability of backscatter generation is less than expected: if the rate counter is accurate to the true mcp signal rate to within roughly 10% then then introduction of new sources must reduce the probability. Despite these shortcomings, the model accurately accounts for the zero, one, and two electron events which comprise 98% of all events. For the purposes of estimating the background signal, this is more than accurate enough. Only in extreme cases where triple ionization is the signal of interest would the model and respective probabilities have to be refined further.

B.2 Background Variance

In the last two sections, the majority of collection events in the spectrometer were modeled, giving probabilities that can now be applied to discovering erroneous signals in TDC events. There are two type of error signal: intra and inter-event errors. Intra-event errors results from an false coincidence assignment within the TDC event. In this case, for the August 2016 H2 data, this would be the association of an ion with an incorrect electron or the reverse. In data sets with more than one ion, this could be the association of two wrong ions. Of course, the greater the number of electrons required in coincidence (for double ionization) the more probable is an error. The inter-event error results from background signal overlaying the signal of interest in phase space. This error could be

caused by the repetition of the jet dot, or the presence of the hot gas stripe, or another very closely spaced ionization channel signal. These errors accumulate at constant rates and can be background subtracted with enough staistics. All errors have a fixed probability (and therefore rate) relative to the total spectrometer signal and in aggregate can best best be modeled as poisson distributions.

The problem of calculating the variance for each bin of a histogram requires the application of Wald's theorem. Wald's theorem defines the mean and variance of a group of identically randomly distributed variables, x_k, that have a sum controlled by an random variable n_j with integer number:

$$S_j = \sum_{k=0}^{n_j} x_k, \tag{B.25}$$

where x has a mean μ_x and variance σ_x and likewise for n there is μ_n and variance σ_n. In this application n represents the number entries in a bin and x the weight of each entry. Wald's theorem states that the mean of S_j is

$$\mu_s = \mu_n \ \mu_x \tag{B.26}$$

and the variance is

$$\sigma_s = \mu_n \ \sigma_x^2 + \mu_x^2 \ \sigma_n^2. \tag{B.27}$$

To apply the theory to the histogram set the $x_k = 1$, yielding $\mu_x = 1$ and $\sigma_x = 0$. The n_j are defined by some continuous probability distribution descretized to give a probability of landing in each one of the bins. This is the multinomial distribution with mean $\mu_n = n_j$ and variance $\sigma_n^2 = n_j(1 - n_j/N)$. The variance of a histogram bin is then

$$\sigma_s^2 = n_j(1 - \frac{n_j}{N}). \tag{B.28}$$

For large values of N, the total number of trials, the second term drops and we are left with

$$\sigma_s = \sqrt{n_j}, \tag{B.29}$$

which is the familiar term used to describe the variance in a histogram bin. It is easy to see that there are significant corrections when there are high concentrations of events in a few bins. This is important, because many of the signals, the jet dot being the primary example, have a concentrated spatiotemporal distribution.

For any given total number of events M, there are i different signals N_i. If a bin is determined to have multiple signals s_i feeding into it, then the total value in the bin must be

$$S_l = \sum_{i=1}^{l} s_i. \tag{B.30}$$

In this case the means add and the errors add in quadrature. It is trivial to show that the error remains the square root of the total number of events in the bin.

All that remains is to find the total contribution in each bin from each signal in order to find the ratio of standard deviations. With these values in hand, we can meaningfully ask the question of whether background fluctuations are significant and to do this we need the standard error. The standard error is a measure of the standard deviation of the mean of a signal. In other words, given a finite sample and the mean calculated from that sample, the standard error is how far the calculated mean may diverge from the true mean of the underlying process. Within each bin, if the signal of interest standard error is not greater than the standard error of the confounding error signals then it cannot be said that random fluctuations in the confounding signals are not influencing the observed signal. Of course, additionally, we would like to evaluate if the signal of interest is a reasonably good measure or if more data needs to be collected. Similarly, the standard error of the inter-event signals determines the efficacy of background subtraction. Only if the standard error is much less

than the absolute value of the background can anything be gained from subtracting one background from another.

B.2.1 Relative Rates & Transformations

In order to calculate the standard mean and error, the number of collected events must be defined for each signal. Given the variability in the rate of data collection from experiment to experiment, rates can only be defined relative to some reference signal and this reference must be chosen before any variance can be discussed. Ultimately all rate equations are limited by most prominent signal in the spectrometer: the jet dot single ionization, which can comprise up to 90% of the observed signal. Not only is single ionization the most direct way to calculate expected rates based on relative cross sections for photoionization found in the literature, but it is also a predominant source of noise. I will derive the rates relative to the jet dot rate. The ratio of the various signals relative to the jet dot are given in table B.5.

	Signal		
Ion	Jet Dot	Displaced Jet Dot	Electron Ghost
Ratio	1	.005	.16
Electron	Backscatter	Ionization	Ion Ghost
Ratio	3.04	.96	.04

Table B.5: Background signal rates as a ratio of the jet dot signal as collected by the detectors. These ratios already incorporate detection efficiency and are the real ratios seen in offline analysis.

A note on the structure of electron signals in the spectrometer; the magnetic field of the spectrometer forces the electrons into a cyclical flight path and thereby distributes them across the electron detector. There is no good way to seperate the random electrons from photoionization electrons spatially. As seen in a the fish spectra of figure B.2, the random electrons are differentiable in time: here the backscatter electrons form a broad carpet underlying the distribution. the time spread of the randomly generated electrons is goverened by their energy which is typically on the order of the photon energy minus the work function of the metal. The majority of the metal in the spectrometer is copper and has

a work function of $4.5eV$. The photon energy for the August H2 dataset is $18.56eV$ yielding a backscattered electron energy of $14eV$. These electrons have more than enough energy to impact at all flight times in the $328ns$ modulus range. Hence the backscattered electrons have a flat distribution that covers the entire detector in space and time.

Consider how each signal is distributed into its' respective phase spaces. In addition to the probability that a signal will be generated and collected in an event, each signal also has a probability of landing in a particular spot of the phase space distribution. Since each ALS shot samples each of the m_x, m_y, and m_t subdivisions according to the distribution $P[x_i, y_j, t_k]$, the total number of trials in bin $N_{i,j,k}$ is

$$N_{i,j,k} = P[x_i]\ P[y_j]\ P[t_k]\ N. \tag{B.31}$$

As stated in the introduction at the beginning of this section, the probability for each error signal follows the poisson distribution and for a large number of events the standard deviation in any dimension is the observed value in the bin divided by the square of the number of observations:

$$\sigma_{ijk} = \sqrt{N_{i,j,k}}. \tag{B.32}$$

Importantly, this is a terrible measure of error for bins with less than about 30 events. Sparse data often underfills histograms below the 30 event level.

We wish to transform the distribution from space and time coordinates into momentum, energy, and angles (in momentum space). Effectively this means transforming $dxdydt$ into $dp_x dp_y dp_t$. To accomplish this transformation we must employ the Jacobian, which requires the equations of transformation from spacetime to momentum space. To transform the linear spatial dimensions of the ions into momentum space, the positions must be divided by the time:

$$p_x = m\frac{x}{t}. \tag{B.33}$$

The spatial transform for the electron is complicated by the cyclotron frequency. However, the backscatter electrons are found to be uniform in space, so we can adopt the same transformation as for the ions. The fale coincidence photoelectrons will have identical distribution to the real electrons and will always be proportional to the actual signal, so the momentum transformation is not nescesary.

The transformation for the electron time follows from the quadratic

$$0 = (d_2 + d_1) - v_2\ t_2\ - \frac{p_t}{m_e} * t_1 - \frac{1}{2}at_1^2, \tag{B.34}$$

where d_1 and d_2 are the acceleration and drift distance respectively from the interaction point to the spectrometer. The veolicty in the drift stage is

$$v_2 = \frac{p_t}{m_e} + at_1, \tag{B.35}$$

and this yields directly time t_2:

$$t_2 = \frac{d_2}{\frac{p_t}{m_e} + at_1}. \tag{B.36}$$

The total time, $t = t_1 + t_2$, is

$$t = t_1 + \frac{d_2}{\frac{p_o}{m_e} + at_1}. \tag{B.37}$$

The solution for t_1 comes from substituting the values for v_2 and t_2 and solving the resulting quadratic:

$$t_1 = \frac{\frac{p_o}{m_e} \pm \sqrt{\left(\frac{p_o}{m_e}\right)^2 + 2ad_1}}{a}. \tag{B.38}$$

Finally, when substituted into the equation for t

$$t = \frac{\frac{p_o}{m_e} \pm \sqrt{\left(\frac{p_o}{m_e}\right)^2 + 2ad_1}}{a} + \frac{d_2}{\frac{2p_o}{m_e} \pm \sqrt{\left(\frac{p_o}{m_e}\right)^2 + 2ad_1}}. \tag{B.39}$$

The Jacobian calls for the derivative dt/dp, which is a complicated function that doesn't give much insight. We can make the simplifying assumption that the electron momentum doesn't have an effect on the flight time. This is roughly true as the electron momentum spread is often only a fraction of the total flight time in the spectrometer. With this assumption

$$\frac{dt}{dp} = \frac{1}{a\ m}\frac{d_1 - d_2}{d_1} = -\frac{1}{a\ m}, \tag{B.40}$$

where the spectrometer specific geometry of $2d_1 = d_2$ is used. This demonstrates that an increase in momentum towards the electron detector results in a shorter flight time at a rate proportional to the inverse of the acceleration field. We can work backwards and integrate to produce the usefull relation:

$$t = -\frac{p_t}{a\ m} + C \Rightarrow -\frac{p_t}{a\ m}, \tag{B.41}$$

which effectively linearizes the spectrometer and from which the relation between the position and momenta becomes:

$$x = -\frac{p_x\ p_t}{a\ m^2}. \tag{B.42}$$

The Jacobian for the electron transformation is then:

$$J_e[p_x, p_y, p_t] = \begin{vmatrix} \frac{\partial x}{\partial p_x} & \frac{\partial x}{\partial p_y} & \frac{\partial x}{\partial p_t} \\ \frac{\partial y}{\partial p_x} & \frac{\partial y}{\partial p_y} & \frac{\partial y}{\partial p_t} \\ \frac{\partial t}{\partial p_x} & \frac{\partial t}{\partial p_y} & \frac{\partial t}{\partial p_t} \end{vmatrix} = \begin{vmatrix} -\frac{p_t}{a\ m^2} & 0 & -\frac{p_x}{a\ m} \\ 0 & -\frac{p_t}{a\ m^2} & -\frac{p_y}{a\ m} \\ 0 & 0 & \frac{-1}{a\ m} \end{vmatrix} = \frac{p_t^2}{a^3 m^3}. \tag{B.43}$$

Hence the momentum volume for the electrons transforms like:

$$dx\ dy\ dt = \frac{p_t^2}{a^3 m^5} dp_x\ dp_y\ dp_t. \tag{B.44}$$

The consequence of uniform binning then dictates that the density of states in both spaces must be related by

$$\begin{aligned} \mu_{spacetime} &= \tfrac{p_t^2}{a^3 m^5}\mu_{mom} \\ \tfrac{a\ m^3}{t^2}\mu_{spacetime} &= \mu_{mom} \end{aligned} \tag{B.45}$$

For a uniform density in spacetime, the density in momentum space decreases as the inverse square of the time. Therefore, the highest density of false events is localized closest to the time where $p_t = 0$.

There is no drift region for the ions and we can solve the quadratic for p_o:

$$t = \frac{\frac{p_t}{m_i} \pm \sqrt{\left(\frac{p_t}{m_i}\right)^2 + 2ad}}{a} = D[p_t]. \tag{B.46}$$

With the same linear assumption about the relation between flight time and p_t as for the electrons the Jacobian for the ions is

$$J_i[p_x, p_y, p_t] = \begin{vmatrix} \frac{\partial x}{\partial p_x} & \frac{\partial x}{\partial p_y} & \frac{\partial x}{\partial p_t} \\ \frac{\partial y}{\partial p_x} & \frac{\partial y}{\partial p_y} & \frac{\partial y}{\partial p_t} \\ \frac{\partial t}{\partial p_x} & \frac{\partial t}{\partial p_y} & \frac{\partial t}{\partial p_t} \end{vmatrix} = \begin{vmatrix} \frac{D[t]}{m} & 0 & F[p_t] \\ 0 & \frac{D[t]}{m} & F[p_t] \\ 0 & 0 & D'[p_t] \end{vmatrix} = \frac{p_t^2}{a^3 m^3}. \tag{B.47}$$

Again, the same result is that random ion coincidences decrease with the inverse square of the time of flight away from time zero., where $p_t = 0$ by definition.

Signal	Distribution Shape	X	Y	*time*
Jet Dot	Gaussian	$2\sigma_x = 1.78mm$	$2\sigma_y = 2.44mm$	$2\sigma_t = 17.96ns$
Displaced Jet Dot	Gaussian	$2\sigma_x = 1.78mm$	$2\sigma_y = 1.78$	$\sigma_t = 17.96ns$
Hot Gas Stripe	Gaussian in X and t, Flat in Y	$2\sigma_x = 1.78mm$	$\Delta_y = 80mm$	$2\sigma_x = 1.78mm$
Electron Ghost	Gaussian	$\sigma_x =$	$\sigma_y =$	$\sigma_t =$
Backscatter	Flat	$\Delta_x = 80mm$	$\Delta_y = 80mm$	$\Delta_t = 328.25ns$
Ionization	Fish		Signal of Interest	
Ion Ghost	quasi-Gaussian	$2\sigma_x = 22.8mm$	$2\sigma_y = 16.05mm$	$2\sigma_t = 21.36ns$

Table B.6: Form of the principle signal distributions in space and time.

Signal	σ	$Volume(s * mm^2)$	Adjusted σ
Jet Dot	$s_n = 1/282$	156.00	$s_\eta = 2.3 * 10^{-5}$
Displaced Jet Dot	$s_n = 1/282$	156.00	$s_\eta = 1.1 * 10^{-7}$
Electron Ghost	$s_n =$		s_η
Backscatter	$s_n =$	$2.01 * 10^6$	s_η
Ionization		Signal of Interest	
Ion Ghost	$\sigma_n =$	7816	s_η

Table B.7: Variance of each signal with respect to number. Phase space volume. Variance density.

B.2.2 Intra-event & Inter-event Signals

Calculating intra event probabilities is more difficult than originally thought. Need to refer back to the electron calculations and use summations to grab the relevant cases. This is where the model comes in handy.

By far the most important case of Intra-event signals is the association of a background electron with an ion. The probability that, given an ion is collected, the associated electron is collected is $c_{elec} = .384$. If $R_{ionization}$ is the rate of ionization in the spectrometer, then

$$R_{ionization}\ c_{ion} = 1, \tag{B.48}$$

by definition of the jet dot as our rate standard. Then the number of ionization electrons must be:

$$R_{elec} = R_{ionization}\ c_{elec} = \frac{c_{elec}}{c_{ion}} = .96, \tag{B.49}$$

as given in table B.4. The probability of both electron and ion being collected is then

$$R_{ion+elec} = R_{ionization}\ c_{ion}\ c_{elec} = c_{elec} = .386. \tag{B.50}$$

The ratio of unassigned ionization electron events to correct electrons is then

$$\frac{R_{elec} - R_{ion+elec}}{R_{ion+elec}} = \frac{\frac{c_{elec}}{c_{ion}} - c_{elec}}{c_{elec}} = \frac{1}{c_{ion}} - 1 = 1.5. \tag{B.51}$$

From table B.5, the ratio of good electrons to backscattered electrons is then 1 : 7.8. Clearly there is a large probability that some of these electrons will be result in false coincidences.

A simple, but wrong, assumption would be that the ratio of these rates would yield the probability of false coincidence. However, approximately half of all TDC events register no electrons and a significant fraction (10%) register 2 or more electrons. Therefore, the distribution is not one to one and a simple accounting will not be enough to determine relative rates. We must return to the previously verified model of electron hits to discover the true percentage of false coincidences.

Before breaking out the full architecture of the model, we can get a rough estimate if we assume that there are no events that collect more than 1 electron and that the distribution of ions is split between zero and one electron per ion according to the ratio in table B.4, roughly the number of 1 electron events is 80% of the 0 electron events. The total number of events with 1 electron is then $1.0/1.80 = .55$. It follows from our prior assumption that .386 of this rate must be good electrons, leaving $.55 - .386 = .17$ to be comprised of both unassociated ionization electrons or backscattered electrons. Regardless, the rate of false to true coincidence is:

$$\frac{R_{false}}{R_{true}} = \frac{.17}{.55} = .31 \rightarrow 31\%. \tag{B.52}$$

We can expect 31% of the total ionization signal to be false coincidences for the jet dot. The 31% must follow the ratio of the false ionization to the backscatter $.96/3.04 = .315$, meaning roughly 10% the total lies in false ionization and 21% lies in backscatter. The logic can be generalized for all ionizations if we change the ratio of the total electron rate relative to the specific channel. For most channels, the ionization rate in question is much smaller than the total ionization and 31% is almost exclusively composed of backscattered electrons.

The situation is not as dire as it seems: we are saved by our ability gate on particular events in phase space. Of these two portions, the backscatter is not so problematic because

Scenario	Associated Electron Rate	Scenario Probablitiy	Modeled Probability
Ion & Backscatter Electron	3.06	21%	24.3%
Ion & Random Photoelectron	.576	10%	4.72%
Ion & True Photoelectron	.384	69%	71.0%

Table B.8: Results of a back of the envelope calculation of the probability for false coincidence scenarios compared with the probabilites generated from the electron model with the number of electrons summed from 1 to 3.

the electrons are distributed uniformly throughout the phase space. Upon energy or momentum gating, the rate percentage will reduce as the fraction of phase space which is gated out: easily more than 90% for backscattered electrons.

The more disruptive signal is the false ionization, which in the worst case may be localized to the same phase space as the true signal. However, given that these electrons are produced by ionization, they are very probably seperated by at least a bunchmarker in time. Here again the phase space gating is instrumental: a false electron will yield a new time for the ion that may distort the ion's momentum enough to move it outside the gate. This self correcting effect is mitigated when ions have very long flight times relative to the bunchmarker and can therefore "absorb" more of a time offset without falling out of the phase space gate.

The expected distribution of false coincidences follows from spherical momentum gates. Consider the sphere along the time of flight momentum direction. The region near the great circle perpendicular to the time of flight direction will have a much broader acceptance of time of flight momentum shifts than the portion of the sphere closer to the "poles" of the time of flight axis. We can therefore expect a $cos(\theta)$ distribution of false coincidences around the sphere, where θ is the polar angle with respect to the time of flight axis.

Now we can bring the full enumeration model of the electrons to bear. There are four scenarios which we will consider: the collection event fails for the true electron and a backscatter electron takes its place, the collection fails for the true electron but another photoionization electron takes its place, the collection of the true electron succeeds, or no

electron is collected at all. To simplify the calculation we will leave out the ghost artifacts. Previously we calculated that the probability of an event with n electrons to be:

$$P_{photo}[X = n] = \sum_{j=1}^{\infty} \sum_{i=0}^{\infty} F_B[30, i, p_{back}]\ F_B[30, j, p_{photo}]\ F_B[i + j, n, c_{elec}]\ F_B[j, 1, c_{ion}], \quad \text{(B.53)}$$

which we must modify for our purposes. For the first case mentioned above, we replace the third term with the following two terms:

$$F_B[i, n, c_{elec}]\ (1 - c_{elec})^j, \quad \text{(B.54)}$$

the first models the number of ways of collecting the backscatter electrons and the second is the probability that no ionization electrons are collected. For the second case above, we have to replace the third term with

$$F_B[j - 1, n, c_{elec}]\ (1 - c_{elec})^{i+1}, \quad \text{(B.55)}$$

where the first term is the probability of collecting all ionization electrons except the correct one and the second term is the probability that only the incorrect electron is captured. For the third case above we replace the third and fourth term with

$$F_B[j, n, c_{elec} * c_{ion}]\ (1 - c_{elec})^i, \quad \text{(B.56)}$$

where the first term is the odds that both the electron and ion are collected (dependently) and the second term is the probability that no backscattered electrons are collected. Finally, the fourth case is easily computed by setting $n = 0$ in the original equation. The final step is to sum each case for the number of electrons from 1 to an upper limit n_{max}, which we choose to be 3 as 3 is the point at which the model becomes inaccurate. Now the relative

probabilities are easily calculated and displayed in the rightmost column of table B.8. There is a strong agreement, but we see that the number of false photoionization coincidences is lower than the back of the envelope computation.

In conclusion, we are finally in a position to characterize the intra event errors. For weak signals, the background error is mostly from backscatter and comprises 29% of the total signal before gates are applied. This work can be extended by applying the phase space density estimates from the previous section to determine the false coincidence error rates. We leave the specifics of the application as future work.

Appendix C

Data Calibration

This appendix provides an overview of the calibration for each dataset. The lookup table corrections generated from the $.88eV$ photoelectrons from single ionization of Helium is used on all four data series: b, d, e, f. Section b appears to be the best calibrated. It is also the dataset taken right after the calibration run used to generate the lookup table. There is a slight tilt to the electrons in the ϕ_{yz} vs. E_e histograms for datasets d, e, and f. Clearly the field shifted slightly - most probably the direction of the magnetic field. One of the two magnetic field coils were removed and replaced when vacuum was broken to repair a phosphor in the main chamber. On the whole, the electron calibration is satisfactory and likely cannot be improved as there are no other extensive calibration runs at the field settings shown.

The ion calibration histograms are shown on a log scale to highlight the broad features and separate them from a particularly strong pollution signal, visible as a bright dot in the p_x vs. p_y histograms. The pollution appears to come from reflected signals originating at the jet dot. The signal is eliminated when gates are placed to isolate the specific vibrational spectra, but appear here for the broader gates used to adjust parameters.

C.1 Data Series b

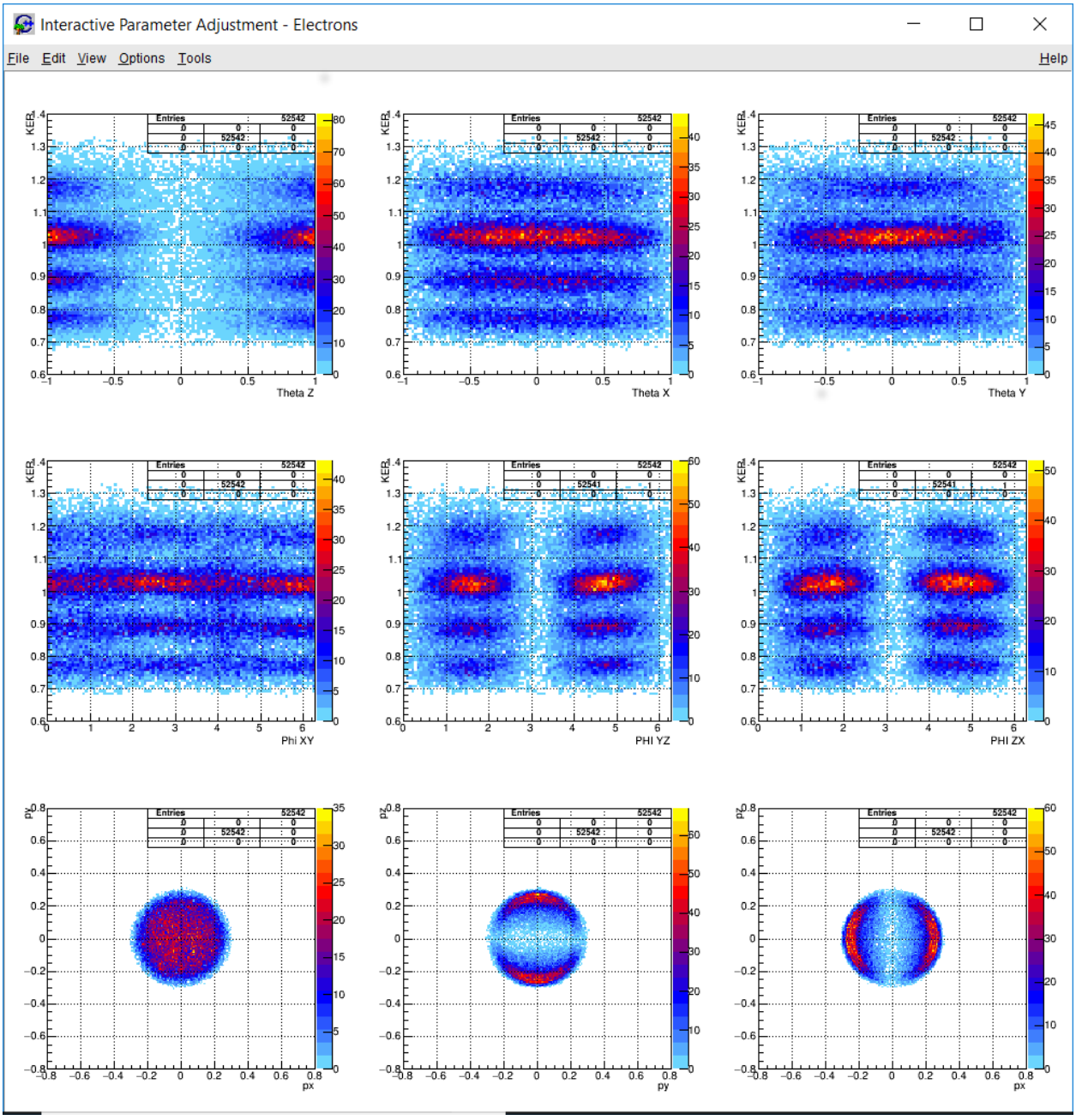

Figure C.1: Electron Calibration Spectra from series b. Top row, left to right: θ_z, θ_x, θ_y vs. E_e. Center row, left to right: ϕ_{xy}, ϕ_{yz}, ϕ_{zx} vs. E_e. Bottom row, left to right: p_x vs. p_y, p_y vs. p_z, p_z vs. p_x.

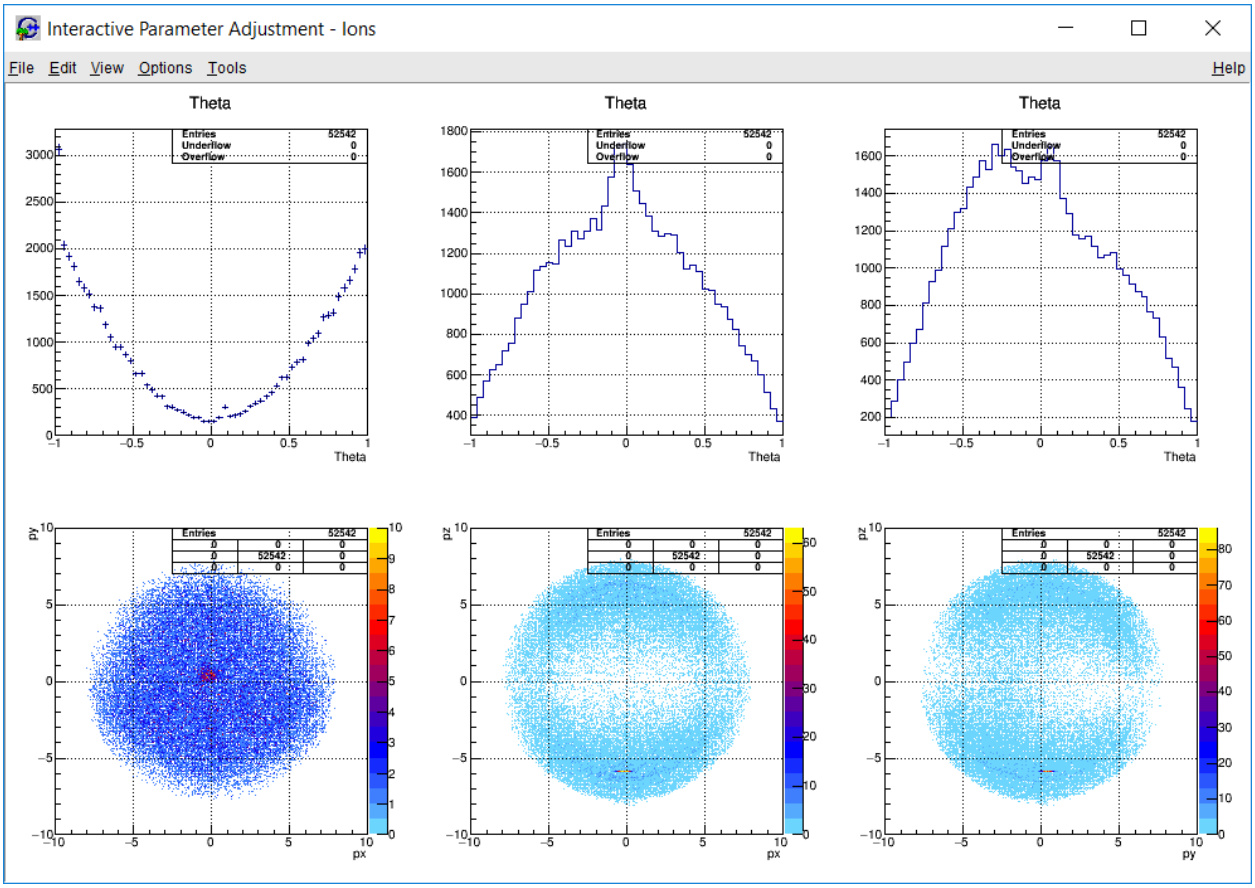

Figure C.2: Ion Calibration Spectra from series b. Top row, left to right: θ_z, θ_x, θ_y. Bottom row, left to right: p_x vs. p_y, p_y vs. p_z, p_z vs. p_x.

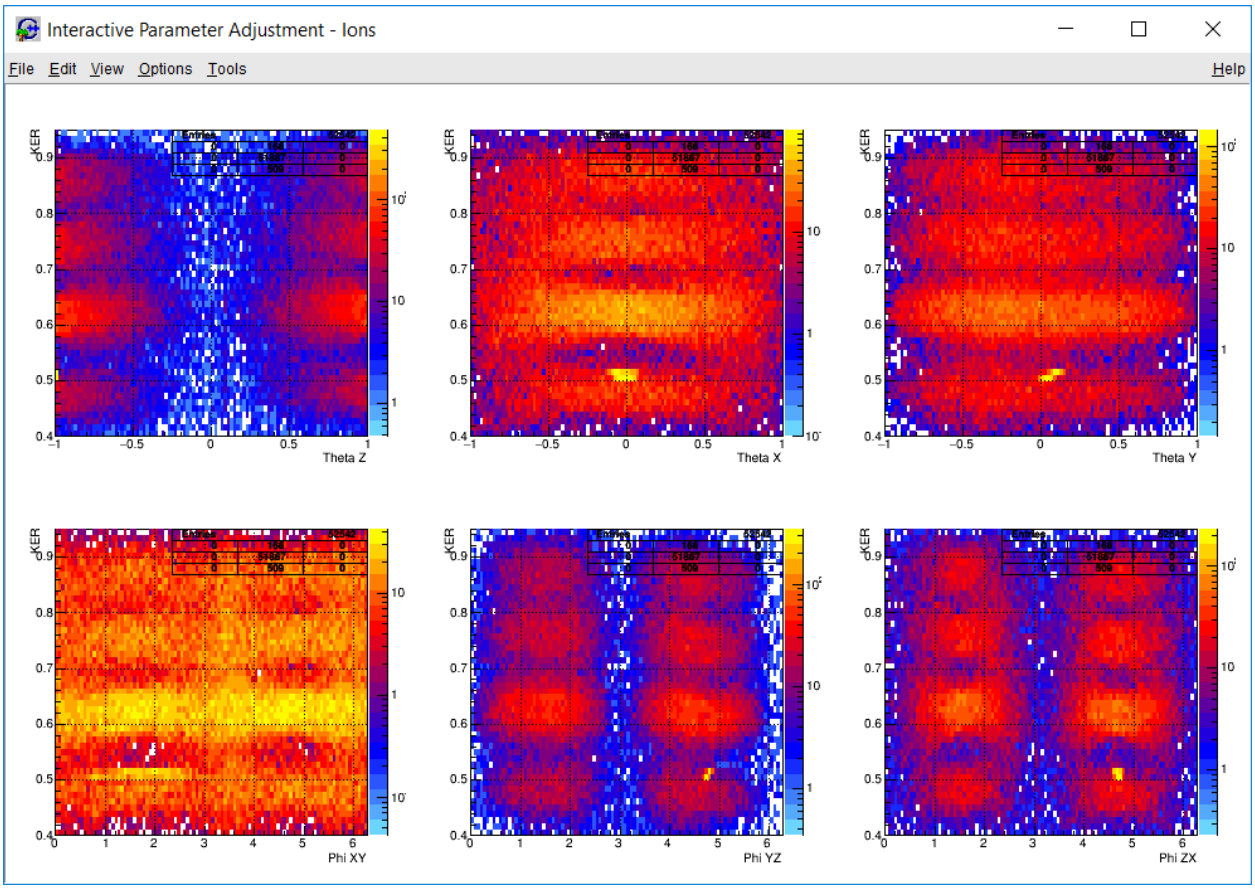

Figure C.3: Ion Calibration Spectra from series b. Top row, left to right: θ_z, θ_x, θ_y vs. KER. Bottom row, left to right: ϕ_{xy}, ϕ_{yz}, ϕ_{zx} vs. KER.

C.2 Data Series d

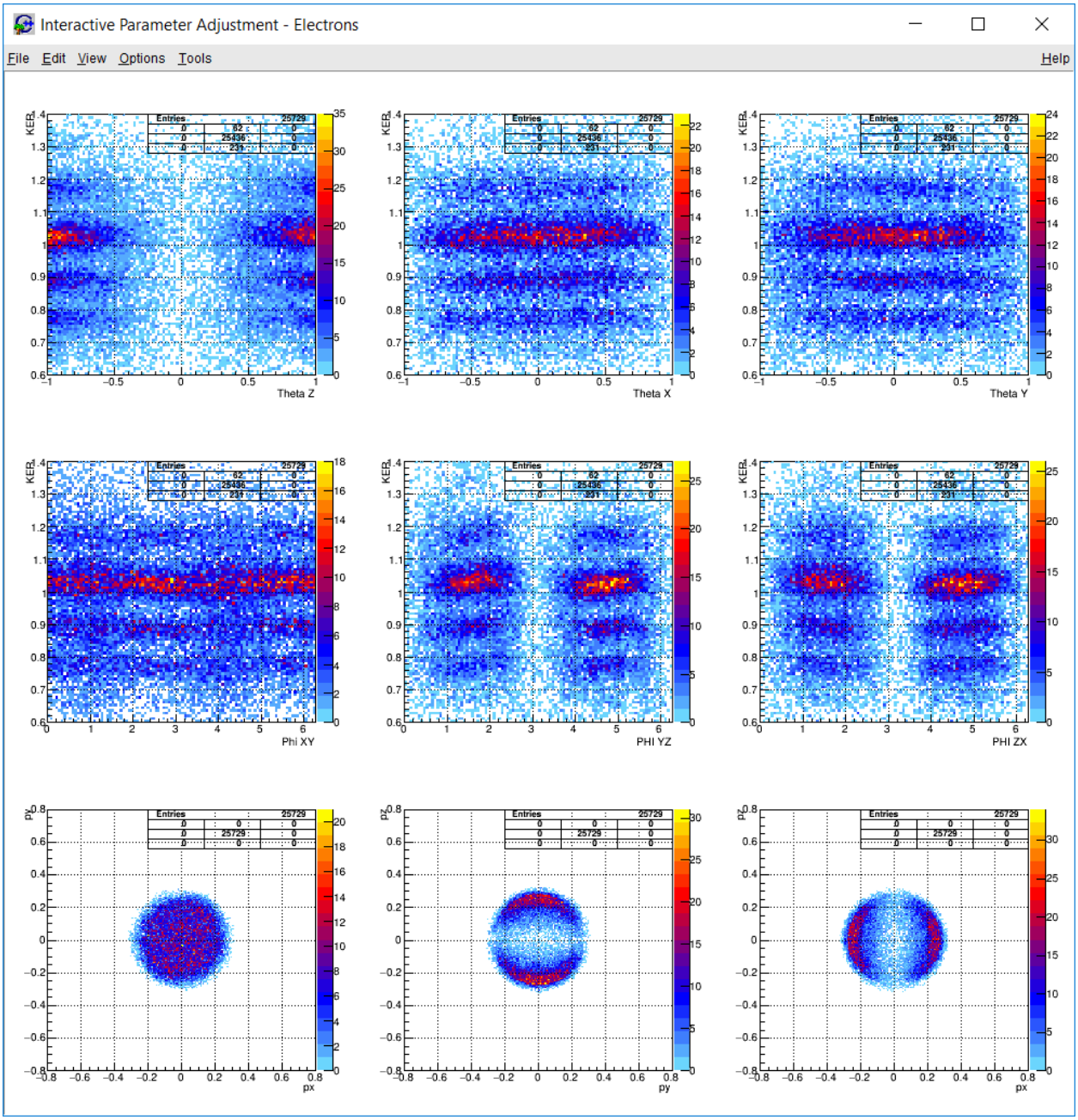

Figure C.4: Electron Calibration Spectra from series d. Top row, left to right: θ_z, θ_x, θ_y vs. E_e. Center row, left to right: ϕ_{xy}, ϕ_{yz}, ϕ_{zx} vs. E_e. Bottom row, left to right: p_x vs. p_y, p_y vs. p_z, p_z vs. p_x.

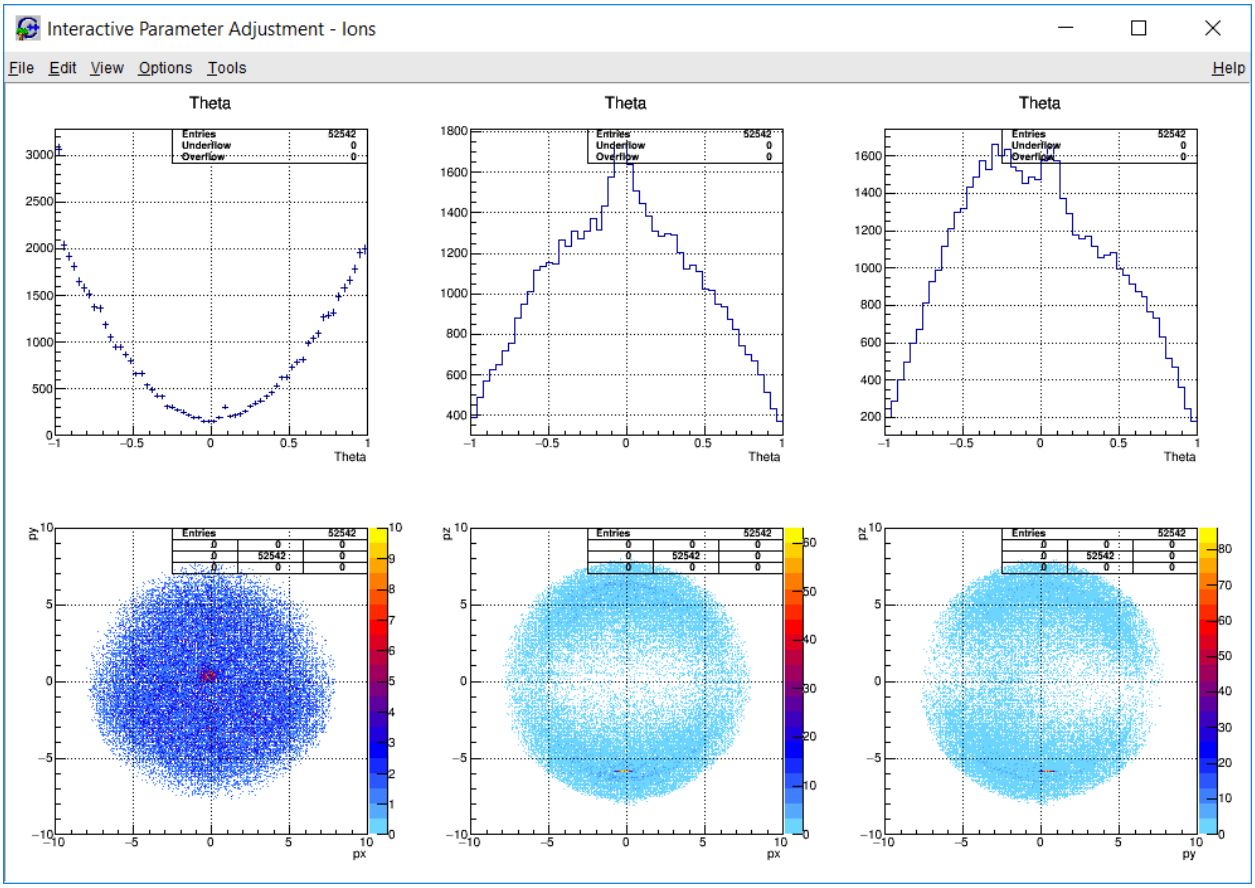

Figure C.5: Ion Calibration Spectra from series d. Top row, left to right: θ_z, θ_x, θ_y. Bottom row, left to right: p_x vs. p_y, p_y vs. p_z, p_z vs. p_x.

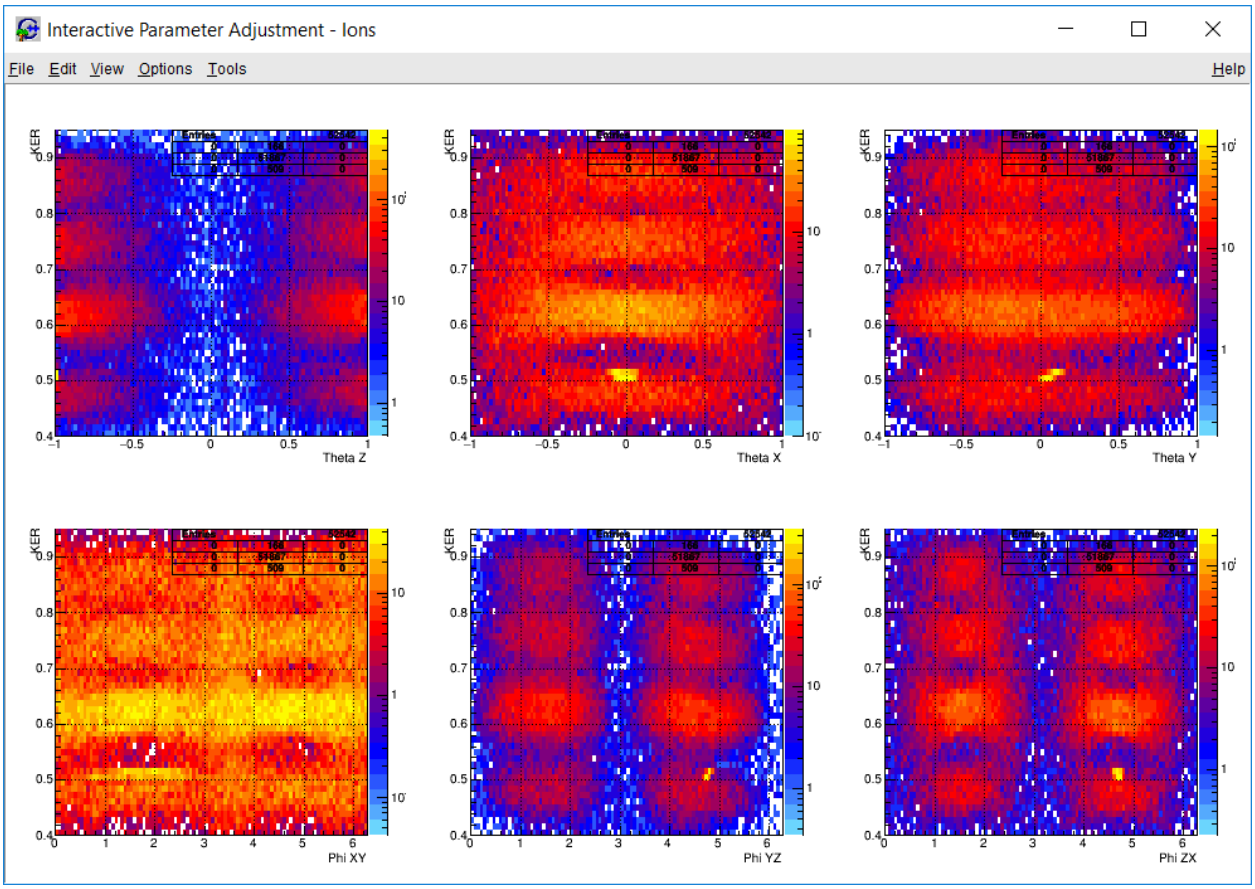

Figure C.6: Ion Calibration Spectra from series d. Top row, left to right: θ_z, θ_x, θ_y vs. KER. Bottom row, left to right: ϕ_{xy}, ϕ_{yz}, ϕ_{zx} vs. KER.

C.3 Data Series e

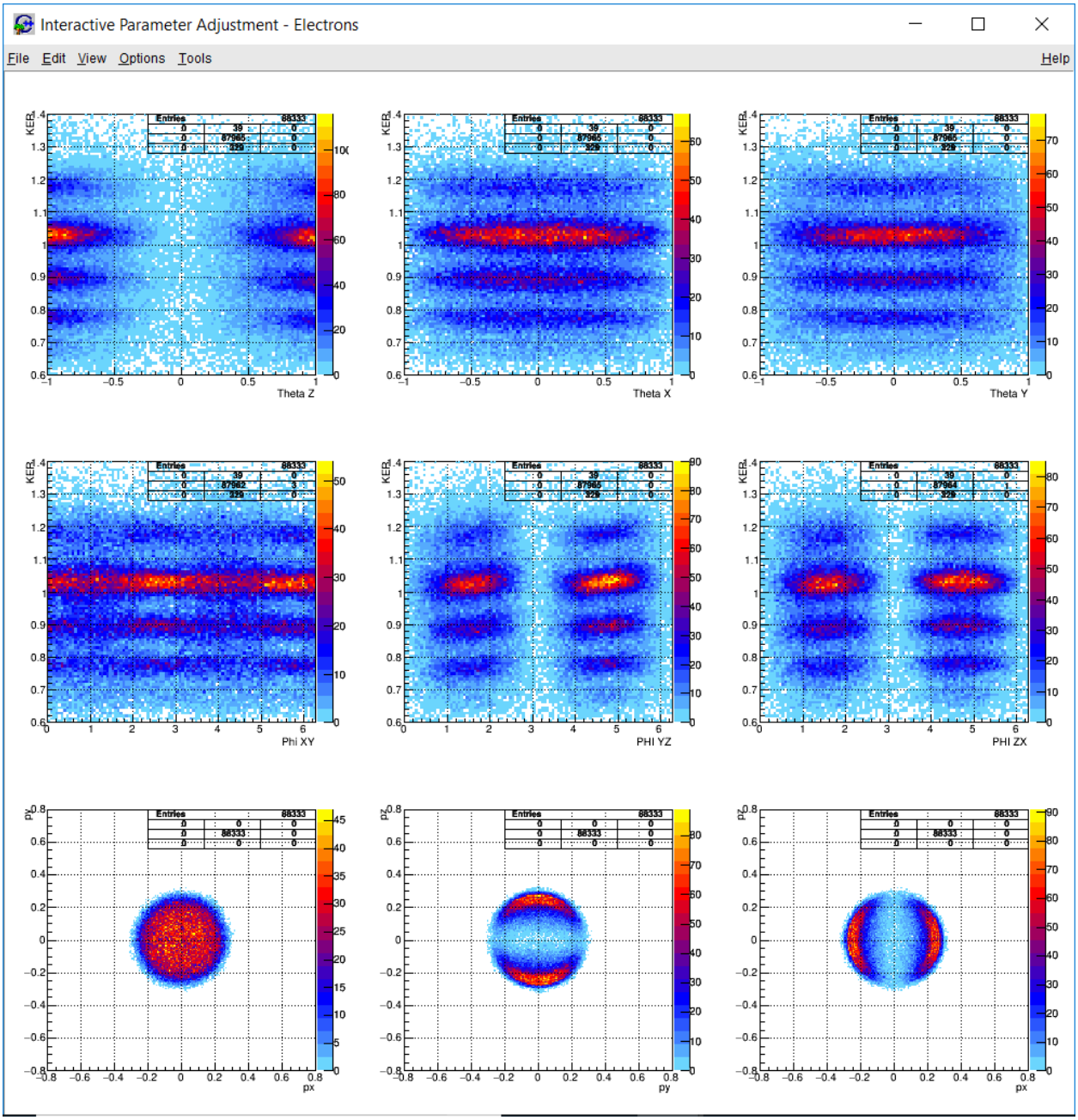

Figure C.7: Electron Calibration Spectra from series e. Top row, left to right: θ_z, θ_x, θ_y vs. E_e. Center row, left to right: ϕ_{xy}, ϕ_{yz}, ϕ_{zx} vs. E_e. Bottom row, left to right: p_x vs. p_y, p_y vs. p_z, p_z vs. p_x.

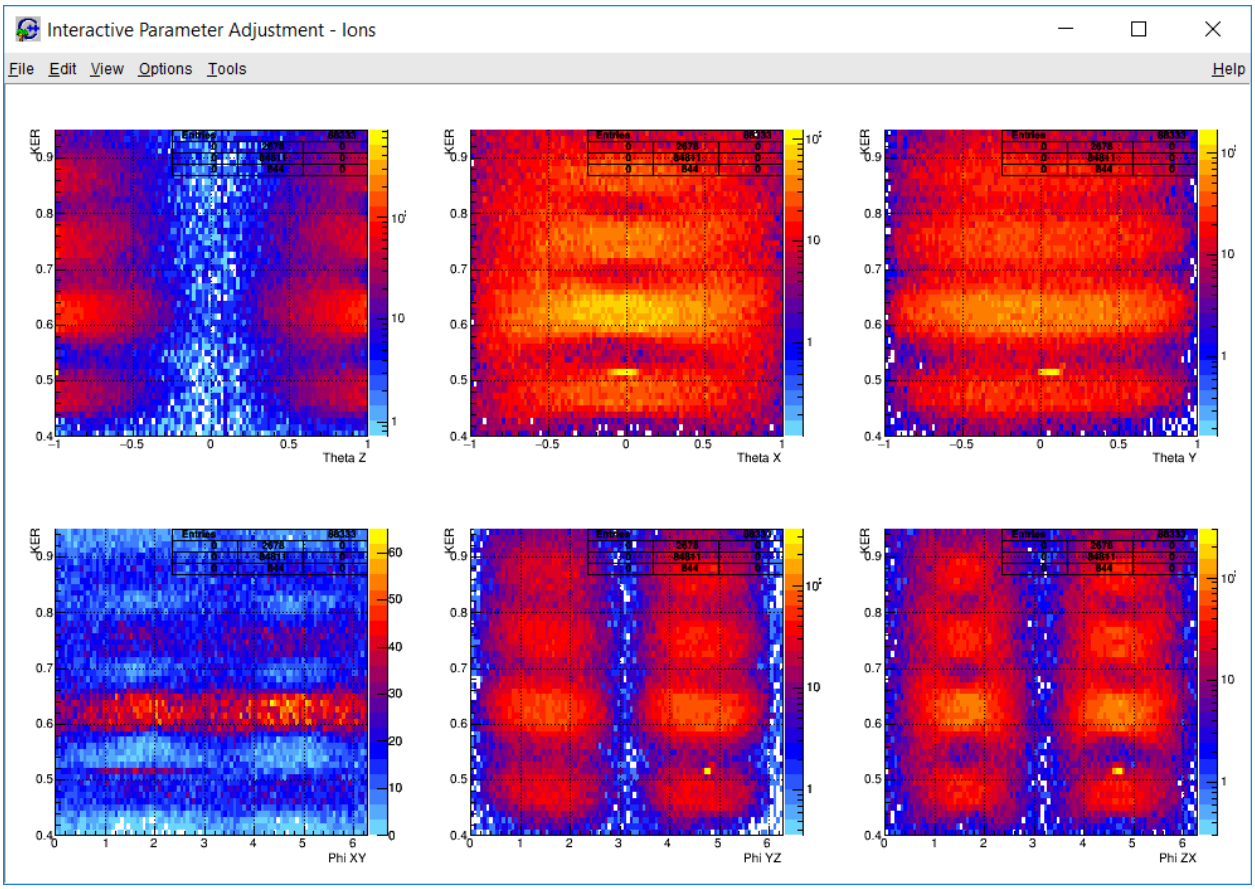

Figure C.8: Ion Calibration Spectra from series e. Top row, left to right: θ_z, θ_x, θ_y. Bottom row, left to right: p_x vs. p_y, p_y vs. p_z, p_z vs. p_x.

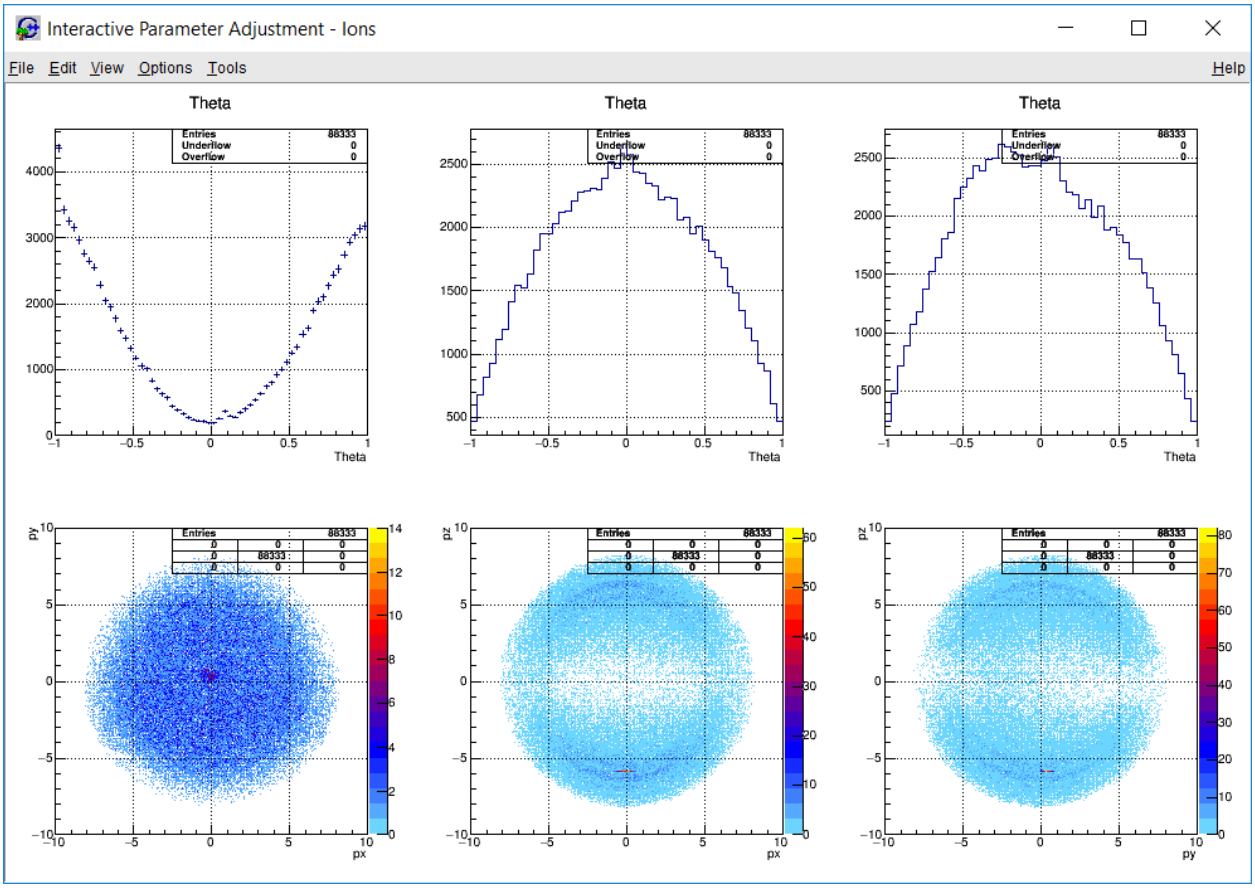

Figure C.9: Ion Calibration Spectra from series e. Top row, left to right: θ_z, θ_x, θ_y vs. KER. Bottom row, left to right: ϕ_{xy}, ϕ_{yz}, ϕ_{zx} vs. KER.

C.4 Data Series f

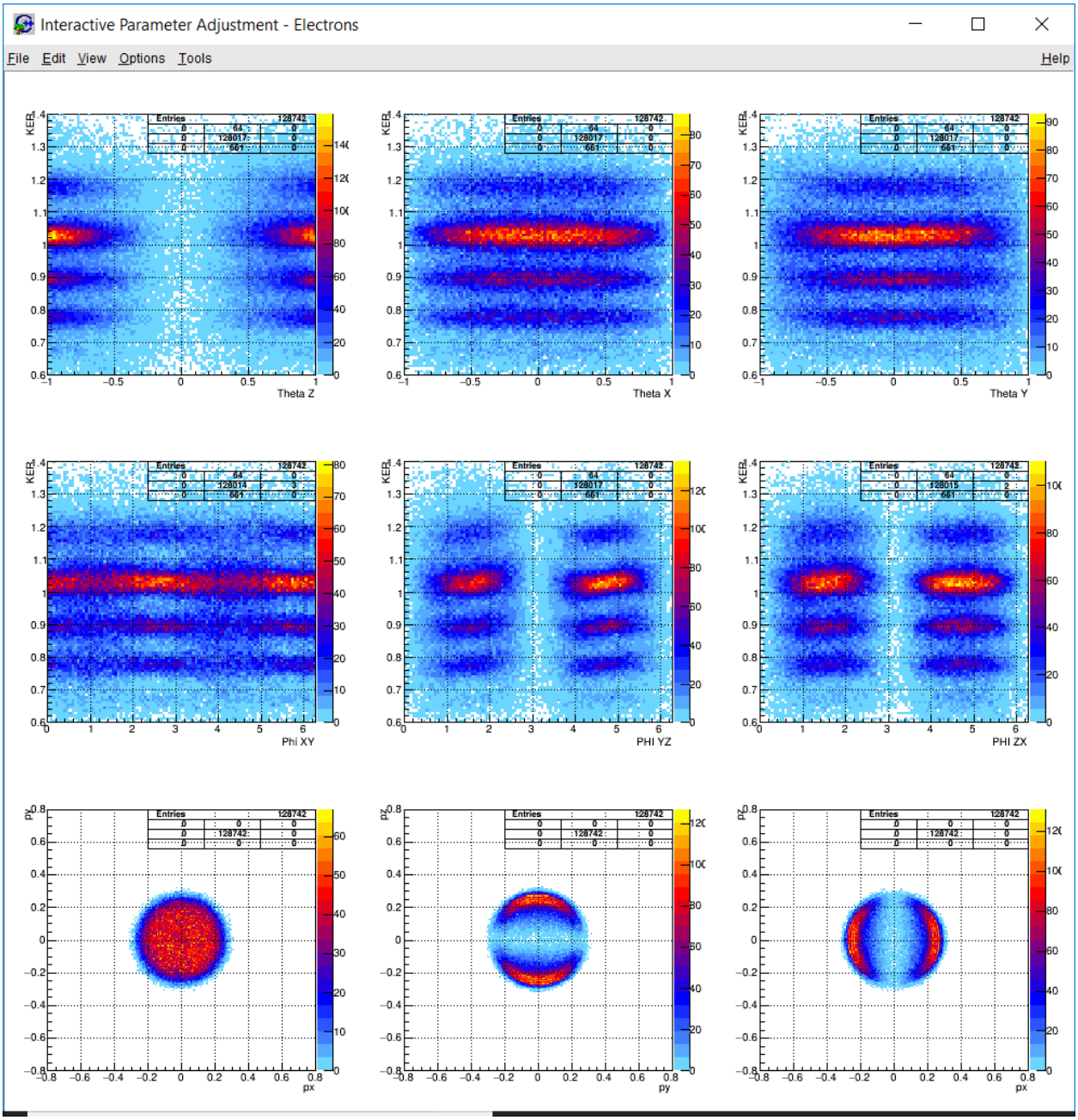

Figure C.10: Electron Calibration Spectra from series f. Top row, left to right: θ_z, θ_x, θ_y vs. E_e. Center row, left to right: ϕ_{xy}, ϕ_{yz}, ϕ_{zx} vs. E_e. Bottom row, left to right: p_x vs. p_y, p_y vs. p_z, p_z vs. p_x.

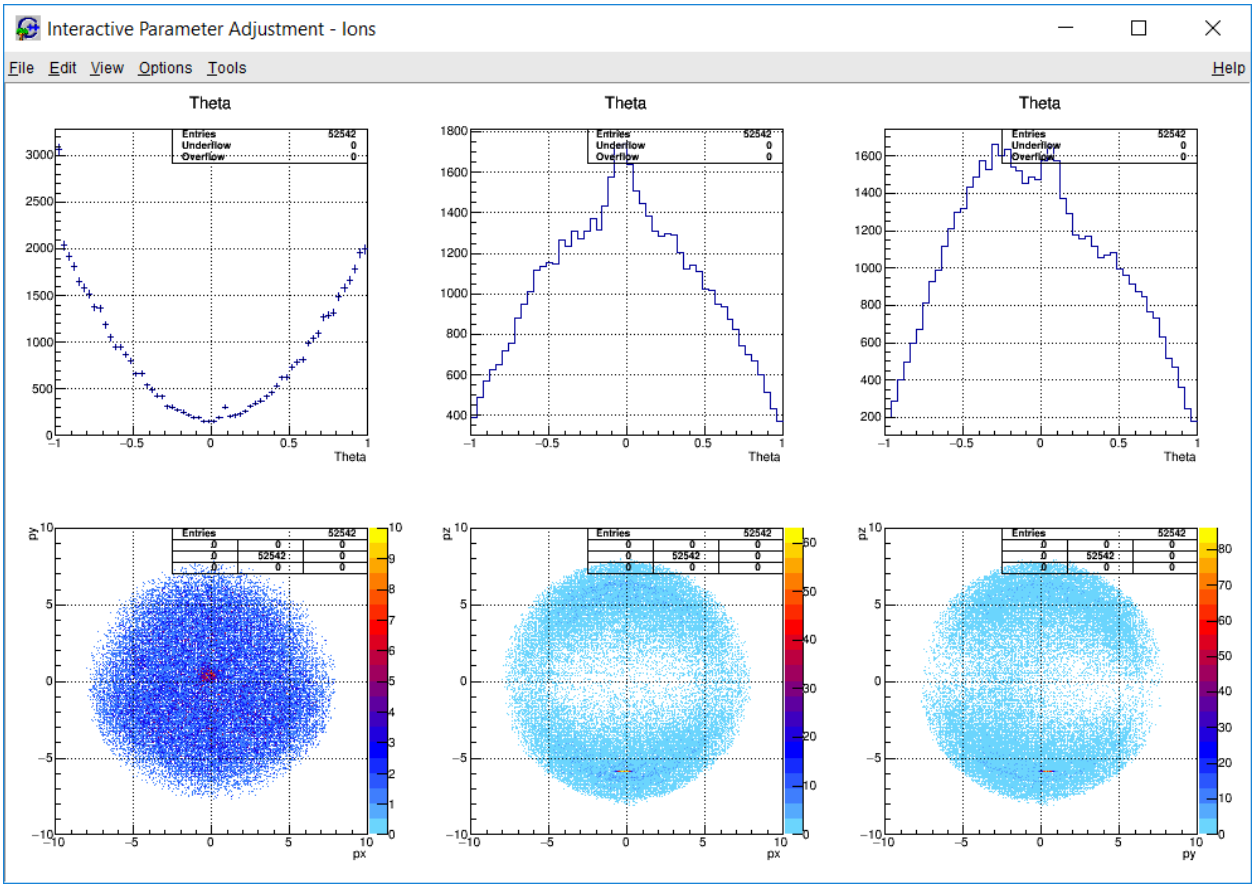

Figure C.11: Ion Calibration Spectra from series f. Top row, left to right: θ_z, θ_x, θ_y. Bottom row, left to right: p_x vs. p_y, p_y vs. p_z, p_z vs. p_x.

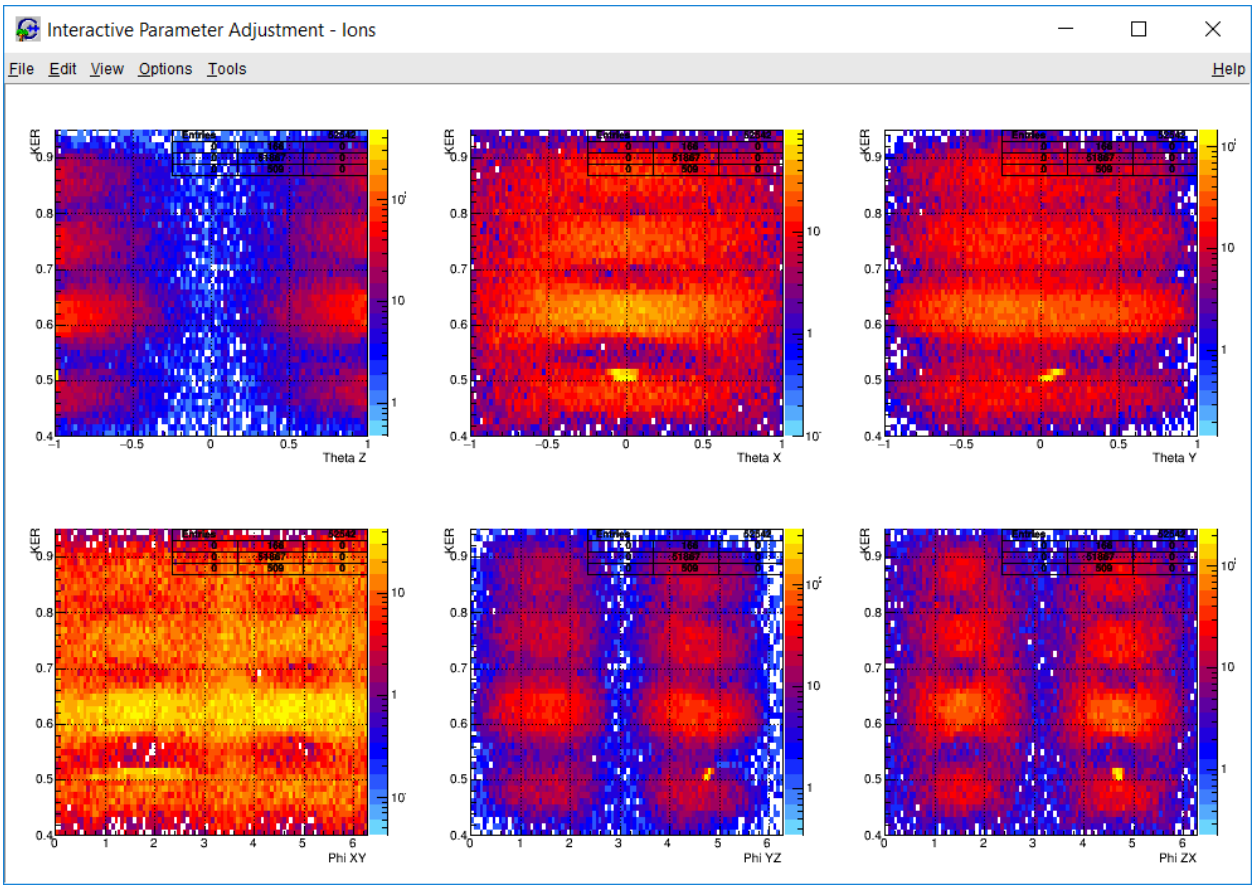

Figure C.12: Ion Calibration Spectra from series f. Top row, left to right: θ_z, θ_x, θ_y vs. KER. Bottom row, left to right: ϕ_{xy}, ϕ_{yz}, ϕ_{zx} vs. KER.

Appendix D

Difference Measurements

This appendix contains a compilation of difference measurements. These measurements rely on the huge number of events available in the single color channel to support background subtraction between laser-on and laser-off signals.

D.1 Data Series b

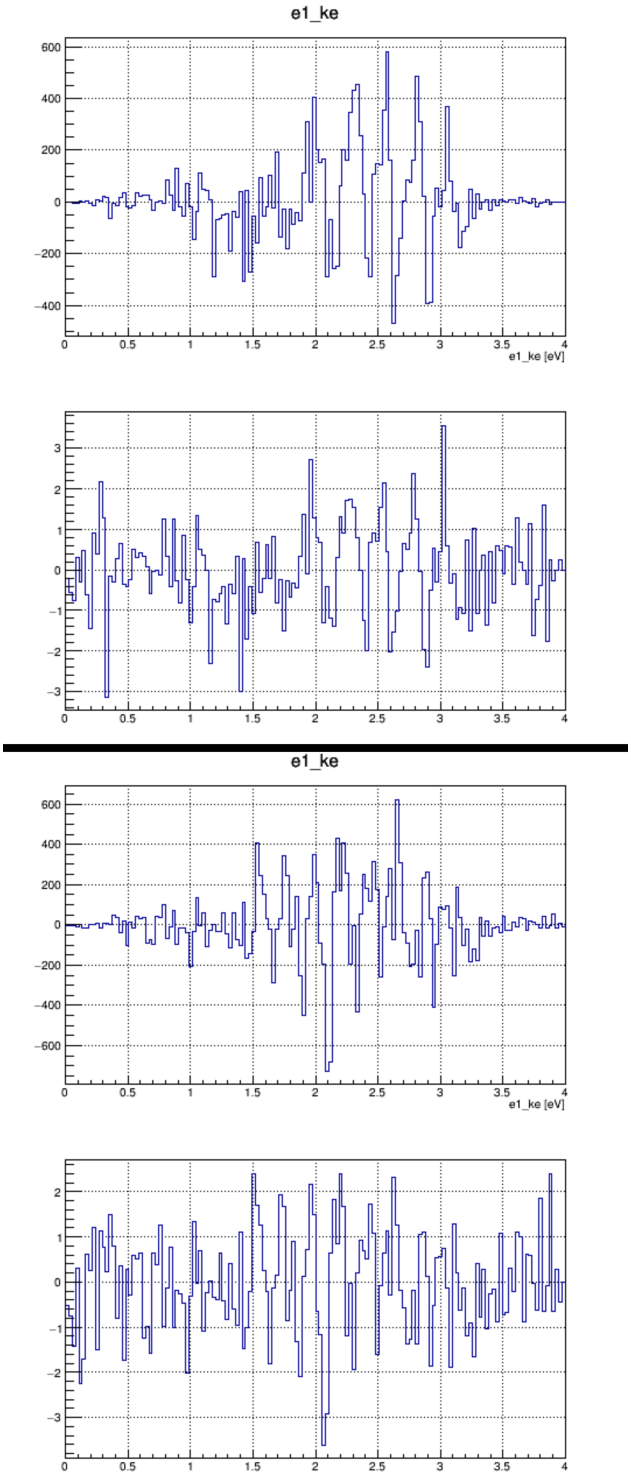

Figure D.1: Electron kinetic energy spectra from the H_2+ channel. The top two spectra are gated on the electron half of the spectrometer and the bottom two for the ion half, as demarcated by the black line. Top plot for each pair is a direct subtraction. Bottom plot are the residuals from a chi square fit.

D.2 Data Series d

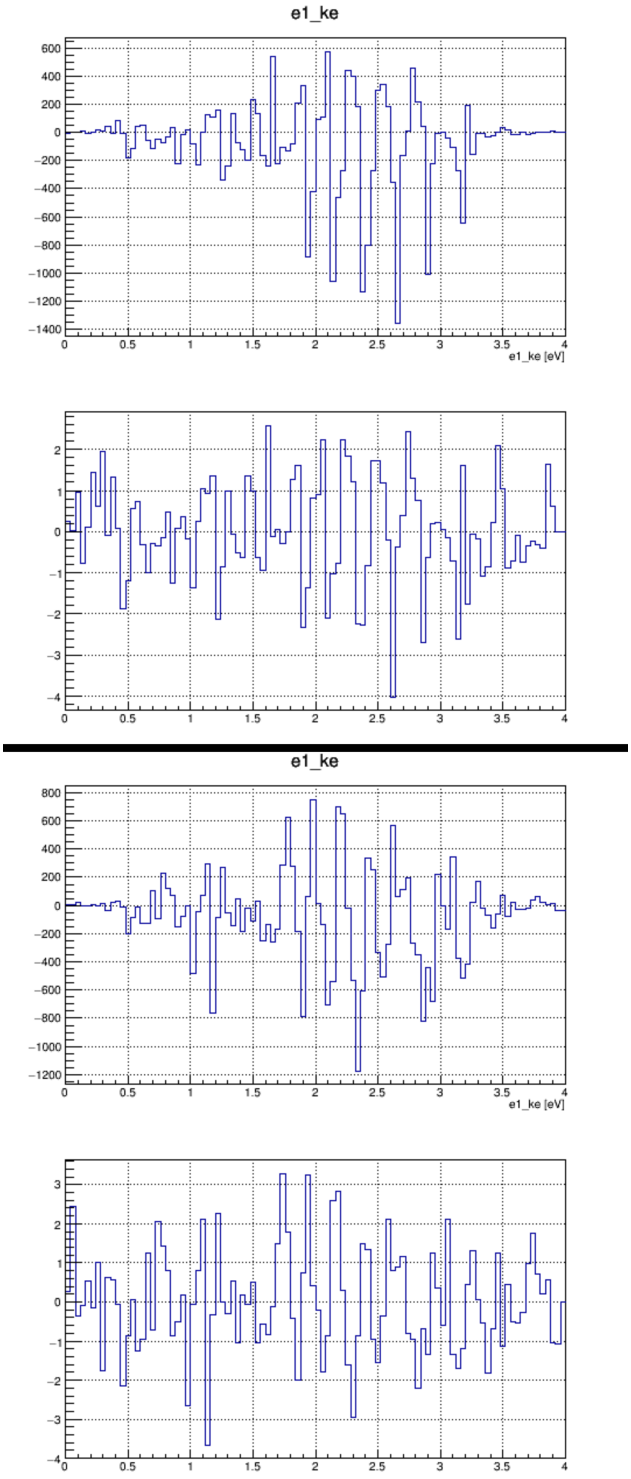

Figure D.2: Electron kinetic energy spectra from the H_2+ channel. The top two spectra are gated on the electron half of the spectrometer and the bottom two for the ion half, as demarcated by the black line. Top plot for each pair is a direct subtraction. Bottom plot are the residuals from a chi square fit.

D.3 Data Series e

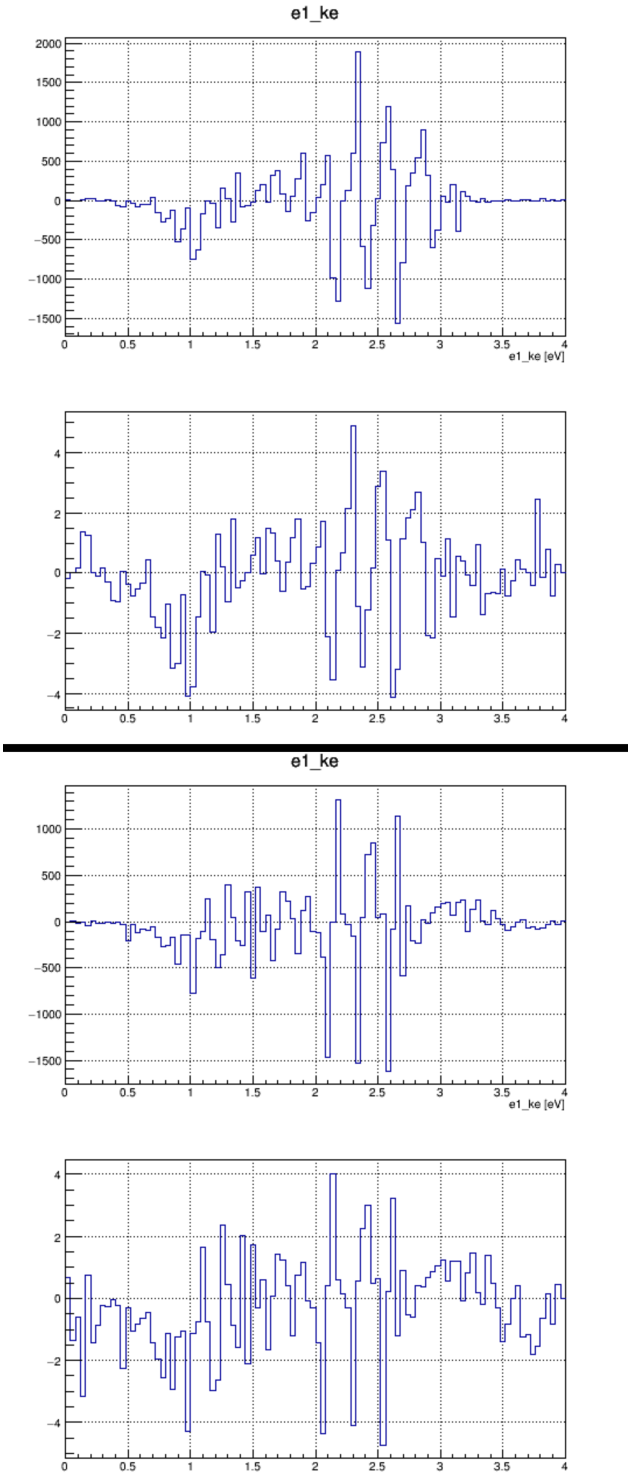

Figure D.3: Electron kinetic energy spectra from the H_2+ channel. The top two spectra are gated on the electron half of the spectrometer and the bottom two for the ion half, as demarcated by the black line. Top plot for each pair is a direct subtraction. Bottom plot are the residuals from a chi square fit.

D.4 Data Series f

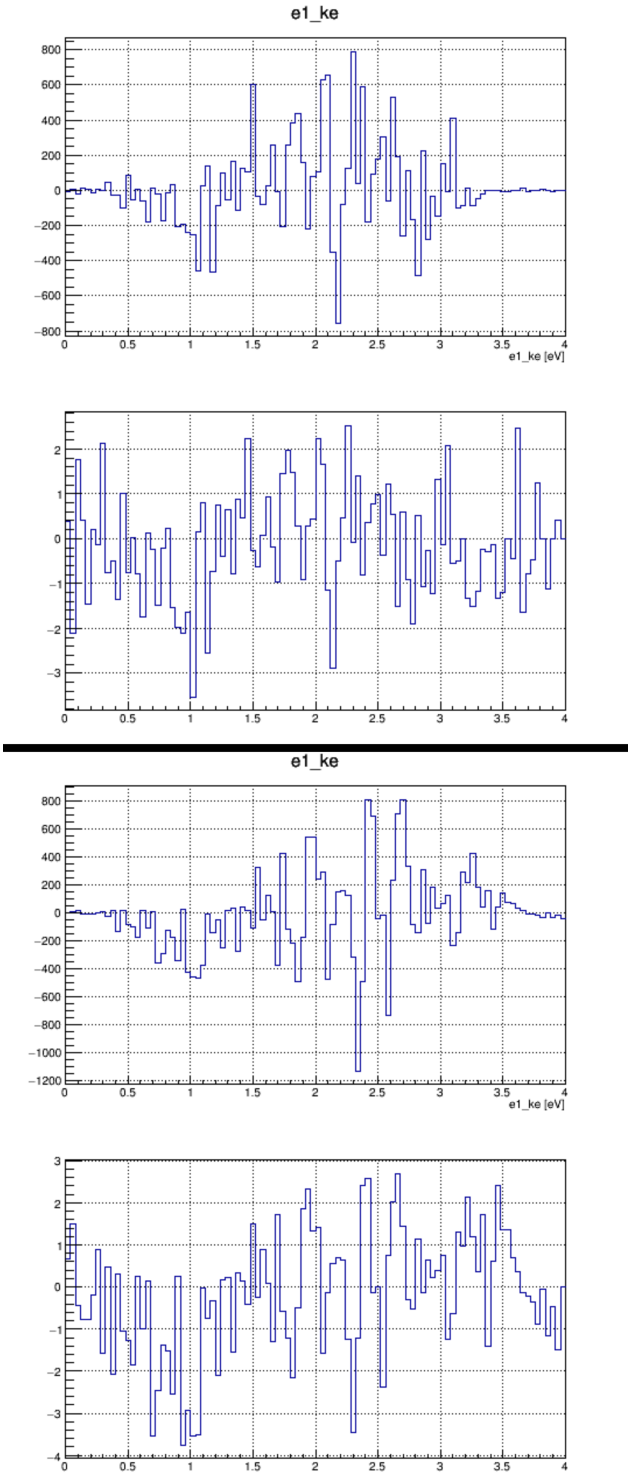

Figure D.4: Electron kinetic energy spectra from the H_2+ channel. The top two spectra are gated on the electron half of the spectrometer and the bottom two for the ion half, as demarcated by the black line. Top plot for each pair is a direct subtraction. Bottom plot are the residuals from a chi square fit.

Appendix E

2-Color Measurements

This appendix contains a compilation of angular spectra for datasets b, d, e and f.

E.1 Data Series b

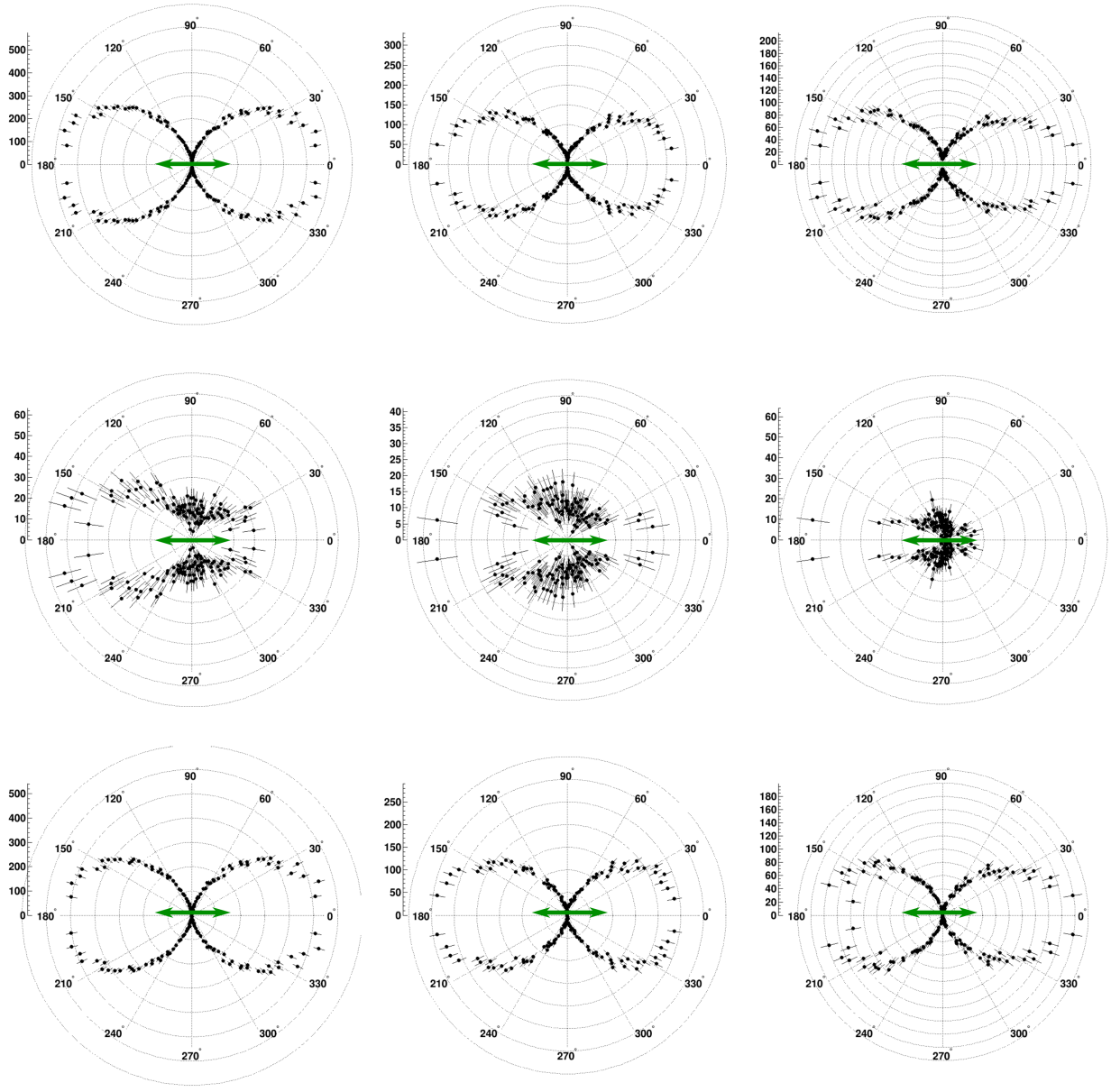

Figure E.1: Laser-dissociated $H+$ angular distributions relative to the laser polarization. Columns left to right: $\nu = 10, 11, 12$. Top row: laser-on channel. Middle row: laser-off channel - the background. Bottom row: laser-off channel subtracted from laser-on channel.

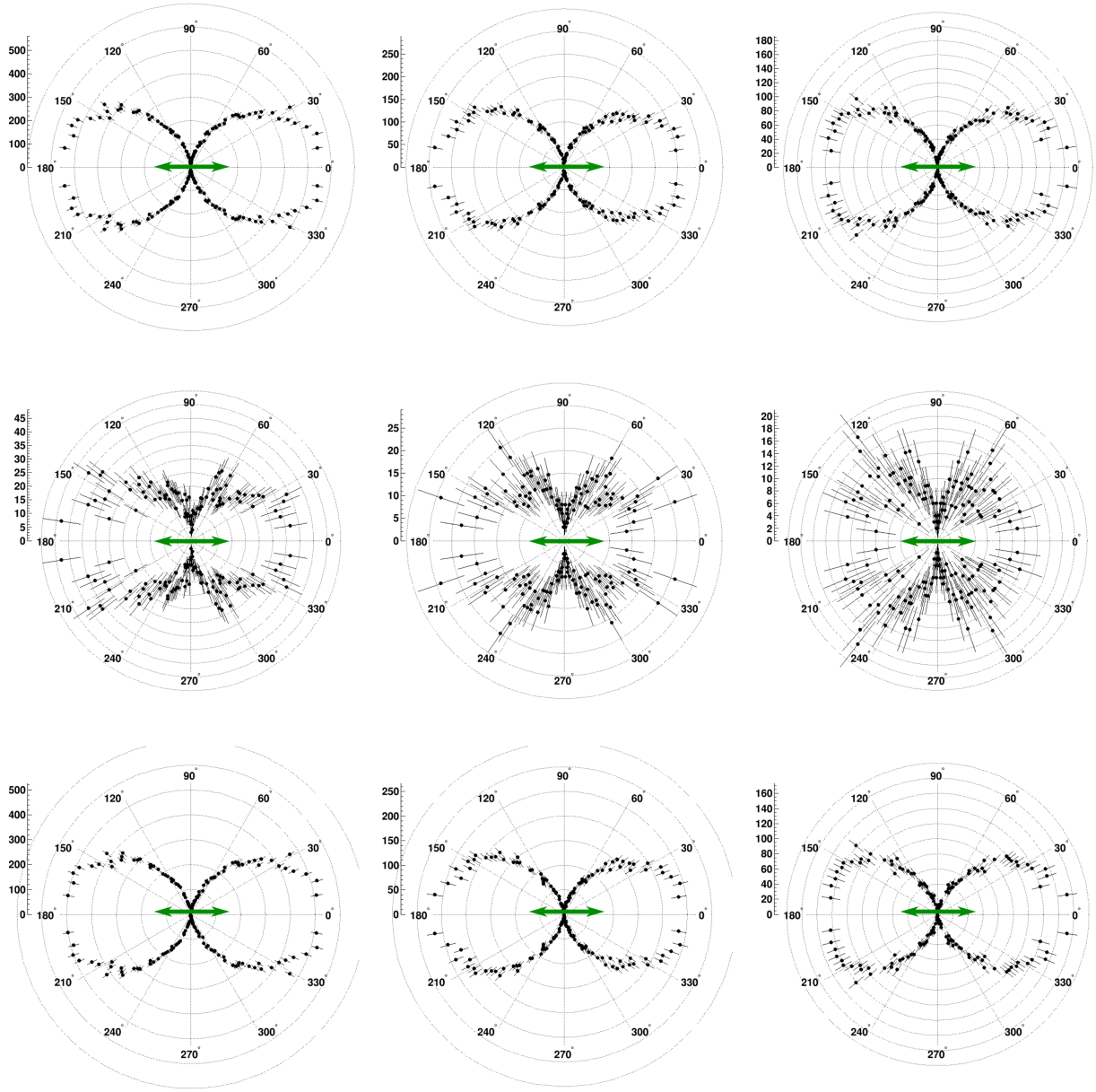

Figure E.2: Photoelectron angular distributions relative to the XUV polarization. Columns left to right: $\nu = 10, 11, 12$. Top row: laser-on channel. Middle row: laser-off channel - the background. Bottom row: laser-off channel subtracted from laser-on channel.

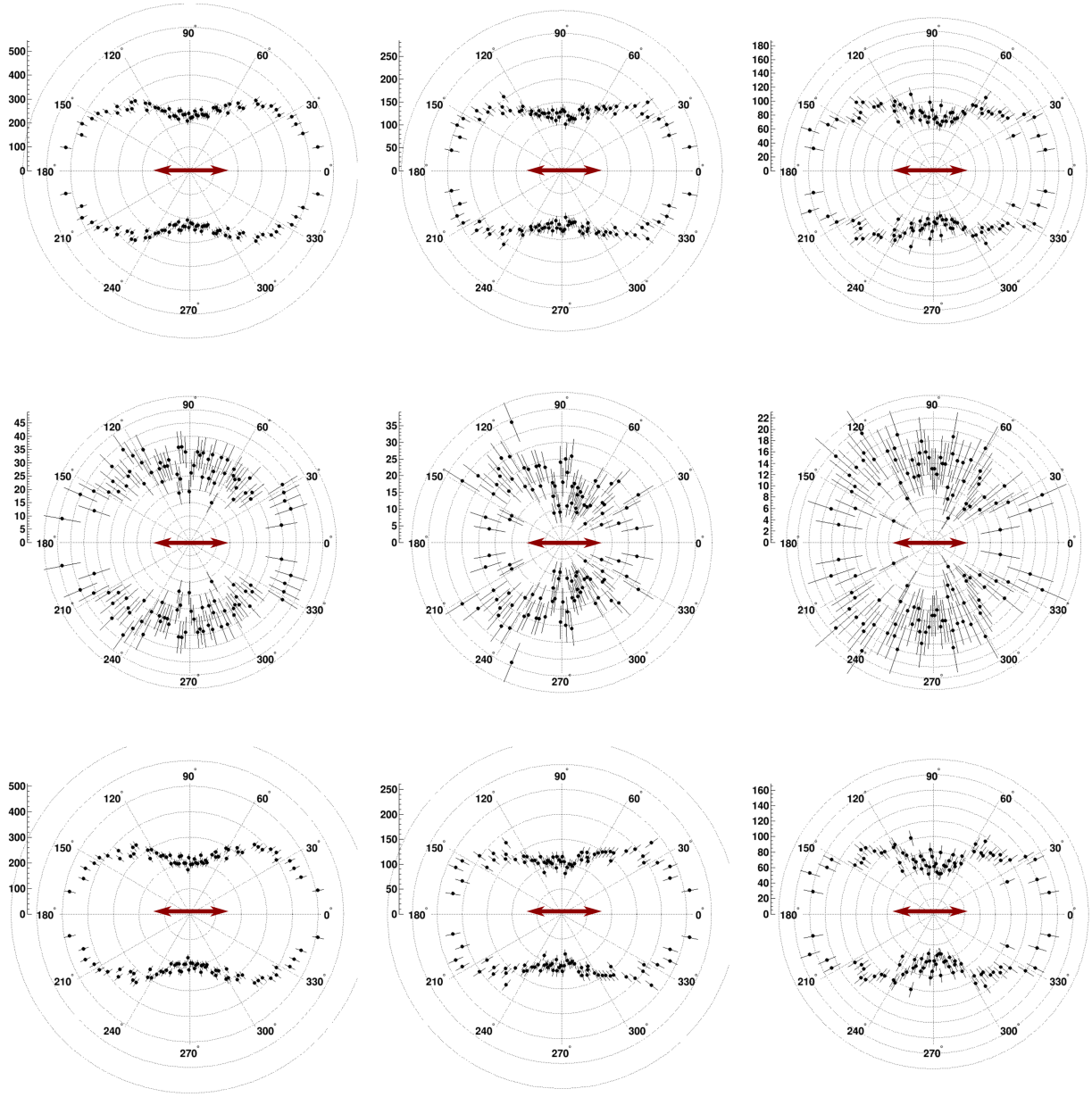

Figure E.3: Molecular frame photoelectron angular distributions relative to the emission direction of the $H+$ directed towards 0°. Columns left to right: $\nu = 10, 11, 12$. Top row: laser-on channel. Middle row: laser-off channel - the background. Bottom row: laser-off channel subtracted from laser-on channel.

E.2 Data Series d

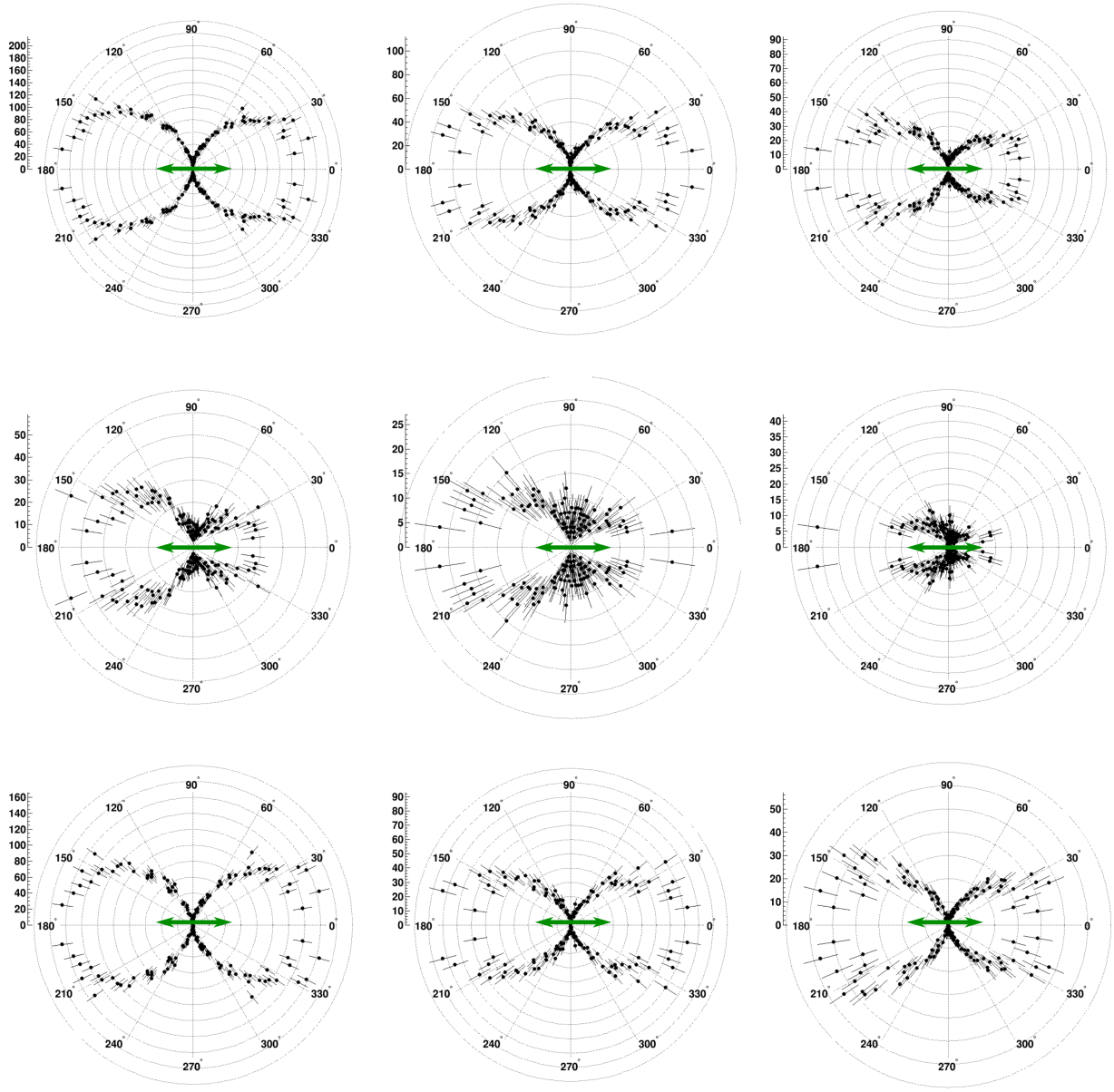

Figure E.4: Laser-dissociated $H+$ angular distributions relative to the laser polarization. Columns left to right: $\nu = 10, 11, 12$. Top row: laser-on channel. Middle row: laser-off channel - the background. Bottom row: laser-off channel subtracted from laser-on channel.

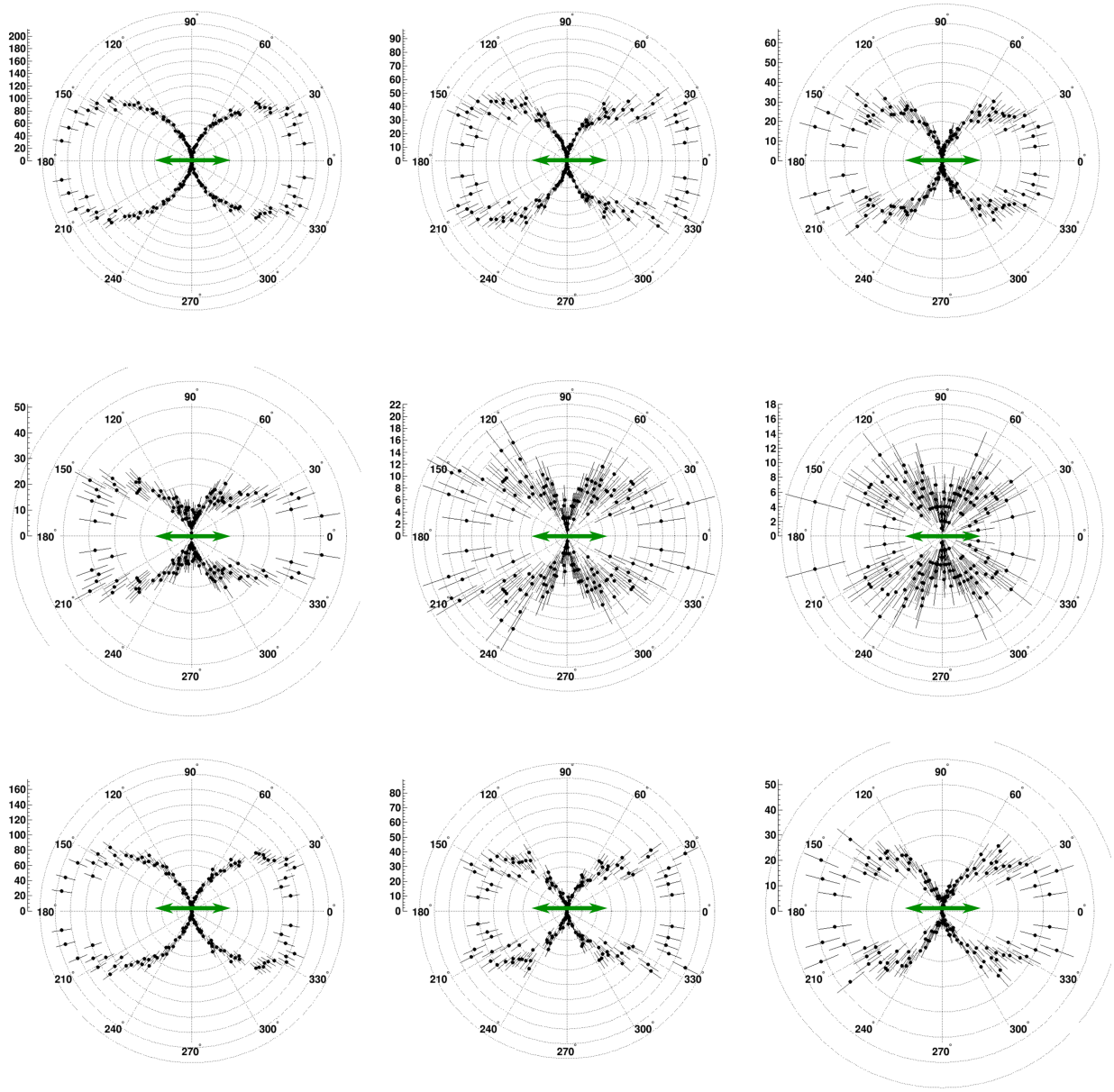

Figure E.5: Photoelectron angular distributions relative to the XUV polarization. Columns left to right: $\nu = 10, 11, 12$. Top row: laser-on channel. Middle row: laser-off channel - the background. Bottom row: laser-off channel subtracted from laser-on channel.

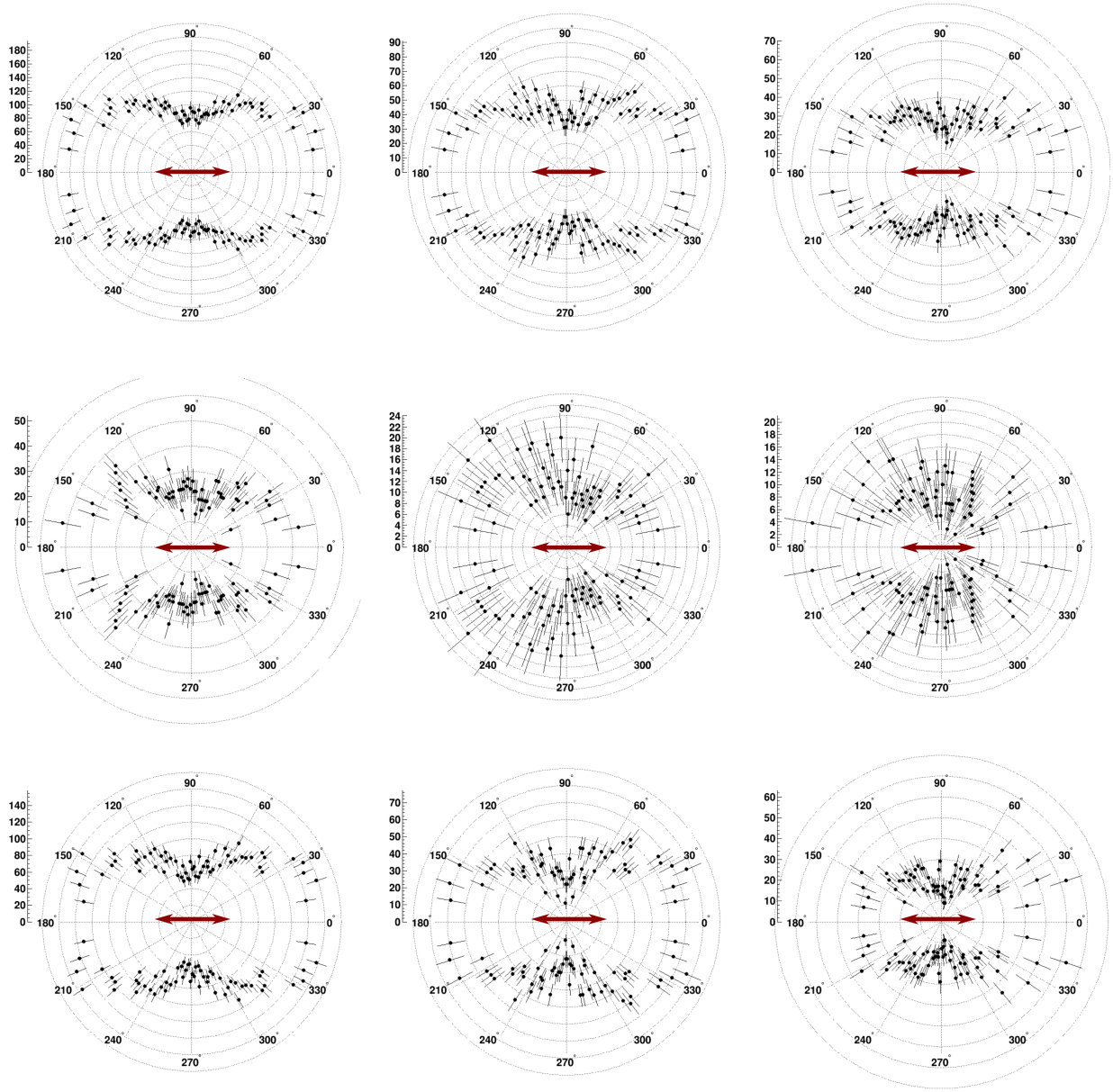

Figure E.6: Molecular frame photoelectron angular distributions relative to the emission direction of the $H+$ directed towards 0°. Columns left to right: $\nu = 10, 11, 12$. Top row: laser-on channel. Middle row: laser-off channel - the background. Bottom row: laser-off channel subtracted from laser-on channel.

E.3 Data Series e

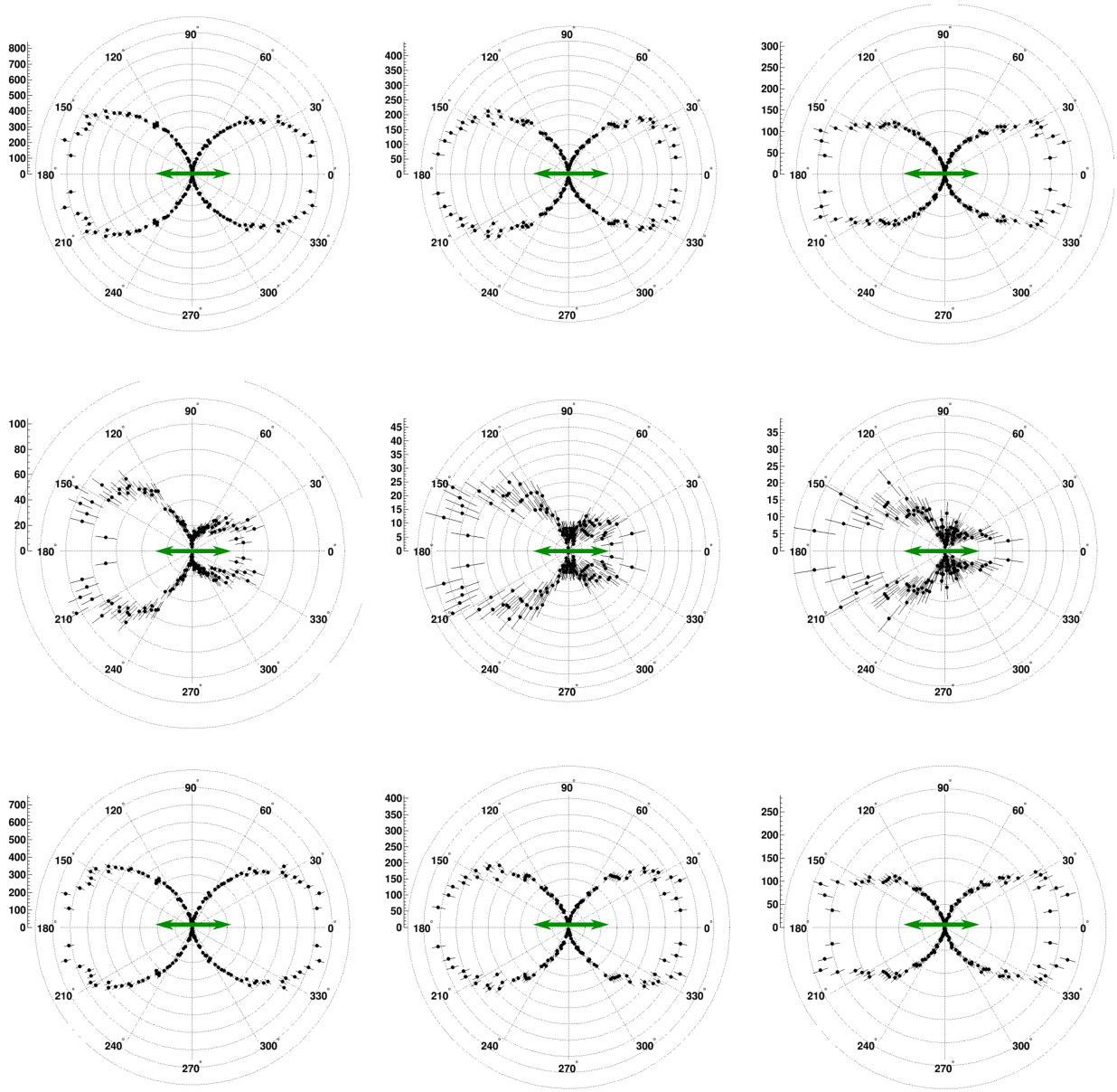

Figure E.7: Laser-dissociated $H+$ angular distributions relative to the laser polarization. Columns left to right: $\nu = 10, 11, 12$. Top row: laser-on channel. Middle row: laser-off channel - the background. Bottom row: laser-off channel subtracted from laser-on channel.

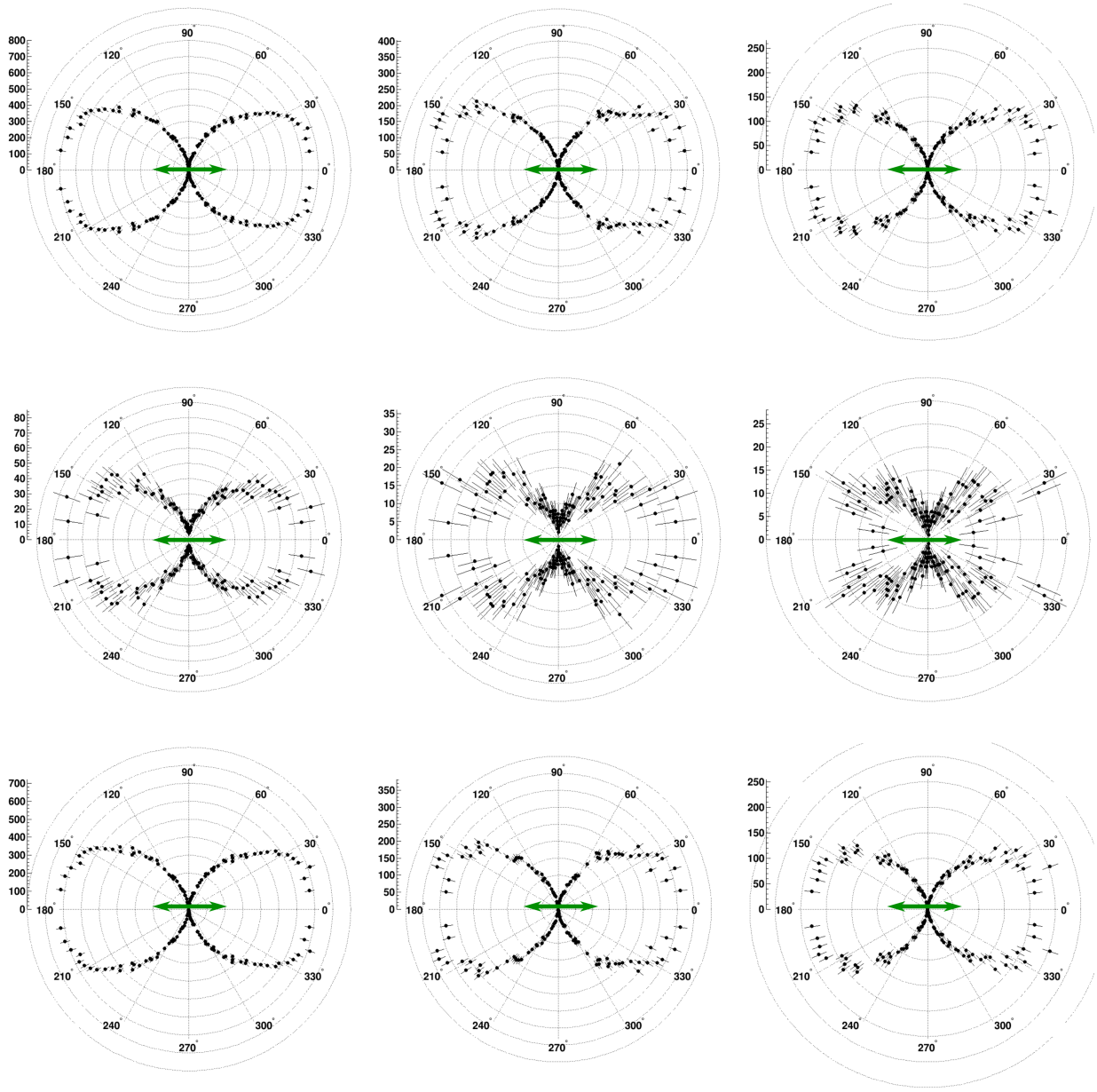

Figure E.8: Photoelectron angular distributions relative to the XUV polarization. Columns left to right: $\nu = 10, 11, 12$. Top row: laser-on channel. Middle row: laser-off channel - the background. Bottom row: laser-off channel subtracted from laser-on channel.

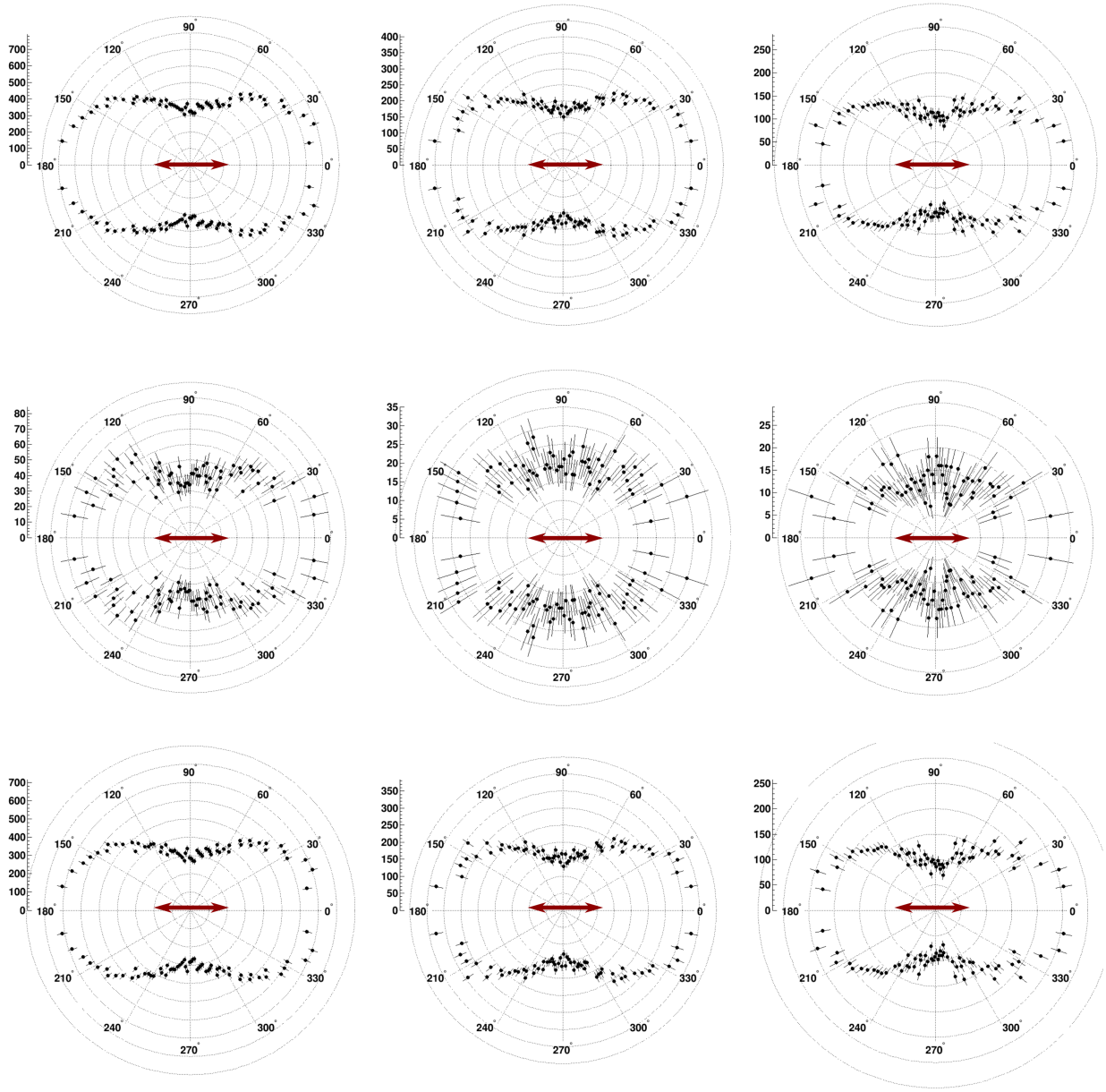

Figure E.9: Molecular frame photoelectron angular distributions relative to the emission direction of the $H+$ directed towards 0°. Columns left to right: $\nu = 10, 11, 12$. Top row: laser-on channel. Middle row: laser-off channel - the background. Bottom row: laser-off channel subtracted from laser-on channel.

E.4 Data Series f

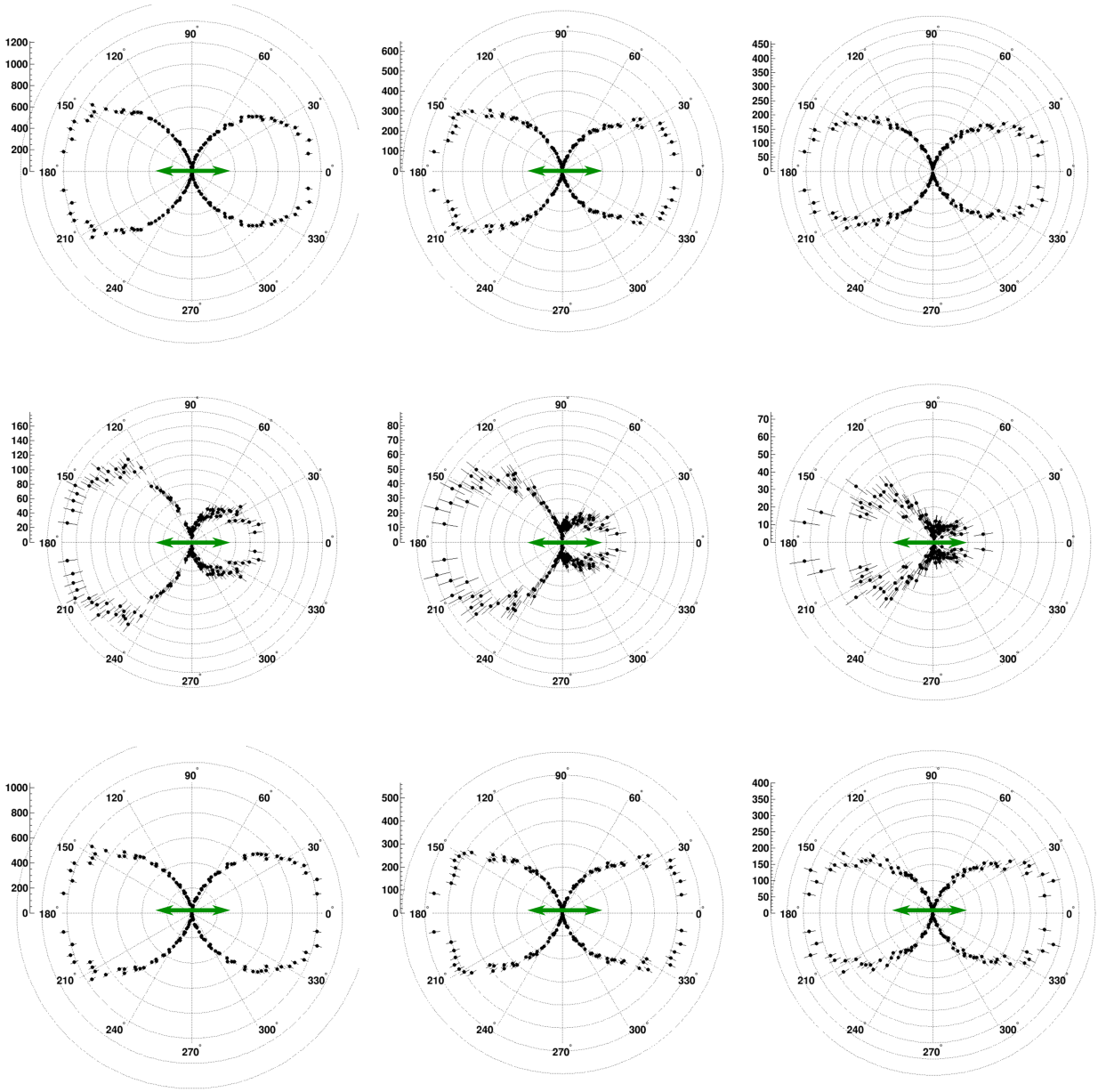

Figure E.10: Laser-dissociated $H+$ angular distributions relative to the laser polarization. Columns left to right: $\nu = 10, 11, 12$. Top row: laser-on channel. Middle row: laser-off channel - the background. Bottom row: laser-off channel subtracted from laser-on channel.

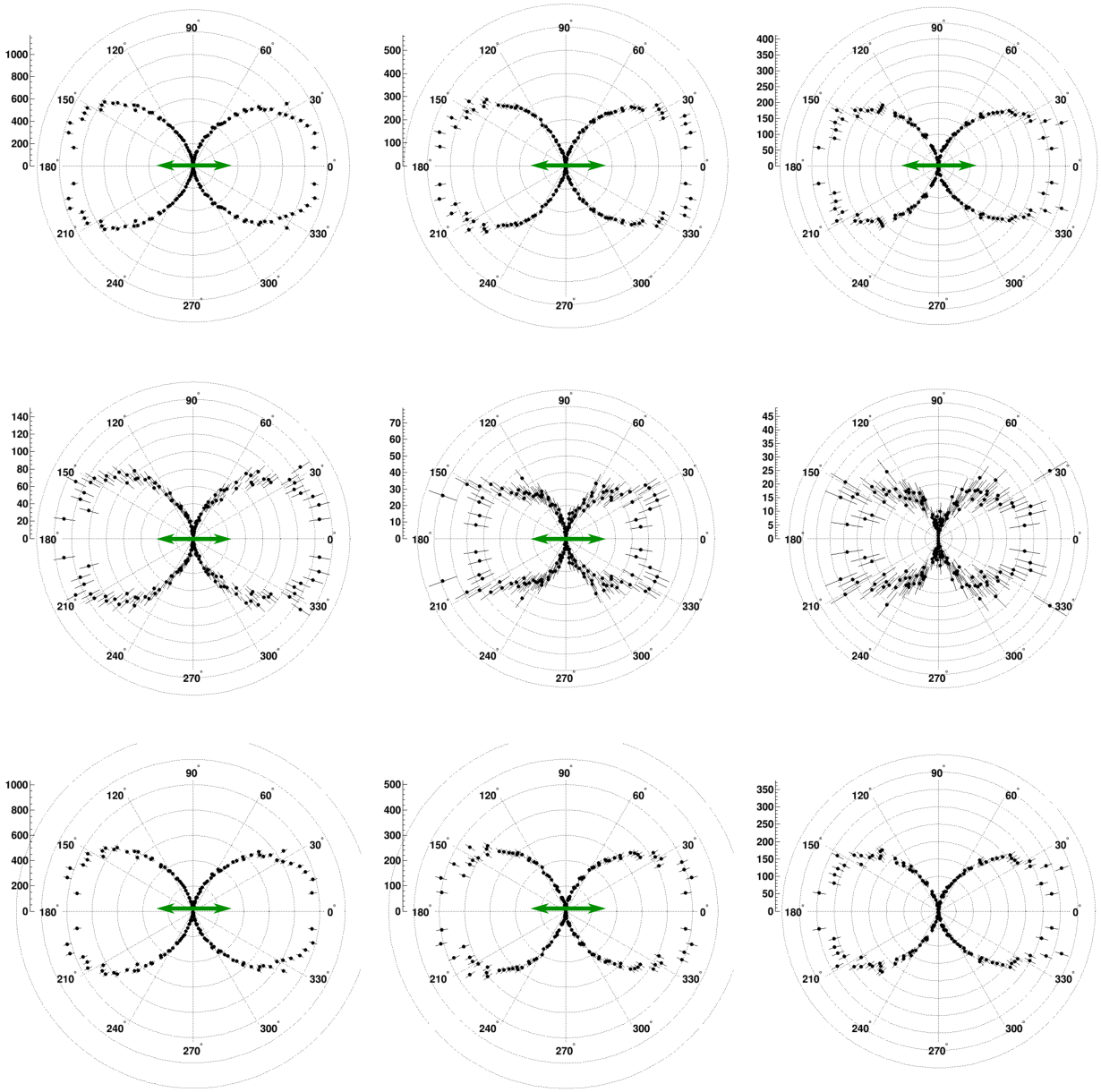

Figure E.11: Photoelectron angular distributions relative to the XUV polarization. Columns left to right: $\nu = 10, 11, 12$. Top row: laser-on channel. Middle row: laser-off channel - the background. Bottom row: laser-off channel subtracted from laser-on channel.

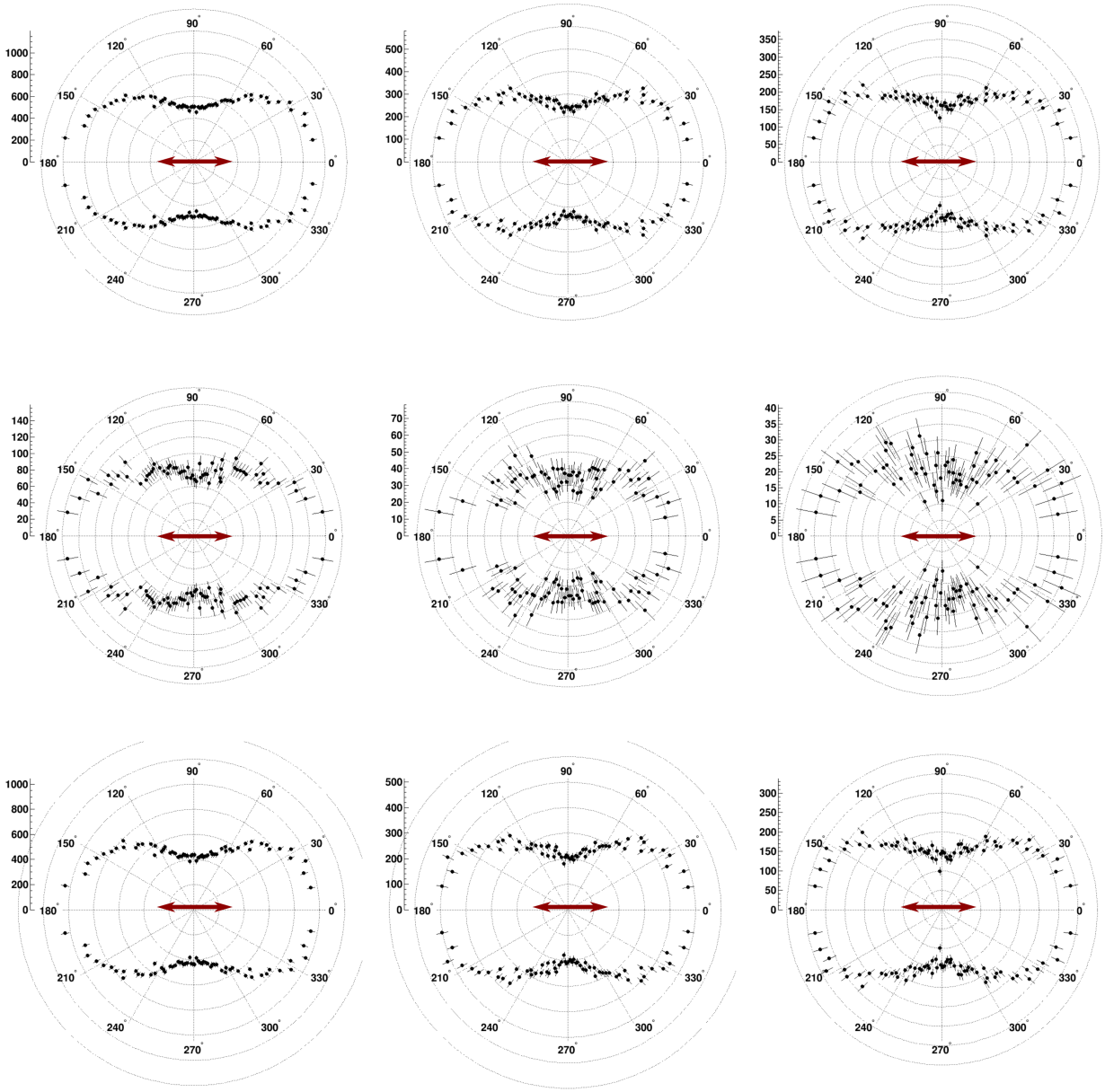

Figure E.12: Molecular frame photoelectron angular distributions relative to the emission direction of the $H+$ directed towards 0°. Columns left to right: $\nu = 10, 11, 12$. Top row: laser-on channel. Middle row: laser-off channel - the background. Bottom row: laser-off channel subtracted from laser-on channel.

Appendix F
Analysis Code

Here we present select code from the analysis software.

F.1 Electron Momentum Calculations

```
1  // ************************************************************
2  // **
3  // ** calculate momenta for electron x,y direction (magnetic field)
4  // ** using Mirko's functions.
5  // **
6  // ************************************************************
7
8  double calc_px(double tof_ns, double x_mm, double y_mm, double mass_amu,
       double charge_au, double BField_ns, bool BField_clockwise = true) {
9
10 double px;
11
12 if(mass_amu<1.0) {
13 double w,a,b;
14
15 double m = mass_amu * MASSAU * MEKG;
16 double q = charge_au * COULOMB;
17 double pau = m*300.e6/137.;
18
19 double fieldB = 2.*m*3.14159 / (q * BField_ns * 1e-9);
20
21 if(BField_clockwise)
22 fieldB = -fieldB;
23
24 w = q / m * fieldB;
25 a = (1. - cos(w * tof_ns*1.e-9)) / w;
26 b = (sin(w * tof_ns*1.e-9)) / w;
27
28 px = m * (x_mm/1000. * b + a*y_mm/1000.) / (a*a + b*b);//Re-derived 3/21/2017
29
30 //px = m * (x_mm/1000. * b - a*y_mm/1000.) / (a*a + b*b); //Finally corrected.
       This is absolutely correct. Nope
31 //px = m * (x_mm/1000. * b + a*y_mm/1000.) / (a*a + b*b);
32 // px = (m*w/2) * (x_mm/1000. * cot(w * tof_ns*1.e-9/2) + y_mm/1000.) // this
       line equals the above line
33
34 ////////////////////////////////////////////////////////////
35 /////wrong defined - clockwise and counterclockwise mixed up/////
36 ////////////////////////////////////////////////////////////
37 //px = m * (x_mm/1000. * b - a*y_mm/1000.) / (a*a + b*b);
```

```
38 // px = (m*w/2) * (x_mm/1000. * cot(w * tof_ns*1.e-9/2) - y_mm/1000.) // this
       line equals the above line
39 px = px / pau;
40 } else {
41 double vau = 2.1877e+6;
42 px = x_mm/1000. / ((tof_ns)*1e-9) / vau * mass_amu * MASSAU;
43 }
44 return px;
45 }
46
47 double calc_py(double tof_ns, double x_mm, double y_mm, double mass_amu,
       double charge_au, double BField_ns, bool BField_clockwise = true) {
48
49 double py;
50
51 if(mass_amu<1.0) {
52
53 double w,a,b;
54
55 double m = mass_amu * MASSAU * MEKG;
56 double q = charge_au * COULOMB;
57 double pau = m*300.e6/137.;
58
59 double fieldB = 2.*m*3.14159 / (q * BField_ns * 1e-9);
60
61 if(BField_clockwise)
62 fieldB = -fieldB;
63
64 w = q / m * fieldB;
65 a = (1. - cos(w * tof_ns*1.e-9)) / w;
66 b = (sin(w * tof_ns*1.e-9)) / w;
67
68 py = m * (-x_mm/1000. * a + b*y_mm/1000.) / (a*a + b*b); //Re-derived
       3/21/2017
69
70 //py = m * (x_mm/1000. * a + b*y_mm/1000.) / (a*a + b*b); //Finally corrected.
       This is absolutely correct. Nope!
71 //py = m * (x_mm/1000. * a + b*y_mm/1000.) / (a*a + b*b);
72
73 //py = m * (-x_mm/1000. * a + b*y_mm/1000.) / (a*a + b*b);
74 //px = (m*w/2) * (-x_mm/1000. * cot(w * tof_ns*1.e-9/2) + y_mm/1000.) // this
       line equals the above line
75
76 ////////////////////////////////////////////////////////////
77 /////wrong defined - clockwise and counterclockwise mixed up/////
78 ////////////////////////////////////////////////////////////
79 //py = m * (-x_mm/1000. * a - b*y_mm/1000.) / (a*a + b*b); //[original code]
80 //py = m * (x_mm/1000. * a + b*y_mm/1000.) / (a*a + b*b); // corrected by
       Jonathan
81 //px = (m*w/2) * (x_mm/1000. * cot(w * tof_ns*1.e-9/2) + y_mm/1000.) // this
       line equals the above line
82 py = py / pau;
83
84 } else {
```

```
85 double vau = 2.1877e+6;
86 py = y_mm/1000. / ((tof_ns)*1e-9) / vau * mass_amu * MASSAU;
87 }
88
89 return py;
90 }
```

F.2 LUT Generation

Below is the function that generates the lookup table. File IO operations have been omitted for brevity.

```
1  void LUT_class::add_event(double x, double y, double z, double E){ //Tricky
       way to pass the LUT by reference
2  //Iterate through and find the bin corresponding to x, y, position. Then add t
       to that bin and the nearest neighbors.
3  double phi = atan2(x,y);
4  if(phi< 0){ phi = 2*3.14159+ phi;}
5  double r = sqrt(x*x + y*y + z*z);
6  double costheta = z/r;
7  double dnk, upk, dnl, upl;
8  double k_test, j_test;
9  double energy = this->Energy_LUT_values[0];
10 double windowScale = 100;
11 double windownMin = .05*energy;
12 double window = windownMin;
13 //double (LUT)[100][60][4];
14
15 //negative half
16 if(costheta <= 0){
17 for(int i =0; i<99; i++){ //Iterate through r
18 if((costheta <= this->neg_Raw_LUT[i][0][0] && costheta >= this->neg_Raw_LUT[i
       +1][0][0]) || (costheta < this->neg_Raw_LUT[99][0][0])){ // If found the
       correct r
19 if(costheta < this->neg_Raw_LUT[99][0][0]){i=99;}//Capture overflow.
20 //if(true){
21 for(int j=0; j<59; j++){ //Iterate through phi
22 if( phi >=this->neg_Raw_LUT[i][j][1] && phi <=this->neg_Raw_LUT[i][j+1][1]){
       //If found the correct phi
23
24 this->written++;
25 //if(energy/((this->neg_Raw_LUT[i][j][3])/windowScale) < windownMin){  window
       = windownMin;} else { window = energy/((this->neg_Raw_LUT[i][j][3])/
       windowScale);}
26 //if(fabs((this->neg_Raw_LUT[i][j][2])-E) < window) this->neg_Raw_LUT[i][j][2]
       = ((this->neg_Raw_LUT[i][j][2])*(this->neg_Raw_LUT[i][j][3]) + E)/((this
       ->neg_Raw_LUT[i][j][3])+1); //Add the t to the bin average value.
27 //if(fabs((this->neg_Raw_LUT[i][j][2])-E) < window) this->neg_Raw_LUT[i][j][3]
       += 1; //Increment the bin counter by 1
28
29 dnk = i; upk = i;
30 if(i-2 >= 0){dnk = i-2;}else{dnk = 0;} //The nearest neighbors are hard coded
       here
```

```
31 if(i+2 <100){upk = i+2;}else{upk = 99;} //add one because this will include +2
       in the for loops.
32
33 for(int k = dnk; k <= upk; k++){ // Extend binning in r direction by n=4.
       There should be n^2 additions. There are 4 cases for phi.
34 if(energy/((this->neg_Raw_LUT[k][j][3])/windowScale) < windownMin){  window =
       windownMin;} else { window = energy/((this->neg_Raw_LUT[k][j][3])/
       windowScale);}
35 if(fabs((this->neg_Raw_LUT[k][j][2])-E) < window) this->neg_Raw_LUT[k][j][2] =
       ((this->neg_Raw_LUT[k][j][2])*(this->neg_Raw_LUT[k][j][3]) + E)/((this->
       neg_Raw_LUT[k][j][3])+1); //Add the t to the bin average value.
36 if(fabs((this->neg_Raw_LUT[k][j][2])-E) < window) this->neg_Raw_LUT[k][j][3]
       += 1; //Increment the bin counter by 1
37
38 for(int l = 1;l < 3; l++){//The nearest neighbors are hard coded here
39 if(j-l < 0){ //negative phi extension
40 if(energy/((this->neg_Raw_LUT[k][60+(j-l)][3])/windowScale) < windownMin){
       window = windownMin;} else { window = energy/((this->neg_Raw_LUT[k][60+(j-
       l)][3])/windowScale);}
41 if(fabs((this->neg_Raw_LUT[k][60+(j-l)][2])-E) < (this->neg_Raw_LUT[k][60+(j-l
       )][2])/((this->neg_Raw_LUT[k][60+(j-l)][3])/window)) this->neg_Raw_LUT[k
       ][60+(j-l)][2] = ((this->neg_Raw_LUT[k][60+(j-l)][2])*(this->neg_Raw_LUT[k
       ][60+(j-l)][3]) + E)/((this->neg_Raw_LUT[k][60+(j-l)][3])+1); //Add the t
       to the bin average value.
42 if(fabs((this->neg_Raw_LUT[k][60+(j-l)][2])-E) < (this->neg_Raw_LUT[k][60+(j-l
       )][2])/((this->neg_Raw_LUT[k][60+(j-l)][3])/window)) this->neg_Raw_LUT[k
       ][60+(j-l)][3] += 1; //Increment the bin counter by 1
43 }
44
45 if(j-l >= 0){
46 if(energy/((this->neg_Raw_LUT[k][j-l][3])/windowScale) < windownMin){ window =
       windownMin;} else { window = energy/((this->neg_Raw_LUT[k][j-l][3])/
       windowScale);}
47 if(fabs((this->neg_Raw_LUT[k][j-l][2])-E) < window) this->neg_Raw_LUT[k][j-l
       ][2] = ((this->neg_Raw_LUT[k][j-l][2])*(this->neg_Raw_LUT[k][j-l][3]) + E)
       /((this->neg_Raw_LUT[k][j-l][3])+1); //Add the t to the bin average value.
48 if(fabs((this->neg_Raw_LUT[k][j-l][2])-E) < window) this->neg_Raw_LUT[k][j-l
       ][3] += 1; //Increment the bin counter by 1
49
50 }
51
52 if(j+l < 60){
53 if(energy/((this->neg_Raw_LUT[k][j+l][3])/windowScale) < windownMin){ window =
       windownMin;} else { window = energy/((this->neg_Raw_LUT[k][j+l][3])/
       windowScale);}
54 if(fabs((this->neg_Raw_LUT[k][j+l][2])-E) < window) this->neg_Raw_LUT[k][j+l
       ][2] = ((this->neg_Raw_LUT[k][j+l][2])*(this->neg_Raw_LUT[k][j+l][3]) + E)
       /((this->neg_Raw_LUT[k][j+l][3])+1); //Add the t to the bin average value.
55 if(fabs((this->neg_Raw_LUT[k][j+l][2])-E) < window) this->neg_Raw_LUT[k][j+l
       ][3] += 1; //Increment the bin counter by 1
56
57 }
58
59 if(j+l >= 60){ //positive phi extension
```

```
60 if(energy/((this->neg_Raw_LUT[k][(j+1)-60][3])/windowScale) < windownMin){
       window = windownMin;} else { window = energy/((this->neg_Raw_LUT[k][(j+1)
       -60][3])/windowScale);}
61 if(fabs((this->neg_Raw_LUT[k][(j+1)-60][2])-E) < window) this->neg_Raw_LUT[k
       ][(j+1)-60][2] = ((this->neg_Raw_LUT[k][(j+1)-60][2])*(this->neg_Raw_LUT[k
       ][(j+1)-60][3]) + E)/((this->neg_Raw_LUT[k][(j+1)-60][3])+1); //Add the t
       to the bin average value.
62 if(fabs((this->neg_Raw_LUT[k][(j+1)-60][2])-E) < window) this->neg_Raw_LUT[k
       ][(j+1)-60][3] += 1; //Increment the bin counter by 1
63 }
64 }
65 }
66
67 break; //break out of the phi loop, no need to iterate more.
68 }
69 }
70
71 break; //break out of the r loop, no need to iterate more.
72 }
73 }
74 }
75
76 if(costheta > 0){
77 //positive half
78 for(int i =0; i<99; i++){ //Iterate through r
79 if( (costheta >= this->pos_Raw_LUT[i][0][0] && costheta <= this->pos_Raw_LUT[i
       +1][0][0]) || (costheta > this->pos_Raw_LUT[99][0][0])){ // If found the
       correct r
80 if(costheta > this->pos_Raw_LUT[99][0][0]){i=99;}
81 //if(true){
82 for(int j=0; j<59; j++){ //Iterate through phi
83 if( phi >=this->pos_Raw_LUT[i][j][1] && phi <= this->pos_Raw_LUT[i][j+1][1] ){
84
85 //if(energy/((this->pos_Raw_LUT[i][j][3])/windowScale) < windownMin){  window
       = windownMin;} else { window = energy/((this->pos_Raw_LUT[i][j][3])/
       windowScale);}
86 //if(fabs((this->pos_Raw_LUT[i][j][2])-E) < window) this->pos_Raw_LUT[i][j][2]
        = ((this->pos_Raw_LUT[i][j][2])*(this->pos_Raw_LUT[i][j][3]) + E)/((this
       ->pos_Raw_LUT[i][j][3])+1); //Add the t to the bin average value.
87 //if(fabs((this->pos_Raw_LUT[i][j][2])-E) < window) this->pos_Raw_LUT[i][j][3]
        += 1; //Increment the bin counter by 1
88
89 dnk = i; upk = i;
90 if(i-2 >= 0){dnk = i-2;}else{dnk = 0;} //The nearest neighbors are hard coded
       here
91 if(i+2 <100){upk = i+2;}else{upk = 99;} //add one because this will include +2
        in the for loops.
92
93 for(int k = dnk; k <= upk; k++){ // Extend binning in r direction by n=4.
       There should be n^2 additions. There are 4 cases for phi.
94 if(energy/((this->pos_Raw_LUT[k][j][3])/windowScale) < windownMin){  window =
       windownMin;} else { window = energy/((this->pos_Raw_LUT[k][j][3])/
       windowScale);}
```

```
95  if(fabs((this->pos_Raw_LUT[k][j][2])-E) < window) this->pos_Raw_LUT[k][j][2] =
        ((this->pos_Raw_LUT[k][j][2])*(this->pos_Raw_LUT[k][j][3]) + E)/((this->
    pos_Raw_LUT[k][j][3])+1); //Add the t to the bin average value.
96  if(fabs((this->pos_Raw_LUT[k][j][2])-E) < window) this->pos_Raw_LUT[k][j][3]
    += 1; //Increment the bin counter by 1
97
98  for(int l = 1;l < 3; l++){ //The nearest neighbors are hard coded here
99  if(j-l < 0){ // negative phi extension
100 if(energy/((this->pos_Raw_LUT[k][60+(j-l)][3])/windowScale) < windownMin){
    window = windownMin;} else { window = energy/((this->pos_Raw_LUT[k][60+(j-
    l)][3])/windowScale);}
101 if(fabs((this->pos_Raw_LUT[k][60+(j-l)][2])-E) < window) this->pos_Raw_LUT[k
    ][60+(j-l)][2] = ((this->pos_Raw_LUT[k][60+(j-l)][2])*(this->pos_Raw_LUT[k
    ][60+(j-l)][3]) + E)/((this->pos_Raw_LUT[k][60+(j-l)][3])+1); //Add the t
    to the bin average value.
102 if(fabs((this->pos_Raw_LUT[k][60+(j-l)][2])-E) < window) this->pos_Raw_LUT[k
    ][60+(j-l)][3] += 1; //Increment the bin counter by 1
103 }
104
105 if(j-l >= 0){
106 if(energy/((this->pos_Raw_LUT[k][j-l][3])/windowScale) < windownMin){ window =
     windownMin;} else { window = energy/((this->pos_Raw_LUT[k][j-l][3])/
    windowScale);}
107 if(fabs((this->pos_Raw_LUT[k][j-l][2])-E) < window) this->pos_Raw_LUT[k][j-l
    ][2] = ((this->pos_Raw_LUT[k][j-l][2])*(this->pos_Raw_LUT[k][j-l][3]) + E)
    /((this->pos_Raw_LUT[k][j-l][3])+1); //Add the t to the bin average value.
108 if(fabs((this->pos_Raw_LUT[k][j-l][2])-E) < window) this->pos_Raw_LUT[k][j-l
    ][3] += 1; //Increment the bin counter by 1
109 }
110
111 if(j+l < 60){
112 if(energy/((this->pos_Raw_LUT[k][j+l][3])/windowScale) < windownMin){ window =
     windownMin;} else { window = energy/((this->pos_Raw_LUT[k][j+l][3])/
    windowScale);}
113 if(fabs((this->pos_Raw_LUT[k][j+l][2])-E) < window) this->pos_Raw_LUT[k][j+l
    ][2] = ((this->pos_Raw_LUT[k][j+l][2])*(this->pos_Raw_LUT[k][j+l][3]) + E)
    /((this->pos_Raw_LUT[k][j+l][3])+1); //Add the t to the bin average value.
114 if(fabs((this->pos_Raw_LUT[k][j+l][2])-E) < window) this->pos_Raw_LUT[k][j+l
    ][3] += 1; //Increment the bin counter by 1
115 }
116
117 if(j+l >= 60){ //positive phi extension
118 if(energy/((this->pos_Raw_LUT[k][(j+l)-60][3])/windowScale) < windownMin){
    window = windownMin;} else { window = energy/((this->pos_Raw_LUT[k][(j+l)
    -60][3])/windowScale);}
119 if(fabs((this->pos_Raw_LUT[k][(j+l)-60][2])-E) < window) this->pos_Raw_LUT[k
    ][(j+l)-60][2] = ((this->pos_Raw_LUT[k][(j+l)-60][2])*(this->pos_Raw_LUT[k
    ][(j+l)-60][3]) + E)/((this->pos_Raw_LUT[k][(j+l)-60][3])+1); //Add the t
    to the bin average value.
120 if(fabs((this->pos_Raw_LUT[k][(j+l)-60][2])-E) < window) this->pos_Raw_LUT[k
    ][(j+l)-60][3] += 1; //Increment the bin counter by 1
121 }
122 }
123 }
```

```
124
125 break; //break out of the phi loop, no need to iterate more.
126 }
127 }
128
129 break; //break out of the r loop, no need to iterate more.
130 }
131 }
132 }
133 };
```

F.3 LUT Implementation

Below is the code used to implement the lookup table.

```
1  void particle_class::LUT_IT_UP(double (&neg_LUT)[100][60][4], double (&pos_LUT
   )[100][60][4], double tzero){ //Pass by reference a large LUT array
2  double phi = atan2(this->phy->mom.x,this->phy->mom.y);
3  if(phi< 0){ phi = 2*3.14159 + phi;}
4  double theta = this->phy->mom.Theta();
5  bool found = false;
6  double scale_factor;
7
8  if(cos(theta) <= 0.){
9  for(int i =0; i<99; i++){ //Iterate through r
10 if((cos(theta) <= neg_LUT[i][0][0] && cos(theta) >= neg_LUT[i+1][0][0]) || (
   cos(theta) < neg_LUT[99][0][0])){ // If found the correct r
11 if(cos(theta) < neg_LUT[99][0][0]){i=99;}//Capture overflow.
12 for(int j=0; j<59; j++){ //Iterate through phi
13 if( phi >=neg_LUT[i][j][1] && phi <=neg_LUT[i][j+1][1]){
14
15 scale_factor = 0;
16 this->phy->mom.x = this->phy->mom.x*sqrt(neg_LUT[i][j][2]); //No smoothing
   here. Implement linear smoothing later
17 this->phy->mom.y = this->phy->mom.y*sqrt(neg_LUT[i][j][2]);
18 this->phy->mom.z = this->phy->mom.z*sqrt(neg_LUT[i][j][2]);
19 found = true;
20 break;
21 }
22 }
23 }
24 if(found) break;
25 }
26 }
27
28 if(cos(theta) > 0.){
29 for(int i =0; i<99; i++){ //Iterate through r
30 if( (cos(theta) >= pos_LUT[i][0][0] && cos(theta) <= pos_LUT[i+1][0][0]) || (
   cos(theta) > pos_LUT[99][0][0]) ){ // If found the correct r
31 if(cos(theta) > pos_LUT[99][0][0]){i=99;}//Capture overflow.
32 for(int j=0; j<59; j++){ //Iterate through phi
33 if( phi >=pos_LUT[i][j][1] && phi <=pos_LUT[i][j+1][1]){
34 scale_factor = 0;
```

```
35 this->phy->mom.x = this->phy->mom.x*sqrt(pos_LUT[i][j][2]); //No smoothing
       here. Implement linear smoothing later
36 this->phy->mom.y = this->phy->mom.y*sqrt(pos_LUT[i][j][2]);
37 this->phy->mom.z = this->phy->mom.z*sqrt(pos_LUT[i][j][2]);
38 found = true;
39 break;
40 }
41 }
42 }
43 if(found) break;
44 }
45 }
```

Appendix G
Simion Code

This appendix contains the SIMION .gem files used for simulating the fringe field and spectrometer line mode.

G.1 Fringe Field

Below is the code used for the mesh fringe field simulation.

```
1  PA_Define(3789,2400,1,C,Y,E)
2
3  ;This is Ave Gatton's mod of JB Williams detector simulation. A grid is
       attempted.
4
5  ;1 grid = 0.1mm/3 = .033mm = 33um
6  ; rectangular mesh spacing needs 200um*.11 = 22um and grid lines every ~10 gu.
7  ; Replace the rectangular mesh with a circular grid. To preserve the
       transmittance *and* the linear circumference to surface area, you must
       half the size (to first approximation).
8  ; Circular mesh spacing needs 100um*.2 = 20um with grid lines every ~5 gu.
9  ; So the grid will be too large by a factor of 1.5. That is, each grid box
       will be ~150um wide where it should be 100. This is still pretty close
       though.
10 ; 2400/5 = 480 gridlines.
11
12
13
14 ;mcp stack and ring
15 locate(0,0){
16 e(1){
17 fill{
18 within{
19 polyline( 0,2250,        0,0,     3,0,     3,2250,          0,2250,
       0,1776,                    90,1977,        90,2250,        0,2250)
20 }
21 }
22 }
23 }
24
25 include(mesh2.gem) ;includes a very large "mesh" (collection of single dots),
       in the file.
26 ;thick end plate moved to mesh file
27
28 ;the global locate move
29 locate(51,0){
30
31 ;spec plate 1
```

```
32 locate(540,0,0,1,180){
33 e(3){
34 fill{
35 within{
36 box(0,2400,15,1950)
37 }}}}
38
39
40 ;spec plate 2
41 locate(705,0,0,1,180){
42 e(4){
43 fill{
44 within{
45 box(0,2400,15,1950)
46 }}}}
47
48 ;spec plate 3
49 locate(870,0,0,1,180){
50 e(5){
51 fill{
52 within{
53 box(0,2400,15,1950)
54 }}}}
55
56
57
58 ;spec plate 4
59 locate(1035,0,0,1,180){
60 e(6){
61 fill{
62 within{
63 box(0,2400,15,1950)
64 }}}}
65
66
67
68 ;spec plate 5
69 locate(1200,0,0,1,180){
70 e(7){
71 fill{
72 within{
73 box(0,2400,15,1950)
74 }}}}
75
76 ;spec plate 6 missing jet plate
77 ;locate(1365,0,0,1,180){
78 ;        e(8){
79 ;            fill{
80 ;                within{
81 ;                    box(0,2400,15,1950)
82 ;        }}}}
83
84 ;spec plate 7
85 locate(1530,0,0,1,180){
```

```
86  e(8){
87   fill{
88   within{
89   box(0,2400,15,1950)
90   }}}}
91
92   ;spec plate 8
93   locate(1695,0,0,1,180){
94   e(9){
95   fill{
96   within{
97   box(0,2400,15,1950)
98   }}}}
99
100  ;spec plate 9
101  locate(1860,0,0,1,180){
102  e(10){
103  fill{
104  within{
105  box(0,2400,15,1950)
106  }}}}
107
108
109  ;spec plate 10
110  locate(2025,0,0,1,180){
111  e(11){
112  fill{
113  within{
114  box(0,2400,15,1950)
115  }}}}
116
117  ;spec plate 11
118  locate(2190,0,0,1,180){
119  e(12){
120  fill{
121  within{
122  box(0,2400,15,1950)
123  }}}}
124
125
126  ;spec plate 12
127  locate(2355,0,0,1,180){
128  e(13){
129  fill{
130  within{
131  box(0,2400,15,1950)
132  }}}}
133
134  }
135
136
137
138
139  ;spec plate 13
```

```
140 locate(2571,0,0,1,180){
141 e(14){
142 fill{
143 within{
144 box(0,2400,15,1950)
145 }}}}
146
147
148 ;spec plate 14
149 locate(2736,0,0,1,180){
150 e(15){
151 fill{
152 within{
153 box(0,2400,15,1950)
154 }}}}
155 ;spec plate 15
156 locate(2901,0,0,1,180){
157 e(16){
158 fill{
159 within{
160 box(0,2400,15,1950)
161 }}}}
162 ;spec plate 16
163 locate(3066,0,0,1,180){
164 e(17){
165 fill{
166 within{
167 box(0,2400,15,1950)
168 }}}}
169 ;spec plate 17
170 locate(3231,0,0,1,180){
171 e(18){
172 fill{
173 within{
174 box(0,2400,15,1950)
175 }}}}
176 ;spec plate 18
177 locate(3396,0,0,1,180){
178 e(19){
179 fill{
180 within{
181 box(0,2400,15,1950)
182 }}}}
183
184 ;spec plate 19 (this is the last accel plate and the front of the plate/grid
      should be at 1182gu
185 locate(3546,0,0,1,0){
186 e(20){
187 fill{
188 within{
189 ;polyline( 0,800, 0,0, 0,800, 0,650, 30,675, 30,700, 61,700, 81,719, 81,800,
      0,800)
190 polyline( 0,2400, 0,0, 0,2400, 0,1950, 90,2025, 90,2100, 183,2100, 243,2157,
      243,2400, 0,2400)
```

```
}}}}
```

G.2 Line Mode

Below is the code used for the line mode spectrometer simulation.

```
;PA_Define(3789,2400,1,C,Y,E)
;PA_Define(6263,1578,1,C,Y,E)
PA_Define(5396,1818,1,C,Y,E)

;This is a clean and simple simulation of the spectrometer. The goal is a rough approximation to a zoom effect on the interaction region.

; 80mm x 237.4mm PA size in mm
; 1 grid = 0.1mm/3 = .044mm = 44um
; Grids are modelled as ideal perfect surfaces of transmittance
; 18 plates accel region (1 missing)
; 23 plates electron drift
; 5mm between plates, .4 mm plate thickness (Use 1 gu), 3mm mesh holders.
; No detector simulation: detector grid to detector grid only.




;Recoil Grid
locate(0,0){
e(1){
fill{
within{
polyline(       0,0,
1,0,
1,1477,
69,1477,
69,1795,
0,1795
)
}
}
}
}

;//////////////////////////////////////////////////////////////////////////////////////////

;the global locate move to end of the recoil mesh
locate(69,0){

;spec plate 1
locate(113,1477,0,1,0){
e(2){
fill{
within{
```

```
45 box(0,0,9,341)
46 }
47 }
48 }
49 }
50
51 ;spec plate 2
52 locate(236,1477,0,1,0){
53 e(3){
54 fill{
55 within{
56 box(0,0,9,341)
57 }
58 }
59 }
60 }
61
62
63 ;spec plate 3
64 locate(359,1477,0,1,0){
65 e(4){
66 fill{
67 within{
68 box(0,0,9,341)
69 }
70 }
71 }
72 }
73
74
75 ;spec plate 4
76 locate(482,1477,0,1,0){
77 e(5){
78 fill{
79 within{
80 box(0,0,9,341)
81 }
82 }
83 }
84 }
85
86 ;spec plate 5
87 locate(605,1477,0,1,0){
88 e(6){
89 fill{
90 within{
91 box(0,0,9,341)
92 }
93 }
94 }
95 }
96
97 ;Skip Plate 6: the jet gap/ target region
98 ;spec plate 6
```

```
99  ;locate(738,1477,0,1,0){
100 ;       e(7){
101 ;               fill{
102 ;                       within{
103 ;                               box(0,0,9,341)
104 ;                       }
105 ;               }
106 ;       }
107 ;}
108
109 ;spec plate 7
110 locate(861,1477,0,1,0){
111 e(7){
112  fill{
113 within{
114 box(0,0,9,341)
115 }
116 }
117 }
118 }
119
120 ;spec plate 8
121 locate(974,1477,0,1,0){
122 e(8){
123  fill{
124 within{
125 box(0,0,9,341)
126 }
127 }
128 }
129 }
130
131 ;spec plate 9
132 locate(1097,1477,0,1,0){
133 e(9){
134  fill{
135 within{
136 box(0,0,9,341)
137 }
138 }
139 }
140 }
141
142 ;spec plate 10
143 locate(1220,1477,0,1,0){
144 e(10){
145  fill{
146 within{
147 box(0,0,9,341)
148 }
149 }
150 }
151 }
152
```

```
153 ;spec plate 11
154 locate(1343,1477,0,1,0){
155 e(11){
156 fill{
157 within{
158 box(0,0,9,341)
159 }
160 }
161 }
162 }
163
164 ;spec plate 12
165 locate(1466,1477,0,1,0){
166 e(12){
167 fill{
168 within{
169 box(0,0,9,341)
170 }
171 }
172 }
173 }
174
175 ;spec plate 13
176 locate(1589,1477,0,1,0){
177 e(13){
178 fill{
179 within{
180 box(0,0,9,341)
181 }
182 }
183 }
184 }
185
186 ;spec plate 14
187 locate(1712,1477,0,1,0){
188 e(14){
189 fill{
190 within{
191 box(0,0,9,341)
192 }
193 }
194 }
195 }
196
197 ;spec plate 15
198 locate(1835,1477,0,1,0){
199 e(15){
200 fill{
201 within{
202 box(0,0,9,341)
203 }
204 }
205 }
206 }
```

```
207
208 ;spec plate 16
209 locate(1958,1477,0,1,0){
210 e(16){
211 fill{
212 within{
213 box(0,0,9,341)
214 }
215 }
216 }
217 }
218
219 ;spec plate 17
220 locate(2081,1477,0,1,0){
221 e(17){
222 fill{
223 within{
224 box(0,0,9,341)
225 }
226 }
227 }
228 }
229
230 ;spec plate 18
231 locate(2204,1477,0,1,0){
232 e(18){
233 fill{
234 within{
235 box(0,0,9,341)
236 }
237 }
238 }
239 }
240
241 } ; End accel region locate
242
243
244 ;//
       ////////////////////////////////////////////////////////////////////////////////
245 ;Electron Drift Mesh
246 locate(2386,0){
247 ;Mesh Holder, no hard grid
248 e(19){
249 fill{
250 within{
251 polyline(       0,1477,
252 69,1477,
253 69,1795,
254 0,1795
255 )
256 }
257 }
258 }
```

```
259
260 ;Non-electrode ideal grid
261 e(20){
262 fill{
263 within{
264 box(    0,0,
265 0,1477,
266 )
267 }
268 }
269 }
270
271 };End Electron Drift Locate
272
273 ;//
       ////////////////////////////////////////////////////////////////////////////////
274 ;Begin electron Drift Region
275 locate(2455,0){
276
277 ;spec plate 19
278 locate(113,1477,0,1,0){
279 e(21){
280 fill{
281 within{
282 box(0,0,9,341)
283 }
284 }
285 }
286 }
287
288 ;spec plate 20
289 locate(236,1477,0,1,0){
290 e(22){
291 fill{
292 within{
293 box(0,0,9,341)
294 }
295 }
296 }
297 }
298
299
300 ;spec plate 21
301 locate(359,1477,0,1,0){
302 e(23){
303 fill{
304 within{
305 box(0,0,9,341)
306 }
307 }
308 }
309 }
310
```

```
311
312 ;spec plate 22
313 locate(482,1477,0,1,0){
314 e(24){
315 fill{
316 within{
317 box(0,0,9,341)
318 }
319 }
320 }
321 }
322
323 ;spec plate 23
324 locate(605,1477,0,1,0){
325 e(25){
326 fill{
327 within{
328 box(0,0,9,341)
329 }
330 }
331 }
332 }
333
334 ;spec plate 24
335 locate(728,1477,0,1,0){
336 e(26){
337 fill{
338 within{
339 box(0,0,9,341)
340 }
341 }
342 }
343 }
344
345 ;spec plate 25
346 locate(851,1477,0,1,0){
347 e(27){
348 fill{
349 within{
350 box(0,0,9,341)
351 }
352 }
353 }
354 }
355
356 ;spec plate 26
357 locate(974,1477,0,1,0){
358 e(28){
359 fill{
360 within{
361 box(0,0,9,341)
362 }
363 }
364 }
```

```
365 }
366
367 ;spec plate 27
368 locate(1097,1477,0,1,0){
369 e(29){
370 fill{
371 within{
372 box(0,0,9,341)
373 }
374 }
375 }
376 }
377
378 ;spec plate 28
379 locate(1220,1477,0,1,0){
380 e(30){
381 fill{
382 within{
383 box(0,0,9,341)
384 }
385 }
386 }
387 }
388
389 ;spec plate 29
390 locate(1343,1477,0,1,0){
391 e(31){
392 fill{
393 within{
394 box(0,0,9,341)
395 }
396 }
397 }
398 }
399
400
401 ;spec plate 30
402 locate(1466,1477,0,1,0){
403 e(32){
404 fill{
405 within{
406 box(0,0,9,341)
407 }
408 }
409 }
410 }
411
412 ;spec plate 31
413 locate(1589,1477,0,1,0){
414 e(33){
415 fill{
416 within{
417 box(0,0,9,341)
418 }
```

```
419 }
420 }
421 }
422
423 ;spec plate 32
424 locate(1712,1477,0,1,0){
425 e(34){
426 fill{
427 within{
428 box(0,0,9,341)
429 }
430 }
431 }
432 }
433
434 ;spec plate 33
435 locate(1835,1477,0,1,0){
436 e(35){
437 fill{
438 within{
439 box(0,0,9,341)
440 }
441 }
442 }
443 }
444
445 ;spec plate 34
446 locate(1958,1477,0,1,0){
447 e(36){
448 fill{
449 within{
450 box(0,0,9,341)
451 }
452 }
453 }
454 }
455
456 ;spec plate 35
457 locate(2081,1477,0,1,0){
458 e(37){
459 fill{
460 within{
461 box(0,0,9,341)
462 }
463 }
464 }
465 }
466
467 ;spec plate 36
468 locate(2204,1477,0,1,0){
469 e(38){
470 fill{
471 within{
472 box(0,0,9,341)
```

```
473 }
474 }
475 }
476 }
477
478 ;spec plate 37
479 locate(2327,1477,0,1,0){
480 e(39){
481 fill{
482 within{
483 box(0,0,9,341)
484 }
485 }
486 }
487 }
488
489 ;spec plate 38
490 locate(2450,1477,0,1,0){
491 e(40){
492 fill{
493 within{
494 box(0,0,9,341)
495 }
496 }
497 }
498 }
499
500 ;spec plate 39
501 locate(2573,1477,0,1,0){
502 e(41){
503 fill{
504 within{
505 box(0,0,9,341)
506 }
507 }
508 }
509 }
510
511 ;spec plate 40
512 locate(2696,1477,0,1,0){
513 e(42){
514 fill{
515 within{
516 box(0,0,9,341)
517 }
518 }
519 }
520 }
521
522 ;spec plate 41
523 locate(2819,1477,0,1,0){
524 e(43){
525 fill{
526 within{
```

```
box(0,0,9,341)
}
}
}
}


} ; End drift region locate

;Electron Spec Grid
locate(5387,0){
e(44){
fill{
within{
polyline(       0,0,
1,0,
1,1795,
0,1795
)
}
}
}
}

;locate(2455,0){
;       ;lens insert
;       locate(1343,0){
;               e(45){
;                       fill{
;                               within{
;                                       polyline(       0,114,
;                                                               5,114,
;                                                               5,119,
;                                                               0,119
;                                                               )
;                               }
;                       }
;               }
;       }
;}
```

Appendix H
ROOT Macros

This appendix contains select macros for the ROOT data-analysis program. We have chosen to include only macros used to generate background subtracted and chi-squared fit tests.

H.1 Background Subtraction

```
1  #include "TMath.h"
2  #include <stdio>
3
4  void SubSub(){
5
6  gDirectory->cd("/ion LASER");
7  TH1D* hi1 = (TH1D*)gDirectory->Get("e1_ke_HD_pos");
8
9  gDirectory->cd("/ion ALS");
10 TH1D* hi2 = (TH1D*)gDirectory->Get("e1_ke_HD_pos");
11
12 //
       ////////////////////////////////////////////////////////////////////////////////
13
14 if (hi1->GetNbinsX() != hi2->GetNbinsX())
15 {
16 cout << "Histos have to have the same binning" << endl;
17 return 0;
18 }
19
20 TString HistoName = hi1->GetName();
21 HistoName += "_sub";
22
23 TString HistoTitle = hi2->GetName();
24 HistoTitle += " substracted from ";
25 HistoTitle += hi1->GetName();
26
27
28 TH1D * sub = new TH1D(HistoName.Data(), HistoTitle.Data(), hi1->GetNbinsX(),
       hi1->GetXaxis()->GetXmin(), hi1->GetXaxis()->GetXmax());
29
30 sub->Add(hi1, hi2, 1, -1);
31
32 double summary = 0;
33 for (int i; i <= hi1->GetNbinsX(); i++) {
34 summary += fabs(sub->GetBinContent(i));
35 }
```

```
36 cout << endl; cout << summary; cout << endl;
37
38 sub->Draw("HIST");
39
40
41 return;
42 }
```

H.2 Chi-squared Fit

```
1  void ChiChi(){
2
3  gDirectory->cd("/ion_LASER");
4  TH1D* hi1 = (TH1D*)gDirectory->Get("e1_ke_HD_neg");
5
6  gDirectory->cd("/ion_ALS");
7  TH1D* hi2 = (TH1D*)gDirectory->Get("e1_ke_HD_neg");
8
9  if (hi1->GetNbinsX() != hi2->GetNbinsX())
10 {
11 cout << "Histos_have_to_have_the_same_binning" << endl;
12 return 0;
13 }
14
15 //Set up the residual array to receive the residuals
16 int residualN = hi1->GetNbinsX();
17 double *res = new double[residualN];
18
19 //Perfomr ChiSquare Test
20 hi1->Chi2Test(hi2, "UW_P", res);
21
22 //Set up the residual histogram.
23 TString HistoName = hi1->GetName();
24 HistoName += "_sub";
25
26 //TString HistoTitle = hi2->GetName();
27 TString HistoTitle = "Laser_and_ALS_Residuals";
28 //HistoTitle += hi1->GetName();
29
30 TH1D * residualHist = new TH1D(HistoName.Data(), HistoTitle.Data(), hi1->
       GetNbinsX(), hi1->GetXaxis()->GetXmin(), hi1->GetXaxis()->GetXmax());
31 for (int i = 1; i <= hi1->GetNbinsX(); i++){
32 residualHist->SetBinContent(i, res[i]);
33 }
34
35
36 //sub->Add(hi1, hi2, 1, -1);
37
38 residualHist->Draw("HIST");
39
40 delete[] res;
41 return;
42 }
```